

# The silicon strip detector of the ATLAS Inner Tracker: from individual sensing units to multi-module petal structures



**tu** technische universität  
dortmund

**Alessia Renardi**

PhD in Physics  
Deutsches Elektronen-Synchrotron  
University of Dortmund

Hamburg 2022

Der Fakultät Physik der TU Dortmund zur Erlangung des akademischen Grades eines Doktors der Naturwissenschaften vorgelegte Dissertation.

1. Gutachter : Prof. Dr. Kevin Kröniger (Technische Universität Dortmund)
  2. Gutachter : Prof. Dr. Ingrid-Maria Gregor (Universität Bonn & DESY Hamburg)
- Vorsitzender der Prüfungskommission : Prof. Dr. Wolfgang Rhode (TU Dortmund)  
Vertretung der wiss. Mitarbeiter : Dr. Jörg Debus (TU Dortmund)

Datum der mündlichen Prüfung: 04. April 2022

# Abstract

Nowadays particle detector technology is taking big steps forwards and new devices dedicated to particle physics show very high performance. Particularly the semiconductor detectors have advanced significantly and are used for tracking purposes in the *A Toroidal LHC Apparatus* (ATLAS) experiment at CERN thanks to their excellent spacial resolution: the compact size of the silicon and its high granularity allow to reach a precision measurement of few tens of microns.

This thesis is focused on the upgrade of the ATLAS tracking detector required for the *High Luminosity Large Hadron Collider* (HL-LHC), starting in 2027. The HL-LHC foresees an integrated luminosity of  $L = 3000 \text{ fb}^{-1}$ , which comes with an unprecedented rate of proton collisions, with a pile-up of  $\langle \eta \rangle = 200$ , and very high radiation doses. As the current inner detector has not been designed for the HL-LHC environmental conditions, an all-silicon *Inner Tracker* (ITk) will take its place during Phase-II upgrade of the ATLAS experiment.

The ITk strip endcap sub-detector is the main topic of this PhD project. The investigation covers the assembly of silicon strip endcap modules and their loading on a local support structure. The building and loading procedures are presented as well as results of quality control (QC) tests carried out on prototyping components to establish their working performance and the fulfillment of the specifications. This work provides the procedure optimization in order to achieve the requirements imposed by the collaboration.

Results on prototyping components, such as a fully electrical module and a semi-electrical petal, both built and tested at DESY, are presented. They are followed by tests on an electrical petal performed at low temperature with the evaporative  $\text{CO}_2$  cooling technique. The QC tests carried out on all prototypes have demonstrated that they have been properly assembled and are fully functional. Moreover they fulfil the respective requirements validating therefore the components design and the building methods.

# Zusammenfassung

In der heutigen Zeit macht die Detektortechnologie große Fortschritte, und neue Geräte für die Teilchenphysik sind sehr leistungsstark. Insbesondere die Halbleiterdetektoren haben sich erheblich weiterentwickelt und werden dank ihrer exzellenten räumlichen Auflösung im *A Toroidal LHC Apparatus* (ATLAS) Experiment am CERN für die Spurrekonstruktion eingesetzt. Die dünnen Siliziumsensoren sowie die hohe Granularität ermöglichen Präzisionsmessungen mit einer Auflösung von einigen zehn Mikrometern.

Die vorliegende Arbeit befasst sich mit dem Upgrade des ATLAS-Spurdetektors, das für den im Jahr 2027 in Betrieb gehenden High Luminosity Large Hadron Collider (HL-LHC) erforderlich ist. Der HL-LHC sieht eine integrierte Luminosität von  $L = 3000 \text{ fb}^{-1}$  vor, was mit einer bisher unerreichten Rate von Protonkollisionen mit einem Pile-up von  $\langle \eta \rangle = 200$  und sehr hohen Strahlungs Dosen einhergeht. Da der derzeitige innere Spurdetektor nicht für die Umgebungsbedingungen des HL-LHC ausgelegt ist, wird er während des Phase-II-Upgrades durch den neuen, vollständig aus Siliziumsensoren bestehenden *Inner Tracker* (ITk) ersetzt werden.

Der ITk-Streifen-Endkappen-Subdetektor ist das Hauptthema dieses PhD-Projekts. Es umfasst den Zusammenbau von Siliziumstreifen-Endkappenmodulen und deren Montage auf einer lokalen Trägerstruktur. Es werden die Konstruktions- und Montageverfahren sowie die Ergebnisse von Qualitätskontrolltests vorgestellt, die an Prototypkomponenten durchgeführt wurden, um deren Funktionalität sowie die Erfüllung der Spezifikationen sicherzustellen. Im Rahmen dieser Arbeit wurden die Verfahren optimiert, um die von der Kollaboration gestellten Anforderungen zu erfüllen. Es werden Ergebnisse zu Prototypkomponenten, wie beispielsweise einem vollständig elektrischen Modul und einem halbelektrischen Petals vorgestellt, die beide bei DESY gebaut und getestet wurden. Des Weiteren werden Tests an einem elektrischen Petal vorgestellt, die bei niedrigen Temperaturen mit der  $\text{CO}_2$ -Verdunstungskühltechnik durchgeführt wurden. Die an allen Prototypen durchgeführten Qualitätskontrolltests haben gezeigt, dass sie ordnungsgemäß zusammengesetzt wurden und voll funktionsfähig sind. Darüber hinaus erfüllen sie die entsprechenden Anforderungen, so dass das Design der Komponenten und die Bauverfahren validiert wurden.

# Table of Contents

<b>Introduction</b>	<b>1</b>
<b>1 The ATLAS experiment at CERN</b>	<b>3</b>
1.1 The Large Hadron Collider . . . . .	3
1.1.1 Luminosity . . . . .	4
1.1.2 The accelerators . . . . .	5
1.2 The ATLAS experiment . . . . .	8
1.2.1 Inner Detector . . . . .	11
1.2.2 Calorimeter . . . . .	14
1.2.3 Muon Spectrometer . . . . .	16
1.2.4 Trigger and Data Acquisition . . . . .	18
1.3 Phase-I upgrade of the ATLAS experiment . . . . .	19
<b>2 Physics goals of HL-LHC and ITk layout</b>	<b>21</b>
2.1 Physics motivation . . . . .	22
2.1.1 Higgs Boson measurements at HL-LHC . . . . .	23
2.1.2 Standard Model at HL-LHC . . . . .	24
2.1.3 Beyond Standard Model . . . . .	25
2.2 Phase-II upgrade of the ATLAS detectors . . . . .	26
2.3 The ITk layout . . . . .	27
2.3.1 Radiation environment . . . . .	29
2.3.2 Material Budget . . . . .	30
2.3.3 Channel Occupancy . . . . .	31
2.3.4 Track Reconstruction . . . . .	33
<b>3 The ITk Project</b>	<b>35</b>
3.1 The Inner Tracker . . . . .	35
3.1.1 Local support . . . . .	36
3.1.2 Silicon Modules . . . . .	40
3.1.3 End of Substructure card . . . . .	44

3.2	DESY involvement in the ITk Strip project . . . . .	46
<b>4</b>	<b>Assembly of Silicon Modules and Quality Control</b>	<b>51</b>
4.1	Reception tests on module components . . . . .	51
4.1.1	Sensor reception . . . . .	51
4.2	Module building procedure . . . . .	53
4.2.1	Pressure calibration of the glue . . . . .	53
4.2.2	R0 Star power-board gluing tools . . . . .	57
4.3	Quality Control on Modules . . . . .	61
4.3.1	Metrology . . . . .	61
4.3.2	Electrical test . . . . .	64
<b>5</b>	<b>Module loading and qualification of petals</b>	<b>75</b>
5.1	QC on a Local Support Structure . . . . .	75
5.1.1	Electrical tests on cores . . . . .	76
5.1.2	Mechanical properties . . . . .	78
5.1.3	Thermal tests . . . . .	79
5.2	Module on core placement procedure . . . . .	86
5.2.1	Experimental setup . . . . .	87
5.2.2	Camera offset . . . . .	88
5.2.3	Glue pattern for modules . . . . .	89
5.2.4	Module placement . . . . .	92
5.2.5	EoS card placement . . . . .	94
5.2.6	Touch-down function . . . . .	94
5.2.7	Software for the loading . . . . .	95
5.3	Semi-electrical petal . . . . .	97
5.4	Quality control on Petals . . . . .	99
5.4.1	Glue amount . . . . .	99
5.4.2	Final Survey on sensor fiducial marks . . . . .	99
5.4.3	Metrology measurements . . . . .	102
5.4.4	Electrical test . . . . .	105
<b>6</b>	<b>Petal testing at low temperature</b>	<b>113</b>
6.1	Motivation . . . . .	113
6.2	Experimental setup . . . . .	115
6.2.1	Petal reception test . . . . .	117
6.3	Power consumption of Star chipset . . . . .	118

6.3.1	The thermo-electrical model . . . . .	118
6.3.2	Experimental power calculation . . . . .	121
6.4	Electrical at low CO <sub>2</sub> temperature . . . . .	123
6.4.1	Module noise analysis . . . . .	124
6.4.2	Noise investigation on the R2 module . . . . .	128
6.4.3	IV curves on sensors . . . . .	130
6.4.4	Input noise estimation on Star modules . . . . .	132
6.5	Thermal analysis and comparison with FEA simulation . . . . .	134
6.5.1	FEA simulation . . . . .	137
6.5.2	Temperature comparison of the petal electronics . . . . .	140
	<b>Conclusion</b>	<b>143</b>
	<b>Bibliography</b>	<b>146</b>

# List of Figures

1.1	Drawing of the LHC accelerator complex . . . . .	5
1.2	Schedule of LHC experiments from the first collision in 2010 to HL-LHC in Run4, as in December 2021 . . . . .	7
1.3	Structure and sub-detectors of the ATLAS experiment at CERN . . .	9
1.4	Section of the ATLAS experiment at CERN, perpendicular to the beam line and diagram of particles path in the detector . . . . .	10
1.5	Inner Detector structure of the ATLAS experiment . . . . .	11
1.6	Working principle of a n-in-p AC-coupled silicon microstrip detector .	13
1.7	Structure and location of the electromagnetic and hadronic calorimeters in the ATLAS experiment . . . . .	16
1.8	Structure of the muon spectrometer in the ATLAS experiment . . . .	17
1.9	A quarter of the section of the muon spectrometer . . . . .	18
2.1	Higgs boson mass measurements from the individual and combined analysis of ATLAS and CMS . . . . .	22
2.2	Feynman diagrams of the Higgs boson productions at LHC . . . . .	24
2.3	Cross-section times branching fraction measurements of the $\gamma\gamma$ Higgs production mode . . . . .	24
2.4	Cross-section times branching fraction measurements of the $4l$ Higgs production mode . . . . .	24
2.5	Feynman diagram for the stop decay $\tilde{t} \rightarrow t + \tilde{\chi}_1^0$ . . . . .	26
2.6	Exclusion limits and discovery of the top squark . . . . .	26
2.7	Schematic depiction of a quarter section of the latest version of the ITk Layout . . . . .	28
2.8	1 MeV neutron equivalent fluence in the ATLAS ITk . . . . .	30
2.9	Total ionising dose (TID) in the ATLAS ITk . . . . .	30
2.10	Material distribution of one quadrant of the ITk detector . . . . .	31
2.11	Integrated radiation lengths distribution as function of $\eta$ , within the ITk volume . . . . .	31

2.12	Average channel occupancy of the ITk detector . . . . .	32
2.13	Real and ghost hits in case of orthogonal and small angle crossing strips	33
2.14	Number of silicon hits per track as function of $\eta$ . . . . .	34
3.1	Schematic of the ITk detector for the ATLAS Phase-II upgrade . . . . .	36
3.2	Internal structure of the petal core . . . . .	37
3.3	Section view of the bus tape . . . . .	38
3.4	Technical drawing of the strip petal core . . . . .	39
3.5	Picture of the internal structure of a petal core . . . . .	40
3.6	Latest strip endcap petal design, front side, populated with Star modules and a Master EoS glued on the petal core. . . . .	41
3.7	Fiducial marks on HPK sensors. . . . .	42
3.8	Position of sensor fiducial marks . . . . .	42
3.9	Architecture of the readout in ABC 130 and ABC Star chipset . . . . .	43
3.10	Layout of the R0 Star power-board with all its electrical components.	44
3.11	Sketch of the module components and nominal thickness of the module components and glue layers . . . . .	45
3.12	End-of-Substructure prototypes for the Petal, Master and Slave card .	46
3.13	Cold box testing setup for endcap module testing . . . . .	47
3.14	Sketch of a strip endcap portion with one service tray . . . . .	48
3.15	Strip endcap global structure placed on the super frame and petal insertion tool . . . . .	50
3.16	ISO6 cleanroom at DESY Hamburg dedicated to the ITk activities. .	50
4.1	IV curve on the R2 sensor before and after module assembly . . . . .	52
4.2	CV curve on the R2 sensor before and after module assembly . . . . .	52
4.3	Glue pattern for chips . . . . .	54
4.4	Glue pattern for hybrids . . . . .	54
4.5	R2 Star module built at DESY . . . . .	54
4.6	R2 tooling set to assemble modules . . . . .	55
4.7	Pressure calibration of Polaris glue . . . . .	56
4.8	Designs and aluminum prototypes of the R0 Star power-board gluing tools . . . . .	58
4.9	Dummy R0 Star power-board gluing test . . . . .	59
4.10	Glue amount applied using the power-board stencil . . . . .	59
4.11	Glue pattern design for stencils: from the top R2, R3 and R4-R5 power-boards respectively. . . . .	60

4.12	Flatness measurements on bare R2 sensor before gluing: 20 $\mu\text{m}$ . . . . .	63
4.13	Flatness measurements on R2 sensor after hybrid gluing: 22 $\mu\text{m}$ . . . . .	63
4.14	Metrology measurements on the R2 hybrid . . . . .	64
4.15	Closer look at the R2 module structure . . . . .	65
4.16	Testing setup for the R2 Star module . . . . .	66
4.17	Readout chain used for Star module/hybrid testing. . . . .	66
4.18	Strobe delay test on R2H0 hybrid, S0. . . . .	68
4.19	Cumulative y projection of chip 1 in R2H0, S0. . . . .	68
4.20	Strobe delay values for each ABC chip of the R2 module . . . . .	69
4.21	Threshold scan in R2H0, S0, injecting 1.5 fC on single channel of the ABC chips. . . . .	70
4.22	Y projection (s-curve) of channel 100 in R2H0, S0, after the threshold scan injecting 1.5 fC. . . . .	70
4.23	Gaussian fit on the $V_{T50}$ distribution, in DAC counts, for three values of injected charges in R2H0, ABC chip 1 . . . . .	70
4.24	Linear fit on mean values of each distribution to get the gain and the offset . . . . .	70
4.25	Response curve on single ABC channel using the function in equation 4.6. . . . .	71
4.26	Gain values measured on R2 module for each ABC chip channel. . . . .	72
4.27	Input noise values measured on R2 module for each ABC chip channel. . . . .	72
4.28	Input noise measured on R2H0, stream 0, using different number of triggers for the three point gain scan. . . . .	72
4.29	Efficiency and noise occupancy as function of the threshold for an irradiated Star module . . . . .	73
5.1	Schematic path of the cable shields from PP0 to PP1 . . . . .	77
5.2	Metrology on the petal core, front side. . . . .	79
5.3	Metrology on the petal core, back side. . . . .	79
5.4	CO <sub>2</sub> phase diagram as function of pressure in logarithmic scale. . . . .	81
5.5	Testing setup for the thermal analysis inside the cleanroom. . . . .	82
5.6	Petal core placed inside the PTM for thermal tests and held by a custom-made frame. . . . .	82
5.7	IR picture recorded on a front side of the petal core at $T_{CO_2} = -20^\circ\text{C}$ . . . . .	83
5.8	Petal core thermogram recorded at $T_{CO_2} = -20^\circ\text{C}$ with linear and polygonal markers . . . . .	84

5.9	Analysis on linear markers at different CO <sub>2</sub> temperature. . . . .	85
5.10	Analysis on polygonal markers at different CO <sub>2</sub> temperature. . . . .	85
5.11	Strip orientation in an endcap silicon sensor compared to the beam line	86
5.12	Full setup used to load modules on the petal core . . . . .	88
5.13	Glue pattern dispensed on the core and coverage check . . . . .	90
5.14	Fully loaded petal with glass sensors . . . . .	91
5.15	Metrology measurements on the R0 glass sensor . . . . .	91
5.16	Sketch of the gantry table with coordinate systems . . . . .	94
5.17	Current trend as function of time during the touch-down function . .	95
5.18	Matlab GUI interface and fit to a $K$ sensor fiducial marker . . . . .	96
5.19	Result of a module placement after fitting 10x $K$ fiducial marks . . .	96
5.20	Semi-electrical petal built at DESY in January 2020. . . . .	98
5.21	Examples of F sensor fiducials fitted by the camera. . . . .	100
5.22	Survey on the R0 module loaded on the semi-electrical petal . . . . .	101
5.23	Module placement error of the semi-electrical modules . . . . .	101
5.24	Laser measurements on a R0 module . . . . .	102
5.25	Semi-electrical petal placed on the Smartscope glass for metrology measurements . . . . .	103
5.26	Metrology measurements performed on the semi-electrical petal, in the xy plane . . . . .	103
5.27	Flatness measurements performed on the semi-electrical petal, in the xz plane . . . . .	104
5.28	Testing setup and readout chain of the semi-electrical petal. . . . .	105
5.29	Low voltage current values after the configuration of the modules . .	106
5.30	Noise results for R0 module after loading . . . . .	108
5.31	Before/after loading noise comparison for R1 module . . . . .	108
5.32	Before/after loading noise comparison for R2 module . . . . .	108
5.33	Before/after loading noise comparison for R3 module . . . . .	109
5.34	Before/after loading noise comparison for R4 module . . . . .	109
5.35	Before/after loading noise comparison for R5 module . . . . .	109
5.36	Strobe delay test on R3 hybrids on petal, configured individually . . .	110
5.37	Strobe delay test on R3 module on petal with all hybrids configured .	110
5.38	Strobe delay test on R3 module when all 4 hybrids are configured together with the other modules on petal. . . . .	111

6.1	Electrical petal fully populated with Star modules and EoS master card on the front side. . . . .	114
6.2	Digilent Genesys2 (black board) with FMC-QSFP-ITk (blue board) used to connect the optical fiber to the FPGA. . . . .	116
6.3	Readout chain for electrical petal testing. . . . .	116
6.4	Placement of the petal inside the PTM . . . . .	116
6.5	Equipment for electrical test on the bench during the petal reception test. . . . .	117
6.6	Thermo-electrical model for silicon modules loaded on a local support	119
6.7	Power values from the components specification and the estimation obtained using the thermo-electrical model . . . . .	121
6.8	Current values, read out from the LV power supply, as function of number of ABC chip on each module . . . . .	123
6.9	Input noise measured in R4 module when the CO <sub>2</sub> cooling is set to -20°C . . . . .	124
6.10	Closer look at the petal electronics . . . . .	125
6.11	Input noise measured for all modules at different CO <sub>2</sub> temperature . .	126
6.12	Input noise measured before the loading for all modules . . . . .	127
6.13	Input noise measured after the loading for all modules . . . . .	127
6.14	Input noise levels on R2 module at different CO <sub>2</sub> set-points. . . . .	128
6.15	Gain values measured on the R2H1 hybrid at different CO <sub>2</sub> set-points	128
6.16	Output noise calculated in R2H1 hybrid at different CO <sub>2</sub> set-points .	129
6.17	Additional HV biasing of the R2 sensor . . . . .	130
6.18	Noise levels on R2 module after the HV fix . . . . .	130
6.19	IV curves on single sensor at 0°C CO <sub>2</sub> temperature . . . . .	131
6.20	HV ramp up of the R0 module at -10°C CO <sub>2</sub> temperature . . . . .	132
6.21	Petal thermograms for different CO <sub>2</sub> temperature . . . . .	134
6.22	Petal thermogram at -34°C. . . . .	135
6.23	Selection to group the pixels in ten areas, including the EoS. . . . .	135
6.24	Temperature average, standard deviation and span calculated for each module area and EoS card . . . . .	135
6.25	Mean temperature of each module as function of CO <sub>2</sub> set-point on MARTA cooling machine. . . . .	135
6.26	Temperature discrepancy between two following CO <sub>2</sub> set-points . . .	136
6.27	Zoomed view of the plot in figure 6.26. . . . .	136
6.28	CAD file of fully populated petal and application of the mesh. . . . .	138

6.29	Petal components and materials with HTC specifications . . . . .	138
6.30	Silicon sensor resistivity versus CO <sub>2</sub> temperature, used for FEA simulation with irradiated sensors . . . . .	138
6.31	Thermo-electrical petal simulation at −10 °C CO <sub>2</sub> temperature at end of life . . . . .	139
6.32	Maximum temperature simulated on petal plotted as function of CO <sub>2</sub> cooling temperature at end of life . . . . .	139
6.33	FEA thermal simulation with probes on the NTC positions to read the temperature. . . . .	140
6.34	Temperature behaviour measured on hybrids and power-board for each module . . . . .	142

# List of Tables

4.1	Nominal glue amounts deposited by the power-board gluing stencil for each type . . . . .	60
4.2	Metrology measurements on the R2 module . . . . .	65
5.1	Flatness values calculated for each module area on both side of a petal core prototype. . . . .	78
5.2	Specification required for loading the endcap modules on the local support structure . . . . .	87
5.3	Origin of each module that was loaded on the petal core. . . . .	97
5.4	Estimation of the total SE4445 glue amount needed for module on core to populate one side. . . . .	100
5.5	Values of flatness and glue thickness for each semi-electrical module loaded onto the petal. . . . .	104
5.6	Summary of endcap module chips and current values measured by the power supply after the individual module configuration. . . . .	106
6.1	Summary of the power consumption estimation of the ITk Strip detector	122
6.2	Current values measured on the LV power supply for each module at each CO <sub>2</sub> set-points. . . . .	122
6.3	CO <sub>2</sub> set points during petal testing and conversion to pressure values.	124
6.4	Nominal values of input noise calculated for each module stream according with their input capacitance. . . . .	133
6.5	Comparison of NTC readings and temperature results from the FEA simulation with CO <sub>2</sub> set to 18 °C . . . . .	141

# Introduction

The understanding of the matter that constitutes the Universe is one of the main open questions of the scientific community. The *Standard Model* (SM) is the most recent theory that was confirmed and validated in 2012 with the discovery of the Higgs boson particle. Physicists have proposed other interesting theories to answer questions that the SM does not provide, such as the neutrino mass and the dark matter nature. Some of the best tools to advance this investigations involve the collision of particle beams at higher energy and luminosity and getting more and more advanced detectors to identify the collisions products.

The *Large Hadron Collider* (LHC) at CERN is the largest circular collider in the world and is the best candidate to study a high number of physics phenomena. Protons collide along the ring in precise points where several detectors with different technologies are placed to record the trajectory, the energy and the momentum of the secondary particles produced by the collision. The *A Toroidal LHC ApparatuS* (ATLAS) experiment is one of the four major experiments built along the LHC ring. An increment of the luminosity, that brings to the High Luminosity era of LHC (HL-LHC), will allow the collection of higher statistics and therefore the possibility to detect new particles and to investigate the interactions with a very low branching ratio.

Current accelerators and detectors are not designed to work in an unprecedented radiation dose and collision rate simulated for the HL-LHC and therefore they require an upgrade. During Long shutdown 3, scheduled for 2025, the ATLAS Inner Detector will be completely replaced by the *Inner Tracker* (ITk) which consists of a pixel silicon sub-system surrounded by the strip detector. This detector upgrade is the main subject of the PhD project.

The first part of this thesis is meant to provide a description of the LHC and the ATLAS experiment, which is presented in chapter 1. A brief description of the ATLAS Phase-I upgrade is also provided. An overview on the physics goals and the analysis planned on the Run 4 dataset in the HL-LHC environment is presented in chapter 2 as well as the ATLAS detector upgrades foreseen for Phase-II. The physical reasons that brought to the latest ITk layout is presented in the same chapter.

Chapter 3 presents in details the structure of the ITk detector with emphasis on the main unit of the strip endcap, the petal and its components: the silicon modules, the local support structure and the End of Substructure card. A brief introduction on the activities that are carried out at DESY within the ITk collaboration is included. The second part of the manuscript contains the main investigations performed during the PhD project. It covers most of the steps in the production chain, starting from the single module unit assembly to the qualification of the petal loaded with electrical modules. Each assembled item is followed by quality control (QC) tests to check its post-building functionality and to assign its readiness for the next assembling step. The mounting of the silicon sensors with their power and front-end electronics is described in detail in chapter 4 as well as metrology and electrical tests, as part of the QC tests at the final stage of the module building.

The evaluation of the thermo-mechanical performance of the local support structures and the results on a prototyping petal core are presented in chapter 5. The procedure to load endcap silicon modules on the core with a required precision is described in the same chapter. A semi-electrical petal was built at DESY with prototyping components to qualify the loading procedure and results of QC tests are presented. Chapter 6 shows the investigation performed on a fully electrical petal loaded with silicon modules. The studies are focused on the electrical tests at low temperature to validate the design of most of the petal components. A thermal analysis is performed to check the heat production when the electronics is powered on and its dissipation via evaporative CO<sub>2</sub> cooling.

Finally the thesis ends providing the conclusions on the global PhD project and summarizing the main physics results of the investigation.

# Chapter 1

## The ATLAS experiment at CERN

The Large Hadron Collider (LHC) is the world's largest and most powerful particle accelerator. It is a two-ring superconducting hadron collider located on the Franco-Swiss border near Geneva, Switzerland, at the European Organization for Nuclear Research (CERN). The ring has a circumference of about 27 km in a 100 m underground tunnel. It is in operation since 2010 and its physics program is extended until 2040. It delivers two proton beams at very high energy which collide in four stations along the ring. Particles generated by the collisions allow the exploration towards new physics frontiers and probing phenomena only theorized so far.

This chapter aims to give an introduction to the LHC provided in section 1.1. The concept of luminosity, quantity used in particle physics to indicate the collider performance, is explained in section 1.1.1. The accelerators complex used to produce such a fast and squeezed proton beam are described in section 1.1.2. The ATLAS experiment is one of the major experiments of LHC and is located in one colliding station. A complete overview on the ATLAS detectors is provided in section 1.2, described in each of its sub-systems: the inner detector (1.2.1), the calorimeter (1.2.2) and the muon spectrometer (1.2.3).

### 1.1 The Large Hadron Collider

The LHC boosts protons using radiofrequency cavities and the beam is focused and curved by magnets [1]. Protons were chosen for the LHC beam because they are charged and stable particles, as only particles with these properties can be accelerated. To obtain the highest energy collisions it is more effective to accelerate massive particles, as protons are, to minimize the energy loss through synchrotron radiation. Proton beams, accelerated to a speed close to that of light in a vacuumed pipe, run along the ring in opposite directions and collide producing massive particles. By measuring their properties, scientists increase the understanding of matter and of the origins of the Universe. These massive particles only last a short time, and almost

immediately decay into lighter particles. The particles emerging from the successive links in this decay chain are identified in the layers of the detectors.

### 1.1.1 Luminosity

In particle physics experiments the energy available for the production of new particles is the most important parameter. The required large energy can only be provided with colliding beams where little or no energy is lost in the motion of the centre of mass system. Besides the energy the number of useful interactions is important especially when rare events with a small production cross section  $\sigma_p$  are studied. The quantity that measures the ability of a particle accelerator to produce the required number of interactions is called *luminosity* and it is the proportionality factor between the number of events per second  $dR/dt$  and the cross section  $\sigma_p$  [2]:

$$\frac{dR}{dt} = L \cdot \sigma_p \quad (1.1)$$

The unit of the luminosity is therefore  $cm^{-2}s^{-1}$ . It can be also expressed in *inverse femtobarn* ( $fb^{-1}$ ): this is the unit typically used to measure the number of collision events per femtobarn of target cross-section, and is the conventional unit for time-integrated luminosity. The barn is a metric unit of area, equal to  $10^{-28}m^2$  ( $1fb = 10^{-39}cm^2$ ), it is approximately the cross-sectional area of an uranium nucleus. The absolute luminosity depends only on the beam parameters and can be written in the form of equation 1.2:

$$L = \frac{n_b f_r n_1 n_2}{2\pi \Sigma_x \Sigma_y} \quad (1.2)$$

where:

- $f_r$  is the accelerator revolution frequency;
- $n_b$  the number of bunches colliding at the interaction point (IP);
- $n_1$  and  $n_2$  are the number of particles in the two colliding bunches;
- $\Sigma_x$  and  $\Sigma_y$  are the horizontal and vertical beam profiles respectively assuming similar characteristics for both beams.

The luminosity is an essential indicator of an accelerator's performance and it can be increased getting a more intense and more focused beam in order to raise the number of collisions.

### 1.1.2 The accelerators

Before the particles arrive at the LHC ring, they undergo a process through a complex of accelerators, as figure 1.1 shows. This is a succession of machines that accelerate particles to increasingly higher energies. Each machine boosts the particle bunches before injecting them into the next machine in the sequence. Starting from negative hydrogen ions  $H^-$ , they are accelerated to an energy of 160 MeV by *Linac 4*, a linear accelerator. The ions are stripped of their two electrons during injection from Linac 4 into the *Proton Synchrotron Booster* to leave only protons, which are accelerated to 2 GeV. The protons are then injected into the *Proton Synchrotron* (PS), another synchrotron which increases the energy to 26 GeV. The last pre-acceleration step is provided by the *Super Proton Synchrotron* (SPS), which increases the beam energy to 450 GeV and injects the protons into the LHC where the beams are accelerated to the nominal collision energy [3].

Inside the ring, two high-energy particle beams travel at close to the speed of light in opposite directions in separate beam pipes kept at ultrahigh vacuum ( $10^{-13} atm$ ). They are guided around the accelerator ring by a strong magnetic field maintained by superconducting electromagnets. Dipoles are used to curve the particle trajectory and quadruples to focus the proton beam. The electromagnets are built from coils of special electric cable ( $Nb_3Sn$ ) that operates in a superconducting state at 12 T,

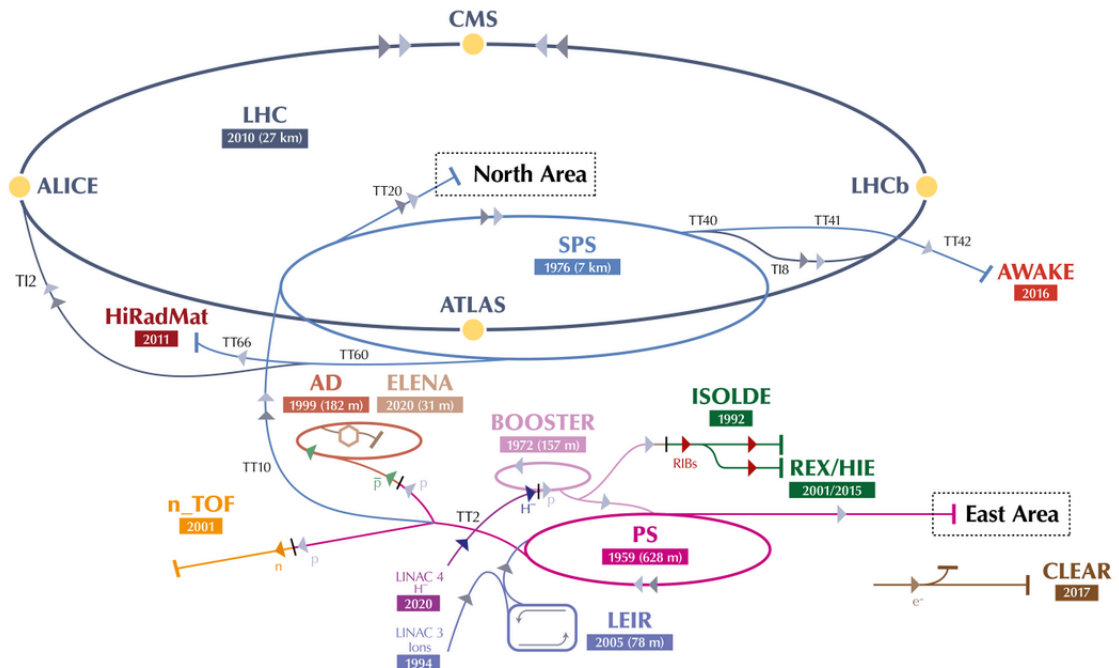


Figure 1.1: Drawing of the LHC accelerator complex [3].

efficiently conducting electricity without resistance or loss of energy. This requires chilling the magnets to  $-271.3^{\circ}\text{C}$  (1.9 K) [4]. For this reason, the accelerator is connected to a distribution system of liquid helium, which cools the magnets down, as well as the other supply services. The LHC ring includes also radiofrequency cavities, which are electromagnetic resonators that accelerate particles and then keep them at a constant energy by compensating for energy losses.

The energy of the beam collision is usually expressed in terms of *energy of the center of mass*  $\sqrt{s}$  and can be obtained as follows. The kinematics of a particle with mass  $m$  can be expressed by its momentum  $\vec{p}$  and energy  $E$  which form a four-vector  $\mathbf{p} = (E, \vec{p})$ . The square  $p^2 = E^2 - \vec{p}^2 = m^2$  provides the *invariant mass* of the system in the rest frame, being the speed of light set to  $c = 1$ . In the collision of two particles of same mass the total centre of mass energy  $E_{cm}$  can be expressed in the form:

$$(\mathbf{p}_1 + \mathbf{p}_2)^2 = E_{cm}^2 = (E_1 + E_2)^2 - (\vec{p}_1 + \vec{p}_2)^2$$

This is the energy available for physics experiments. In the case of a collider where the collision point is at rest in the laboratory frame (i.e.  $\vec{p}_1 = -\vec{p}_2$ ), the centre of mass energy becomes  $s = E_{cm}^2 = (E_1 + E_2)^2$  [5].

As LHC is a circular collider where protons of same energy and mass interact, the energy of the collision is therefore calculated as  $\sqrt{s} = \sqrt{4E^2} = 2E$ .

The first collisions at the LHC were achieved in 2010 at an energy of 3.5 TeV per beam,  $\sqrt{s}=7$  TeV, marking the start of *Run 1* data taking. It delivered  $5\text{fb}^{-1}$  of data with a luminosity peak at  $3 \cdot 10^{33}\text{cm}^{-2}\text{s}^{-1}$ . The current aim of the LHC is to reveal the physics beyond the Standard Model with center-of-mass proton-proton collision energies of up to  $\sqrt{s}=13$  TeV. The years ahead will be exciting as LHC takes experimental physics into unexplored territories maybe with new processes and particles that could change our understanding of energy and matter. These studies can lead to ground breaking discoveries, such as the already discovered Higgs boson in 2012, physics beyond the Standard Model and the development of new theories to better describe our universe.

**The LHC experiments** Particle beams collide at four experimental intersection regions along the LHC ring and corresponding to the underground caverns of the following experiments:

- ATLAS, *A Toroidal LHC ApparatuS* is a general-purpose detector used to investigate the largest range of physics possible, from the search for the Higgs boson to extra dimensions and particles that could constitute the dark matter [6].

- CMS, *Compact Muon Solenoid*, has the same scientific program as the ATLAS experiment, but it uses different technical solution and a different magnet-system design. It is vital for cross-confirmation of any new discoveries made [7].
- ALICE, *A Large Ion Collider Experiment*, is a detector dedicated to heavy-ion physics. It is designed to study the physics of strongly interacting matter at extreme energy densities, where a phase of matter called quark-gluon plasma forms [8].
- LHCb, the *Large Hadron Collider beauty* experiment specializes in investigating the slight differences between matter and antimatter by studying the beauty quark [9].

LHC includes also multiple other smaller experiments around the main detectors which make use of their particle production.

From the first collision, periods of data taking are alternated with Long Shut-downs (LS) during which the accelerators and detectors are upgraded, the first ones to be able to deliver energy and luminosity values that are required by the LHC experiments and the second ones to work under those conditions. Figure 1.2 shows the LHC schedule from 2011 when Run 1 started. After two years the LHC machine provided an integrated luminosity of  $30 \text{ fb}^{-1}$  with  $\sqrt{s}=8 \text{ TeV}$  as center of mass collision energy. Currently LHC is in LS2 for Phase-I upgrade of the ATLAS and CMS experiments. In 2022 Run 3 starts with the energy increased to  $\sqrt{s}=13 \text{ TeV}$  and ends in 2025 reaching an integrated luminosity of  $300 \text{ fb}^{-1}$ .

A new project for LHC was submitted to increase even further the luminosity of the current collider: at the end of 2027 *High-Luminosity LHC* (HL-LHC) will start [11]. As the name suggests, the LHC integrated luminosity will go up to  $3000 \text{ fb}^{-1}$  and to achieve this value new equipment is need to be installed over about 1.2 of the LHC's

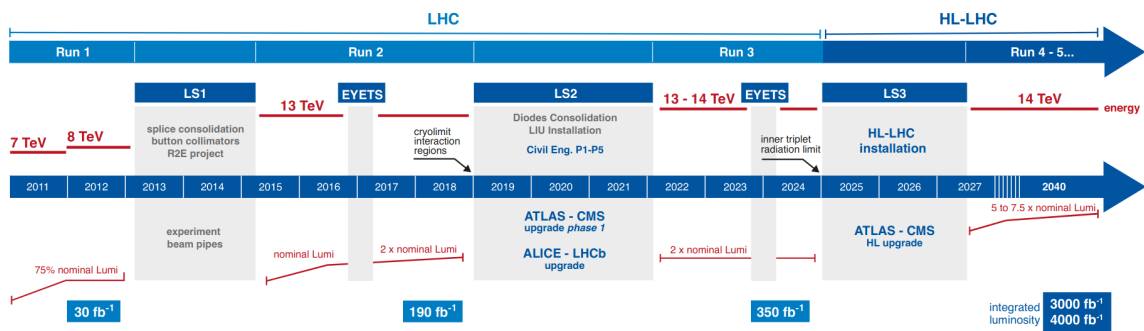


Figure 1.2: Schedule of LHC experiments from the first collision in 2010 to HL-LHC in Run4, as in December 2021 [10].

27 km during LS3. The upgrade includes more powerful focusing magnets and new optics, *crab cavities* [12] for tilting the beam bunches, reinforced machine protection, more compact and powerful bending magnets, innovative superconducting links and an upgraded accelerator chain.

The HL-LHC project is described in chapter 2 explaining the physics motivations that brought to increase the luminosity.

## 1.2 The ATLAS experiment

ATLAS is one of the four major experiments at LHC. An international collaboration, which counts 4000 members from 41 countries all over the world, runs this experiment to explore a large number of physics opportunities that the LHC provides. The ATLAS detector is designed to track and identify particles in order to test the predictions of the Standard Model. The primary focus is to improve the understanding of the fundamental constituents of matter, including the study of the Higgs boson and top quark, but also the search for extra dimensions and particles that could make up dark matter.

Beams of particles delivered by LHC collide at the centre of the ATLAS detector, producing new particles which fly out in all directions. Over a billion particle interactions take place every second, but only 1000 collisions are flagged by the trigger as potentially interesting and recorded for further study, as explained in section 1.2.4. In order to identify all particles produced in the collisions, the experiment is designed with different detection subsystems wrapped concentrically in layers around the IP. According with the nature and geometry of each sub-detector, they are involved in recording either the trajectory, momentum, or energy of particles. These quantities allow the particles to be individually identified and measured right after their production. A huge magnet system bends the paths of the charged particles so that their momentum can be measured as precisely as possible.

ATLAS has the largest volume detector ever constructed for a particle collider, it has a cylindrical symmetry, 44 m long, 25 m in diameter and weights 7000 tonnes. Figure 1.3 shows the ATLAS experiment with its sub-detectors, which can be grouped in three major categories, listed below starting from the beam line:

- *Inner Detector* (ID) is the tracker that measures the momentum of charged particle through the curvature of their trajectory bent by the magnetic field that surrounded the ID.
- *Calorimeters*, electromagnetic (ECAL) and hadronic (HCAL), measure ener-

gies carried by most of the neutral and charged particles. Muons and neutrinos pass through the calorimeters without being seen.

- *Muon Spectrometer* identifies and measures the momentum of muons, it is surrounded by a toroidal magnet to bend the particles' path.

The cylindrical structure of ATLAS and the particles detection can be understood looking at figure 1.4. Protons, neutrons, photons and electrons produce electromagnetic or hadronic showers and all particles generated are absorbed inside the calorimeters. Muons and neutrinos are the only particles that are able to exit the detector. The first ones interact via electromagnetic force and produce a signal in the tracker, ECAL and in the muon detectors, but as they are heavy, they lose a small fraction of their energy in collisions. Neutrinos interact only through the weak force, thus their interaction cross section is too small to be detected in ATLAS and their presence can be often inferred from the missing momentum.

ATLAS uses a right-handed coordinate system with its origin at the nominal IP in the centre of the detector and the z-axis along the beam pipe. The x-axis points from the IP to the centre of the LHC ring, and the y-axis points upward. Cylindrical coordinates  $(r, \varphi)$  are used in the transverse plane, being  $\varphi$  the azimuthal angle around the z-axis. The *pseudorapidity* is defined in terms of the polar angle  $\Theta$  as  $\eta = -\ln(\tan(\Theta/2))$ .

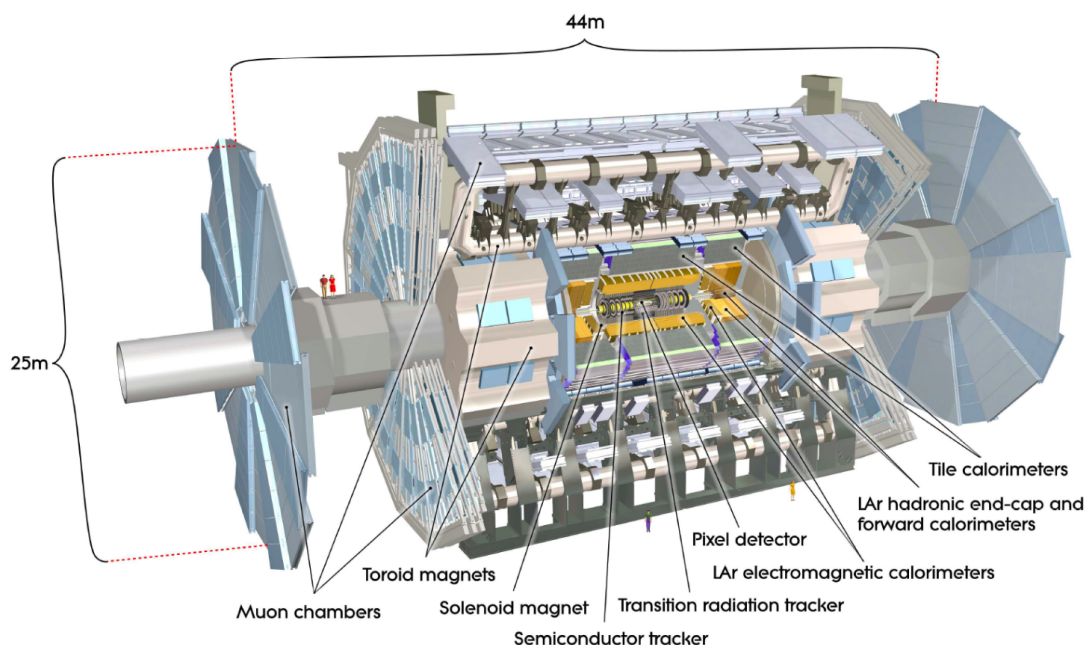


Figure 1.3: Structure and sub-detectors of the ATLAS experiment at CERN [6].

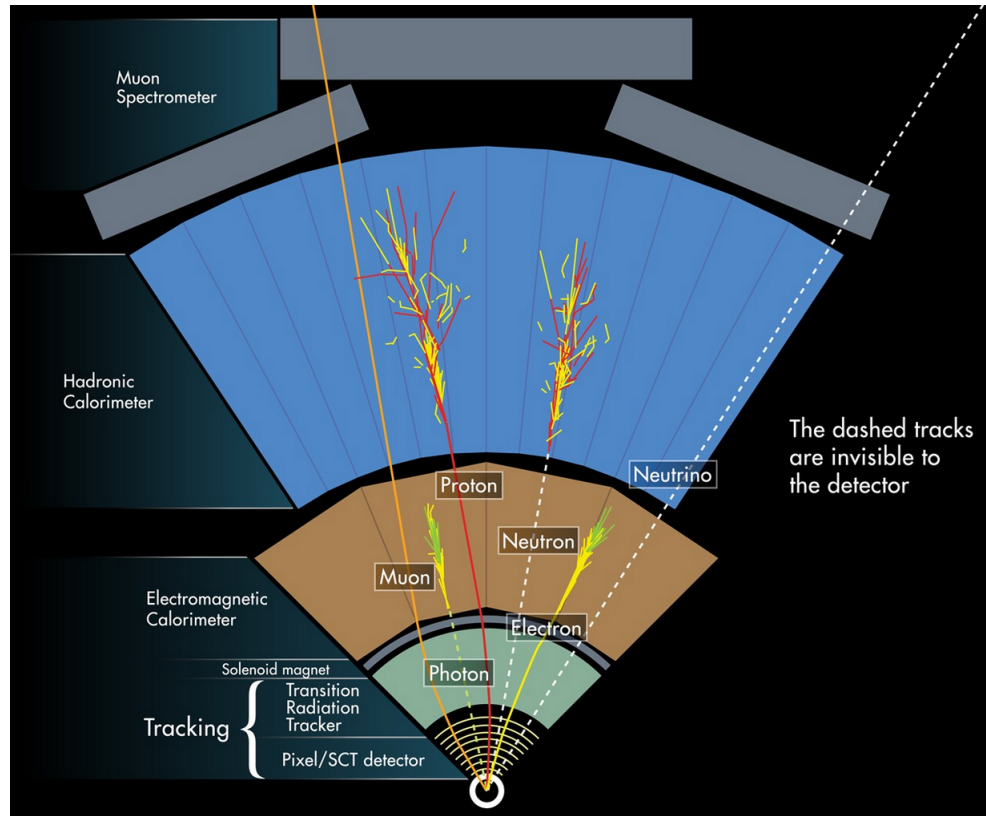


Figure 1.4: Section of the ATLAS experiment at CERN, perpendicular to the beam line and diagram of particles path in the detector [13].

**Magnet System** The whole system includes two types of superconductive magnets that bend the trajectories of each charged particle to allow the measurement of its momentum [14]:

- a central *solenoid magnet* surrounds the ID, it provides 2T magnetic field pointing in the beam direction;
- two *toroidal magnets* that provides 4T tangential magnetic field which run concentrically around the beam axis: a barrel toroid is made of eight separated coils around the hadronic calorimeter, before the muon chambers and two endcap toroids in between the muon wheels, eight coils as well.

The magnet system can be seen in figure 1.3. The superconductive magnets are cooled down with liquid helium to 4.5 K ( $-268^\circ\text{C}$ ) in order to provide the necessary strong magnetic fields. The solenoid is located in a cryostat together with the ECAL, and each toroid in a single cryostat.

### 1.2.1 Inner Detector

The Inner Detector (ID) is the innermost system and the first part of ATLAS to see the decay products of the protons collision. The task of the ID is to reconstruct the tracks and vertices of the event with high efficiency [15]. It contributes, together with the calorimeter and muon systems to the electron, photon and muon recognition, and supplies the important extra signature for short-lived particle decay vertices. Its acceptance covers the pseudo-rapidity region of  $\eta = \pm 2.5$ . The momentum and vertex resolution targets require high-precision measurements to be made with fine-granularity detectors given the very large track density at LHC. Those are, from the beam line, the *Pixel Detector*, *Strip Semiconductor Tracker* (SCT), and *Transition Radiation Tracker* (TRT), all immersed in a 2 T magnetic field parallel to the beam axis. The distribution of these detectors is shown in figure 1.5. They measure the direction, momentum and charge of electrically-charged particles produced in each collision.

The momentum  $\vec{p} = m \vec{v}$  can be calculated from the Lorentz force equation:

$$\vec{F}_L = q \vec{v} \times \vec{B} = m \vec{a} \quad \Rightarrow \quad p_T = mv_T = q \cdot R \cdot B \quad (1.3)$$

The transverse momentum  $p_T$  is therefore obtained from  $q$ , the charge of the particle, and  $R$  the curvature radius of the helicoidal trajectory in the magnetic field  $\vec{B}$ , being

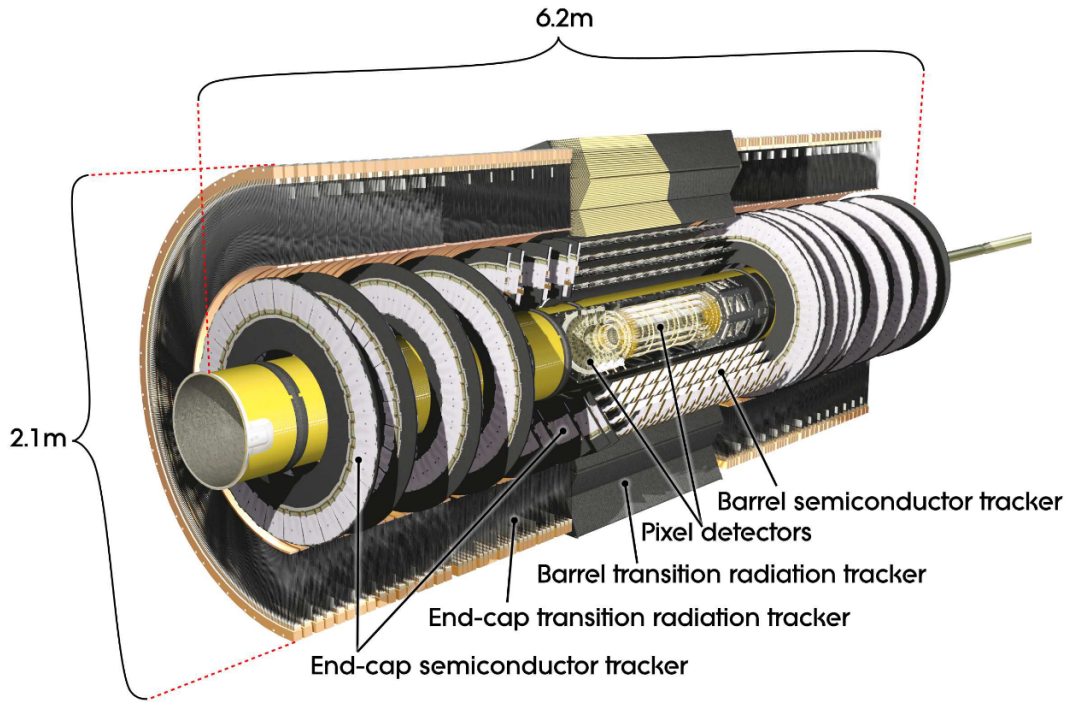


Figure 1.5: Inner Detector structure of the ATLAS experiment [6].

the acceleration  $a = v^2/R$ . Concerning the particle charge, its sign can be derived from the direction of the curvature in the magnetic field and the charge itself is obtained afterwards. The tracker provides the  $p_T/q$  ratio.

The main detectors involved in the track reconstruction are the semiconductors, with the read out segmented in pixel (Pixel detector) or strips (SCT) to increase the granularity. The most common semiconductor used for detection is the silicon, a tetravalent element which is doped with impurity atoms to improve the conductivity behaviour [16]. It becomes:

- *n type* by placing a pentavalent element, called *donor* like phosphorus, to get an excess of conduction electrons ( $e^-$ ) as majority charge carriers;
- *p type* by placing a trivalent element, called *acceptor* like boron, to get an excess of holes (h) as majority charge carriers.

The intrinsic charge carriers density in the silicon at 300 K is typically  $10^{10}/cm^3$  and it has to be reduced by several orders of magnitude in order to detect the charge carries produced by a Minimum Ionizing Particle (MIP),  $\sim 10^4$ . It is achieved by depleting the silicon volume of free charge carriers, using p- or n-type silicon in a reverse-biased pn-junction configuration. The spontaneous recombination of both carrier types in proximity of the junction creates a depletion zone, which is free of charges carries and represents the active volume available for the particles detection. Supplying an external revers bias voltage the thermal equilibrium of spontaneous, generation and recombination of  $e^-/h$  is disturbed and the depletion zone gets wider. An ionising particle penetrates through the bulk of a fully depleted silicon and generates  $e^-/h$  pairs which drift along the electric field, created by the bias voltage  $V_{FD}$ . The electrons drift to the n+ doped side while the holes drift to the p++ back-plane, as shown in figure 1.6. The charge induced on the strips by the movement of the charge carries pairs is then capacitively coupled (AC) to the aluminium readout strips, which are directly (DC) connected to the charge preamplifier of the readout chip. The segmentation in the pn-junctions allows to collect the charges on a small individual strip, providing the information on the position of the crossing charged particle. The position resolution is given by the electrode pitch  $p$ ,  $\sigma = p/\sqrt{12}$ , due to the Gaussian distribution of the collected charge on the strips.

**Pixel Detector** Highest granularity around the vertex region is achieved using semiconductor pixel detectors. The system consists of one barrel with four layers at average radii of  $\sim 5$  cm, 9 cm, and 12 cm. An additional pixel layer, *Insertable B-layer* (IBL) was added at R=3 cm before Run 2 to improve the precision and

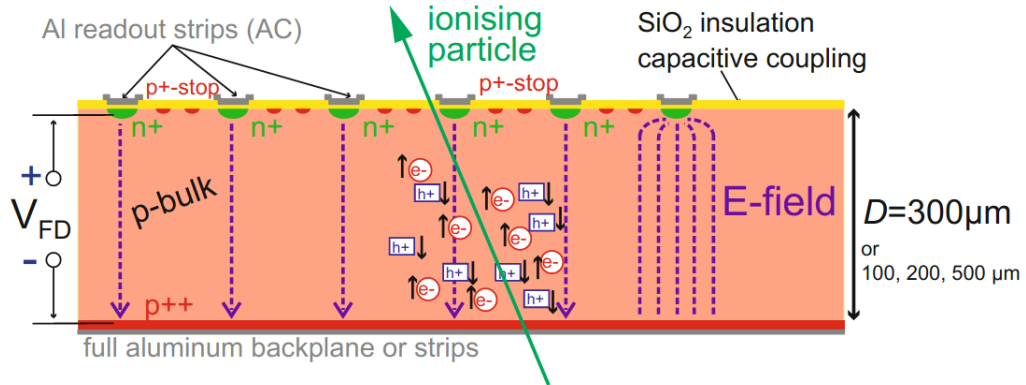


Figure 1.6: Working principle of a n-in-p AC-coupled silicon microstrip detector [17].

the robustness of the measurements. Three disks are located on each side, between radii of 11 and 20 cm, to complete the angular coverage. To maintain an adequate noise performance after radiation damage, the silicon sensors must be kept at low temperature (approximately  $-5$  to  $-10^{\circ}\text{C}$ ) implying coolant temperatures of  $\sim -25^{\circ}\text{C}$ . The sensors are  $250\ \mu\text{m}$  thick silicon pixel detectors, using oxygenated n-type wafers with readout pixels on the  $n^+$ -implanted side of the detector. The silicon pixel is  $50\ \mu\text{m}$  wide and  $250\ \mu\text{m}$  long.

**Strip Semiconductor Tracker** The SCT system is designed to provide four precision measurements per track in the intermediate radial range provided by the binary readout. It contributes to the measurement of momentum, impact parameter and vertex position, as well as providing good pattern recognition by the use of high granularity. Strip silicon sensors of the SCT use a classic single-sided p-in-n technology with AC-coupled readout strips. The module is a double layer strip sensor, the strips follow the axial direction on one side and are rotated by  $40\ \text{mrad}$  stereo angle on the opposite side. The barrel is made out of four cylindrical layers of strip sensors of pitch  $80\ \mu\text{m}$  at  $R=30, 37, 44$  and  $51\ \text{cm}$  and the single SCT endcap is built with nine disks. The SCT detector requires a cooling system too in order to reduce the leakage current due to radiation damage and thus to be operated in the temperature range  $-5^{\circ}\text{C}$  to  $-10^{\circ}\text{C}$ .

**Transition Radiation Tracker** The TRT is based on the use of straw detectors, which can operate at the very high rates and at room temperature. Straw tubes are very basic gas detectors: a tube (cathode biased with negative voltage) of  $4\ \text{mm}$  diameter presents in the centre a  $30\ \mu\text{m}$  diameter gold-plated tungsten wire used as anode. The barrel straws are arranged in 36 layers placed from  $R=55\ \text{cm}$  to

R=110 cm, each divided in two at the centre in order to reduce the occupancy and read out at each end. The endcaps radial straws have the readout at the outer radius. Each channel provides a drift-time measurement, giving a spatial resolution of 170  $\mu\text{m}$  per straw. Low-energy transition radiation (TR) photons, produced when a charged particle passes through an in-homogeneous media, are absorbed in the Xe-based gas mixture. It produces a much larger signal amplitudes than minimum-ionising charged particles. The distinction between TR and tracking signals is obtained on a straw-by-straw basis using separate low and high thresholds in the front-end electronics. Two independent thresholds allow the detector to discriminate between tracking hits, which pass the lower threshold, and TR hits, which pass the higher one.

The ID was installed in ATLAS in 2007 and is operative since the first collision in LHC, but a replacement of the whole system is planned for LS2 to prepare the experiment to HL-LHC. The upgraded version of this detector system is described in detail in section 3.1, as part of ATLAS Phase-II upgrade.

### 1.2.2 Calorimeter

The ATLAS calorimeters are detectors that measure a particle energy by absorbing it. They also measure the position and the direction of the energy release thanks to their segmentation. This information, in conjunction with the momentum information from the ID, allows the particle type to be identified. While the ID can only detect charged particles, the calorimeters are also sensitive to neutral particles as photons and neutrons. It is then possible to identify neutral particles by looking for a calorimeter hit with no correspondent track in the ID. The exception is made for muons and neutrinos which can not be detected in the calorimeters.

Additionally, the ATLAS calorimeters provide trigger functionalities to search for high-energy electrons, photons,  $\tau$  leptons, jets, and events with a high missing transverse energy.

The energy resolution of a calorimeter can be parametrized as the quadratic sum of three terms [18]:

$$\frac{\sigma(E)}{E} = \frac{a}{\sqrt{E}} \oplus \frac{b}{E} \oplus c \quad (1.4)$$

with:

- $a$  being the *stochastic term* related to the fluctuations of number of particles in a shower;
- $b$  depending on the *electronic noise*;

- *c* a constant term that takes into account all the other effects usually determined from the experimental data.

For energies of interest in high-energy physics the noise term is usually negligible. A calorimeter is usually designed to stop entirely most of the particles inside its volume, allowing the deposition of their energy, via interactions with atoms. The particle interaction with specific materials generates a cascade of secondary interactions, so-called shower. The energy of the primary particle is therefore split between the particles of the shower until when the available energy is below the threshold for further interactions. According to the nature of the particle involved in the primary interaction, the shower can be:

- *electromagnetic* (EM) if generated by electrons  $e^-$ , positrons  $e^+$  and photons  $\gamma$  that interact via the electromagnetic force.  $\gamma$  interact via pair production and  $e^-$ ,  $e^+$  emit photons via *Bremsstrahlung*. The shower ends when the  $\gamma$  energy is below the pair production threshold and the rest of energy is lost with ionizing processes.
- *hadronic* (H) if generated by hadrons (neutrons and protons) that interact via strong nuclear force. The energy is lost through hadron production, nuclear de-excitation and pion and muon decays.

The size of the EM shower is usually more compact and shorter than the hadronic one due to the type of interactions involved in the process. Therefore the ATLAS calorimeters size reflect the dimension of the shower that have to absorb. Calorimeters typically consist of layers of passive or absorbing high-density material, interleaved with layers of an active medium able to detect the particle shower.

The components of the ATLAS calorimetry system are: the *Liquid Argon (LAr) Electromagnetic Calorimeter* [19] and the *Tile Hadronic Calorimeter* [20], as shown in figure 1.7, in yellow and gray respectively. They consist of a number of sampling detectors with full  $\phi$  symmetry and coverage around the beam axis. The LAr calorimeters closest to the beam-line are housed in three cryostats, one barrel and two endcaps, cooled down with liquid nitrogen at  $-184^\circ\text{C}$  (87 K) to keep the Argon in liquid form. The barrel cryostat contains the EM barrel calorimeter, whereas the two endcap cryostats each contain an electromagnetic endcap calorimeter (EMEC), a hadronic endcap calorimeter (HEC), located behind the EMEC, and a forward calorimeter (FCal) to cover the region closest to the beam.

These calorimeters cover the range  $|\eta| < 4.9$ , using different techniques suited to the widely varying requirements of the physics processes of interest and of the radiation environment over this large  $\eta$ -range. Over the  $\eta$  region matched to the inner

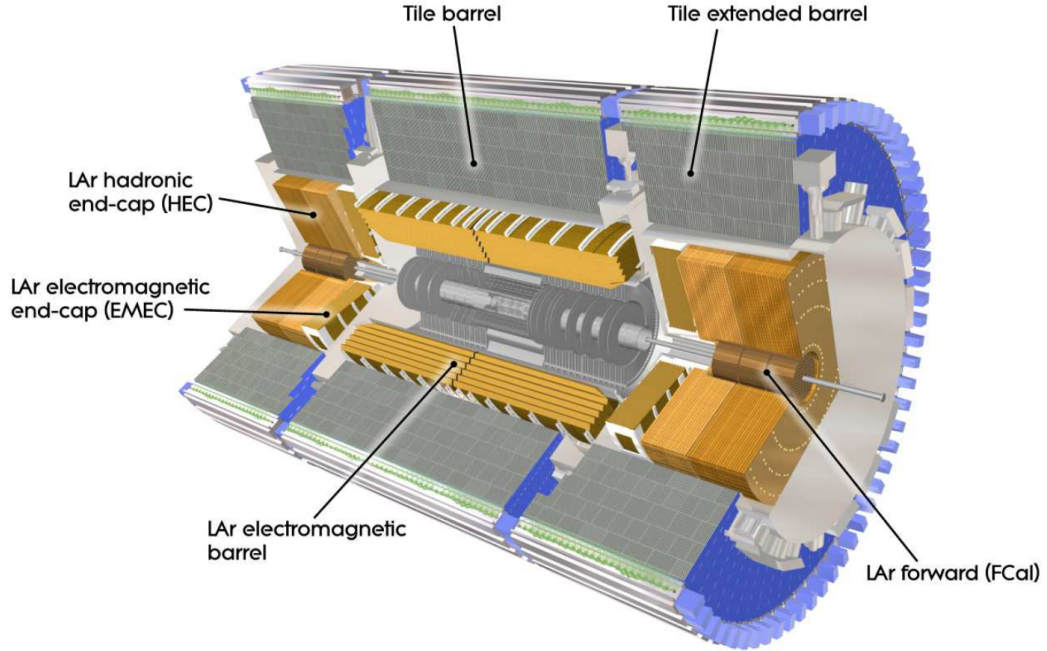


Figure 1.7: Structure and location of the EM and hadronic calorimeters in the ATLAS experiment [6]. In yellow the LAr-based calorimeters (barrel, EMEC, HEC, FCal) are shown and in gray the tile calorimeters.

detector, the fine granularity of the EM calorimeter is ideally suited for precision measurements of electrons and photons. The coarser granularity of the rest of the calorimeter is sufficient to satisfy the physics requirements for jet reconstruction and  $E_T^{miss}$  measurements.

### 1.2.3 Muon Spectrometer

The muon spectrometer (MS) forms the outer part of the ATLAS detector and it is designed to detect muons exiting the barrel and endcap calorimeters and to measure their momentum in the pseudorapidity range  $|\eta| < 2.7$ . It is also designed to trigger on high-energy muons in the region  $|\eta| < 2.4$  [21].

Although most of the particles are absorbed within the calorimeters, muons and neutrinos are able to escape detection. Muons are charged particles that interact electromagnetically and leave a track in the Inner Detector. They do not generate showers in the electromagnetic calorimeter, since they do not emit a significant amount of Bremsstrahlung due to their large mass. They also do not generate showers in the hadronic calorimeters, since they do not interact via the strong force. Although the muon momentum and identification can be performed with the ID, high-energy muons represent an important signature of several interesting phenom-

ena, as Higgs boson physics or new physics processes.

The muon spectrometer is built with different gas detector technologies that can be divided in tracking chambers, with good spatial resolution, and trigger chambers, having a good time resolution. All gas detectors use the ionising effect of radiation upon a gas-filled chamber. If a particle has enough energy to ionize a gas atom or molecule, the resulting electrons and ions cause a current flow which can be measured. The primary pairs can sometimes generate an avalanche of secondary pairs resulting in an amplified signal.

The chambers have in common the same basic design of two electrodes (cathode and anode) with a special fill gas, but each chamber uses a different method to measure the total number of electron-ion pairs that are collected. The strength of the electric field between the electrodes and the type and pressure of the fill gas determines the detector's response to ionizing radiation. The electrodes can be segmented in strips or pads to obtain an extra-information about the position of the crossing particle [22]. The ATLAS muon spectrometer and the location of all gas detector are depicted in figure 1.8 in a 3D view and a section's quarter of it is shown in figure 1.9. Precision-tracking chambers in the barrel region, *Monitored Drift Tube* chambers (MDT's), are located between and on the eight coils of the superconducting barrel toroid magnet, they are arranged in three concentric cylindrical shells ( $\eta < 1$ ) around the beam

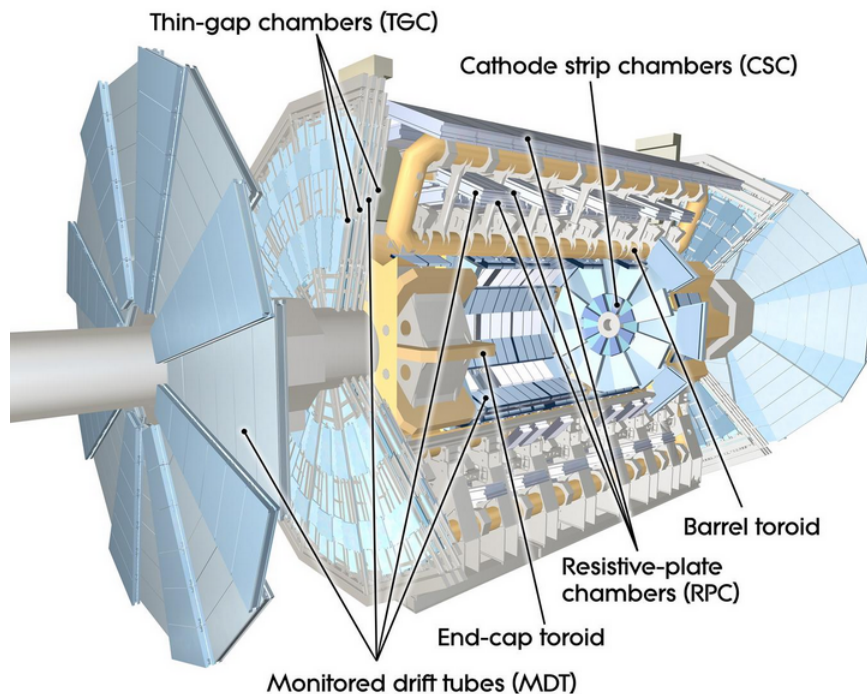


Figure 1.8: Structure of the muon spectrometer in the ATLAS experiment where the four type of chambers are highlighted [6].

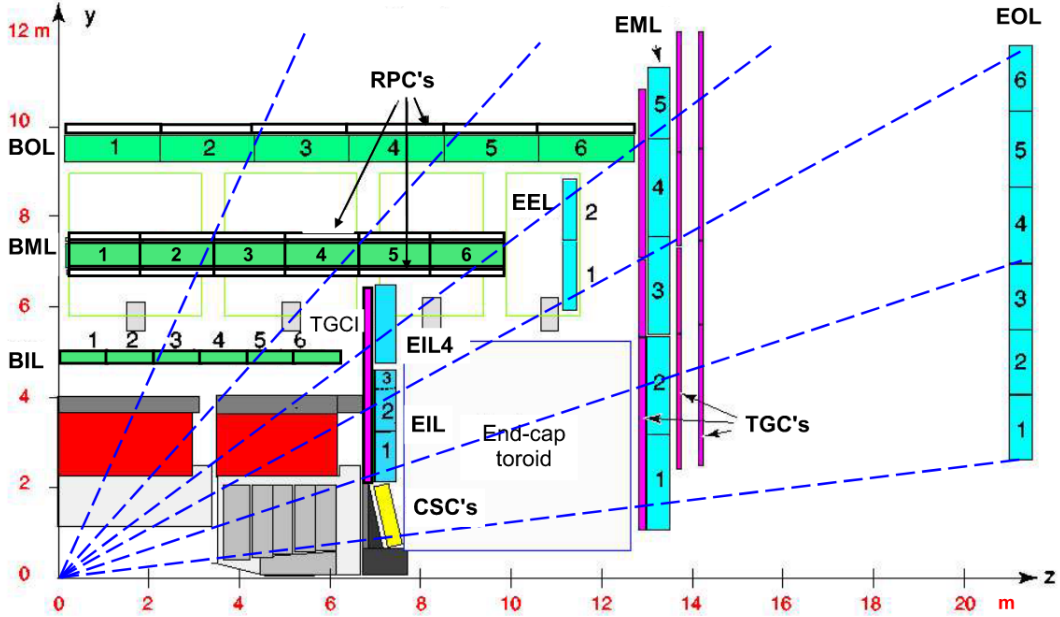


Figure 1.9: A quarter of the section of the muon spectrometer [6]: barrel MDT chambers are shown in green and in cyan in the endcap; barrel RPC in black, endcap TGC in purple.

axis. The trigger function in the barrel is provided by three stations of *Resistive Plate Chambers* (RPCs), used due to good spatial and time resolution as well as adequate rate capability. They are located on both sides of the middle MDT station, and either above or below the outer MDT station.

The endcap muon chambers lay in front (so-called Small wheel) and behind the two endcap toroid magnets, they form large wheels, perpendicular to the  $z$ -axis. In the forward region ( $2 < |\eta| < 2.7$ ), *Cathode-Strip Chambers* (CSC) are used in the innermost tracking layer due to their higher rate capability and time resolution. The trigger is provided by three stations of *Thin Gap Chambers* (TGCs) located near the middle MDT station ( $1 < |\eta| < 2.4$ ). They provide good time resolution and high rate capability. Their spatial resolution is mainly determined by the readout channel granularity. The mechanical structure of the ATLAS trigger chambers must have low thickness to minimize multiple scattering and independent mechanical supports to avoid mechanical stresses on the precision chambers.

### 1.2.4 Trigger and Data Acquisition

The proton bunch crossing frequency in LHC is 40 MHz provided by the bunch spacing of 25 ns. The ATLAS experiment is designed to observe up to 1.7 billion

$pp$  collisions per second with a combined data volume of more than  $60 \cdot 10^6$  MB per second. However, only some of these events will contain interesting characteristics that might lead to new discoveries. The ATLAS trigger system that is involved in the event selection is made of three levels: *Level-1* (L1), *Level-2* (L2), and the *Event Filter*. The flow of data is therefore reduced from  $10^{12}$  to  $10^3$  collisions, corresponding to a final rate of 200 Hz [6]. The L2 and the event filter is also called *High Level Trigger* (HLT). Each trigger level refines the decisions made at the previous level and, where necessary, applies additional selection criteria.

The L1 trigger is implemented using custom-made electronics, while the HLT is almost entirely based on commercially available computers and networking hardware. The functionality of each level trigger is described as follow.

**L1 trigger** The L1 hardware trigger works on a subset of information from the calorimeter (L1Calo) and muon (L1Muon) detectors. It searches for high  $p_T$  muons, electrons, photons, jets, and  $\tau$ -leptons decaying into hadrons, as well as large missing and total transverse energy. High  $p_T$  muons are identified using trigger chambers of the spectrometer, RPCs and TGCs, and the rest of particles from the calorimeter selections. The decision to keep the data from an event is made less than  $2.5 \mu\text{s}$  after the event occurs, reducing the rate to about 75 kHz.

In each event that L1 defines as interesting one, the features, like the position where the event was found, are stored, as well as information on the type of feature identified and the criteria passed, such as the threshold. This information is subsequently used by the high-level trigger.

**High Level trigger** HLT is made of Level-2 trigger and event filter. The L2 selection uses the information provided by the L1 trigger. This trigger level is designed to reduce the trigger rate to approximately 3.5 kHz, with an event processing time of about 40 ms, averaged over all events. The final stage of the event selection is carried out by the event filter, which reduces the event rate to roughly 200 Hz with an event size of approximately 1.3 MB. Its selections are implemented using offline analysis procedures within an average event processing time of the order of 4 s.

### 1.3 Phase-I upgrade of the ATLAS experiment

The LS2 of LHC started in 2019 to allow the replacement of the ATLAS detectors components. When the proton beam resumes for Run 3 data collection, the peak of luminosity is expected to reach  $2 - 3 \cdot 10^{34} \text{cm}^{-2}\text{s}^{-1}$  corresponding to 55 to 80 interactions per crossing (pile-up) with 25 ns bunch spacing, well beyond the initial

design goals. The Phase-I upgrade of the ATLAS experiment addresses the proposed enhancements to the trigger system to cope with luminosity beyond the LHC nominal design value, while retaining the same physics performance. In order to achieve an optimal trigger system as the luminosity increases beyond its nominal design value, a strong reduction of the main source of backgrounds is required: jets mimicking electrons in the calorimeters and fake muons in the forward spectrometer. Keeping trigger rates under control is a major requirement for preparing ATLAS for HL-LHC phase.

The major systems involved in this upgrade are the following:

- the muon spectrometer: the innermost layer of the forward region is completely replaced by the *new Small Wheel* (NSW) [23]. New tracking (*Micro-megas*, MM) and trigger (*small-strip Thin Gap Chamber*, sTGC) detectors are introduced to improve the tracking performance under the higher background;
- increment of the granularity of Liquid Argon Calorimeter (EM and FCal) [24]: new trigger read-out boards are implemented with higher granularity which leads to an improvement in rejecting fake electron triggers;
- Trigger and data acquisition (TDAQ) [25]: the input from the new trigger devices, as NSW and LAr calorimeter, are included in the L1 architecture. Software modifications are needed in the HLT and to be adapted to the modified L1 strategy;

Those upgrades are currently in progress and the LHC beam is expected to restart in March 2022. They were designed to be fully compatible with the physics program of the HL-LHC, where the integrated luminosity is increased by a factor 10 at the end of Run 4.

# Chapter 2

## Physics goals of HL-LHC and ITk layout

After a significant detector and accelerator upgrade scheduled for the long shutdown 3 (LS3), the LHC will start in 2027 to collide protons at the same energy of center of mass  $\sqrt{s}=14$  TeV, but the amount of data that will be produced is increased by a factor 10. The integrated luminosity is expected to be  $3000 \text{ fb}^{-1}$  in 14 years with an average of  $\langle\mu\rangle = 200$  of inelastic collision per beam-crossing, also known as pile-up.

Physicists named this new LHC era with *High Luminosity LHC* (HL-LHC) which represents an extremely challenging environment to the ATLAS experiment, well beyond what it was designed for. One of the major detector upgrades that the ATLAS collaboration decided for Phase-II is the replacement of the Inner Detector with a new all-silicon tracker (ITk) to maintain tracking performance in this high-occupancy environment and to cope with the increase of approximately a factor of ten in the integrated radiation dose.

This chapter gives an overview on the necessity to go higher in luminosity which leads to HL-LHC. Section 2.1 provides a motivation from the physics point of view and the analysis that is planned on the large amount of data that HL-LHC will provide during Run 4. The next section 2.2 discusses briefly the detector upgrades that are planned for the ATLAS experiment. Section 2.3 is entirely focused on the requirements of the new inner tracker: channel occupancy, the number of hits per track for reconstruction purposes and the radiation doses. The latest ITk layout (23-00-03) is also provided and simulations performed in order to get estimations on its performances are presented.

## 2.1 Physics motivation

In the Standard Model (SM) one of the main topics of investigation of the LHC program is the electroweak symmetry breaking [26], it is achieved through the introduction of a scalar field, leading to the prediction of the Higgs boson. The proton-proton collisions at LHC allowed the discovery of a new boson with a mass around 125 GeV, consistent with the SM Higgs particle. Analysing Run 1 data, in 2012 the ATLAS [27] and CMS [28] experiments found the evidence of the Higgs particle, which brought Peter Higgs and Francois Englert to win the nobel prize in Physics in 2013 for *the theoretical discovery of a mechanism that contributes to our understanding of the origin of mass of subatomic particles* [29]. The most precise mass measurements of this spin-0 particle are obtained from the most sensitive decay channels,  $H \rightarrow ZZ^* \rightarrow 4l$  and  $H \rightarrow \gamma\gamma$ , calculating the invariant mass of its decay products. The combined ATLAS and CMS value is  $m_H = 125.09 \pm 0.21(\text{stat.}) \pm 0.11(\text{syst.}) \text{ GeV}$  [30], as shown in figure 2.1. With  $m_H$  known, all properties of the SM Higgs boson, such as its production cross section and partial decay widths, can be predicted. Precise measurements have established that its observed properties, including the spin, parity, and coupling strengths to SM particles are consistent within the uncertainties with those expected theoretically by the model.

The HL-LHC physics program is designed to address fundamental questions about the nature of matter and forces at the subatomic level. The low value of the Higgs boson mass poses the so-called hierarchy problem of the SM [31], which might be

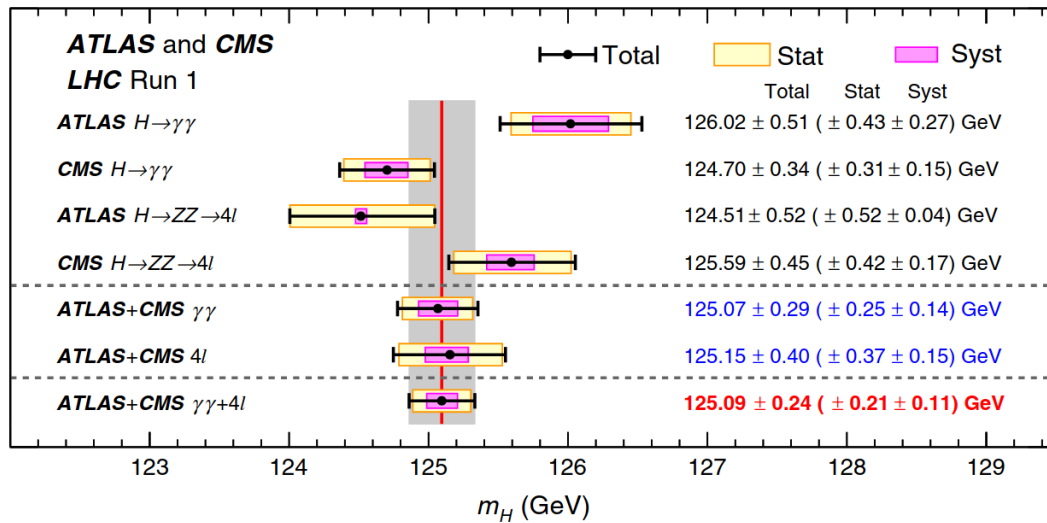


Figure 2.1: Higgs boson mass measurements from the individual and combined analysis of ATLAS and CMS [30].

explained by new physics and a better understanding of electroweak symmetry breaking. If evidence of deviations from the SM, including new particles, are seen before the Phase-II upgrade, the HL-LHC will allow further investigation of the new landscape of particle physics. In the absence of any such hint, the ten-fold increase in data will push the sensitivity for new physics into uncharted territory.

The large statistics brings each analysis group to aim for the discovery of new particles to consolidate the SM or confirm new theory, such as the SuperSymmetry (SUSY) [32], to measure particle properties with high precision and to address questions to which no answers have been found yet. One of those theories concerns the Dark Matter (DM) [33]: its existence has been proved, but there are many hypothesis about its nature. There may be a new *Weakly Interacting Massive Particle* (WIMPs) to explain the existence of DM [34].

The physics program at HL-LHC can be divided in four research groups [35]:

- *Higgs Boson measurements*: considerable improvement is expected in precise measurements of properties of the Higgs boson, e.g. couplings measurements at the percent level, and of the SM production processes;
- *Standard Model*: searches for new physics through the study of rare SM process, searches for new heavy states, and measurements of the properties of any newly discovered particles.
- *Beyond Standard Model*: observation of new particles in the TeV energy scale are expected or at least fixing new lower limits to particle masses;
- *Flavour physics*: understanding of matter-antimatter imbalance measuring the element of the CKM (Cabibbo-Kobayashi-Maskawa) matrix [36], which contains information on the strength of the flavour-changing weak interaction.

In the following, some examples on those analysis are provided.

### 2.1.1 Higgs Boson measurements at HL-LHC

Eight years after the discovery of the Higgs boson, with a significantly larger dataset collected during LHC Run 2 at  $\sqrt{s} = 13$  TeV, the theoretical and experimental particle physics communities started to explore the potential for precision measurements of its properties. This includes studies of Higgs boson production and decays processes, the search for rare decays and production modes, high energy observables, and searches for an extended electroweak symmetry breaking sector.

The mass of the Higgs boson is particularly favourable as it allows to measure directly a large number of its couplings. The dominant production mode is gluon-gluon

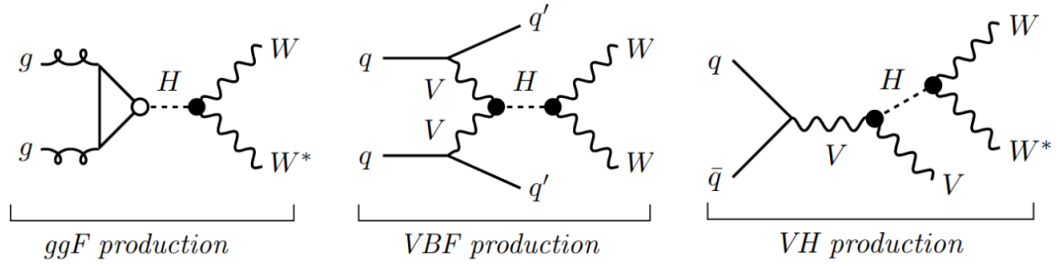


Figure 2.2: Feynman diagrams of the Higgs boson productions at LHC [37]: gluon gluon fusion (ggF), Vector Boson fusion (VBF) and Vector Boson (VH).

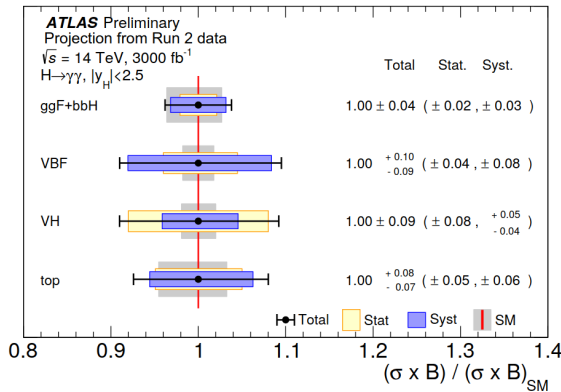


Figure 2.3: Cross-section times branching fraction measurements of the main Higgs production modes in the  $H \rightarrow \gamma\gamma$  decay channel, extrapolated for the HL-LHC dataset [35].

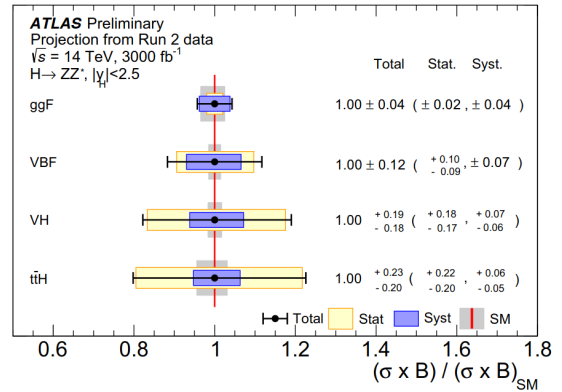


Figure 2.4: Cross-section times branching fraction measurements of the main Higgs production modes in the  $H \rightarrow ZZ^* \rightarrow 4l$  decay channel, extrapolated for the HL-LHC dataset [35].

fusion (ggF), followed by the vector boson fusion (VBF), a factor of 10 lower, and production in association with W and Z bosons (VH), as represented in figure 2.2 by the Feynman diagrams. These data will allow the study of many Higgs boson production and decay modes.

Figures 2.3 and 2.4 show the ratio of the extrapolated  $H \rightarrow \gamma\gamma$  and  $H \rightarrow ZZ^* \rightarrow 4l$  ATLAS measurements of the cross sections times branching ratio of the main Higgs production modes to their respective theoretical SM predictions  $(\sigma \times B)/(\sigma \times B)_{SM}$ . The measurements in those decay channels are extrapolated from the projection of the Run 2 dataset with an increment of the statistics as in HL-LHC.

## 2.1.2 Standard Model at HL-LHC

The LHC results have so far confirmed the validity of the Standard Model of particle physics up to unprecedented energy scales and with great precision in strong and

electroweak interactions, Higgs boson as well as flavour physics including top quark properties. The HL-LHC program, thanks to a ten-fold larger data set, upgraded detectors and expected improvements in the theoretical understanding, will extend the sensitivity to new physics in direct and indirect searches for processes with low production cross sections and harder signatures. In addition, a considerable improvement is expected in precise measurements of properties of SM production processes. Several of these measurements will be limited by the uncertainties on the knowledge of the partonic inner structure of the proton, i.e. Parton Density Functions (PDFs) [38]. Global PDF fits of several HL-LHC measurements will allow a significant improvement in PDF uncertainties and, in turn, in measurements of SM parameters. Anomalies in precision measurements in the SM sector can become significant when experimental measurements and theoretical predictions reach the percent level of precision, and when probing unprecedented energy scales in the multi-TeV regime. These anomalies could give insights to new physics effects from higher energy scales.

### 2.1.3 Beyond Standard Model

In most extensions of the SM, new particles are expected at the TeV scale. To date, no such particles have been observed, implying that:

- their mass is above the current level of sensitivity,
- their production rates are lower than expected, or
- their experimental signatures are very difficult to observe.

These problems can be solved by an increase in centre-of-mass energy, which can benefit the produced states with large cross sections. The higher integrated luminosity helps to improve the sensitivity for final states with lower cross sections, including those produced by electroweak interactions. The HL-LHC will offer new possibilities to test many beyond Standard Model (BSM) scenarios, motivated by long-standing problems such as electroweak naturalness, DM, neutrino masses, the strong CP (Charge conjugation-Parity) problem, and baryogenesis.

An example of SUSY investigation is the search for direct production of top squarks ( $stop \tilde{t}$ ), which is the superpartner of the top quark as predicted by this theory. It requires the stop to be light, with a mass typically below 1 TeV. An increase in luminosity from  $300 \text{ fb}^{-1}$  to  $3000 \text{ fb}^{-1}$  increases the sensitivity to heavy stop or, if stop candidates are found, will allow to measure their properties. The pair-produced stops are assumed to decay to a top quark and a Lightest Supersymmetry Particle LSP (neut-

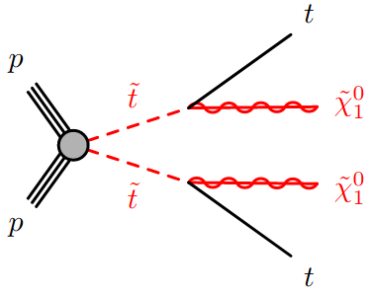


Figure 2.5: Feynman diagram for the stop decay  $\tilde{t} \rightarrow t + \tilde{\chi}_1^0$  [39].

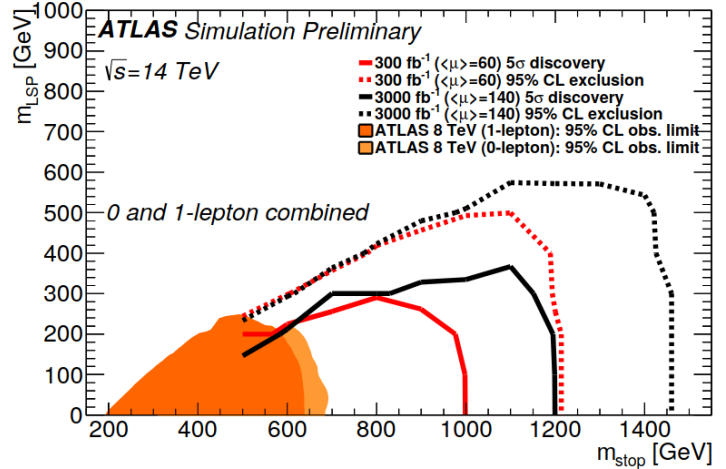


Figure 2.6: The 95% CL exclusion limits and  $5\sigma$  discovery reach for  $300 \text{ fb}^{-1}$  and  $3000 \text{ fb}^{-1}$  in the  $\tilde{t} - \tilde{\chi}_1^0$  mass plane assuming  $\tilde{t} \rightarrow t + \tilde{\chi}_1^0$  [39].

ralino  $\tilde{\chi}_1^0$ ),  $\tilde{t} \rightarrow t + \tilde{\chi}_1^0$  with 100% branching ratio, requiring that  $m(\tilde{t}) - m(\tilde{\chi}_1^0) > m(t)$ . The final state for such a signal is characterized by a top quark pair produced in association with large missing transverse momentum from the undetected LSPs. The Feynman diagram of the stop decay is shown in figure 2.5, the exclusion limits and the discovery potential are shown in figure 2.6 in two different scenarios:  $300 \text{ fb}^{-1}$  and  $3000 \text{ fb}^{-1}$  integrated luminosity for the combination of 1-lepton and 0-lepton analyses, as possible decays of the top quark ( $t \rightarrow Wb$  with  $W^+ \rightarrow l^+\nu$  and  $W^- \rightarrow q'\bar{q}$ ).

## 2.2 Phase-II upgrade of the ATLAS detectors

In order to fulfill the requirements expected in HL-LHC, the ATLAS experiment has planned to have the Phase-II upgrade during LS3, scheduled from 2025 to the middle of 2027 and it involves:

- the tracker: a replacement of the whole ID, introduced in section 1.2.1, is needed due to the increased track rate and extreme radiation levels. The upgraded tracker is called *Inner Tracker* (ITk);
- change of the front-end readout electronics of the LAr (HEC and FCal) [40] and Tile [41] calorimeters. This is required due to ageing caused by radiation damage, and the need for ATLAS to upgrade the trigger architecture, requiring real-time performance capabilities that the current electronics cannot satisfy;
- the muon system: performance increase is required in elements of the muon

spectrometer system, meaning the muon precision tracking as well as the triggering system [42]. A large fraction of the front-end and on- and off-detector readout and trigger electronics will be replaced;

- the trigger and data acquisition system [43]. A new architecture is being developed that is compatible with the constraints imposed by the detector and provides a flexible trigger with the potential to deliver the required performance;
- software and computing, to be able to handle the large event samples and provide simulations and reconstruction code that takes into account the upgrades of the detectors.

The upgraded detector of the ATLAS tracker is described in the following section as it is the main topic of this thesis. In particular the reasons that brought to the latest design of the ITk layout are presented and more details about its structure are provided in section 3.1.

## 2.3 The ITk layout

In order to satisfy the physics requirements of the HL-LHC program, the ATLAS ITk detector was designed to meet stringent criteria for radiation hardness, channel occupancy, track reconstruction efficiency and track parameter resolution. These specifications are reflected in its layout and in each decision that was made to address the physics goals of Run 4. The available space in ATLAS for the ITk detector, also called *envelope*, is constrained by the neutron moderator on the barrel area and by the electromagnetic endcap calorimeter (EMEC) on the forward region.

The ITk is an all-silicon detector consisting of a pixel subsystem with a pseudorapidity coverage of  $|\eta| < 4$  and a strip subsystem covering the interval  $|\eta| < 2.7$ . The pixel subsystem consists of five flat barrel layers and multiple inclined or vertical ring-shaped endcap disks providing coverage in the forward region [44]. The strip subsystem comprises four strip module layers in the barrel region and six disks in the endcaps. Each strip layer/disk provides double measurement per hits due to double-sided modules. The number of pixel/strip barrels and disks and their location in the tracker has to guarantee:

- the hermetic coverage for tracks with transverse momentum  $p_T > 1$  GeV from any primary vertex in  $z = \pm 150$  mm from the nominal IP;
- the required number of hits per track for reconstruction purposes;

- low channel occupancy according with the particle rate expected in that location;
- enough resolution on track parameters such as  $p_T$ .

To get the best track reconstruction the detection layers have to be placed as close as possible to the IP as well as far as possible from it, taking into account the space available in the ITk envelope. It also increases the  $p_T$  resolution as it depends on the path length of the particle in the magnetic field.

An idealised spherical detector built around the IP would give an optimal performance from the perspective of ensuring normal impact of particles on sensors, and reducing the path length through the materials and thus the multiple scattering. The assembling of such a detector is not very practical and the implementation in the envelope is not realistic, therefore a barrel and endcap structures are implemented around the beam pipe and the layers orientation is thought to increase the small hitting angle of particles. An example is provided by the *Pixel Inclined* in the innermost endcap region in ( $400 < z < 1000$ ) mm, where the transition of the incidence angle from the pixel barrel to the pixel endcap is large. This tracking area, very close to the IP, needs to provide high precision measurement, it is instead not required for the strip subsystem because of its lower precision and the amount of material crossed by the coming article is already large. Those considerations brought to the latest layout of the ITk detector depicted in figure 2.7.

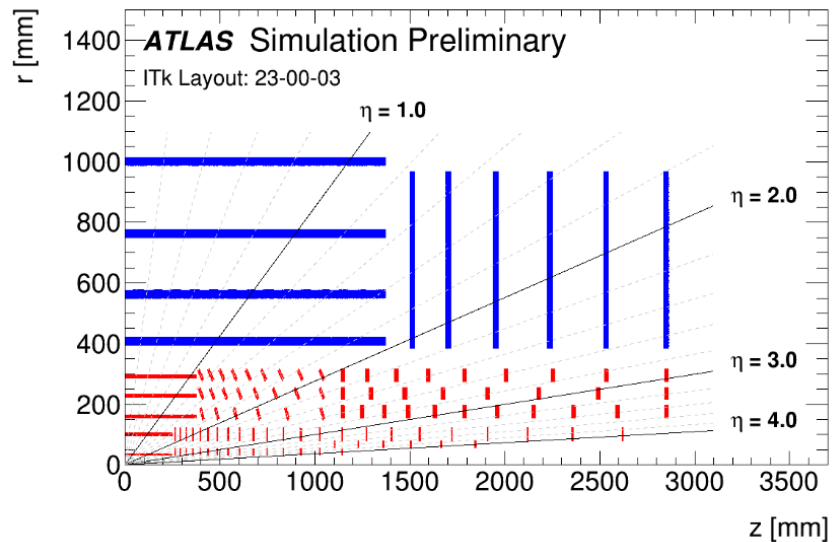


Figure 2.7: Schematic depiction of a quarter section of the latest version of the ITk Layout (23-00-03) [45]. The pixel detector is represented in red and the strip one in blue.

The ITk layout, as it was designed in order to satisfy all the physics requirements, had to be at the same time feasible from the engineering point of view. As the simulation becomes the baseline for the design, it does not take into account factors that appear only after starting the detailed engineering process. The detector layout has to include the clearance between active components and their insertion is one of the engineering aspect that constrained the ITk layout and had to be fulfilled.

**ITk envelope** The ITk size is constrained by other components that are located around it which establish the envelope. The envelope has to include the detector itself and also takes into account all the services and the clearance for the insertion. The main objects that limit the detector size are the beam pipe, the neutron moderator and the EMEC. The tracking detector is surrounded by a polyethylene moderator to moderate neutrons. This decreases the 1 MeV neutron equivalent silicon damage fluence arising from the flux of neutrons entering from the calorimeters. The envelope dimensions can be explained as follows:

- Barrel: the radius of the innermost pixel layer was recently reduced to  $r = 34$  mm due to the expected improvement in tracking performance [45]. The outer radius of the strip barrel is fixed at  $r = 1000$  mm due to the neutron moderator.
- Endcap: the innermost point of the endcap rings was fixed at  $z = 33.2$  mm for tracking purpose. The last endcap disk is constrained by the EMEC. Due to the latest decision to include the *High Granularity Timing Detector* (HGTD) between the ITk and the EMEC, the outer strip endcap disk was moved inward at  $z = 2850$  mm [46].

The HGTD [47] is based on low gain avalanche detector (LGAD) technology and cover the pseudorapidity region  $2.4 < |\eta| < 4.0$ , with a timing resolution of 30 ps for minimum-ionising particles. Making use of the time of flight (ToF) of particles produced by the pp collision, this device helps in the precise assignment of tracks to primary vertices, which is one of the key elements to mitigate the effects of pileup on the event reconstruction algorithms.

### 2.3.1 Radiation environment

Due to the increased luminosity and the associated increase in the number of particles, the expected radiation levels in the ITk will increase by roughly an order of magnitude compared to the present ATLAS Inner Detector. The radiation damage is one of the most important challenges faced by the ITk detector as it significantly deteriorates the performances of the detector by reducing the hit detection efficiency

and increasing the noise occupancy.

The predictions of particle fluences and ionising doses for the ITk layout are simulated assuming an integrated luminosity of  $4000 \text{ fb}^{-1}$  at a centre-of-mass  $\sqrt{s} = 14 \text{ TeV}$ .

Volume damages in the silicon are due to *non-ionising energy loss* (NIEL), consisting in direct particle collisions with atomic nuclei of the crystal lattice which can cause a dislocation or distortion of the lattice. Three main effects are identified as consequences of the Si substrate damage: *change of the effective doping concentration* (type inversion of the bulb, from n to p), *leakage current* (increasing with high fluence and temperature due to thermal excitation) and *trapping* of charge carriers [48]. In the ITk detector silicon sensors are fabricated in p-type wafer, as  $n^+$ -in-p sensors are more radiation tolerant than  $p^+$ -in-n [49]. The simulation in figure 2.8 shows an integrated hadron fluence of over  $1.3 \times 10^{16} \text{ n}_{\text{eq}}/\text{cm}^2$  in the innermost pixel region and  $1.6 \times 10^{15} \text{ n}_{\text{eq}}/\text{cm}^2$  in the strip system. It has been simulated with 1 MeV equivalent neutron fluence, i.e., the fluence of 1 MeV neutrons that would cause the same amount of displacement damage in silicon as the actual mixed particle spectrum.

Figure 2.9 shows the corresponding radiation dose in the ITk, which is 50 Mrad (500 kGy) in the endcap.

### 2.3.2 Material Budget

The choice of the detector layout, in particular the number of layers/disks is driven by another important aspect to be considered in the detector design: the *material budget*. The ITk has to be "transparent" to crossing particles for the following reasons:

- to reduce the multiple scattering when the particles pass through the detector to avoid large deviations from the original trajectory for tracking purpose;

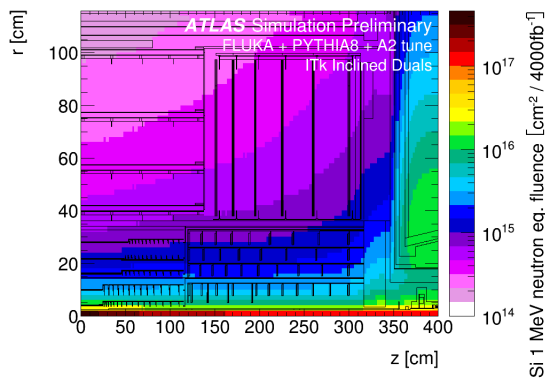


Figure 2.8: 1 MeV neutron equivalent fluence per  $4000 \text{ fb}^{-1}$  of integrated luminosity in the ATLAS ITk [50].

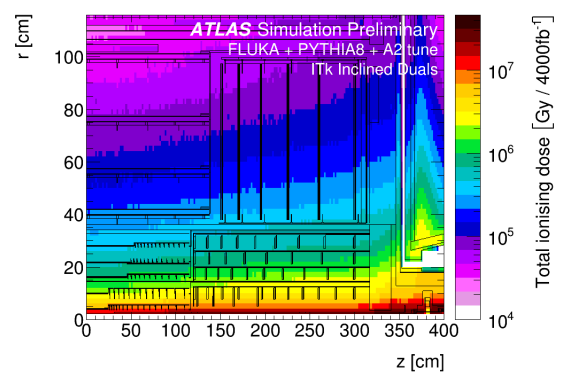


Figure 2.9: Total ionising dose (TID) per  $4000 \text{ fb}^{-1}$  of integrated luminosity in the ATLAS ITk [50].

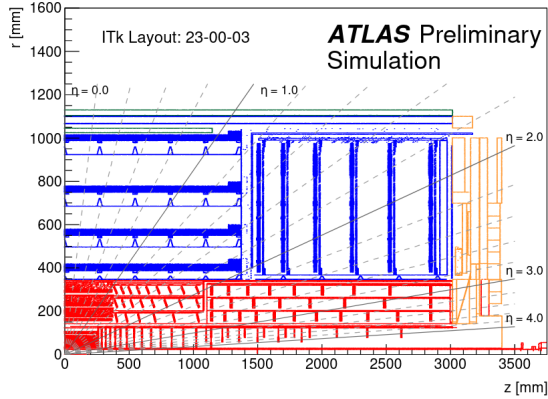


Figure 2.10: Material distribution of one quadrant of the ITk detector, the pixel (strip) detector is shown in red (blue), the neutron moderator in green and the PP1 in orange [45].

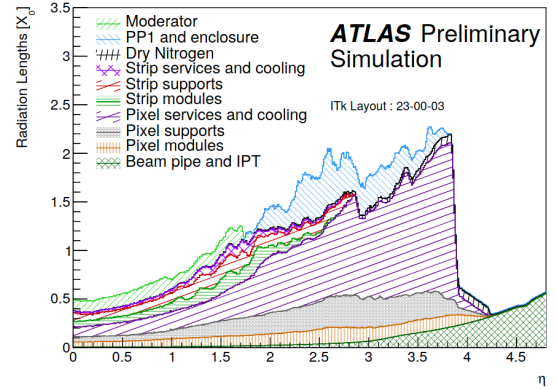


Figure 2.11: Integrated radiation lengths distribution as function of  $\eta$ , within the ITk volume [45]. The detector material is divided in each of its component.

- to minimize the energy loss because of the scattering;
- to allow the particles to reach the calorimeter, placed behind the tracker, for the measurement of their energy.

The distribution of the material in a quarter of the ITk section is shown in figure 2.10: it includes the ITk detector, the moderator, placed around the strip barrel at  $r = 1100$  mm, the enclosure and the patch panel 1 (PP1). PP1 is where the services and cooling needed for the detector are connected. In figure 2.11 one can see the trend of the integrated radiation length  $X_0$  as a function of pseudorapidity  $\eta$  simulating a particle with a straight path at the exit of the ITk volume. The radiation length gives information about the energy loss of particles crossing a specific material with defined thickness. At large  $\eta$  the contribution of the pixel and strip services and cooling, PP1 and the enclosure becomes significant and it can affect the performance of the forward detectors. For example, the choice of using carbon fiber as the main material for the sensor local support and global structure of the ITk was made because of its lightness, robustness and high  $X_0$  [51][52].

### 2.3.3 Channel Occupancy

The fraction of channels per module which register a hit and need to be read out is defined as channel occupancy. It is given by the number of hits divided by the total number of channels in a silicon sensor. The goal is to get a maximum occupancy average of 1% to ensure a robust and efficient pattern recognition, and a maximum

value per event well below 90% to avoid saturation of the readout [37].

The density of particles produced by the protons collision is higher in the region close the IP and gets lower going at higher radius. Due to particles spreading out as they move outwards from their interaction vertex, the sensor strip length gets longer and longer going from beam line to larger radius. This choice has to guarantee at same time hermiticity and high granularity. Therefore the silicon strip pitch and length were chosen to have low occupancy everywhere:

- barrel sensors have parallel strips with a pitch of  $75.5\ \mu\text{m}$  and they exist in two flavors, one has four rows of short strips in z-direction (24.10 mm, which sit in the two inner layers) and the other has two rows of longer strips (48.20 mm, which sit on the two outer layers);
- endcap sensors strips have their own length according with the particle rate of the disk in a specific position and the ring in which they sit. Due to the radial strip orientation the pitch was constrained to be as close as possible to the barrel one.

Figure 2.12 shows the two-dimensional view of the average occupancy in the entire ITk detector. The occupancy in the strip detector is a factor 10 higher than the pixel detector due to the lower strip granularity compared with pixels. In the outer strip disk the occupancy is generally the highest due to back-scattering of particles from the endcap calorimeter.

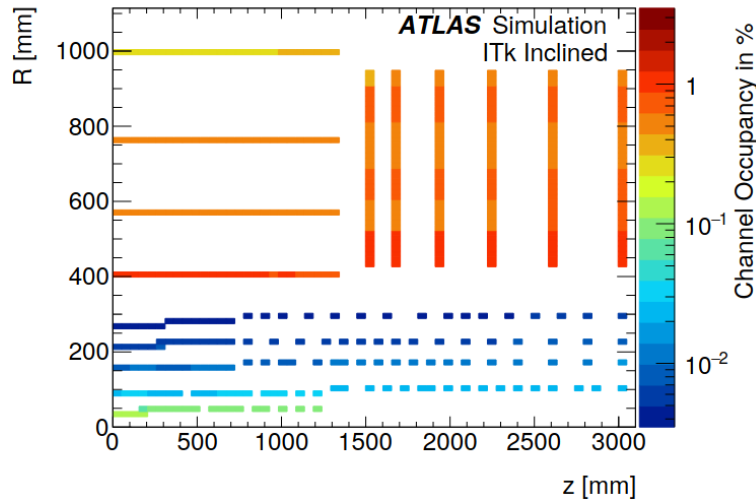


Figure 2.12: Average channel occupancy of the ITk detector calculated from minimum bias events with  $\langle\mu\rangle = 200$  [37].

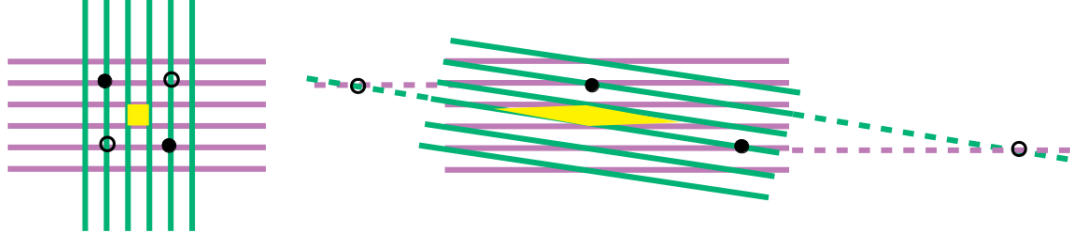


Figure 2.13: Assignment ambiguity of two simultaneous hits in case of orthogonal strips and small angle crossing [48]. The full dot represents the real hit and the circle the ghost one. The yellow area represents the spacial resolution due to the angle between the strips.

### 2.3.4 Track Reconstruction

The single pixel sensor hit provides a 2D measurement. To obtain a bi-dimensional tracking information from the strip silicon sensors, two set of strips are needed on the same layer/disk. A small stereo angle ( $\varphi = 40$  mrad) between strips on opposite sides of a structure in the barrel and endcap system is used to minimize the number of ghost hits. Two simultaneous hits on strips of different readout planes generate two ghost hits too in case of perpendicular strips [48], as shown in figure 2.13. On one side the small stereo angle decreases the probability of ghost hits thanks to the smaller number of crossed strips over the sensor area, in comparison with a normal angle. Therefore the pattern recognition in track finding is simplified. On the other side the stereo angle implementation goes against the spacial resolution, represented in yellow area in the figure, which gets worse compared to using an orthogonal angle. The choice of 40 mrad was made to optimize the ghost hits number and the strip hermeticity.

The reconstruction chain starts with forming clusters from the individual channels for the strip and pixel subdetectors. For the pixel detector the *Time over Threshold* (ToT) information of each channel is converted into a representative charge measurement. Pixel and strip clusters are converted to 3D space-points. The pattern recognition starts building seeds, i.e. combinations of three pixel or strip space-points. The Silicon Track Finding uses seeds to define a search road and implements a combinatorial *Kalman filter* to find track candidates compatible with the initial seed. At this stage tracks are fitted with a global  $\chi^2$ -minimization technique using precise information on material model and magnetic field.

The combination of pixels and double-sided strip modules is designed to have at least nine precision measurements per track for the full width of the expected beam spot size, which is assumed to be Gaussian shaped with a width of 50 mm, for any

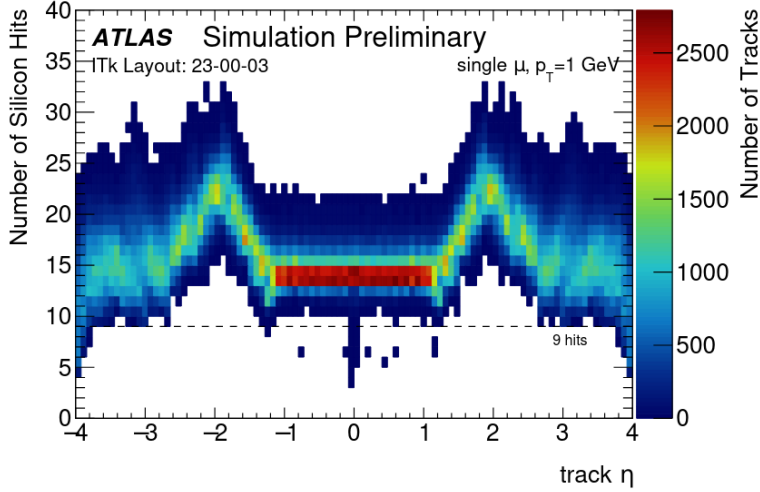


Figure 2.14: Number of silicon hits per track as function of  $\eta$ , a single muon event is simulated with  $p_T = 1$  GeV [45].

charged particle with  $p_T > 1$  GeV traversing the detector in  $|\eta| < 4.0$ .

The number of hits per track, expected from the pixel and the strip sub-detectors, can be observed in figure 2.14, it is shown as a function of pseudorapidity and obtained simulating a single muons with  $p_T = 1$  GeV.

The number of fake tracks, defined as failures in the reconstruction process when hits from different particles are assigned to the same trajectory, could be reduced increasing the number of hits per track. Adding more detection layers in the ITk helps in reducing the random combinatorial collection of hits from different particles. At the same time the additional layers bring more material in the detector: it degrades the performances due to the multiple scattering and increases the cost. Therefore the number of hits per track required for the pattern recognition was optimized in order to address this two factors.

One crucial requirement on the track reconstruction regards the software chain: it is important to reduce the number of fake tracks in order to minimize the total processing time per event. This is driven by the limits of the CPU time consumption.

# Chapter 3

## The ITk Project

The luminosity of the High Luminosity LHC (HL-LHC) will be increased up to  $L = 7.5 \cdot 10^{34} \text{cm}^{-2} \text{s}^{-1}$  while the energy of the colliding particles is left unchanged, at 7 TeV per proton beam. It corresponds to approximately 200 inelastic proton-proton collisions per beam crossing ( $\langle \mu \rangle = 200$ ) [53]. The increase in the integrated luminosity requires a detector able to operate under the exposure to a large particle fluency. The high rate has an impact on the detector occupancy and radiation damage, as explained in the previous chapter, and therefore an upgrade is required for a performing detector under these conditions.

A major upgrade of the ATLAS experiment for Phase-II concerns its tracker, which will be completely replaced by a all-silicon detector, called *Inner Tracker* (ITk). A detailed explanation of the ITk is provided in section 3.1 as it is the main topic of this thesis. A large overview on single component, which are the local support structure, silicon modules and End of Substructure card (EoS), is also given. Section 3.2, is focused on the ITk activities in which the DESY group in Hamburg is involved in.

### 3.1 The Inner Tracker

The inner detector plays an important role in ATLAS physics analysis, as it provides:

- reconstruction of the trajectories of charged particles;
- identification of the primary and secondary vertices;
- heavy-flavour tagging.

The current ATLAS ID, as described in section 1.2.1, was designed to be able to operate under a pile-up average of 23 proton interactions per bunch crossing [6]. It needs to be completely replaced for the Phase-II upgrade due to increased radiation environment, detector occupancy and trigger rate, as well as aging and radiation damage of the existing components.

The new ITk is going to be functional for more than ten years up to the end of the HL-LHC operation and, in that period of time, ATLAS aims for a total of  $4000 \text{ fb}^{-1}$  data collection. The pseudorapidity acceptance is extended from the current value of  $|\eta| = 2.7$  up to  $|\eta| = 4$ , to improve the track reconstruction.

The layout of the ITk detector, as described in section 2.3 and depicted in figure 2.7, is optimised with a focus on tracking performance, cost effectiveness, easy construction and installation.

The new tracking system is an all-silicon detector: it is made of silicon pixel, up to  $|\eta| < 4$ , surrounded by the strip detector covering  $|\eta| < 2.7$ . Both sub-detectors present a central barrel with a cylindrical geometry developed around the beam pipe, and the forward regions are covered by endcap structures with radial symmetry, as shown in figure 3.1. The strip barrel is populated by *staves*, 2.8 m long structure that covers  $|z| < 1400 \text{ mm}$  and where 14 identical modules, with a roughly  $(97 \times 97) \text{ mm}^2$  silicon sensor, are glued onto per side. The number of staves per barrel layer increases with the radius from the beam pipe. Each of the strip endcap disks is divided in 32 identical wedge shaped segments called *petals* and distributed on a radial geometry. The petal is roughly 600 mm long and covers an area  $400 \text{ mm} < r < 1000 \text{ mm}$ . Staves and petals differ in the geometry but they have a very similar structure, both assembled with three primary units: the local support, the silicon modules and the End-of-Substructure (*EoS*) card. In the following there is a dedicated section for every component in which its structure and functionality are explained with a focus on the petal system.

### 3.1.1 Local support

A local support, also called core, is the structure that holds all the detector components. It is a sandwich structure made of a cooling loop and low-density carbon-fibre

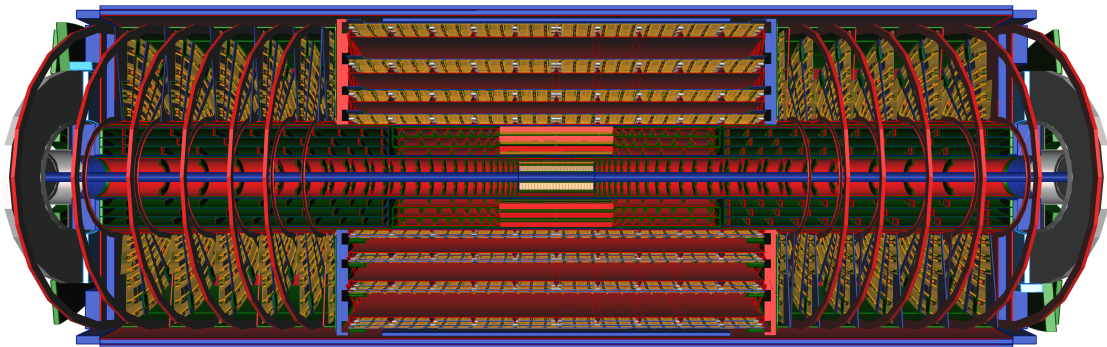


Figure 3.1: Schematic of the ITk detector for the ATLAS Phase-II upgrade [45].

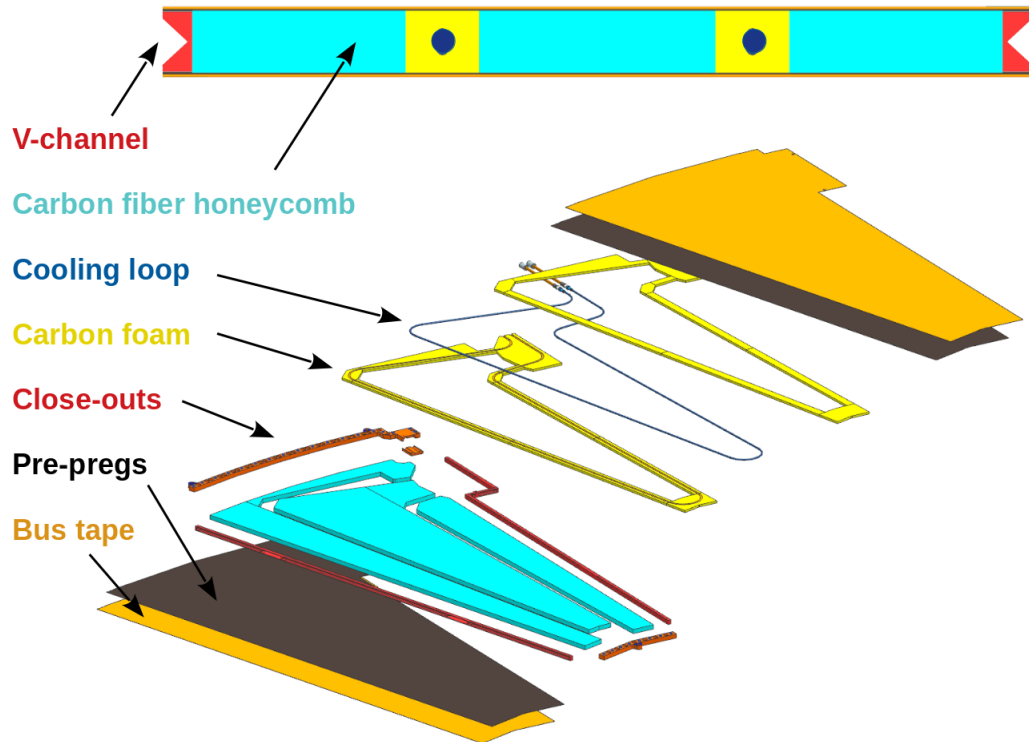


Figure 3.2: Internal structure of the petal core. From the outside there is the bus tape (orange), co-cured with pre-pregs (black), thermal conductivity foam (yellow), a cooling loop (blue), carbon fiber honeycomb (cyan) and close-outs and V-channels (red).

honeycomb, closed by two face-sheets. The face-sheets are obtained by a co-curing process of carbon-fiber sheets with a multi-layer polyimide foil, called bus tape, which provides the electrical lines from the EoS to the modules along the local support. The core is surrounded by close-outs which allow mechanical mounting on the global support structure. Figure 3.2 shows a cross section and an exploded view of the internal structure of the core.

**Bus tape** The bus tape routes the bus lines between the module electronics and the EoS which are directly glued on it. The tape provides the low and high voltage power lines and the high-speed data links, as well as communication lines [54]. The bus tapes are laminated from two layers of copper/polyimide, as can be seen in the stack-up in figure 3.3. The tapes are designed for high reliability and minimum material, the whole thickness is  $185\ \mu\text{m}$ . The copper thickness used for the top and bottom layers is  $17\ \mu\text{m}$ , the polyimide foils are  $25\ \mu\text{m}$  thick for the top and bottom layers and  $50\ \mu\text{m}$  for the base layer. The glue layers are both  $25\ \mu\text{m}$  thick. Openings are cut out around pads to allow standard nickel-gold plating for the exposed pads.

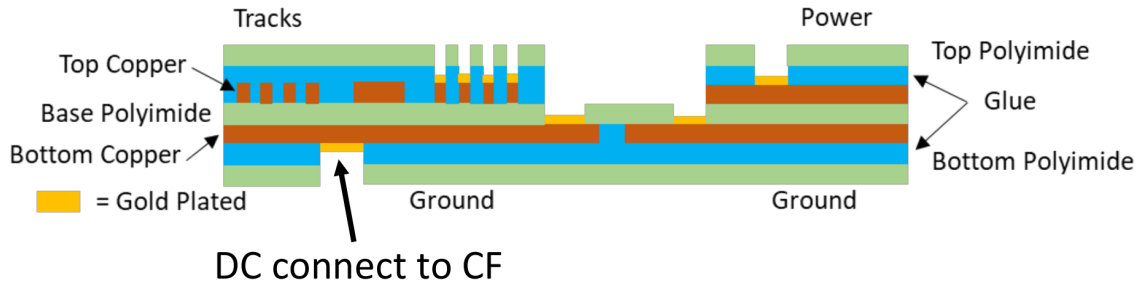


Figure 3.3: Section view of the bus tape: two copper layers (brown,  $17\ \mu\text{m}$  thick each), three polyimide layers (green,  $25\ \mu\text{m}$ ,  $50\ \mu\text{m}$  and  $25\ \mu\text{m}$ ) and the glue sheets holding them together (blue,  $25\ \mu\text{m}$ ).

The separation between exposed HV pads and neighboring pads is greater than  $2.5\ \text{mm}$  to satisfy HV clearance rules.

The polyimide bus tape is co-cured together with three layers of carbon fiber sheets. The sheets are already pre-impregnated with a resin (so-called *pre-preg*) avoiding the need of additional adhesive in the process. The co-curing process is performed in a pressurized autoclave at high temperature ( $3\ \text{bar}$  and  $120\ ^\circ\text{C}$  for four hours, under vacuum). The co-cured layers, called *face-sheets*, assembled together in the sandwich structure provide the required mechanical stiffness. The pre-pregs are oriented with the fibers perpendicular each other ( $0^\circ$ ,  $90^\circ$ ,  $0^\circ$  with  $0^\circ$  fibers placed along the longest side of the core). This configuration is optimized for a light-weight and stiff assembly.

**Cooling loops** The petal is cooled using a dual phase  $\text{CO}_2$  fluid at low temperature to dissipate the heat from the modules. Therefore a titanium pipe runs along the core with an outer diameter of  $2.28\ \text{mm}$  and wall thickness of  $0.16\ \text{mm}$ . The cooling tubes are located in the mid-plane of the local support in order to provide the same cooling power to both sides of the structure to ensure the balance of the thermally induced stresses. The interface between the tube and the face-sheet is created using a thermally conducting carbon foam (Allcomp K9). The glue joints are made using a thermally conducting adhesive (Hysol EA9396 [55]) loaded with 20% (in weight) graphite powder to guarantee the electrical connection. To ensure electrical isolation between the structure and the external cooling services, the cooling loop incorporates two ceramic insulating breaks which are located close to the connectors inside the core at the pipe end.

**Close-outs and petal locators** The petal contour is enclosed by close-outs that are used to avoid possible delamination of the core and to mitigate the effects of external forces applied to the cooling tubes ends during handling. On the long side of

the core, carbon-fibre V-shaped channel (V-channel) close-outs are used for the petal handling and insertion. The top and bottom close-outs are made of high performance electrically insulating thermoplastics (Torlon 4301 [56]) and locator holes are used to connect and hold the petal to the global support structure of the detector. The petal locators consist of two precision holes and a slot: a 4 mm diameter hole at  $r = 379$  mm (inner locator), a 4 mm diameter slot with 2 mm length and a 5 mm diameter hole at  $r = 980$  mm (outer locator). They constrain the movement of the petal to ensure the kinematic mount support. Next to the inner and outer locator holes there are other holes (called fiducial hole) with a diameter of 300  $\mu\text{m}$ , which are used as reference during the module loading procedure, explained in section 5.2. Figure 3.4 shows the technical drawing of the local support structure.

**Low-density core material** Apart from the cooling loop and the close-outs, the remaining volume of the local support is filled with a carbon fiber honeycomb material which is glued to both face-sheets using loaded Hysol as mentioned before. The honeycomb maintains the separation of the face-sheets and the total core thickness of 5.7 mm provides an excellent bending stiffness and ensures a sufficiently flat and robust surface. This allows the mounting of silicon modules making use of a thin glue layer which can absorb the inconsistencies of the core surface. The carbon fiber is chosen over other materials to have an homogeneous Coefficient of Thermal Expansion (CTE) for the core and low Coefficient of Moisture Absorp-

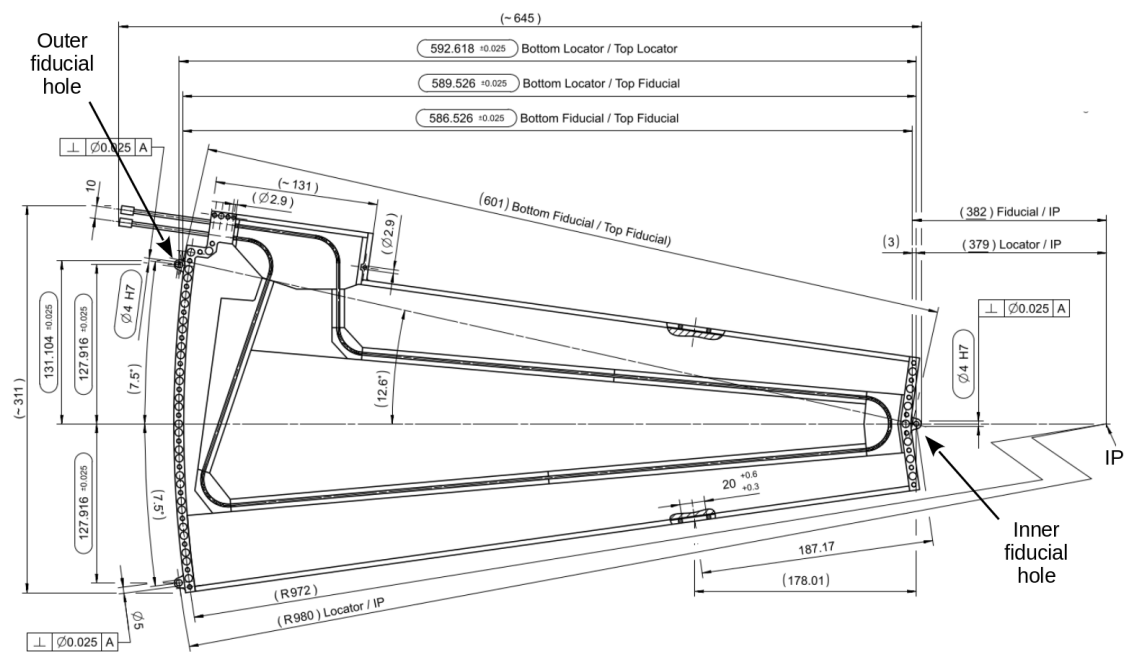


Figure 3.4: Technical drawing of the strip petal core [57].

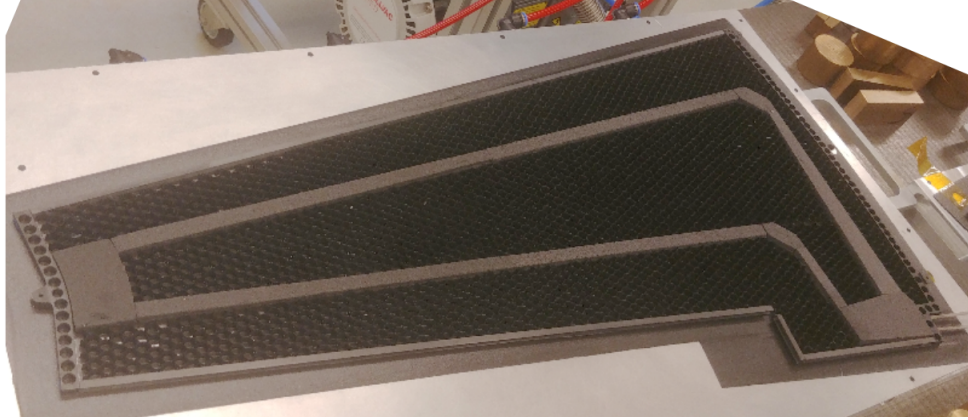


Figure 3.5: Petal core structure with a missing face-sheet that allows to look inside at the carbon honeycomb and foam around the cooling pipe and close-outs.

tion (CMA). The picture in figure 3.5 shows the internal structure of a prototyping petal core built at the DESY workshop.

### 3.1.2 Silicon Modules

The basic active unit of the ITk strip detector is the silicon module. Due to the trapezoidal geometry of the petal in the endcap, six different module designs are required to cover its surface. Each petal side has nine sensors arranged in six rings named from R0 to R5, from the inner radius to the outer. The dimensions of the sensors were chosen to use as few silicon wafers as possible with 32 petals per disk and fully covering the radial range required by the layout. Therefore sensors are manufactured in 6" silicon wafer technology and those on ring number 3, 4 and 5 are split in two to cover the full area. Each endcap module has a different geometry, but it is made of the same components: a silicon sensor, readout electronics, power and monitoring, which are described in the following.

The latest design of the module components that will be used for the ITk production is called *Star* and the prototyping one is called *130*. The main different concerns the electronics and in particular the readout architecture of the ASICs, which is explained in the section about the readout electronics.

The sketch shown in figure 3.6 depicts a strip endcap petal and how modules are oriented on the local support.

**Strip silicon sensor** The sensors have  $n^+$ -type readout implants on a p type, float-zone silicon substrate,  $n^+ - in - p$  technology is chosen as it is more radiation tolerant. The strips are radially distributed and pointing towards the center of the

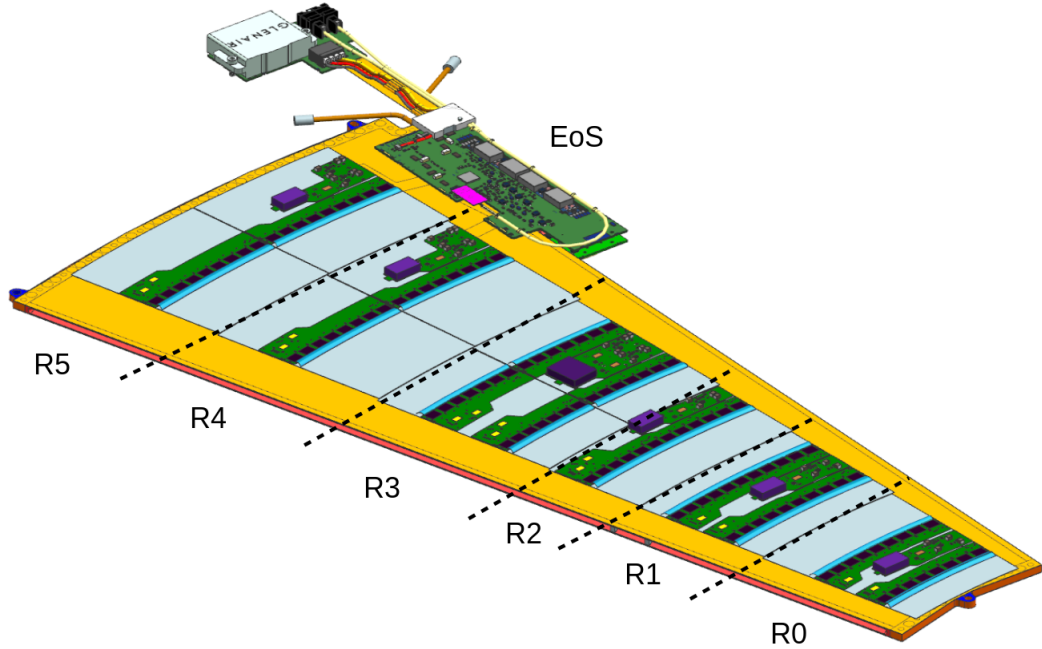


Figure 3.6: Latest strip endcap petal design, front side, populated with Star modules and a Master EoS glued on the petal core.

beam pipe to give a measurement of the  $(r, \varphi)$  coordinate for tracking purposes [58]. A 40 mrad stereo angle is achieved in the endcap sensors by rotating the strips 20 mrad with respect to the radial orientation in each disk, in order to provide the second coordinate measurement. The strip lengths are chosen to balance the strip occupancy with the shortest strips closest to the beam region. This results in sensors having either two or four strip rows of different length. Each row has a multiple of 128 strips to match the readout chip number of input channels. The strip pitch was constrained to be as close as possible to  $75.5 \mu\text{m}$  at the wire-bonding region to allow direct connection between the read-out ASIC and the sensor.

The sensor has four sets of fiducial markers used for different purposes. They are shown in figures 3.7, their location is depicted in figure 3.8.

- type 1, marker  $K$  (x10): they determine the sensor center. These are located along the arcs defined by the outer and inner radius and on the straight sides of the sensor;
- type 2, marker  $E$  (x2). They are located along the straight sides of the sensor and are used to define, together with the sensor center, the sensor radius  $R$  and origin or interaction point;
- type 3 markers  $I$  (x6) to help position the sensor on the petal face. These mark-

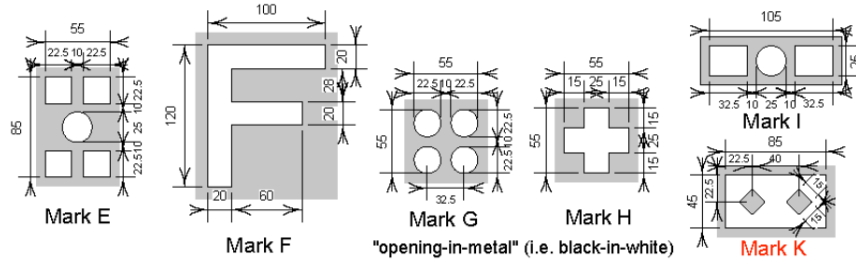


Figure 3.7: Fiducial marks on HPK sensors.

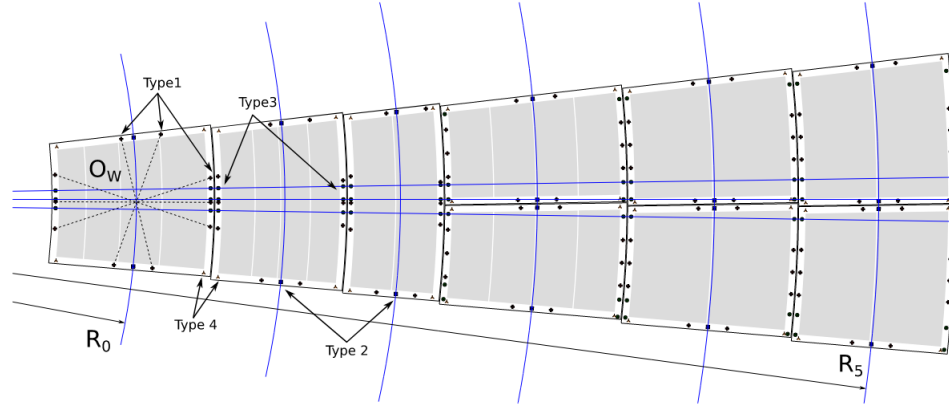


Figure 3.8: Position of sensor fiducial marks [58].

ers are determined by three lines crossing at the interaction point. The center line defines the X axis and the other two are at a constant angle ( $0.15\pi/32$ ) from the center one. They serve to define the angle of the final sensor position and, together with R and O, determine the position of the sensor in the petal;

- type 4, marker  $F$  (x4): they are located at the corners of the sensitive region.

All the markers are at a distance  $\delta=95\ \mu\text{m}$  from the outermost structure of the sensor.

**Readout electronics** A *Printed Circuit Board* (PCB) that hosts the read-out *Application specific Integrated Circuits* (ASICs), called *ATLAS Binary Chip* (ABC), and a *Hybrid Controller Chip* (HCC), is called hybrid. Charged particles passing through the sensor create a signal within the silicon sensor diode. This signal is transmitted through a wire to the front-end ABC, containing 256 channels with pre-amplifiers and discriminators. The signal on each channel is amplified, shaped and then discriminated to provide a binary output, in this way the incoming charge signal is converted into hit information. The HCC receives the signals from the ABCs, builds packets and transmits them to the EoS at 640 Mbit/s. It also receives the clock and control signals (TTC) and distributes those to the ABCs. Depending

on the sensor type, from six to eleven ABC ASICs are grouped onto one hybrid sending data to the same HCC.

A prototyping version of chips was designed in Global Foundries 130nm CMOS technology, called ABC 130 and HCC 130 ASICs. The signals from the ABC 130 chips are collected, grouped in the same package and transmitted to the HCC 130 chip. With HL-LHC, the ASICs architecture could not support the new ATLAS trigger rate requirement of 1 MHz rate and thus a design change was required. The fundamental change in the *Star* design is the interface from ABCs to the HCC [59]: all ABCs communicate directly the serial transfer of data to the HCC, as shown in figure 3.9. The *Star* architecture solved a bottleneck in data transfer to the HCC, which had considerable bandwidth still available. The HCC *Star* required nearly a complete redesign as it must now essentially build events in parallel from fragments coming from all the ABC *Star*.

**Power and monitoring** The power-board provides low voltage power to the front-end electronics of the hybrids, sensor high voltage biasing and module level environmental measurements and control.

The chips' power is provided by a DCDC converter which transforms the 11 V coming from the EoS through the bus tape to 1.5 V. The DCDC regulation is achieved by the *bPOL12V* chip, a radiation hard custom ASIC that employs a buck-converter

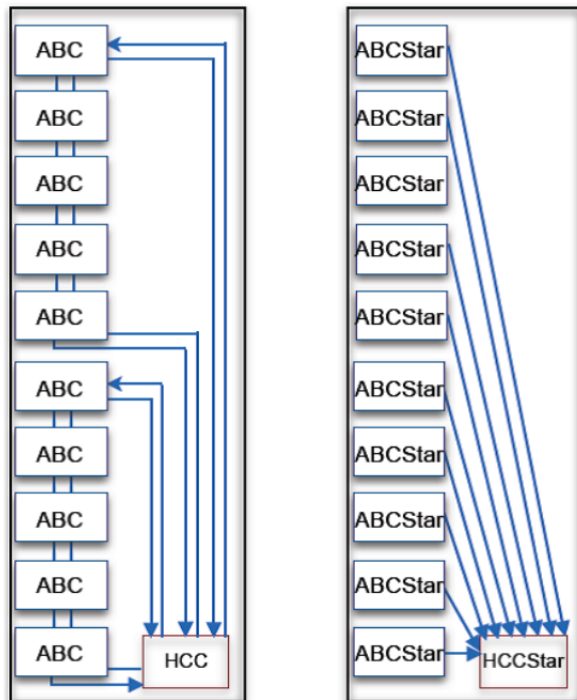


Figure 3.9: Architecture of the readout in ABC 130 and ABC *Star* chipset [59]: in the first design the ABCs are divided in two sub-groups to send their data to the HCC; in the second one, the ABCs communicate individually with the HCC *Star*.

style switching regulator, which requires an external inductance [60]. This inductance is reached by an air-core solenoid coil. Due to its shape and characteristics the coil emits radio frequency noise, which could be picked up by the silicon strips underneath and around the power-board. Therefore the whole DCDC circuit is enclosed by a shield, so called shield-box, to avoid electromagnetic interference. The height of the box determines the highest point of the local support ( $\sim 5$  mm), which constrains the petal position on the endcap disk.

A sensor bias high-voltage switch and a filtering circuit are also present on the same board to monitor the sensor current and to switch off the HV if needed (HVmux chip). The power-board also hosts the *Autonomous Monitor And Control* chip, AMAC, that provides both monitoring and interrupt functionality. It allows the monitoring of voltages, temperatures, measured by NTC (Negative temperature coefficient) thermistors, and sensor bias current on strip modules at a rate of approximately one sample per millisecond. The AMAC is powered by a radiation hardened linear regulator, the *linPOL12V*.

The sketch of the R0 Star power-board is provided in figure 3.10. For endcap modules four power-boards were designed due to the module geometry: R0 and R1 modules are populated with the same power-board, as well as R4 and R5 modules. R2 and R3 module have individual power-board design.

All silicon module components are shown in figure 3.11 and the thickness of the components and glue layers are also specified.

### 3.1.3 End of Substructure card

The End-Of-Substructure (EoS) card is the interface between the petal and the off-detector electronics and additionally also links both LV/HV from the power supplies to the petal as well as the petal grounding [61]. The EoS is situated on the "ear" of the local support structure, one on each side.

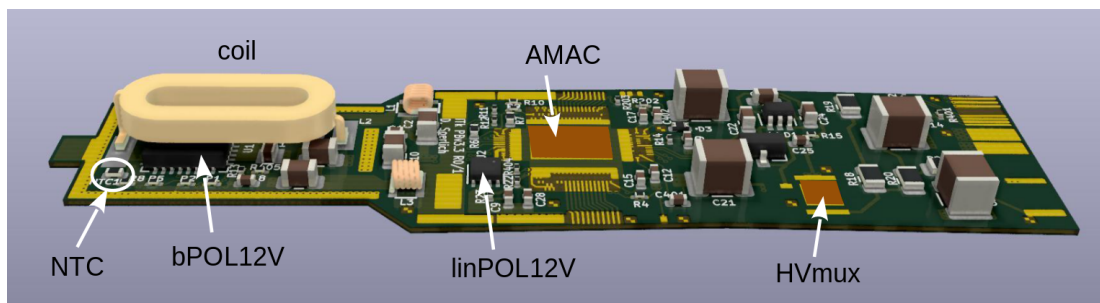


Figure 3.10: Layout of the R0 Star power-board with all its electrical components.

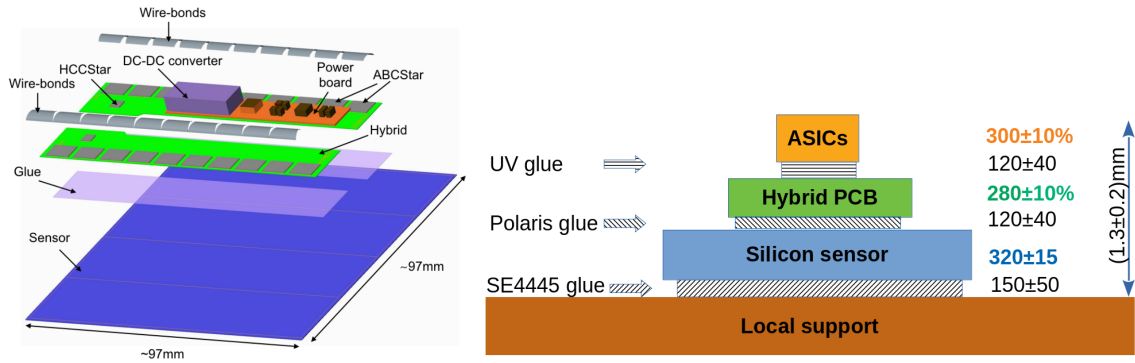


Figure 3.11: Sketch of the module components (left-hand side [37]) and nominal thickness of the module components and glue layers reported in  $\mu\text{m}$  (right-hand side).

The EoS comes in two variants for either side of the structure: the *Master* and the *Slave* that are placed on the front and back side of the petal respectively. Both EoS flavours are populated with two active components: a *low-powered GigaBit Transceivers* (lpGBT) and a *Versatile optical Link* (VL+, also called VTRx+, Versatile Link Plus Transceiver), both radiation-hard ASICs developed at CERN.

Both chips are transceivers: they can transmit and receive the signal and therefore work on the bi-directional way. The module front-end ASICs transfer data to the EoS card on 640 Mbit/s differential lines. The EoS connects up to 28 data lines to the lpGBT chip that provides data serialization and uses 10 Gbit/s VL+ to transmit signals to the off-detector systems through an optical fiber. The lpGBT also recovers the LHC clock and generates clock and control signals for the modules.

Each petal Master and Slave card has those chips. In addition the Master hosts a two-stage DCDC converter to supply the two ASICs on both sides of the petal: in the first stage the incoming 11 V are converted in 2.5 V for the VL+ and then in 1.2 V for the lpGBT and VL+. The Master card is the only one hosting the converter which is mounted on two custom-designed daughter boards, one for each card. A PCB cut-out for the converters is used to gain 1.6 mm, as the DCDC is the tallest component (up to 5 mm due to the shield-box). The picture in figure 3.12 shows both petal EoS prototyping cards: the Master on the top and the Slave on the bottom.

The height limitation on the endcap disk forced to move further a common connector for external power and monitoring. Therefore a flexible continuation of the PCB, called *pig tail*, is added to host a Glenair connector for the HV and LV line and two MPOs (Multi-fiber Push On) connectors for the optical fibers coming from the VL+ chip on the master and slave sides. This extension makes it possible to loc-

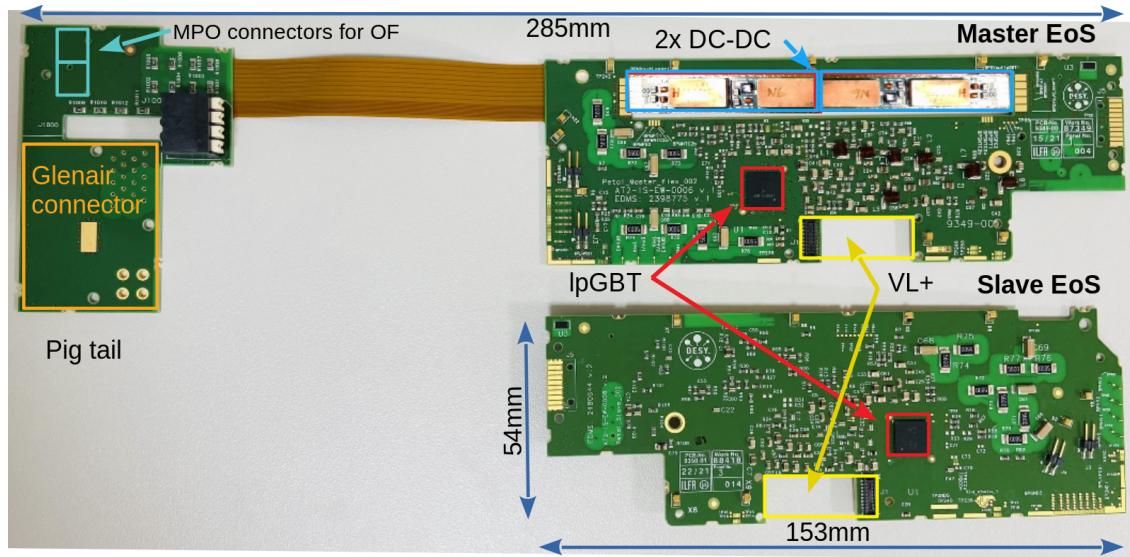


Figure 3.12: End-of-Substructure prototypes for the Petal, Master card on the top and Slave on the bottom. DCDC converters, lpGBTs and VL+ positions are shown. The VL+ chips, the Glenair connector and the MPO for the optical fibers are missing on the cards but the position is highlighted with squares.

ate the connectors for external cables where there is more space, held on the global structure, easing the mechanical integration for the full tracker.

### 3.2 DESY involvement in the ITk Strip project

The ITk collaboration includes several institutes all over the world. The *Deutsches Elektronen-Synchrotron* (DESY) plays a major role in the construction and testing of one of the strip endcap, starting from the assembly of the modules to the insertion of petals into the global structure, including the associated quality control tests (QC). The main activities where the ITk group at DESY is involved are described in the following section.

**QC on bus tape** The petal bus tapes are manufactured by the vendor *EL-GOline* [62]. The tapes are received and their electrical functionality is checked: a custom made bus tape testing robot tests the electrical impedance of differential lines, continuity tests of every line and high voltage inter-resistance tests of the HV lines. A stretch test is also performed to check the potential displacement of fiducial marks, especially after co-curing the tape, which could be a cause of failure as the stretch causes a small shift of the bonding pads. Tests are performed in three steps during the core assembly: on a bare tape, after co-curing, and when the core is fully assembled.

**QC on petal core** The entire petal core assembly during production is carried out by *AVS* (Added Value Solution [63]), but several components are provided by DESY: co-cured face-sheets, cooling loops and machined carbon foam. The total number of petal cores required for both encaps is 384, plus 10% of spares. QC tests are performed on those components to ensure they are delivered up-to-specifications. The petal core QC is performed at IFIC (Valencia) and at DESY-Hamburg. Section 5.1 explains in detail the QC tests and presents results obtained on prototyping cores.

**Module building and testing** During module production, the DESY group in Hamburg will assemble modules for the strip endcap, in particular R2 and R4 flavours, 192 modules of each type are built in three years. The module assembly procedure adopted at DESY is described in chapter 4 together with the QC tests associated with the module construction.

**Cold boxes for module thermal test** After the assembly all modules are tested, the tests performed for modules QC is detailed in section 4.3. A dedicated test to check the functionality in an extreme environment is the thermal cycle from  $-35^{\circ}\text{C}$  to  $40^{\circ}\text{C}$  for ten times [64]. The cold box testing setup was developed and built at DESY and it is shown in figure 3.13.

**EoS card** The EoS card is designed at DESY in all its flavours: two cards for the endcap petal (master and slave) and eight for the stave (four master and four slave). They all have a common electrical schematics, but small differences in the

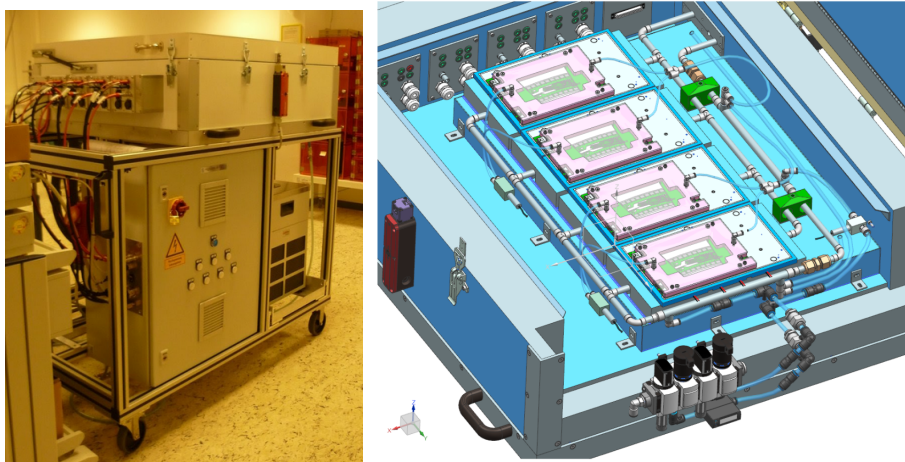


Figure 3.13: Cold box testing setup for endcap module testing. The inside view of the box is provided on the right-hand side.

number of data channels and lpGBT. DESY is the institution responsible of the PCB production and population of 1552 EoS cards for the whole ITk detector, both barrel and endcap. The cards are produced by an external company while the QC of every EoS card is carried out at DESY.

**Module loading** The loading of endcap modules onto the petal cores is performed in four sites within the ITk collaboration: at DESY (Hamburg), Freiburg University, IFIC (Valencia) and TRIUMF (Vancouver) providing petals for both endcaps, 384 in total. Each institute builds and tests electrically 96 petals, plus additional spares, with a rate of two petals a week. This activity is described in detail in chapter 5. The fully loaded petals are then sent from the loading sites and split between DESY and Nikhef (Amsterdam) for the insertion into the global structure of the endcaps.

**Service tray** Each endcap has eight lateral service trays fixed perpendicularly to the disks to hold the cooling pipes, the services and optical fibers all the way to the patch panels 1 (PP1), as shown in figure 3.14, and to add stiffness to the global structure. They are made of carbon fiber reinforced polymer (CFRP) and have to provide grounding and shielding with an electrical resistance  $< 20 \Omega$  between wheel, service tray and cooling pipes to connect to the global Faraday cage [65]. The production of 16 service trays for both endcaps is conducted at DESY and this is the first activity that is successfully completed.

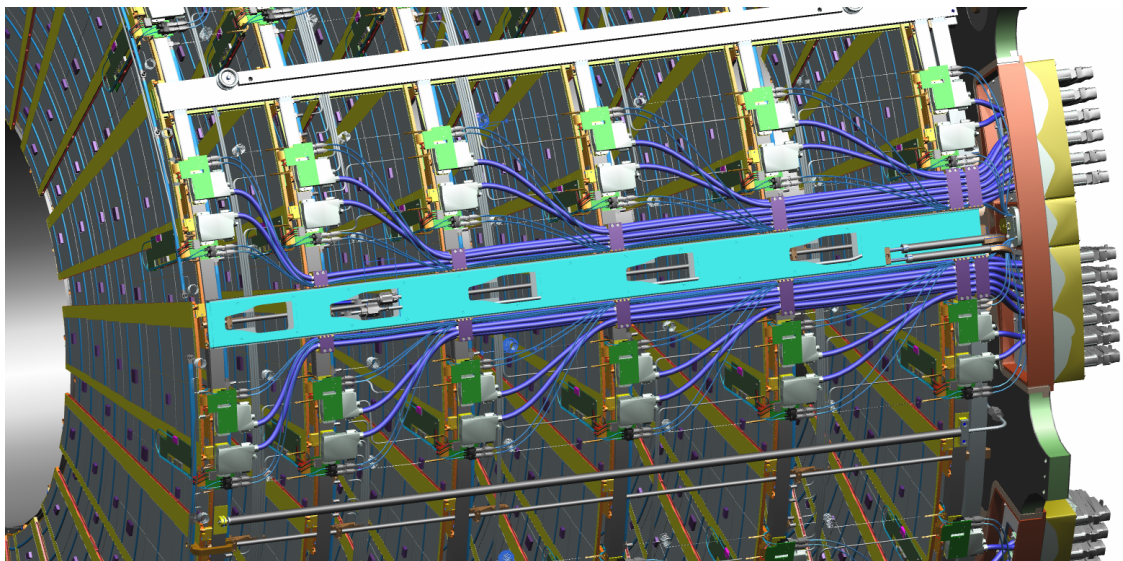


Figure 3.14: Sketch of a strip endcap portion with one service tray. Cooling pipes, cables and optical fibers are connected to the petals and run along the tray until PP1 on the right-hand side of the picture.

**Petal insertion** In order to insert the petals into the endcap global structure a tool is designed and built at DESY. The petal insertion tool allows the pickup of petals and their placement on every location of the endcap structure with high precision. A schematic representation of the petal insertion tool is shown in figure 3.15.

**System test** In order to demonstrate the validity of the ITk endcap project and the behaviour of multiple items arranged in a common environment as close as possible to the final experiment, a setup representing an octant of the endcap structure is under development. Parts are fabricated at Nikhef (Amsterdam), IFIC (Valencia) and DESY (Hamburg). It will be assembled at DESY and populated with 12 fully loaded petals, including all-type cables, cooling pipes and optical fiber, patch panel and power supplies. It will be operated with the *LUCASZ* (Light Use Cooling Appliance for Surface Zones [66]) CO<sub>2</sub> cooling system and the *FELIX* (Front-End LInk eXchange [67]) readout system. A thermal enclosure provides a dry clean environment and also acts as a Faraday cage, replicating the configuration of the real experiment.

**Super Frame** The super frame is the mechanical structure that supports the endcap during transport, petal population and testing. It also allows the insertion of the fully populated endcap into the outer cylinder of the ITk detector at CERN. The super frame is shown in figure 3.15. This tool is designed and manufactured at DESY.

**Detector Assembly Facilities** Most of the upgrade activities at DESY Hamburg are performed at DAF (Detector Assembly facilities): it consists of two cleanrooms, both dedicated for the construction of the ATLAS ITk strip endcap and the CMS Outer Endcap. The environments and the ITk ongoing activities at each laboratory are summarized in the following:

- ISO6 cleanroom: sensor testing, hybrid and module building, module loading, module and petal wire-bonding, module metrology and testing in the cold box, EoS population and testing. The laboratory is shown in figure 3.16;
- ISO7 cleanroom: bus tape testing, petal core thermal QC, EoS thermal cycling, petal metrology and testing, petal insertion and system test.

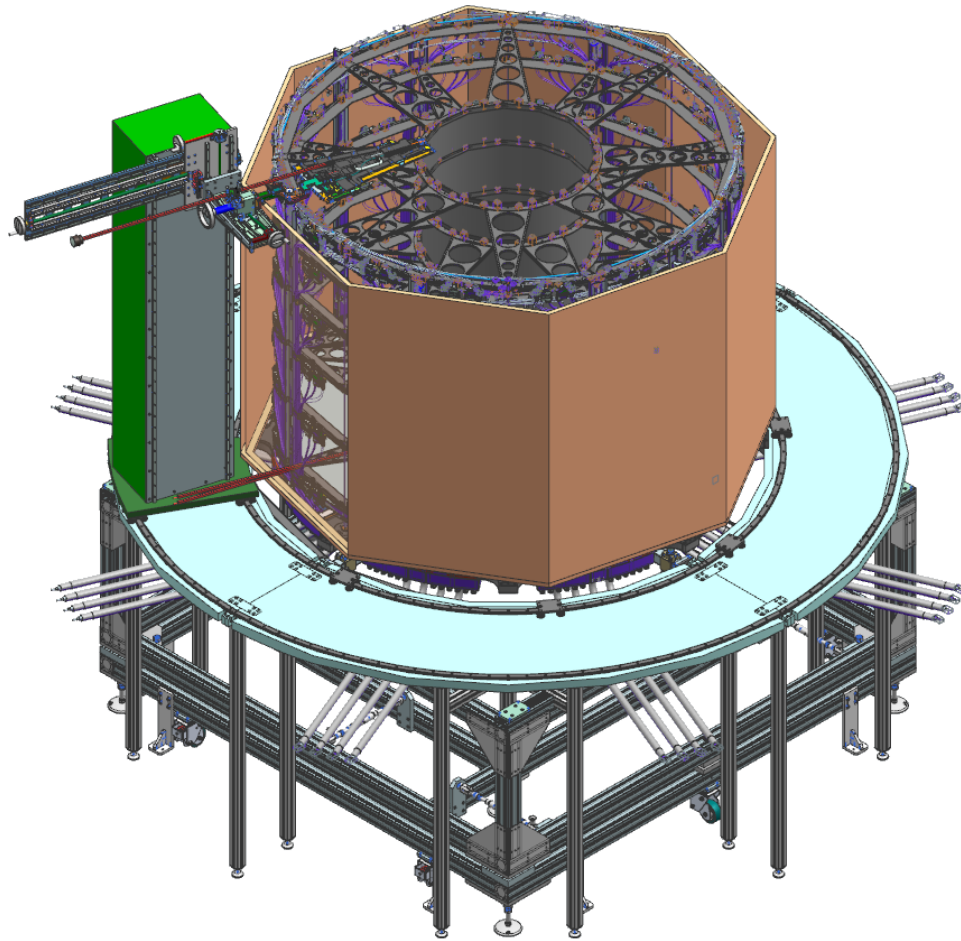


Figure 3.15: Global structure of the strip endcap placed on the super frame and petal insertion tool. The endcap is surrounded by the enclosure.



Figure 3.16: ISO6 cleanroom at DESY Hamburg dedicated to the ITk activities.

# Chapter 4

## Assembly of Silicon Modules and Quality Control

One of the primary activities for the assembly of the Inner Tracker (ITk) for the ATLAS Phase-II upgrade in which the DESY group is involved is module building. It consists of the gluing of front-end chips on the silicon sensor following specific requirements. The module assembly starts with a reception test of all the components to ensure that the shipment has not damaged them.

An electrical R2 Star module was built and tested at DESY for the first time. Its sensor reception test is showed as example in section 4.1 and the step-by-step procedure of the assembly is explained in section 4.2. The metrology and electrical results of quality control (QC) tests performed on the R2 module are shown in section 4.3.

### 4.1 Reception tests on module components

A series of tests are performed on the pre-assembling module components after the shipment to ensure their functionality. Sensors, bare hybrids and power-boards are subjected to visual inspections, metrology and electrical tests to be classified as suitable for the module building. In the following the electrical test for the sensor reception is provided as example.

#### 4.1.1 Sensor reception

Strip silicon sensors are produced by Hamamatsu Photonic K.K. [68] in Japan, sent to Prague for characterization tests and shipped to all the ITk institutes involved in module assembly. In each site two measurements are used to characterize every silicon sensor:

- *I-V measurement* to register the breakdown voltage and the leakage current

trend. The measurement is performed first on the bare sensor making use of a probe station and after the gluing of the electronics via the HV power supply, as can be seen in figure 4.1. On the module the HV, before being supplied to the silicon sensor, passes through a HV filter placed on the power-board, which contains a  $10\text{ M}\Omega$  resistance. The module current values reported in the plot are measured just before the resistance and therefore they are higher than the ones measured on the bare sensor;

- *C-V measurement* to get the overall power consumption and the full depletion voltage, performed before and after the gluing of the electronics. The plot in figure 4.2 shows that the sensor depletion voltage has not changed, being equal to  $-280\text{ V}$  for both curves.

Sensors and modules are stored in a nitrogen cabinet to avoid degrading the sensor performance due to the moisture and surface charges that appear on the sensor surface [69]. The storage of sensors guarantees a relative humidity lower than 10% to avoid an early breakdown, indicated by high leakage current.

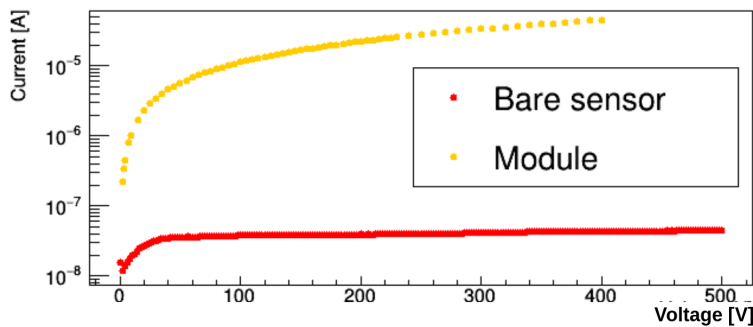


Figure 4.1: IV curve on the R2 sensor, comparing the performance before (red points) and after hybrid and power-board glued on the sensor (yellow points).

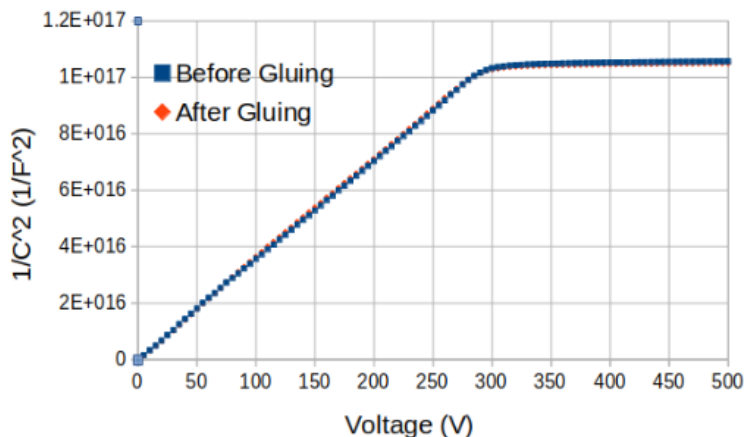


Figure 4.2: CV curve on the R2 sensor, comparing the performance before (on sensor, blue points) and after gluing (on module, red points). Depletion voltage at  $-280\text{ V}$  for both measurements.

## 4.2 Module building procedure

In order to build a module, all components are assembled together and tested through the following steps:

- gluing of ABCs and HCCs ASICs, applying the glue pattern on the hybrid where the chip pads are. The required glue is *Henkel Loctite AA 3525* [70] which is cured with a UV light lamp. Figure 4.3 shows the glue dot applied on the R2 hybrid with a dispensing robot, before and after the chips placement;
- wire-bonding of chips to hybrid and fixation on a proper frame, so-called test-frame, for hybrid testing purposes;
- gluing of the hybrid on the sensor, spreading *Polaris glue* (Polaris Polymers PL-5313 as hardener and PF7006 as resin) on the back side of the hybrid using a stencil or the glue dispensing robot and let it cured for 12 hours. Figure 4.4 shows the glue pattern applied by the dispensing robot and the coverage after the placement on the sensor;
- gluing the power-board using the same glue and same procedure and curing for other 12 hours;
- additional front-end wire-bonds are needed to connect electrically silicon strips, chips and power-board together;
- fixing the module on the test-frame and start with the QC tests on the fully assembled module.

Figure 4.5 shows the R2 assembled module under the microscope for wire-bonds inspection. It is fixed on a test frame making use of polyimide tape due to a lack of the designed R2 test-frame.

### 4.2.1 Pressure calibration of the glue

Chips-to-hybrid, hybrid-to-sensor and power-board-to-sensor gluing use a specific set of tools, designed for the particular geometry of the module, which provide the correct thickness of the glue. Figure 4.6 shows the tooling set dedicated for the R2 Star module assembly: the pickup tool, the chip tray, the hybrid and module vacuum jig. To guarantee the maximum flatness and precision of the assembled module, the silicon sensor is held in place by a module vacuum jig during the whole gluing procedure. A weight is used during the glue curing process to ensure the proper contact between the pickup tool and the module jig.

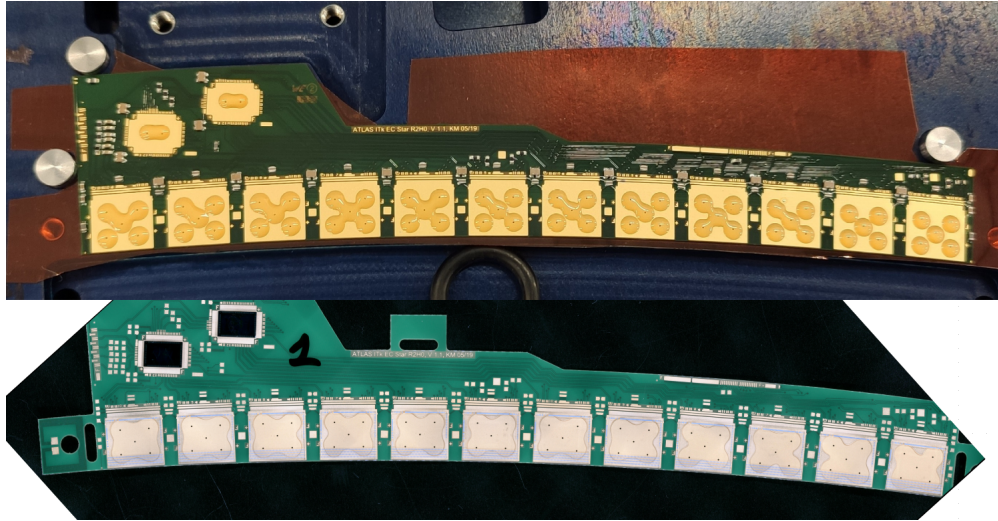


Figure 4.3: Glue pattern for ABC and HCC chips dispensed by the robot and coverage test using dummy glass chips on mechanical hybrid.

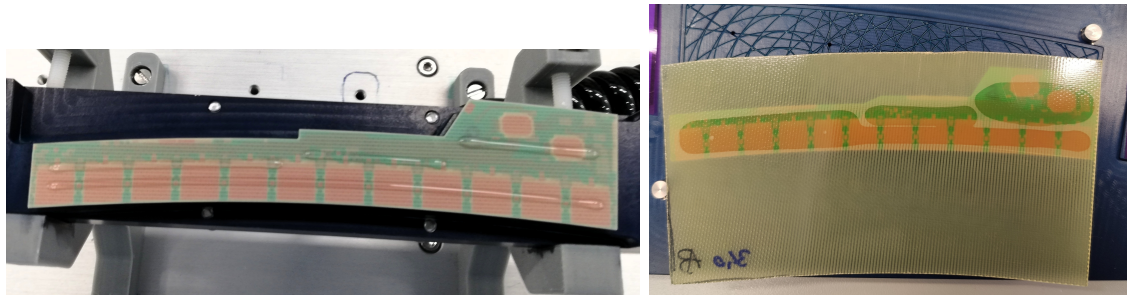


Figure 4.4: Glue pattern for the R2 hybrid dispensed by the robot and coverage test on the sensor performed with mechanical parts.

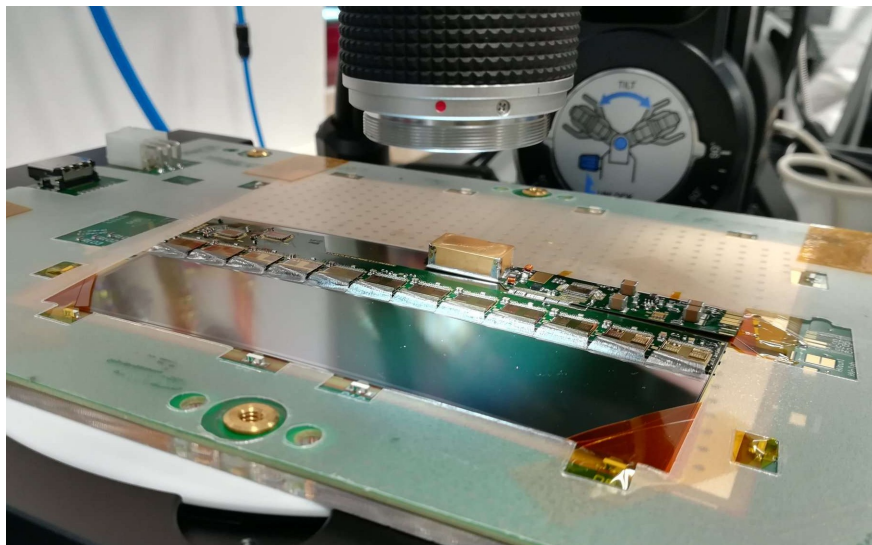


Figure 4.5: R2 Star module built at DESY. The module is completely wire-bonded on the test-frame and is placed under the microscope for the visual inspection.

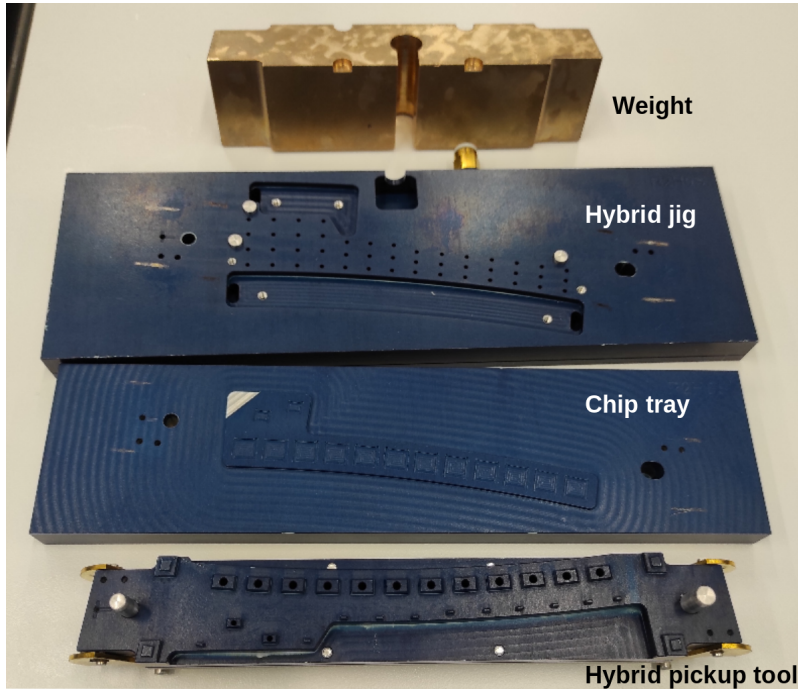


Figure 4.6: R2 tooling set to assemble modules: weight, hybrid vacuum jig, chip tray and hybrid pickup tool.

The amount of glue for each step is decided aiming for the maximum coverage for wire-bonding purpose, avoiding any glue seepage and air bubbles trapped by the glue. The first step, chip-to-hybrid gluing, is performed using the robot to dispense the glue pattern, while in the following two assembling steps the glue can be also applied with a different method, making use of stencils. These two techniques are here explained in more details:

- stencils: they are placed in contact with the back side of the hybrid/power-board when this is held by the pickup tool, and the glue is spread following the specific pattern provided by the stencil;
- gluing robot: the glue is applied by a syringe attached to a robotic arm. The same stencil's pattern can be recreated programming the robot.

At DESY a gluing robot, *Nordson EFD ProPlus* [71], is used to speed up the module production and to guarantee the same precision in the gluing phase. The robot includes stages where the arm can move in X, Y and Z, a camera is attached to the robot's arm to measure fiducials marks on the part and a dispenser (*Nordson EFD Ultimius V* [72]) provides the pressured air for the glue application. In order to achieve a high precision, every time the syringe is fixed to the robot a spacial calibration is needed to define the correct offset between the camera and the needle in all three directions.

The Polaris glue, used to assemble the hybrids and power-board to the silicon sensor,

comes in two components: the resin and the hardener are mixed by weight in a ratio 100:9 respectively. The mixing and degassing are performed using a mixer machine to guarantee a uniform mixture. The glue can be used after 20 minutes from the mixture to get the most appropriate viscosity value with which it is possible to work with. The glue viscosity increases with time after the hardener and resin mixing, therefore a study on the applied air pressure as function of time is needed in order to get the same amount of glue every time. To understand the behavior of the viscosity, tests were performed at different pressure values up to a maximum of 7 bar, limit of the dispenser. At each pressure value the same glue pattern was applied repetitively and the glue weight was measured, as shown in figure 4.7. The pressure as function of time can be obtained from each curve, fitted with an exponential function, when the glue amount is equal to the target of the pattern dispensed on the hybrid, 190 mg for this test. This study shows how crucial is the choice of the right value of pressure in order to dispense the glue independently of its increment of viscosity. The glue mixture can be used for a maximum of roughly 25 minutes, after that the pressure required would exit the setup capability. Shortening the length of the pressured air tube between the dispenser and the syringe helps on the repeatability of the glue amount dispensed by the robot. This calibration test is needed only once to characterize the glue and find the correct pressure increment over time, according to its viscosity.

A good practice before any gluing is to check the consistency of the dispensing provided by the robot for a given mixture. If the glue amount got from the test is greater than  $\pm 10\%$  from the target, the travel speed of the syringe can be adjusted to get closer to target. The speed is set to a higher value to get less glue or to a lower one to get more glue.

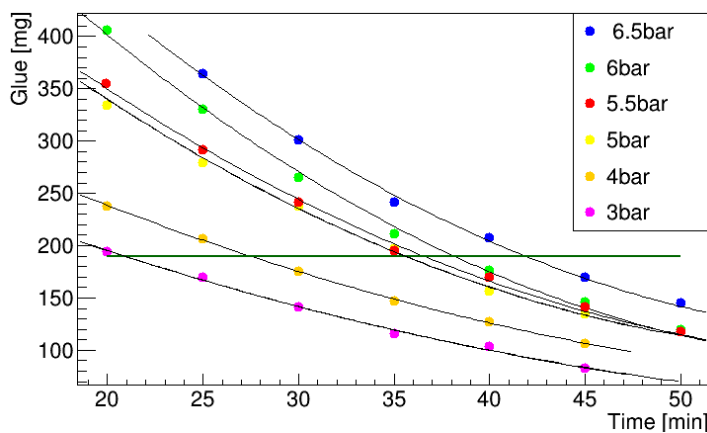


Figure 4.7: Pressure calibration of Polaris glue: the same glue pattern is applied repetitively at different air pressure. The target is 190 mg for the glue pattern used for the test.

## 4.2.2 R0 Star power-board gluing tools

The full set of gluing tools for the latest version of the R0 Star power-board, described in section 3.1.2, was designed, machined and tested at DESY. The set includes:

- a pickup tool that holds the power-board using vacuum pins;
- a tray that allows to pick the board in a precise position thanks to alignment pins;
- a stencil used to apply the glue on the backside of the power-board before the placement on the sensor;

The designs and the tests on those tools are described in the following.

**Pickup tool and tray** The pickup tool design is constrained by the space available on the board to hold it: six vacuum pins are placed where the board does not have components, wires or sensitive areas. A silicone suction cup is used to hold the metallic shield-box to compensate its height variations. The pickup tool has two lateral pins for the alignment, made of steel and different in diameter, 6 mm on the left-hand side and 7 mm on the right-hand side to avoid the wrong placement of the tool on the module jig.

The power-board is glued on the sensor after the hybrids because of the height of the shield-box which would hit the hybrid pickup tool otherwise. In the module jig, the holes for the pickup tool pins allow to place the power-board 500  $\mu\text{m}$  away from the sensor bias and guard rings to avoid glue seepage over it and roughly 1 mm from the closest point of each hybrid to avoid collisions. The power-board position is also chosen looking at the alignment of gold pads on power-board and hybrids to simplify the wire-bonding. The hole on the right side of the tray and module jig are transformed into a slot, 2 mm elongated in the direction of the line that connects the left and right hole, to not fully constrain the tool insertion.

The pictures in figure 4.8 show the sketch and the prototype of the tray and pickup tool (figure 4.8, a and b). The tools were tested using a mechanical R0 Star power-board: the pickup tool can lift the power-board without any damages to its passive components and wire-bonds (figure 4.8, d). It allows to place the power-board on the R0 Star module as shown in figure 4.8 (c).

**Gluing stencil** The stencil is used to apply a specific glue pattern on the back side of the power-boards. Its design was the most challenging part of the tool set due to the specifications required for this tool, which are listed in the following:

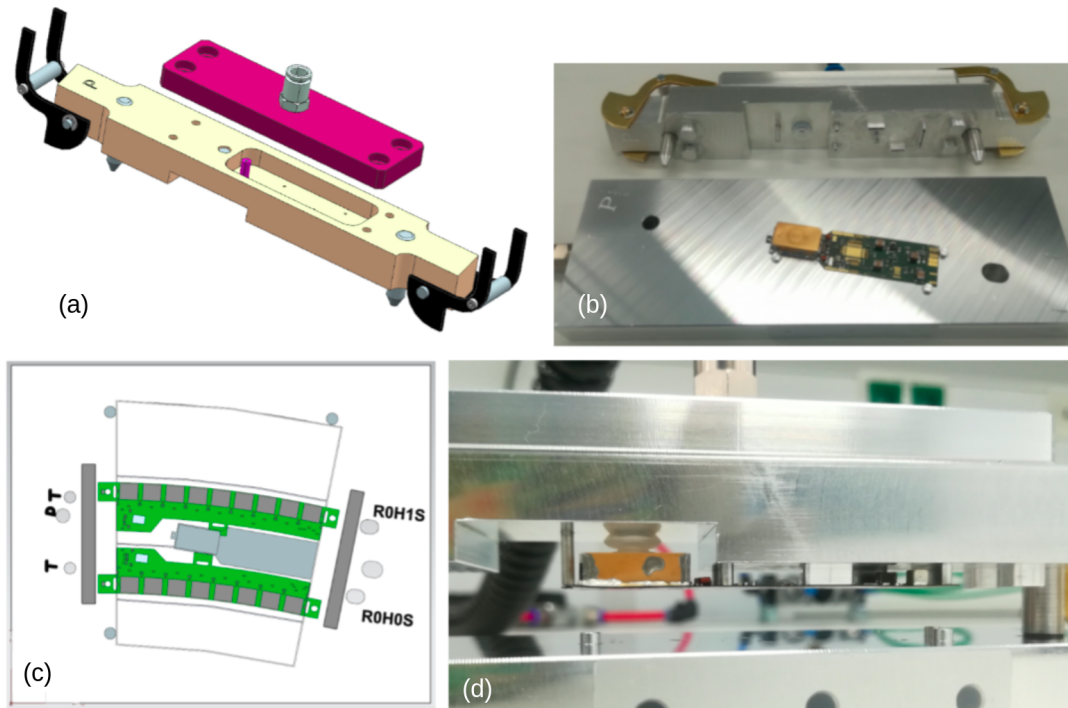


Figure 4.8: Designs and aluminum prototypes of the R0 Star power-board gluing tools: (a) pickup tool design, (b) pickup tool and tray prototypes, (c) R0 Star module design on the module jig, (d) pickup tool holding the mechanical power-board under vacuum.

- 90% glue coverage below the AMAC and bPOL12V chip to guarantee a good thermal contact, and below the wire-bonding pads for stability reasons;
- 30% glue coverage below the rest of the PCB area;
- $(120 \pm 40)$   $\mu\text{m}$  glue thickness (Polaris glue), provided by the pickup tool and the module jig design;
- avoid air trapping after glue compression.

The stencil is only  $200\mu\text{m}$  thick and it is placed in between of two thicker frames, which provide a stiffer support and define the area where the glue is spread. The stencil plus the frame sandwich is attached to the pickup tool that holds the power-board under vacuum. Then a blob of Polaris glue is deposited on one side of the frame slot and swiped only once along the length of the stencil. This allows an easy lift-off of the stencil. Figure 4.9 shows the glue pattern provided by the R0 power-board stencil. Regarding the air trapping, patterns consisting of parallel lines were rejected for the high probability of air bubbles, in favor of glue spots.

The glue pattern of the stencil provides 48% of glue coverage. It should become 80%

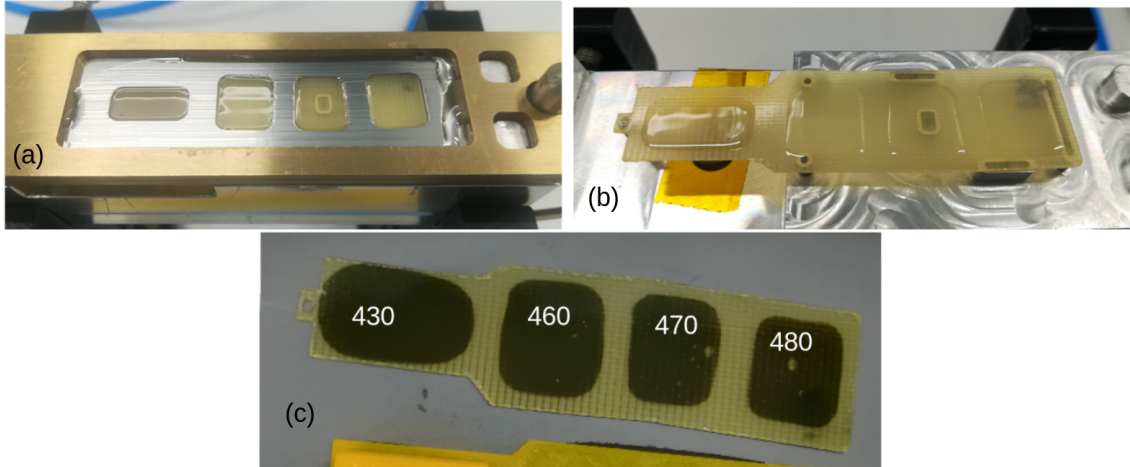


Figure 4.9: Dummy R0 Star power-board gluing test: (a) stencil placed on the power-board and glue applied, (b) glue pattern after removing the stencil, (c) coverage after compressing the glue and glue+power-board height measurements.

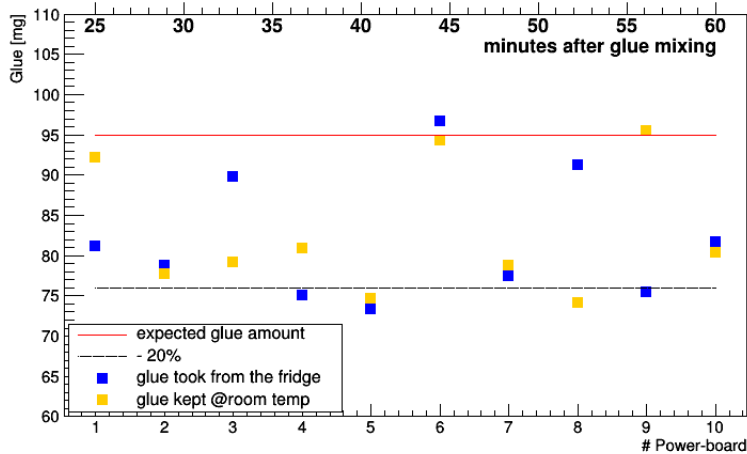


Figure 4.10: Glue amount applied using the stencil, comparison between using glue at room temperature (20 °C) and cold glue (5 °C).

after the glue compression, considering that the volume is constant and the height is reduced from 200  $\mu\text{m}$ , thickness of the stencil, to 120  $\mu\text{m}$  which is the available space for the glue due to the tools design. Given the pattern area, the thickness of the stencil and the glue density, 1.1279  $\text{g}/\text{cm}^3$ , the amount of glue deposited by the stencil should be about 95 mg. A consistency study was performed to check this value. The result of this test reported that the amount of glue is about 15% less of what is expected to be deposited on the power-board, as the plot in figure 4.10 shows. The test was done at two temperatures of the glue (20 °C and 5 °C) and both seem to follow the same behavior. The glue amount average deposited by the stencil is  $(83 \pm 8)\text{mg}$  and  $(82 \pm 7)\text{mg}$  respectively.

Once the glue pattern for the R0 Star power-board was finalized, the geometry was exported and adapted to the shape of the other endcap Star power-boards as shown

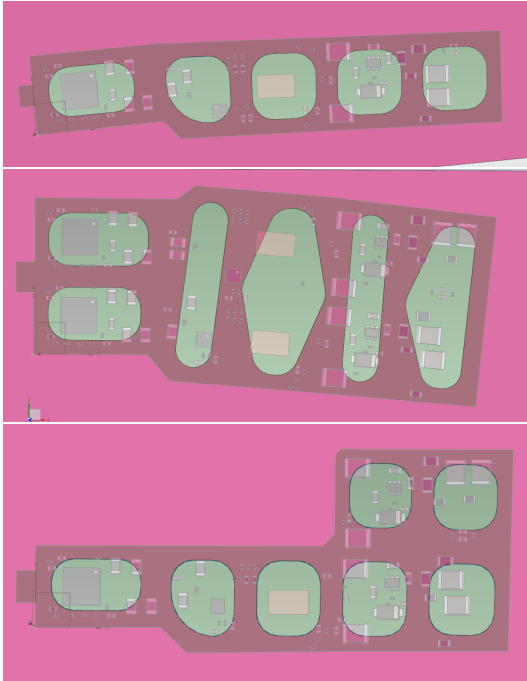


Figure 4.11: Glue pattern design for stencils: from the top R2, R3 and R4-R5 power-boards respectively.

in figure 4.11. The six flavours of endcap modules count only four power-board designs because R0 and R1 module have the same power-board design as well as R4 and R5 module. The main R0 pattern features of the stencil, that are used for the other three power-board glue pattern, are the following:

- 2 mm away from each power-board edge to avoid glue seepage
- $\sim 50\%$  glue coverage before compressing to get the required coverage afterwards
- 200  $\mu\text{m}$  stencil's thickness

In table 4.1 there are the expected glue amounts for each stencil calculated taking into account the pattern area and  $-15\%$  dispensed glue due to the fill factor of the stencil. The error associated to the glue weight is  $\pm 13.7\%$  calculated from the combination of the variance on the layer thickness and the contact area.

PB type	expected glue [mg] $\pm 13.7\%$
R0-R1	79
R2	70
R3	148
R4-R5	97

Table 4.1: Nominal glue amounts deposited by the power-board (PB) gluing stencil for each type,  $\pm 13.7\%$ . The fill factor (15%) is subtracted.

So far only the R0 stencil was tested using dummy components because of a lack of real parts and tools for non-Star R0 modules, which provided a glue amount consistent with the expectation.

## 4.3 Quality Control on Modules

The module building is only the first step of the production chain. For hybrids and modules a series of tests are being designed to cover the quality control (QC) test performed on individual production item to check the functionality of the part. The QC tests on the assembled modules can be grouped in these categories:

- *Visual inspection* on the module to look for glue seepage after curing, damages to components and wire-bond inspection;
- *Metrology measurements* on the module bow, hybrid and power-board glue thicknesses to check if they are within specifications;
- *Electrical test* applying low and high voltage to check the ASICs and sensor performances after gluing.

Each of these checks are described in the following sections and all the plots and results refer to the QC tests performed on the R2 Star module built at DESY.

### 4.3.1 Metrology

After a quick visual inspection under the microscope to check for glue seepage and to take high resolution pictures the module is moved to the machine used for metrology. The measurements are performed using a 3D microscope (Smartscope CNC) [73] having a designed precision measurement of  $\pm 2\mu\text{m}$  in  $z$  and in the center of the lens, according to the manufacturer specifications. The Smartscope allows to get precise measurements even on very high reflective or transparent surfaces (such as the silicon) thanks to a specifically design feature. It is based on the addition of a grid projector for a better control of the contrast measurements on those surfaces. The metrology is performed before the hybrid is bonded to the sensor to access every area on chips and sensor.

**Sensor/Module bow** While sensors themselves are required to be flat within  $\pm 100\mu\text{m}$  upon delivery, the assembly process of modules can affect the overall sensor bow. In order to monitor the impact of gluing on the sensor shape, dedicated metrology measurements are performed at different stages of module assembly. The sensor

shape is mapped based on the measured heights and the sensor bow is calculated based on a fit through the sensor plane. The specification requires a maximum deviation of  $-150\ \mu\text{m}$  and  $50\ \mu\text{m}$  for a concave and convex form respectively. The natural shape of the silicon sensor is expected to be concave of few tens of micron because of its implants. Gluing the electronics on only one face of the sensor increases the concave effect of the final module due to the heat production. To define the bow, five points are measured on the sensor/module: one point at each corner and one roughly in the center. Fixing the origin in the central point of the sensor, the identification of the bow nature is easily obtained looking at the sign of the four measurements, compared with the origin. The QC procedure requires to perform this measurement on bare sensor and then on the assembled module. The values obtained for the R2 module are:  $(9\pm 10)\ \mu\text{m}$  for the sensor and  $(15\pm 10)\ \mu\text{m}$  for the module. The error has been evaluated considering the precision of the machine,  $\pm 2\ \mu\text{m}$ .

The importance of this measurement is related to the loading of the module on the petal core: an uncontrolled bow could cause a lack of glue in presence of a convex module bow, which means a bad thermal contact and a possible risk of module detaching from the core.

A more standard criterion to establish the bow is measuring the flatness. The flatness, according to the ISO standard 12781 [74], is defined as the element contained between two planes, that are distant from each other by a value less than or equal to the specified tolerance value. The orientation of these planes must be chosen so that the greatest distance between them is the minimum possible.

Assume  $\bar{X}, \bar{Y}, \bar{Z}$  to be the average of the point coordinates in each direction and  $x_i = X_i - \bar{X}, y_i = Y_i - \bar{Y}, z_i = Z_i - \bar{Z}$  the coordinates of the measuring points in the new referential. The parameters of the least squares plane ( $z = ax + by$ ) can be estimated from the following expressions, assuming that the deviation measurement is performed according to the  $z$  direction:

$$a = \frac{\sum y_i^2 \cdot \sum z_i x_i - \sum x_i y_i \cdot \sum z_i y_i}{\sum x_i^2 \cdot \sum y_i^2 - (\sum x_i y_i)^2}$$

$$b = \frac{\sum x_i^2 \cdot \sum z_i y_i - \sum x_i y_i \cdot \sum z_i x_i}{\sum x_i^2 \cdot \sum y_i^2 - (\sum x_i y_i)^2}$$

The deviation between the measured points and the reference least squares plane is defined as:

$$e_i = \frac{z_i - ax_i - by_i}{\sqrt{a^2 + b^2 + 1}}$$

Flatness deviation can be defined by the sum of the value of the maximum positive local flatness deviation  $|MAX(e)|$ , with the absolute value of the maximum negative local flatness deviation  $|min(e)|$ , the peak-to-valley flatness deviation is so obtained:

$$Flatness = |MAX(e)| + |min(e)| \quad (4.1)$$

which must be compared with the value of flatness tolerance, to check if the actual surface flatness is in accordance with the corresponding specification.

Figure 4.12 and 4.13 show the grid of points measured on the sensor using the jig as reference plane. The flatness measured on the bare sensor before gluing is  $20\ \mu\text{m}$  and  $22\ \mu\text{m}$  after the hybrid gluing. Both values are well within the specifications.

**Glue thickness** The glue thickness underneath the chips is calculated measuring points on the hybrid bonding pads around the chip and on the chip itself. Figure 4.14 shows the distribution of the points measured on chips (yellow points) and hybrid (blue points measured on the bonding pads). Knowing the nominal thickness of the chip ( $300\ \mu\text{m}$ ) it is possible to estimate the glue height. The same procedure is followed to determine the hybrid to sensor glue layer, having previously measured

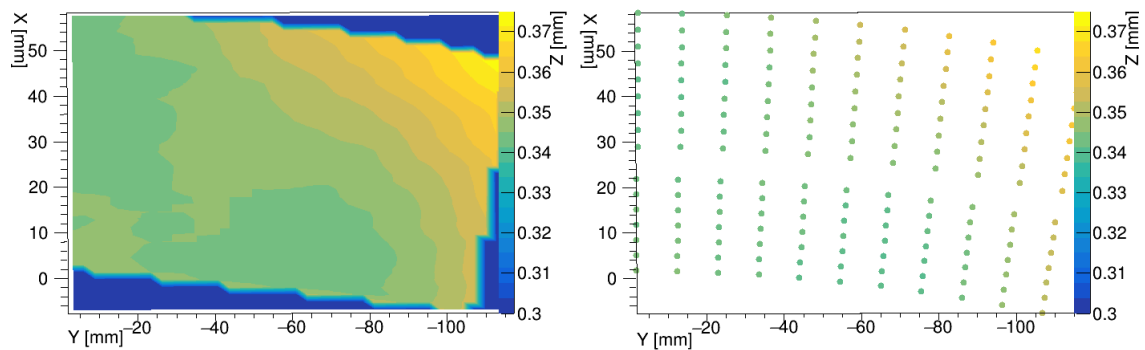


Figure 4.12: Flatness measurements on bare R2 sensor before gluing:  $20\ \mu\text{m}$ .

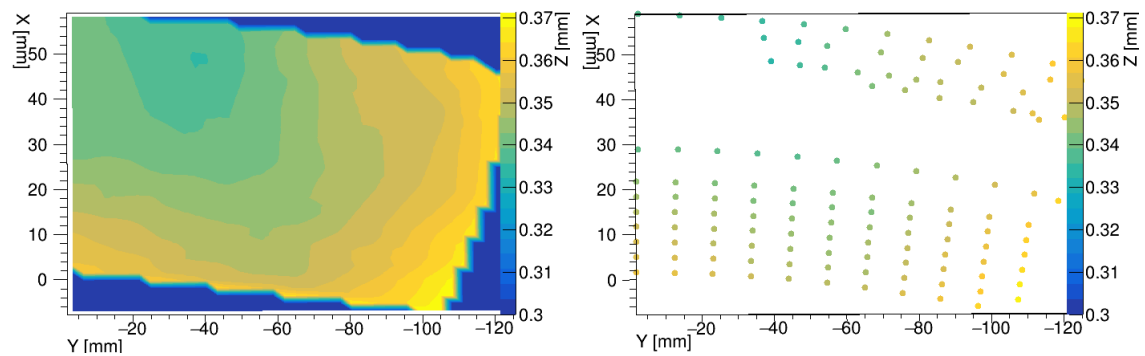


Figure 4.13: Flatness measurements on R2 sensor after hybrid gluing:  $22\ \mu\text{m}$ .

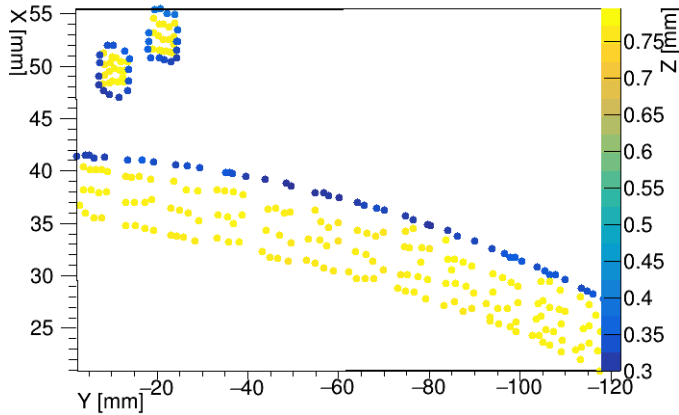


Figure 4.14: Metrology measurements on the R2 hybrid, yellow points are measured on chips and the blue one on the hybrid which are used for the calculation of the glue thickness.

the thickness of the hybrid, which is  $(212 \pm 11) \mu\text{m}$  using as reference the bonding pads.

The specifications require the glue to be  $(120 \pm 40) \mu\text{m}$  for both glue layers. In table 4.2 the glue thickness is listed for each ASICs with its standard deviation. Only HCC2 has a different glue height: this is likely due to a lack of vacuum under the hybrid in correspondence of this chip. Since the glue amount was tuned for a  $250 \mu\text{m}$  hybrid, a shim was used to balance the different thickness of the electrical hybrid ( $210 \mu\text{m}$  thick) used to build the R2 module. This additional layer underneath the hybrid closed the vacuum hole under HCC2. The shim layer is the orange foil in figure 4.3 underneath the hybrid.

### 4.3.2 Electrical test

The basic read-out tests performed on single hybrid and then on the assembled module focus on the front-end gain and overall hybrid noise, chip calibration and trimming, varying the injected charge and the threshold. Noise values per channel are used to identify broken or missing wire-bonds, as well as noisy or dead ASIC channels. The module testing checks the post assembly hybrid functionality and the final module performance. On a Linux PC (CentOS7) the so-called software ITSDAQ [75] [76] is installed and used to send commands and collect data from the ASICs under various conditions. After a description of the experimental setup needed to perform the electrical tests on modules and hybrids an explanation of each test is provided and some electrical results obtained on the R2 module are also shown.

Figure 4.15 shows the R2 Star module with the electronics division to understand the results provided by ITSDAQ. The R2 hybrid, even though is physically only one part, it is read out from the software as two, *R2H0* and *R2H1* with six front-

Chip	ASICs-Hybrid [ $\mu\text{m}$ ]	Hybrid-Sensor [ $\mu\text{m}$ ]
ABC1	148 $\pm$ 4	129 $\pm$ 15
ABC2	145 $\pm$ 2	129 $\pm$ 13
ABC3	143 $\pm$ 4	129 $\pm$ 15
ABC4	147 $\pm$ 3	129 $\pm$ 14
ABC5	141 $\pm$ 5	129 $\pm$ 16
ABC6	137 $\pm$ 4	130 $\pm$ 15
ABC7	138 $\pm$ 2	129 $\pm$ 13
ABC8	144 $\pm$ 4	129 $\pm$ 15
ABC9	148 $\pm$ 7	129 $\pm$ 18
ABC10	146 $\pm$ 2	129 $\pm$ 13
ABC11	149 $\pm$ 3	129 $\pm$ 14
ABC12	151 $\pm$ 3	130 $\pm$ 14
HCC1	147 $\pm$ 6	131 $\pm$ 17
HCC2	115 $\pm$ 2	159 $\pm$ 13

Table 4.2: Metrology measurements on the R2 module to define the chip to hybrid and hybrid to sensor glue heights for each ASICs. The chips are numbered from left to right looking at figure 4.14.

end chips each connected to the individual HCC. The sensor has two rows of strips: *Stream0* is the upper one passing below the hybrid and power-board and *Stream1* is the row on the bottom. Each ABC, having 256 channels, is wire-bonded to 128 strips on each stream.

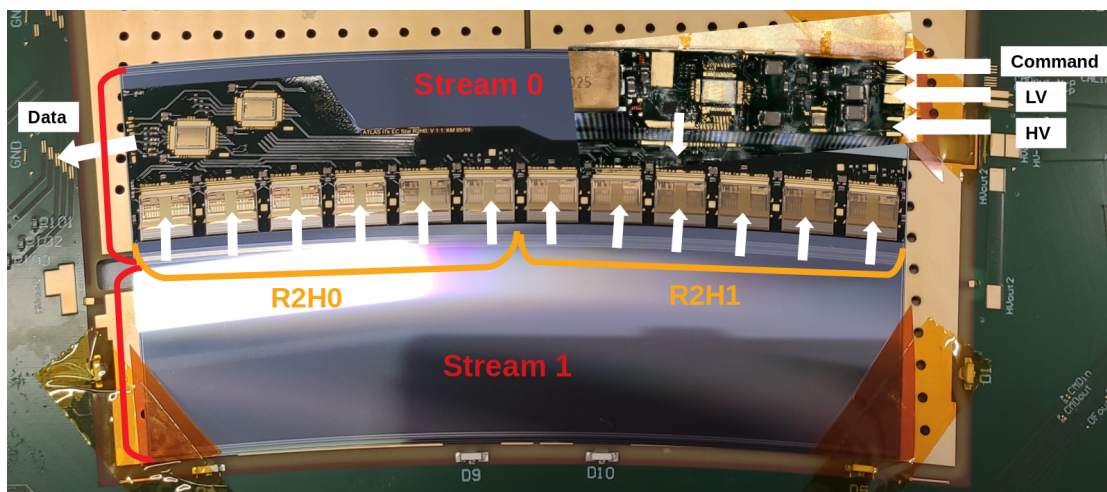


Figure 4.15: Closer look at the R2 module attached on the test frame for electrical test. Stream 0 (S0), which runs under the hybrid, and stream 1 (S1) are highlighted as well as the two portions of the hybrid, R2H0 and R2H1.

**Experimental setup** In order to perform electrical tests the module is attached and wire-bonded to a test frame. Wire-bonds on the right-hand side are mainly involved in providing low voltage to the chips through the power-board, after the 11 V conversion made by the DCDC, the chips get 1.5 V. The ones on the left-hand side are instead involved in the data transmission from the HCC through a mini display cable. The device used to supply high voltage to the back plane of the sensor is a *Keithley2410*.

A custom-made coldbox was used to test electrically the modules. The test-frame is screwed on a cooling jig, which provides also a ground connection, placed into the box and tightly closed to avoid any light exposure. The nitrogen is constantly flushed into the box to avoid any trace of humidity. The cooling system is necessary whenever electrical components are switched on and for this purpose a water chiller was used to cool down the module. The setup used for testing is shown in figure 4.16 and the readout chain is illustrated in figure 4.17. The read-out chain

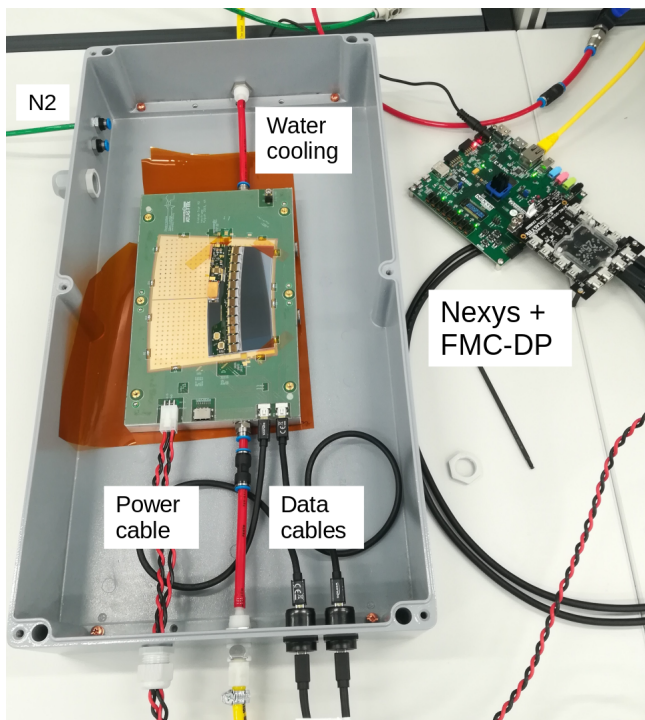


Figure 4.16: Testing setup for the R2 Star module. The module on test-frame is placed inside the box and connected to the readout chain (FCM-DP and Nexys).

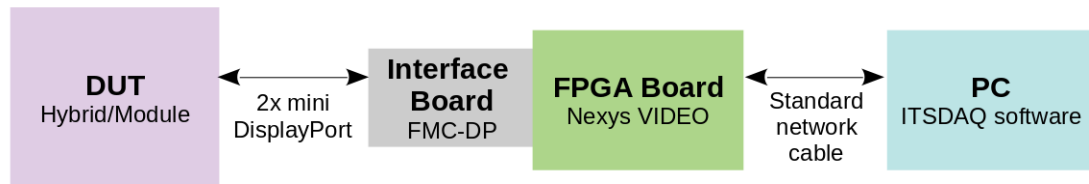


Figure 4.17: Readout chain used for Star module/hybrid testing.

includes a Digilent Nexys VIDEO [77] as FPGA (*Field Programmable Gate Array*) board where the ITSDAQ firmware is loaded via SD card. It is connected to the PC through standard Ethernet cable. The interface with the device under test (DUT) is done by a custom board, FMC-DP (*FPGA Mezzanine Card-Display Port*) board, in which two data cables (mini Display Port) are plugged in. One cable establishes the communication with the AMAC and the other is used for the *Timing and Trigger Control* (TTC). This setup is used to perform a preliminary test with particular focus on the wire-bonds. During the module production, if the communication is established correctly, the module is moved into the designed module cold box, explained in the previous chapter, section 3.2, for further tests during the thermal cycling in extreme temperature conditions.

**Capture chip ID** The first step is to establish communication with all chips, returning, if successful, the ID number assigned to each HCC and ABC ASICs. This digital test allows the user to find out if the chips work fine and if they are properly wire-bonded.

**Strobe delay** It is a scan that sets the timing (delay) of an injected calibration pulse with respect to the arrival time of the command to actually issue that pulse. This ensures that the discriminators, always firing at the clock frequency, will be synchronous with the calibration signal.

The correct setting varies between ASICs due to process variations and over time due to sensitivity to some conditions such as temperature. During a strobe delay scan, a charge of approximately 4 fC is injected into each readout channel, which is subsequently read out repeatedly at a readout threshold of 2 fC [78]. The injected charge is provided by the calibration capacitor arrays included in the ASIC circuitry. The varying parameter is the delay in the injection strobe between the clock edge and the pulse generation, over the full range of potential delays (6 bits representing approximately 50 ns). Outside a window of approximately 25 DAC (Digital-to-Analogue Converter) units, where injected charges are reliably registered, signals are out of phase with the ASIC's discriminator and can not be detected. The correct setting is chosen based on the timing of the edges of this window. The delay is set for each individual ASIC at 57% of the distance from the rising edge using the average value of the channels. This value of the strobe delay was selected based on a more detailed scan of the pulse shape and the noise at different delay values.

Figure 4.18 show the strobe delay scan done for each channel of the chips in R2H0, stream 0 (768 channels in total given by 128 channels for each of the six ASICs), and the y projection of the cumulative curve of chip 1 in figure 4.19. Here the fit is

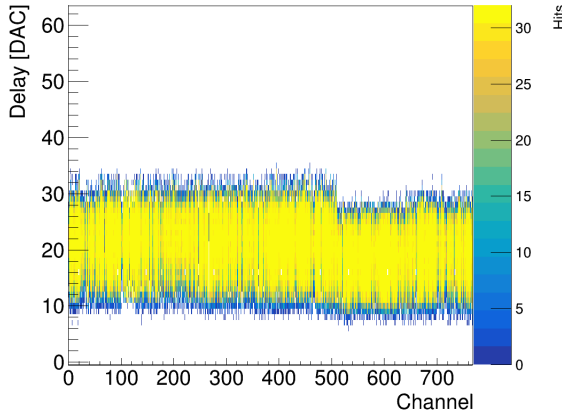


Figure 4.18: Strobe delay test on R2H0 hybrid, S0.

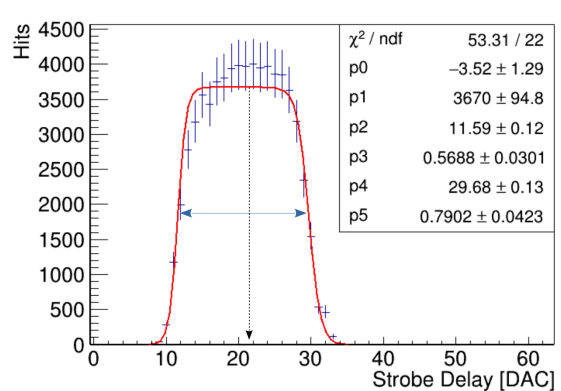


Figure 4.19: Cumulative y projection of chip 1 in R2H0, S0.

executed using a double Fermi-Dirac function,  $f_{up}$  on the rising edge and  $f_{down}$  on the falling edge, to get the width of the temporal window:

$$f(x) = p_0 + (f_{up} \cdot f_{down}) = p_0 + p_1 \left( \frac{1}{1 + e^{-(x-p_2)/p_3}} \cdot \frac{1}{1 + e^{(x-p_4)/p_5}} \right) \quad (4.2)$$

where:

- $p_0$  is the baseline value
- $p_1$  is the normalization factor
- $p_2$  and  $p_4$  are the inflection points on the x axis
- $p_3$  and  $p_5$  are proportional to the difference between the points at which the histogram goes from 10% to 90% of its maximum value, respectively for the rising edge and the falling one

Therefore the strobe delay value of each ABC chip is defined as  $p_2 + 0.57(p_4 - p_2)$ . All values for the R2 ABC chips are plotted in figure 4.20. Physically the R2 hybrid has 12 ABC chips, but 24 values are displayed in this plot because every ASIC reads data from S0 and S1 stream independently.

**Response curve** The response of the amplifier for each readout channel (silicon strip) is measured using a sequence of threshold scans to evaluate the chip performance, such as input and output noise, and gain. The threshold scan is performed by injecting a certain charge via calibration capacitors and varying the threshold value of the discriminator from zero to its maximum, depending on the charge. For each injected charge, the resulting distribution is expected to be a step function ideally, which becomes an *S-curve* due to smearing from noise effects.

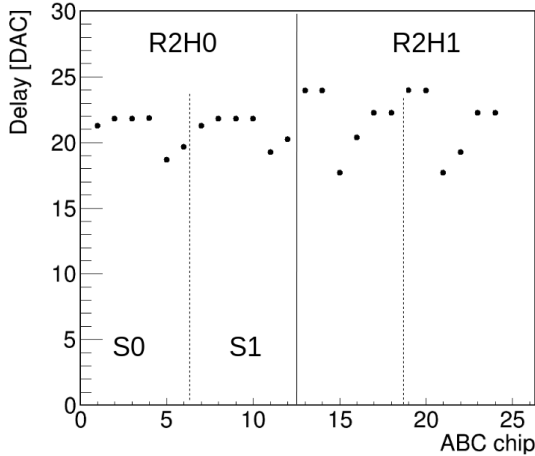


Figure 4.20: Strobe delay values for each ABC chip of the R2 module, considering that every chip collects data from two streams.

The S-curve, or sigmoid curve, is fitted with the following function related to a skewed error function  $Er f(x)$ :

$$Er f(x) = \frac{2}{\sqrt{\pi}} \int_x^{\infty} e^{-t^2} dt \quad (4.3)$$

$$f(x) = \frac{p_0}{2} \left( 1 + Er f\left(\frac{x - p_1}{p_2}\right) \right) = \frac{p'_0}{1 + e^{(x-p'_1)/p'_2}} \quad (4.4)$$

where the parameters  $p'_0, p'_1, p'_2$  have the same meaning of  $p_1, p_4$  and  $p_5$  in equation 4.2. The point of the curve where the efficiency reaches the 50% of hits is called *50% occupancy*,  $V_{T50}$ . The test is called *three point gain* when it is run for only three values of injected charges, 0.5 fC, 1 fC and 1.5 fC, and *response curve* when the values are ten, up to 6 fC. An example of threshold scan is reported in figure 4.21 when 1.5 fC is injected in the R2H0 hybrid, stream 0. In figure 4.22 the y projection of the same scan in channel number 100 can be observed.

The  $V_{T50}$  values for each channel at each injected charge fill an histogram and the mean and sigma are extrapolated by a Gaussian fit on the distribution, as shown in figure 4.23. The sigma provides the information about the *output noise* in DAC counts. The mean values are plotted as function of charge for single channel, as shown in figure 4.24. The resulting curve can be fitted linearly with the equation 4.5 for lower range of charge to obtain values of the estimated discriminator *offset* (mV at 0 fC, the line's intercept) and the *gain* of each channel (slope of the function).

$$V_{T50}[mV] = Gain[mV/fC] \cdot Q[fC] + offset[mV] \quad (4.5)$$

Over a larger range of injected charge the response curve is not linear anymore and it can be fitted using the following function:

$$V_{T50}[mV] = \frac{p_0}{1 + e^{-Q/p_1}} + p_2 \quad \Rightarrow \quad Gain = \frac{dV_{T50}}{dQ} \quad (4.6)$$

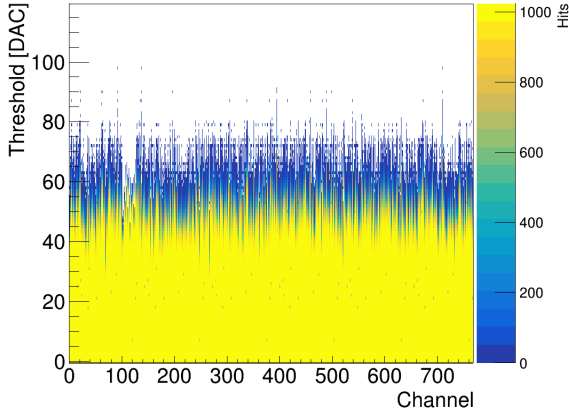


Figure 4.21: Threshold scan in R2H0, S0, injecting 1.5 fC on single channel of the ABC chips.

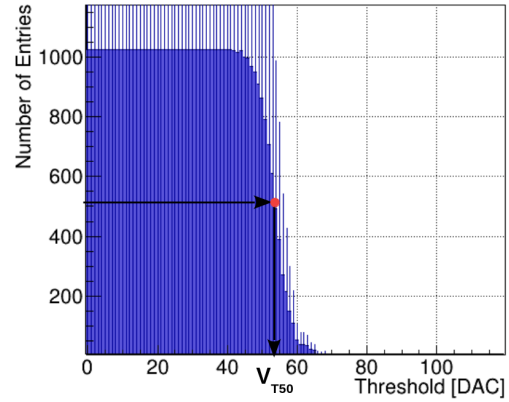


Figure 4.22: Y projection (s-curve) of channel 100 in R2H0, S0, after the threshold scan injecting 1.5 fC.

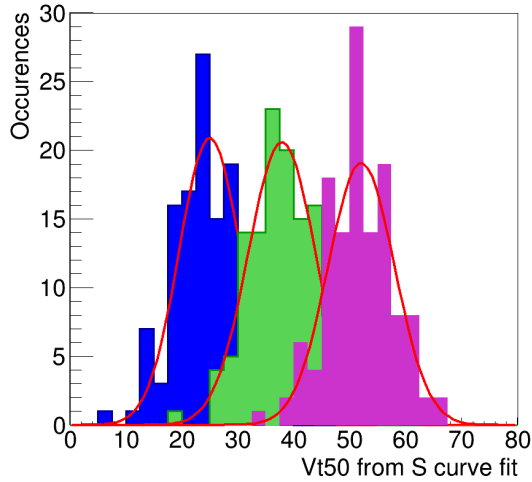


Figure 4.23: Gaussian fit on the  $V_{T50}$  distribution, in DAC counts, for three values of injected charges in R2H0, ABC chip 1: 0.5 fC (blue curve), 1 fC (green curve) and 1.5 fC (purple curve)

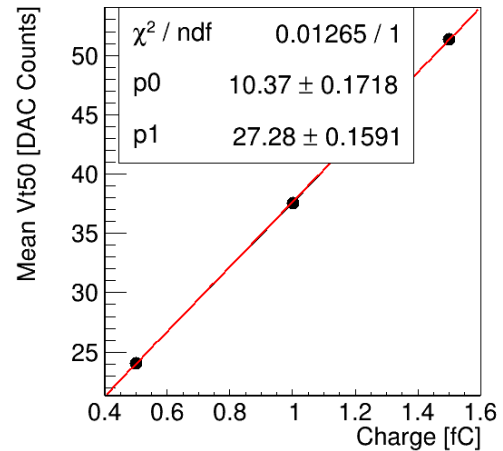


Figure 4.24: Linear fit on mean values of each distribution to get the gain ( $p_1$ ) and the offset ( $p_0$ ).

where the gain is obtained from the first derivative of the function. An example of response curve is shown in figure 4.25 where ten values of charge are injected and the  $V_{T50}$  values are fitted with the function 4.6.

The gain is the amplification of the signal given by the pre-amplifier and it can be used to convert the output noise (the sigma of the Gaussian distribution) into the *input noise* that is the derived noise at the input of the amplifier, reported in

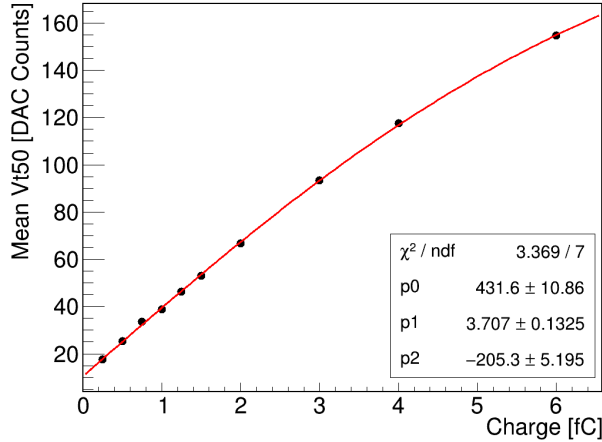


Figure 4.25: Response curve on single ABC channel using the function in equation 4.6.

electrons (equivalent noise charge,  $1 \text{ ENC} = 1.6 \cdot 10^{-4} \text{ fC}$ ). The relation is shown in equation 4.7.

$$\text{InputNoise}[fC] = \frac{\text{OutputNoise}[mV]}{\text{Gain}[mV/fC]} \quad (4.7)$$

The final values of gain and input noise have a 20% safety factor added to them. The ITSDAQ software provides the values in DAC counts, but they can be converted in mV multiplying the value by 2.7, after the 20% is added [78].

The values of gain and input noise of the R2 module are plotted in figure 4.26 and 4.27 respectively for single channel. The values are shown for both sensor streams,  $S0$  and  $S1$ , and for both hybrids, R2H0 and R2H1. Only three ABC chips in R2H1 are responding correctly due to an improper configuration settings. The few red points at roughly 400 ENC in figure 4.27 are channels that are not wire-bonded to the sensor strips, they were used to check the noise level in comparison with bonded channels. Comparing the input noise in  $S0$  and  $S1$  of the same hybrid, a 4% increment is measured in  $S0$  and it is explained by the presence of hybrid and power-board glued on that stream. The glue layer behaves like a capacitor and introduces an additional factor to the sensor capacitance which increases the noise level. A detailed explanation about the module noise estimation is given in section 6.4.4.

The magenta and green dashed lines in figure 4.27 indicate the level of noise expected in stream  $S0$  (650 ENC) and  $S1$  (600 ENC) respectively. The measured values are higher than expectation and some adjustments on the electronics circuits were needed due the prototyping components.

The noise level is highly dependent on the statistics used to run the test: greater number of triggers provides a high statistic measurement, but also a higher noise, as shown in figure 4.28. This is because with a small number of triggers the low occupancy tail in the S-curve is underpopulated, which results in S-curve fits returning

a narrower noise profile. As the number of triggers is increased, the tail is better populated, resulting in increased, and more correct, noise measurements.

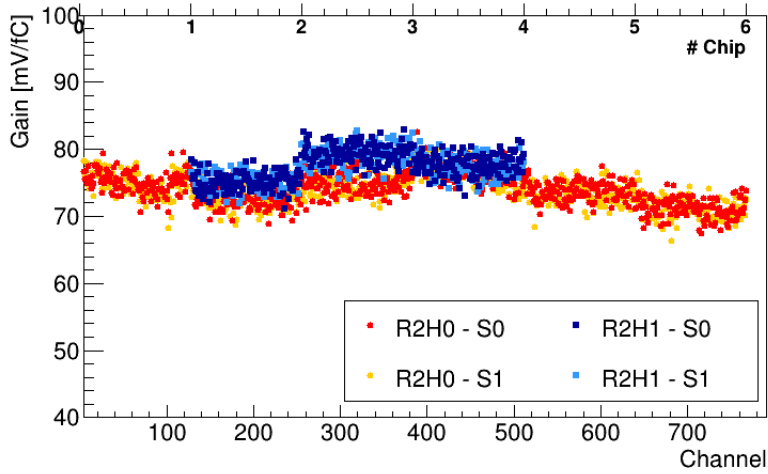


Figure 4.26: Gain values measured on R2 module for each ABC chip channel.

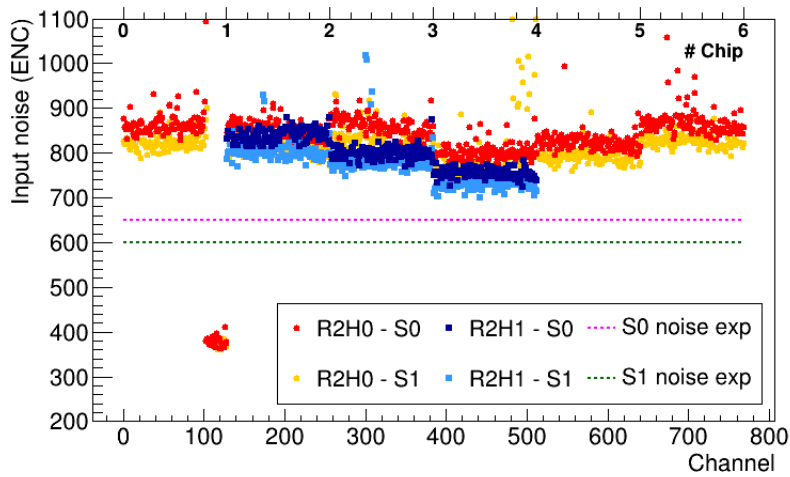


Figure 4.27: Input noise values measured on R2 module for each ABC chip channel.

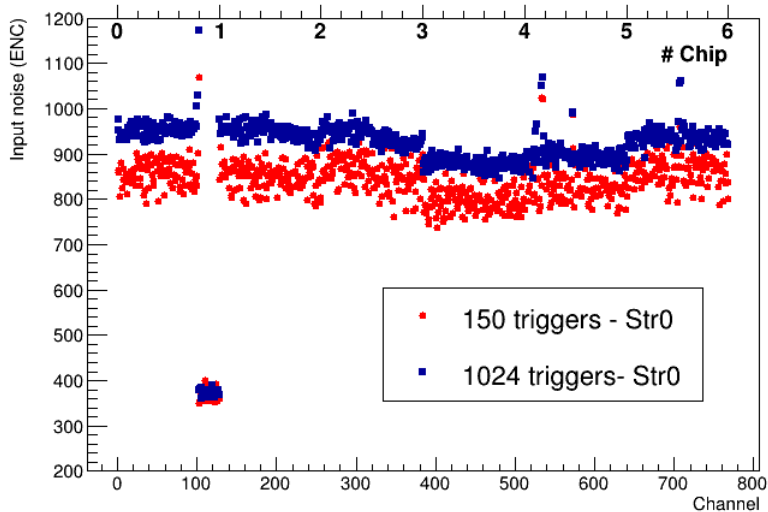


Figure 4.28: Input noise measured on R2H0, stream 0, using different number of triggers for the three point gain scan.

**Noise occupancy** This test measures the noise occupancy (NO) as a function of threshold and the scan is done without injecting any charge. This test is useful for measuring the noise for a module under different conditions, such as the temperature. The requirement for the ITk Strip Detector is having less than  $10^{-3}$  channel noise occupancy at a threshold resulting in a detection efficiency greater than 99% at the end of life of HL-LHC [37].

An example of noise occupancy measurement for an irradiated module during a test beam is shown in figure 4.29, as function of the threshold. It was tested by a 5 GeV electron beam at DESY-II Testbeam Facility. The module was irradiated by neutrons to a fluence of  $1.05 \times 10^{15} n_{eq}/cm^2$  at Jozef Stefan Institute (JSI) in Ljubljana. The blue and red dashed lines indicate the ITk requirements on hit detection efficiency and noise occupancy respectively. The dashed areas show the threshold range in which the ITk Strip requirements are satisfied:

$$0.33 \text{ fC} < \text{threshold} < 0.55 \text{ fC}.$$

**Trim Range** During the operation of a module, readout thresholds are not set for individual channels, but for full readout chips. An operating threshold is chosen to be as low as possible while also minimizing noise occupancy ( $< 1\%$ ). In order to ensure a uniform response of all module channels to which the same readout

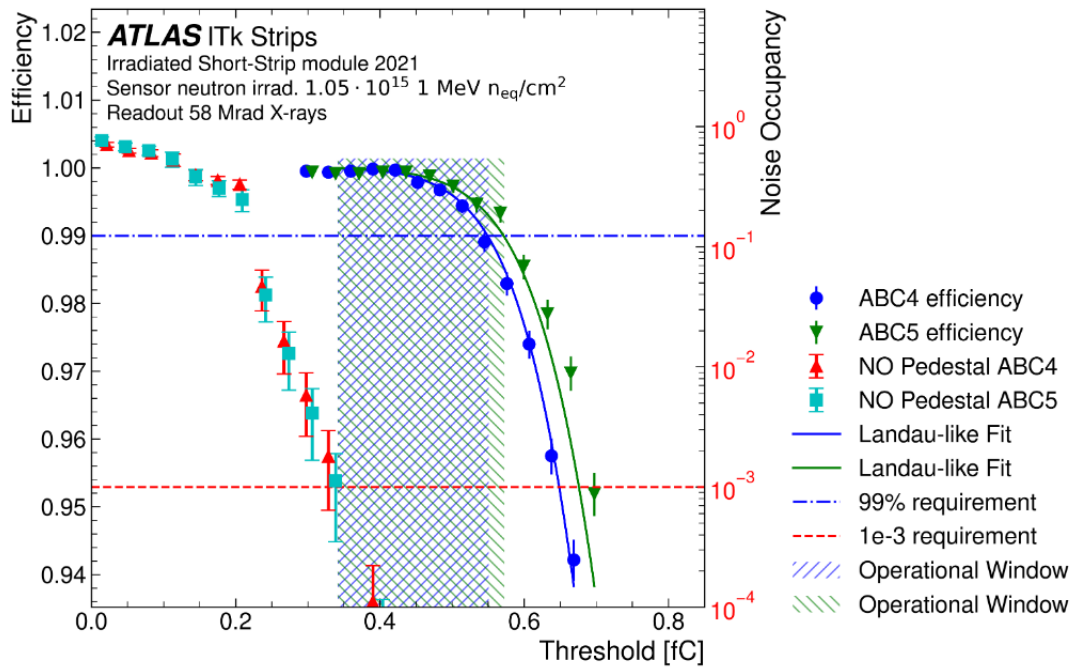


Figure 4.29: Efficiency and noise occupancy of two ABC chips as function of the threshold for an irradiated Star module [79].

threshold is applied, S-curve positions can be shifted in the threshold range. While an efficiency curve can not be moved towards lower thresholds, it can be moved towards higher thresholds by adding an offset, which has to be determined by channel, to the pedestal. In order to find a threshold to which a majority of channels can be trimmed, a scan over the TrimDAC values and the Trim Range is performed. A chosen charge is injected into the front-ends and the trims adjusted so that the thresholds align for a particular chip-level threshold. The Trim Range is chosen to allow as fine tuning as possible while including as many channels as possible. Thus, all channels on a chip are trimmed by adding the tuned offset value to their threshold, leading to a uniform distribution of  $V_{T50}$  on all channels of the same chip.

**Conclusions** The QC test results performed on the R2 Star module demonstrated that the building procedure developed at DESY and the tooling set permit to assemble modules within specifications. The module bow and the glue layer thicknesses are well under control and no glue seepage is observed. The usage of the glue dispensing robot is proved to be a very useful and reliable machine to apply the required amount of glue. The glue pattern designed for the R2 Star module is used as baseline to generate the one for the R4 Star module, as they are the module flavours that DESY is going to build for the module production.

The R2 module responded correctly to the electrical test, the input noise result is slightly higher than the expected level because of the usage of prototyping components of the electronics.

# Chapter 5

## Module loading and qualification of petals

The main components required to build a petal are the modules and the local support structure, also called petal core, both explained in section 3.1. The module as well as the petal core have to go through several quality control (QC) tests before being glued together. The module QC tests have been described in detail in section 4.3 and the tests concerning the local support are explained in this chapter, section 5.1. The modules and the core that pass all the checks are selected for the loading procedure: this step is very important and it needs to be extremely precise to achieve a good final object. The mounting technique developed within DESY and the ITk collaboration is discussed step by step in section 5.2.

In order to verify the precision of the loading procedure a *semi-electrical petal* was assembled at DESY in January 2020: a petal core was populated with semi-electrical modules. The petal assembly and the results of the QC tests performed on it are shown in section 5.3 and 5.4 respectively.

### 5.1 QC on a Local Support Structure

The local support, thought as a carbon fiber honeycomb in a sandwich structure with face-sheets and an embedded cooling loop, as described in section 3.1.1, goes under mechanical, electrical and thermal tests. They are required to verify the quality of the assembly and the fulfilment of the specifications [80]. Two institutes, DESY and IFIC, Valencia, are involved in performing those tests right after the core production carried out by the industry.

### 5.1.1 Electrical tests on cores

All materials in the detector volume which conducts electricity must be connected to ground so that the charge deposited by the exposure to charged particle radiation can drain away. The only ground connection must be through a *Faraday cage*, it is an enclosure used to block electromagnetic fields which interfere with the signal produced by the passing particle. It is therefore constructed to provide grounding and EMI shielding to the entire ITk detector. It must include a complex envelope that encompasses the detectors, cables and many services. The bulkhead, at the outer end of the endcap structure, constitutes one of the sides of the primary Faraday cage of the ITk detector. It represents the interface between the Endcap and the off-detector where all cables and services are plugged in the Patch Panel 1 (PP1). The ground (GND) for the data transmission lines from the single petal has to be connected to the Faraday cage independently, constituting the *Internal Reference Point* (IRP) for each pair of EoS (master and slave) to the cage. Both faces of the petal core are electrically connected together by the lowest copper layer of the bus tape. The tape is in direct contact with conductive core materials such as carbon fiber and graphite-loaded glue. Front and back bus tapes are therefore connected across the core and the GND is accessible by specific pads (ground pads) on the bus tape. Module GND is wire-bonded on those pads and it is driven by the LV return line on the bus tape to the EoS.

The petal core is in addition insulated from the global structure where it is inserted thanks to electrical breaks added at both ends of the titanium cooling loop. The carbon fiber global structure, the skeleton of the endcap, holds the petals using three pins, called locking points, that fit into the petal locators. Both the petal locators in the petal core and the locking points in the global structure are made out of electrical insulating material, Torlon 4301 [56], therefore guaranteeing the insulation of the petal with respect to the global structure.

The type I cables are the ones that connect the EoS to the PP1 and are the only way to take out the IRP from each petal. The HV and LV return are extracted from the EoS and, via cable shields, are brought to the bulkhead of the Faraday cage, connected to PP1 and direct back to the power supplies. The black line in figure 5.1 indicates the cable shield that brings the IRP to the Faraday cage.

The service trays, described in section 3.2, are made of carbon fiber, hosting the inlet and outlet cooling pipes and the services. Eight service trays are attached to each disk of the endcap. They provide a low resistance path connecting the pipes and the disks to the Faraday cage and therefore guarantee a *Common Reference Ground* (CRG) connection, common to the whole endcap structure [65]. They are

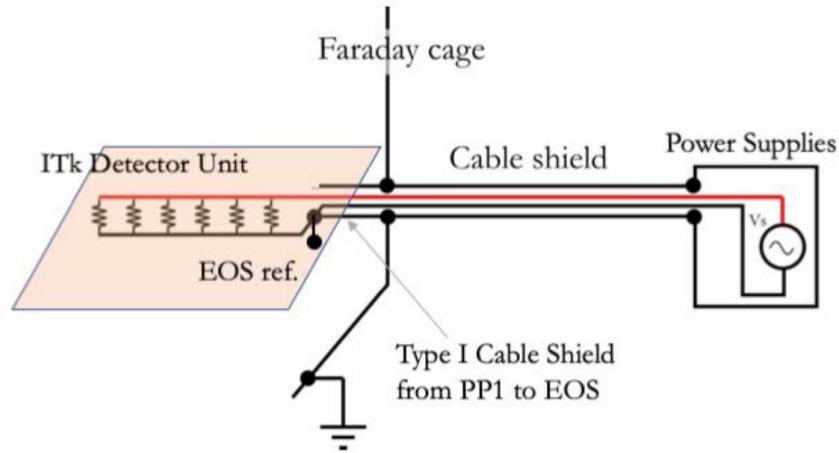


Figure 5.1: Schematic path of the cable shields connected to the power supply passing by the service tray and Faraday cage [81].

shielded from the cables to avoid mixing the IRP and the CRG.

The grounding system of the endcap can be summarized as follows [81]:

- Internal detector reference point (IRP): the local line that collects the GND from the modules and petal core of each individual local support is transported from the EoSs to the Faraday cage via cable shields and insulated from the global structure. It requires a low impedance to the Faraday cage;
- Common reference GND (CRG): the global structure, including service trays and cooling pipes, is connected to the Faraday cage. It requires a low resistance to the Faraday cage;
- Each IRP is isolated from the CRG all the way to the Faraday cage.

This explanation on the ITk grounding introduces the importance of the electrical tests for the core QC. The goal is to check the grounding and shielding of the local support performing the following measurements:

- *grounding*: very low electrical impedance ( $\sim 2 \Omega$ ) between the two petal faces is measured with a tester using the ground pads on the bus tape;
- *insulation*: high electrical impedance ( $\geq 20 \text{ M}\Omega$ ) is measured between the grounding pad of the core and titanium pipe ends;
- the *bus tape at the final stage of the core assembly*: the differential lines and power/monitoring traces on the tape are checked after the core assembly with the bus tape testing robot to guarantee their functionality.

The bus tape, placed on a vacuum chuck, is tested with a robot and the resistance

of lines is measured by probing the bonding pads. If broken lines and short circuits between all neighbouring lines are found or the leakage current is too high ( $> 20$  nA) the bus tape is rejected. A stretch test is performed to check the eventual displacement of fiducial marks, especially after co-curing the tape, which could be a cause of failures the stretch causes a shift of the bonding pads.

### 5.1.2 Mechanical properties

The flatness of the core and the petal locators' dimension and position are measured using the Smartscope [73] to check if they are within the geometrical specifications. The requirement on the flatness demands for a local fluctuation  $< 50$   $\mu\text{m}$  on each sensor area to ensure a proper thermal interface between modules and local support and to allow a precise module mounting. An example of flatness measurements is shown in figure 5.2 and 5.3: more than 2000 points are measured on the front and back side respectively of a petal core prototype in the regions where the modules are located. The flatness is obtained using the same formula explained in section 4.3.1 and the values are listed in table 5.1 for each module area, the flatness of most of the module areas fulfils the mechanical requirements.

A particular importance for the module loading is given to the dimensions of the petal locator and fiducial holes, as they determine the precise location of the modules into each core and the cores into the detector. Tight tolerances for those components were specified for that purpose, and they are checked with the Smartscope.

Module	Points	Front side [ $\mu\text{m}$ ]	Points	Back side [ $\mu\text{m}$ ]
R0	252	47.5	227	53.2
R1	264	55.6	218	37.0
R2	250	46.8	214	37.9
R3S0	257	39.6	233	48.6
R3S1	205	29.2	230	44.9
R4S0	251	57.7	260	39.3
R4S1	217	32.4	256	48.8
R5S0	267	59.0	269	51.2
R5S1	231	64.4	269	52.7
Global	2194	142.8	2176	104.4

Table 5.1: Flatness values calculated for each module area on both side of a petal core prototype.

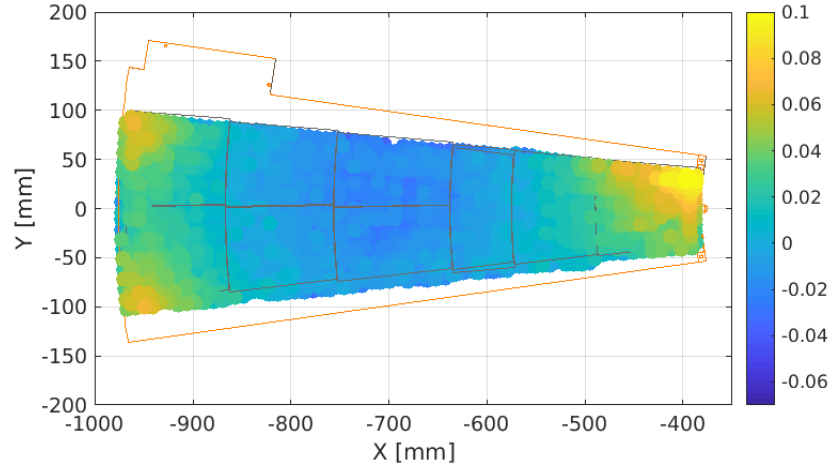


Figure 5.2: Metrology on a prototype of petal core, front side.

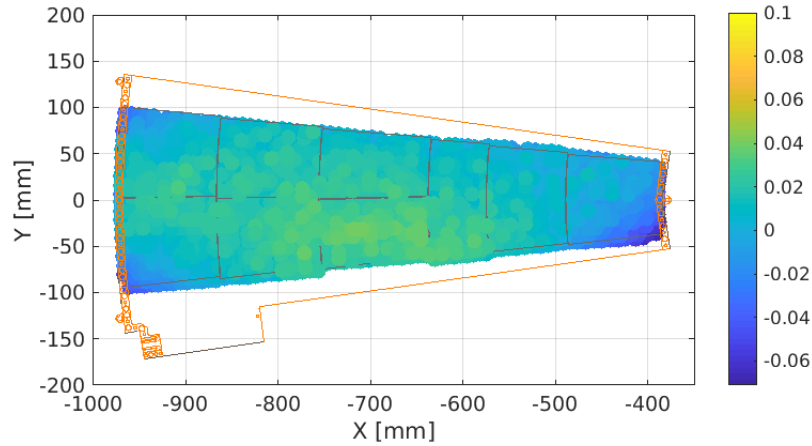


Figure 5.3: Metrology on a prototype of petal core, back side.

### 5.1.3 Thermal tests

The core provides the cooling for the heat created in the silicon modules by their associated on-detector electronics. A sufficient thermal contact to the modules is required via the glue and the core surface to allow the dissipation of the heat. The main reasons for the cooling application is to decrease the electronic noise due to the heat and to avoid the *sensor thermal runaway*. This phenomenon occurs when the system becomes thermally unstable, the heat generated in the detector exceeds the cooling capacity of the system [17]. A particle that passes through the sensor could physically destroy the sensor. A simulation to estimate the critical temperature of irradiated sensors is described in section 6.5.1.

Thermal tests are important to investigate the cooling behaviour of the local support and how the core components have been assembled together. A broken interface between the materials causes the interruption of the heat transfer and a silicon

module, placed on top of it, cannot be cooled down properly. Delamination of the core is a consequence of a failure during the core assembly, mainly when two materials are not properly glued together, for example the carbon foam or honeycomb carbon fiber and the facesheet. Another example where delamination can occur is during the cutting of the sacrificial edges of the facesheet at the last step of the core manufacture. The required thermal impedance of the core is defined by its thermal path: the cooling is provided by evaporative CO<sub>2</sub> in the titanium cooling loop, embedded in the high thermal conductivity carbon foam and therefore transmitted to the carbon fiber surface. The minimal operating temperature for a petal coolant is  $-35\text{ }^{\circ}\text{C}$  [37]. The QC measurement for the thermal performance of a core uses the concept of infrared thermography performed in a dedicated test setup involving the cooling of the petal core to the required temperature under defined ambient conditions. The technique of infrared thermography, also called infrared thermal imaging, is used for the assessment of the petal's thermal performance. An InfraRed (IR) camera detects the emitted radiation from an object in the IR range of the electromagnetic spectrum, typically between 9 and 14  $\mu\text{m}$ , and produces spatially-resolved images of the detected radiation. As the emitted radiation of the object depends on its temperature, the detected radiation can be converted into temperature values to create an image of the temperature distribution of the object, called thermogram. Looking at a core thermogram during a cold test the delamination effect is shown as an interruption of the cooling path or as a region of unusual high temperature. The IR thermography allows temperature measurements without direct interference to the object like a direct probe measurement; the IR picture is taken in real time and the temperature distribution can be observed during the operation condition changes. The main disadvantage of IR thermal imaging concerns the displayed temperature: it is usually not the real temperature of the object. The detected radiant power is the sum of multiple sources, namely the *emitted*, *transmitted* and *reflected* radiant power. Normalizing the expression of the conservation of the energy, the emissivity is obtained from the total reflexivity, the transmissivity can be neglected as most of the solid materials are opaque in the IR spectrum [82]:

$$emissivity(\epsilon) + reflexivity(r) + transmissivity(\tau) = 1 \quad \Rightarrow \quad \epsilon = 1 - r$$

The emissivity coefficient goes from 0 to the ideal condition of a black body ( $\epsilon = 1$ ) depending on the material properties.

The ambient condition plays an important role in the definition of the temperature via the IR imaging, especially when the temperature of the testing object with low emissivity is lower than the one of the air. In this case the contribution given by

the ambient prevails affecting the temperature of the object, which appears to be closer to the ambient. For example when an object with very low emissivity, such as highly reflective surfaces (silicon sensors, read out chips and shield boxes) is tested at  $-35^{\circ}\text{C}$ , the temperature read out by the IR camera is higher than reality due to the influence of the air which has higher temperature ( $20^{\circ}\text{C}$ ).

**CO<sub>2</sub> cooling technique** The dual-phase CO<sub>2</sub> cooling is the one chosen to cool down the whole ITk detector in the ATLAS experiment thanks to the following reasons [37]:

- a large latent heat transfer is possible due to the phase change energy for the transition of liquid to gaseous CO<sub>2</sub> and allows for low mass flows of the coolant (of the order of few g/s);
- a low pressure drop allows to use small pipe diameters reducing the material budget of the cooling services in the detector and guarantee a high heat transfer capability due to Heat Transfer Coefficient (HTC) values of typically  $8000\text{ W}/(\text{m}^2\text{K})$ ;
- a high thermal stability is reached due to the high pressure in the system;
- CO<sub>2</sub> is a natural, non-toxic and non-flammable gas and well suited for high-energy physics application as it is mostly radiation resistant and non-magnetic.

Figure 5.4 shows the CO<sub>2</sub> phase diagram: the pressure is plotted as function of enthalpy. The isotherm lines are also shown to understand the thermodynamic

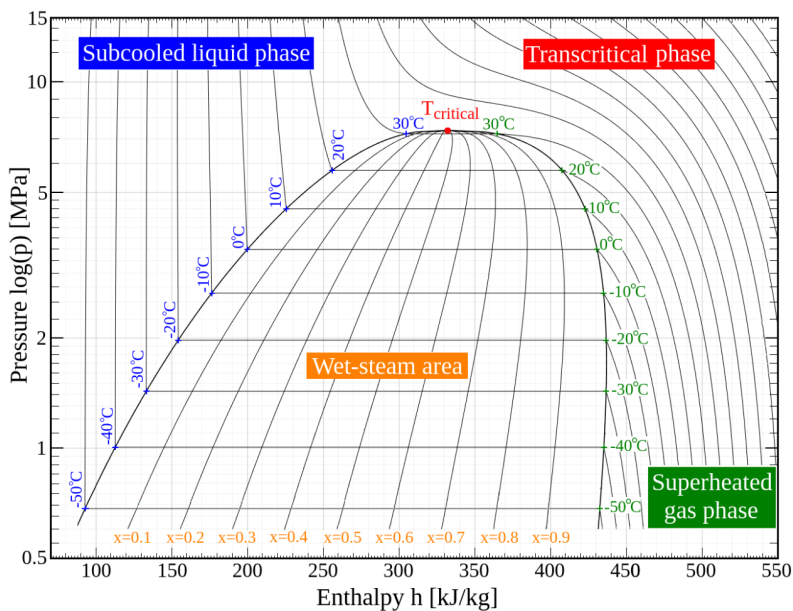


Figure 5.4: CO<sub>2</sub> phase diagram as function of pressure in logarithmic scale. The gas, liquid and solid states of CO<sub>2</sub> are highlighted with isotherm lines.

processes happening in the evaporative  $\text{CO}_2$ , which is tied to work in the wet-stream area. The cooling machine provides liquid  $\text{CO}_2$  which partially evaporates absorbing the heat from the detector. For a high cooling performance the gas ratio can be up to 35%, which is transformed in a pressure drop of maximum [83]:

$$\Delta p = p_{inlet} - p_{outlet} < 1.2 \text{ bar} \quad \Rightarrow \quad \Delta T = T_{inlet} - T_{outlet} < 3^\circ\text{C}$$

At the pipe outlet the liquid  $\text{CO}_2$  pressure is lower due to the presence of the gas and this is reflected in a temperature drop too:  $(p, T)_{inlet} > (p, T)_{outlet}$ .

A machine that provides all these features in a compact size is *MARTA*: Monoblock Approach for a Refrigeration Technical Application [84]. This system guarantees a stable operation in requested temperatures, a precise control of the parameter and repeatability in a wide range of operation, from  $-35^\circ\text{C}$  to  $20^\circ\text{C}$ .

**Setup for the thermal test** Thermal tests are performed inside a custom-made box, called Petal Thermal Measurement chamber (PTM). Figure 5.5 shows the PTM



Figure 5.5: Testing setup for the thermal analysis inside the cleanroom.

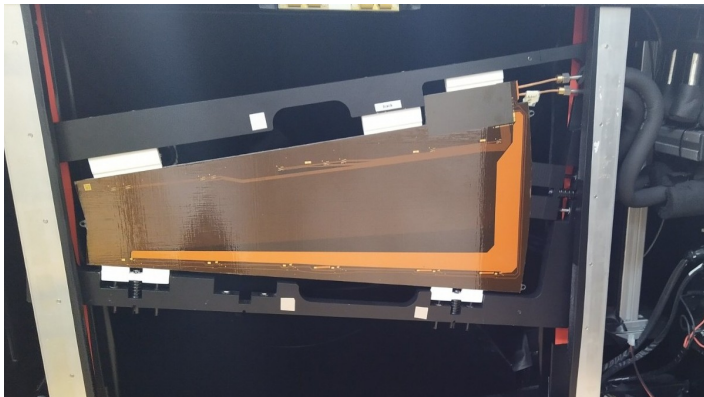


Figure 5.6: Petal core placed inside the PTM for thermal tests and held by a custom-made frame.

chamber on the right-hand side and the MARTA cooling system connected to it. An IR camera is placed inside the chamber to take pictures to allow the thermal analysis. The core is held inside the chamber by a custom frame which uses its lateral V-channels, as shown in figure 5.6. Thermocouples are used to measure the humidity and temperature inside the PTM and devices to control the  $\text{CO}_2$  pressure at the inlet and outlet of the cooling pipes. A more detailed description on the setup is provided in section 6.2.

**Infra-red imaging analysis** In the following section, an example of the thermogram analysis of a prototyping core is provided. A first qualitative analysis regarding the detection of delamination is done looking at figure 5.7: the cooling path should appear regular without any interruptions and with roughly the same temperature observed along the pipe. This thermogram was recorded at a  $\text{CO}_2$  temperature set point of  $-20^\circ\text{C}$ . The temperature range is fixed by the lowest temperature recorded on the thermogram,  $-15^\circ\text{C}$  measured on the core along the cooling pipe, and the maximum one measured in the surrounding air,  $18^\circ\text{C}$ . During the QC test for the core production a visual comparison of each core thermogram is made with an ideal petal core, so-called *golden core*, obtained combining prototype test results with simulation using a FEA technique (Finite Element Analysis) [85]. In this way all the ambient condition that can affect the temperature detection are taken into account. Currently the development of the golden petal is still under discussion among the ITk community members.

A more quantitative investigation on the same IR image is made using two different markers to evaluate the temperature [52]:

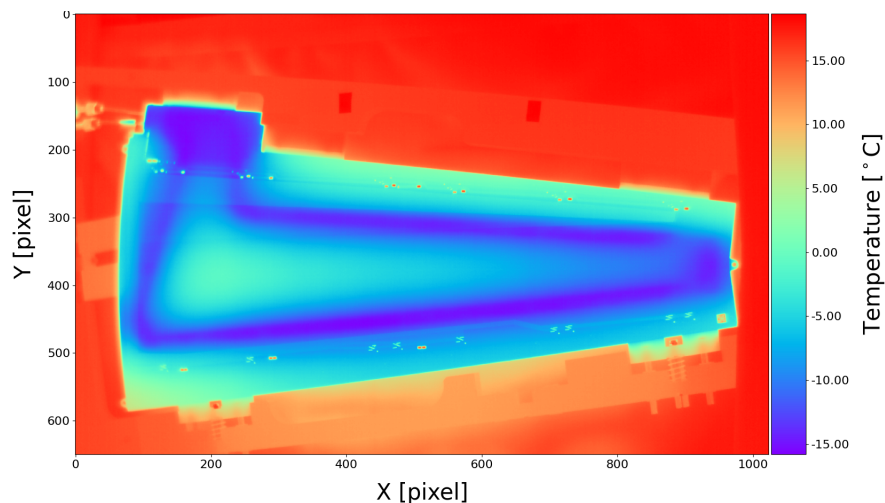


Figure 5.7: IR picture recorded on a front side of the petal core at  $T_{\text{CO}_2} = -20^\circ\text{C}$ .

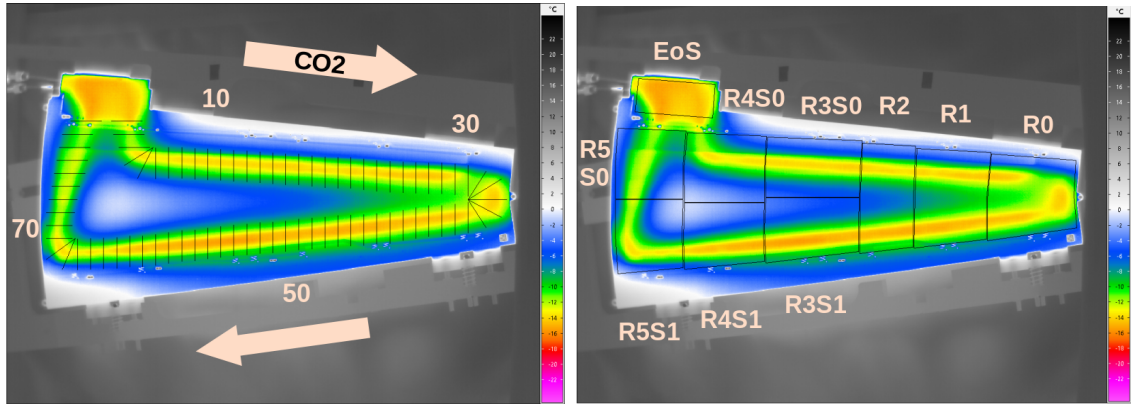


Figure 5.8: Thermogram on a petal core recorded at  $T_{CO_2} = -20^\circ\text{C}$ , front side, with 78 linear markers equally distributed on the cooling pipe (left side) and ten polygonal markers to identify the module areas (right side). The temperature range scale goes from  $-25^\circ\text{C}$  to  $25^\circ\text{C}$ .

- 78 linear and equidistant markers are distributed along the cooling pipe to study the evolution of the  $\text{CO}_2$  temperature, shown in figure 5.8, left side;
- ten polygonal markers are used to highlight the module regions, including the EoS area, illustrated in figure 5.8 right side, and to calculate the temperature average of each one.

For this petal core, three different  $\text{CO}_2$  set-points have been chosen to test the thermal property:  $20^\circ\text{C}$ ,  $-20^\circ\text{C}$  and  $-23^\circ\text{C}$ . The plot in figure 5.9 shows the results obtained from the analysis with linear markers at the three  $\text{CO}_2$  set points. The temperature is quite stable along the full length of the cooling pipe. Only a small defect is observed around marker ID 30 where the temperature slightly increases just before the U-bending of the pipe, probably due to the delamination effects.

In addition, the thermal investigation on the module regions is plotted in figure 5.10: the temperature in all regions is comparable for each  $\text{CO}_2$  set point. The coldest region is the one where the EoS is located, since this area is very much covered by the inlet and outlet pipe, compared with its surface.

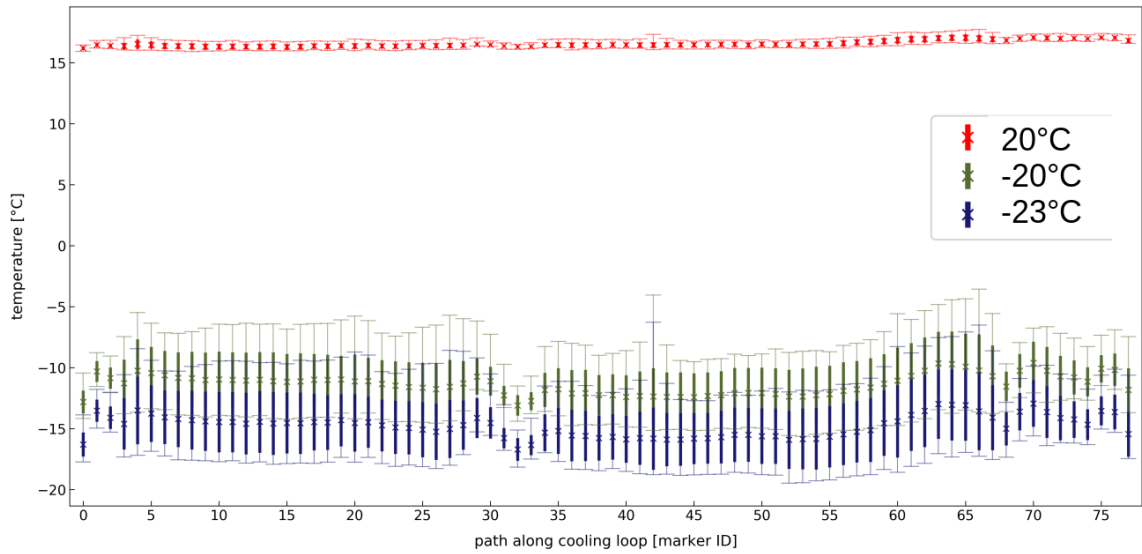


Figure 5.9: Analysis on each linear marker performed on a petal core, front side, at  $T_{CO_2} = -23^\circ\text{C}$  (blue),  $-20^\circ\text{C}$  (green),  $20^\circ\text{C}$  (red). Each marker reports the temperature average (cross), the standard deviation (thick bar) and the span (thin bar).

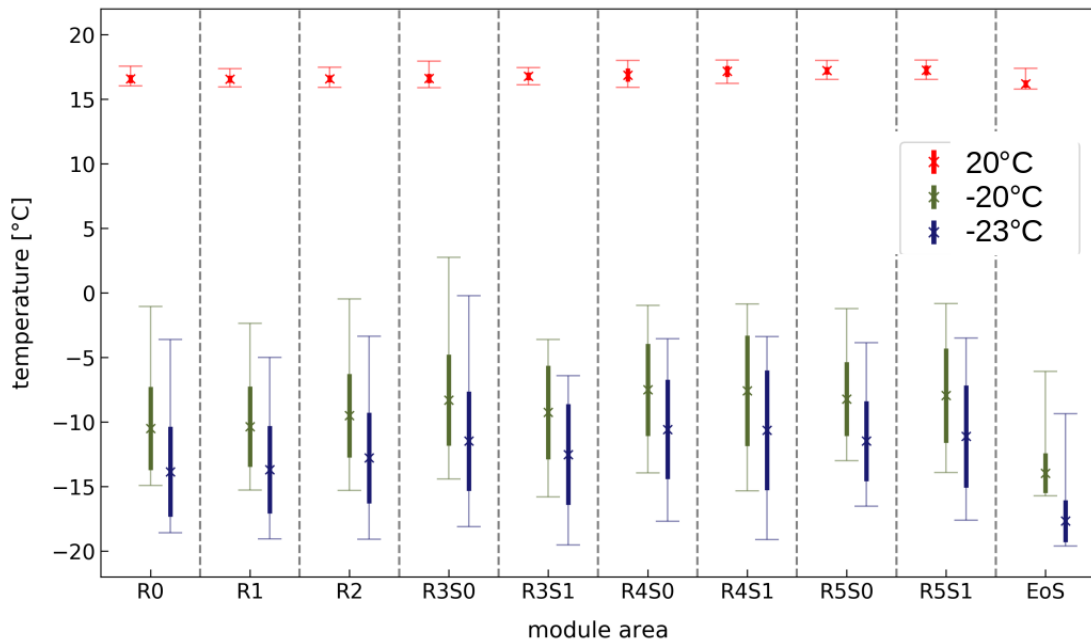


Figure 5.10: Analysis on polygonal markers performed on a petal core, front side, at  $T_{CO_2} = -23^\circ\text{C}$  (blue),  $-20^\circ\text{C}$  (green),  $20^\circ\text{C}$  (red). Each marker reports the temperature average (cross), the standard deviation (thick bar) and the span (thin bar).

## 5.2 Module on core placement procedure

Electrical modules that successfully pass all QC tests, as explained in section 4.3, are shipped to module loading sites where they are glued on cores, which passed their QC tests too. This section is focused on the module loading technique and how to achieve the requirements in terms of precision and functionality. The correct placement of modules on the core is a crucial step for the full detector as it determines the local hermiticity of the active area.

Firstly, arguments on the petal design about the loading precision are given to justify the requirements, then a brief description of the experimental setup mounted in an ISO6 cleanroom is provided and finally the procedure developed to load modules on the core is explained.

**Physical requirements for the module loading accuracy** Specifications of the module placement are required to firstly avoid collisions between neighbor modules, for HV clearance ( $\sim 500 \mu\text{m}$  as inter-module space) and for the global overlap and hermiticity requirements of the detector which are looser than the inter-module spacing. The loading tolerance is also connected to the stereo angle of the silicon sensor's strips. The endcap sensors are designed with strips radially distributed and pointing few degrees away from the beam axis, directed to F point in figure 5.11. The sensor layout is chosen to cover the petal with active strips, minimising the dead space such as guard rings and physical gaps between sensors. The required placement precision allows also the achievement of the stereo angle of  $\varphi=40 \text{ mrad}$  between silicon strips mounted on the opposite sides of the same core, as discussed in

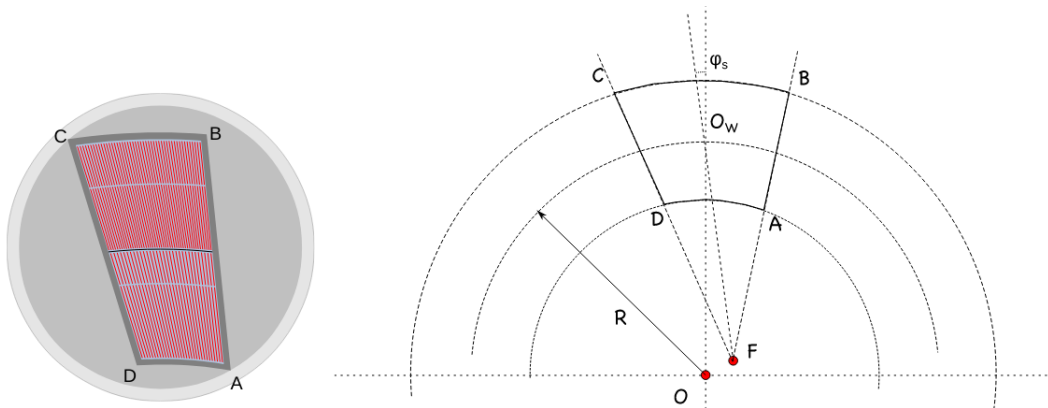


Figure 5.11: Strip orientation in an endcap silicon sensor compared to the beam line [58].

Requirements	value
Placement accuracy	$\pm 50 \mu\text{m}$
Glue thickness	$(150 \pm 50) \mu\text{m}$
Glue coverage	60% - 90%

Table 5.2: Specification required for loading the endcap modules on the local support structure [86].

section 2.3.4. Finally the specifications for the module on core procedure are listed in table 5.2 [86]. The reason for such a tight placement accuracy has been previously given, while the specifications required for the module gluing are explained in section 5.2.3.

### 5.2.1 Experimental setup

In order to place and glue modules on cores, the following equipment is required in the cleanroom:

- *Aerotech gantry system* (AGS10000)[87] is the robot used to pick and place modules with a precision of  $5 \mu\text{m}$  making use of custom tooling and custom dedicated software;
- *Ultimus V Nordson EFD* glue dispenser [72] to automatically apply the appropriate glue patterns on the core for the gluing of electrical components;
- *COGNEX In-Sight 8000* [88] camera with automated pattern recognition capabilities;
- a 3D laser (SmartRay ECCO 55.050) [89] for post-mounting metrology;
- *National Instruments DAQ 9476* [90] switcher for automated control of vacuum and pressured air;
- LEDs for sensor and core fiducial illumination;
- mechanical tooling: assembly frames to hold the core in place on the gantry table and a vacuum jig to hold all module flavours before loading. Vacuum pickup tools are used to pick modules from the jig and move them on the core.

Figure 5.12 shows the gantry robot with all the tools and devices needed to load modules in a cleanroom environment.

The goal of this activity is to get an automated placement procedure which picks and places each module on petal cores within a lateral accuracy of  $\pm 50 \mu\text{m}$  in x and y direction. The z coordinate is controlled by spacers used to define the thickness of

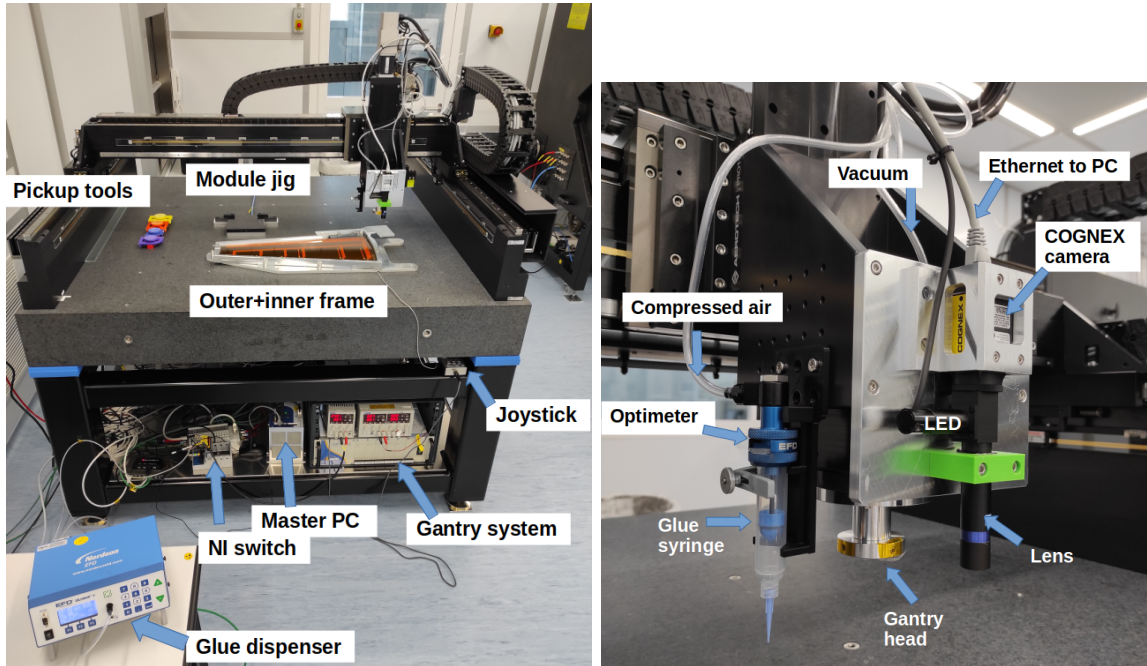


Figure 5.12: Full setup used to load modules on the petal core and zoom on the tools attached to the gantry arm (glue syringe, camera and laser).

the glue applied for the module mounting.

This procedure is achieved through the following steps:

- position finding of petal core and modules on the global reference system of the gantry table using the camera to measure the fiducials;
- manual spacers application and glue dispensing on the local support following a defined pattern;
- placement of modules and EoS in the correct position on the petal core;
- quality control test to check the accuracy of the assembly and the electrical performances of the modules.

All these steps are described in the following.

### 5.2.2 Camera offset

An important parameter that needs to be addressed before starting the placement is the camera offset, defined as the distance in the XY plane between the gantry head (center of rotation and translation) and the central axis of the camera, attached to it. The precision of this value can significantly affect the accuracy of the placement. The camera offset value is at first roughly estimated by measuring it with a rule

and it is then fine measured with the following procedure. A random spot, located roughly in the center of a sensor and used as reference, is measured with the camera. The sensor is picked up on this exact point and rotated by  $180^\circ$ . The reference point is measured again and the deviation from the pre-rotation position is added to the rough offset value. The process is iterated a few more times until the difference becomes less than  $10\ \mu\text{m}$ . The camera holder was made of metal to provide a stable mechanical support avoiding any movements of the camera during the module placement, which implies the offset value change.

A good practice is to check the offset value every time a loading of real modules is scheduled or when the precision of the machine has to be verified.

### 5.2.3 Glue pattern for modules

An important feature of the loading method that needs to be carefully studied is the glue pattern. The glue application on the petal core is the first step of the loading procedure and has to satisfy the following requirements:

- the glue has to cover between 60% and 90% of the sensor area, important to provide a reliable mechanical support on the core and a high thermal contact between the silicon and the support structure;
- the nominal glue thickness is  $(150\pm 50)\ \mu\text{m}$  to absorb the maximum module bow and local support surface tolerance in the glue. The correct thickness is provided by the application of polyimide spacers on the core at each pickup tool foot location. The maximum average spacing between the sensor and the local support that is allowed is  $200\ \mu\text{m}$  in order to include the module bowing above the spacers. The specification requires a maximum module flatness deviation of  $-150\ \mu\text{m}$  and  $50\ \mu\text{m}$  for a concave and convex module shape respectively, as explained in section 4.3.1.

The glue required to mount the modules is *Dow Corning Thermal Interface Material SE4445* [91], it is provided in two components to be mixed by weight in 1:1 ratio. It is a thermally conductive silicone gel. Once the two glue components are weighed and properly mixed, the glue is moved into a syringe that is held on one side of the gantry arm by a customized 3D printed holder. An optimizer is used to increase accuracy and consistency through precise mechanical regulation of air pressure and volume as the piston travels. It automatically increases airflow as the syringe barrel empties for optimal throughput. During the glue tests a reasonable working time span of the glue was found due to its viscosity variation: the glue dispensing output

is optimized in the first 20 minutes after the mixing, afterwards the glue becomes very viscous and it is no longer possible to dispense it with this method.

The software combines the gantry movement with the glue dispenser function using a I/O connector and sets the air and vacuum pressure lines. Depending on the module to load, the glue is spread on the petal surface following a specific pattern. After several trials with dummy silicon sensors the pattern was optimized to achieve the required glue thickness and coverage: the strategy chosen for it is to apply many thin lines to avoid mechanical stress of the sensor when the gantry pushes it down spreading the glue and to allow ways out for the air.

The glue pattern design was developed for the R0 module and it was easily adjusted to all the other modules. The common features of the pattern are keeping the glue lines 5 mm away from each sensor edge and the distance between lines to be 3.4 mm. The satisfactory pattern is achieved using 4 bar as air pressure and 1" H<sub>2</sub>O as vacuum, a plastic tapered smooth-flow tip with 0.25 mm opening and a gantry motor speed set to 60 mm/s. These variables were studied by measuring the thickness of glue lines dispensed at different pressure and speed. The line that was closer to the required glue thickness was chosen as reference for the pattern.

The glue thickness is provided by 120 μm thick polyimide adhesive tape used as spacers, placed on the petal core surface just underneath the feet of the pickup tool. The purpose of those is to ensure that, when the module is loaded and the glue is compressed, the spacers define the minimum height of the module with respect to the local support. The spacers are placed on the core together with a tape used as mask in order to keep clean the area from the dispensed glue. The glue pattern was studied by placing a transparent adhesive foil on a petal core and gluing glass sensors. Figures 5.13 show the glue dispensed on the petal core before and after

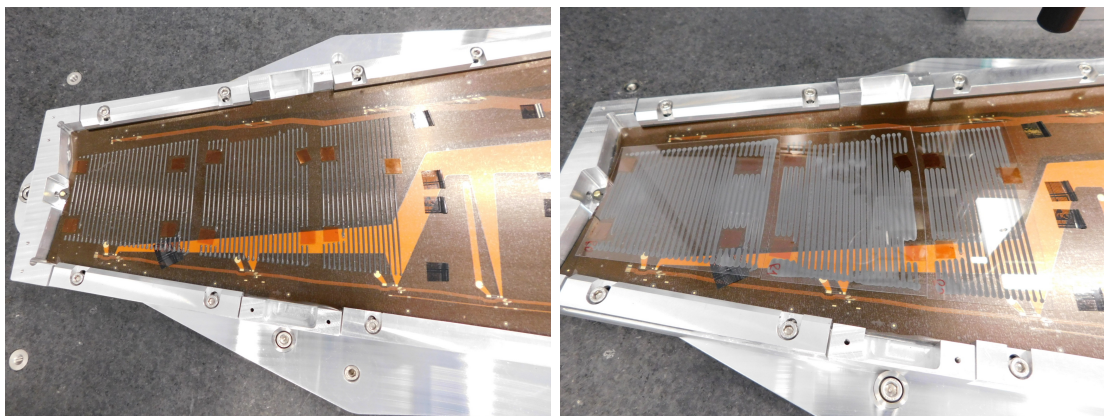


Figure 5.13: Glue pattern dispensed on the core (left side) tested with glass sensors to check the coverage after the compression of the glue (right side).

the glass placement. Here polyimide spacers and the mask are also visible in orange and black respectively. The test was also performed dispensing glue with a different aging. On R5S0 location a newer glue was used and a higher coverage was found using the same dispensing settings, as shown in figure 5.14. A different behavior of the viscosity was observed, which increases as function of glue aging. To get again the required coverage, the speed motion of the gantry arm and the opening of the tip can be optimized, according to the glue viscosity.

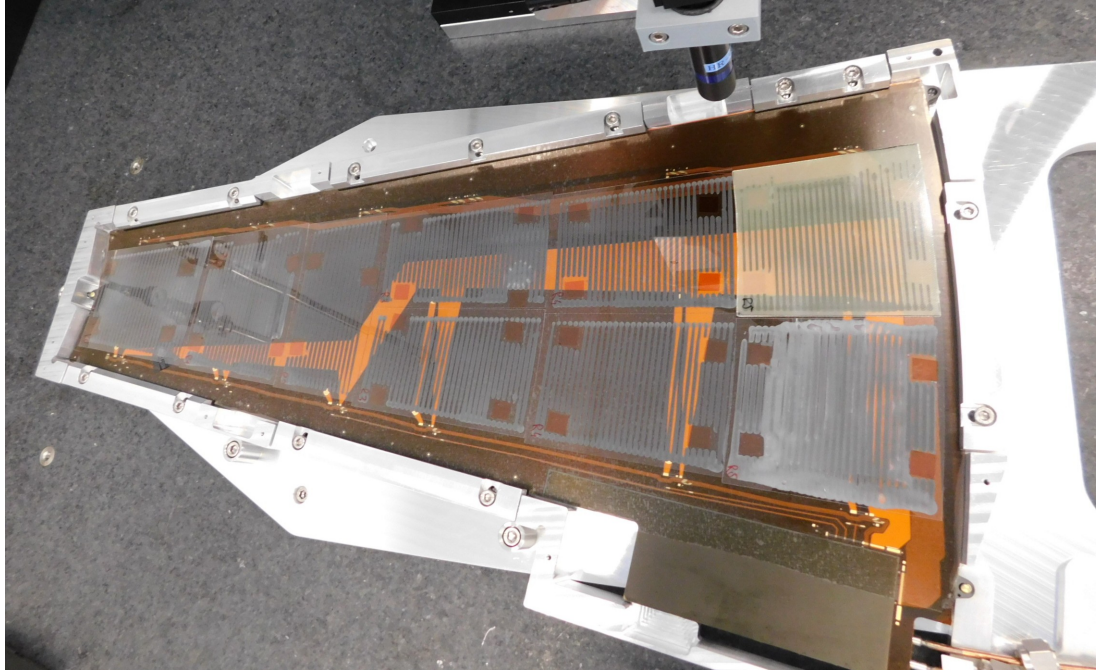


Figure 5.14: Fully loaded petal with glass sensors to check the glue pattern and the coverage after compressing the glue. In R5S0 a higher coverage is obtained due to the use of a newer glue.

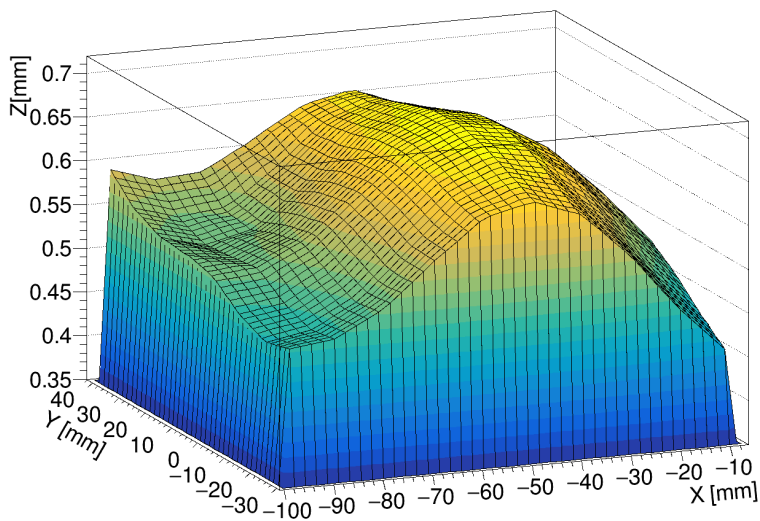


Figure 5.15: Metrology measurements on the R0 glass sensor after gluing, the values on the Z axis take into account the glue and the glass thickness ( $320\ \mu\text{m}$ ).

Smartscope measurements on the R0 glass sensor after the gluing on the petal core are shown in figure 5.15. The glass assumed a convex shape and the height average is  $(575 \pm 89) \mu\text{m}$  which includes also the glass thickness ( $320 \mu\text{m}$  as nominal value). Therefore the glue thickness is  $(255 \pm 89) \mu\text{m}$  that respects the requirements within the standard deviation error. For this result it is necessary to highlight that in general an electrical module is stiffer than the glass used for this test because of the presence of its glued components and its bow is concave, as explained in section 4.3.1. Therefore the gantry, during the gluing, pushes the module bowing in the opposite direction decreasing it.

Finally the optimized glue pattern, tested with glass sensors, demonstrated that the requirements in terms of glue coverage and thickness are achieved. The thermal performances of the glue pattern was checked performing electrical tests on the semi-electrical petal, in which the modules were mounted using this pattern, it is explained in section 5.3.

#### 5.2.4 Module placement

Another aspect of the placement procedure concerns the module recognition using the sensor fiducial marks, the latest version of the software uses the type *K* (a description about that is given in section 3.1.2). The module is placed on a vacuum jig, designed to be suitable for all endcap module flavours. It is used to keep the module in place during the measurement of the camera over the fiducial marks, three on each curved edges, in order to identify its position and orientation on the gantry table. For the same purpose the camera moves checking also the petal core position looking at its two fiducial holes ( $300 \mu\text{m}$  large), located next to the two locator holes as described in 3.1.1. The camera is able to recognize automatically all fiducials, circle and *K*, fits its shape and define the position of the center used as reference. The camera needs a training to be able to recognize the pattern of each fiducial; it is achieved through the software provided by the company, *In-Sight Explorer 5.7.3*. The petal core is placed in a metallic assembly frame (or also called inner frame), held all around its edges to guarantee the maximum stability. This frame is then located on an outer frame, screwed on the granite table. Three LEDs are implemented into the outer frame to light the fiducial holes from the bottom when the core is placed on its front and back side. Three aligning pins are used to place the inner frame correctly on it, pushed against them.

After the module and core recognition, the module is moved from the jig to the petal core using the proper pickup tool. Four designs are needed to load all nine modules due to their geometries. The tool touches the sensor on four feet where

rubber O-rings are inserted in a circular slot machined on each foot to get a softer touch avoiding damages of the silicon and improve the vacuum socket.

Each module is placed in an exact location on the local support structure with respect to the two fiducial holes in the petal system. The local origin of coordinates is coincident with the center of the inner one and the x axis,  $\widehat{X}_{Local}$ , runs along the petal center line. The relative position of the modules can be found on the CAD files and it has to be roto-translated in the global coordinate system of the gantry to allow the robot to place the module correctly. A representation of the coordinate systems is shown in figure 5.16: in red the global coordinate system, centered in the top-left corner of the table, in cyan the local coordinate system, centered in the inner fiducial hole. The orange line connects the two petal fiducial holes and it is rotated by  $12.6^\circ$  from  $\widehat{X}_{Local}$  provided by the core design, as shown in figure 3.4. The following equation is used to translate the coordinates from the local coordinate system to the global system:

$$\begin{cases} X_{Global} = X_{Local} \cdot \cos(\alpha) + Y_{Local} \cdot \sin(\alpha) + X_0 \\ Y_{Global} = -X_{Local} \cdot \sin(\alpha) + Y_{Local} \cdot \cos(\alpha) + Y_0 \end{cases}$$

$$\alpha = \arctan\left(\frac{Y_1 - Y_0}{X_1 - X_0}\right) \pm 12.6^\circ$$

where

- $\alpha$  is the angle between the *Gantry* and *Petal* coordinate systems,
- $(X_0, Y_0)$  and  $(X_1, Y_1)$  are the coordinates of the inner and outer petal fiducial hole centres respectively to allow the translation of the origin,
- the angle  $12.6^\circ$  is negative on the front petal side and positive on the back one.

Those coordinates are measured by the camera, therefore the offset has to be subtracted from them.

After the single module is placed on the petal core, the pickup tool and the gantry arm are kept in place for roughly 15 minutes to wait for a first glue curing stage.

Finally the relative position of the modules on the petal core is checked to define the accuracy of the placement. This survey is done by measuring the position of each of 10 K fiducial marks on the sensor with the camera and evaluating the distance from the nominal position. This final measurement defines the precision of the module loading. A second survey of the modules is performed with an independent system as part of the QC and is described in section 5.4.2.



Figure 5.16: Sketch of the gantry table, top view, with focus on the global (in red) and local (in blue) coordinate systems.

### 5.2.5 EoS card placement

The EoS is glued on the core before the modules as it has less fragile components. The glue is dispensed on core in the same way as explained for the modules, but the  $120\ \mu\text{m}$  polyimide spacers have a strip shape. The alignment of the card needs to allow the wire-bonding of the EoS to the bus tape. The rigidity of the card (1.6 mm thick) plus the existence of mechanical positioning pins allows for a reliable manual placement of the board without the need of automation.

For the EoS master, the main card is glued first and the two DCDC boards afterwards to allow a better alignment of their bonding pads. The VL+ chip is connected also afterwards to the card for the electrical tests.

### 5.2.6 Touch-down function

In order to get a controlled touch-down of the pickup tool's feet onto the module a touch-down function is implemented in the code. This function uses a *Current Feedback* that the gantry provides. It is given by a piezo-electric device that translates mechanical force into electrical current. The z motion is performed for a total distance of 3 mm, moving at  $0.225\ \text{mm/s}$ , in which the contact point has to be found. The motion stops when two consecutive current drops are greater than the established threshold. The threshold is set to 0.11 A, chosen after a trial error method where the touch-down function was successful and the vacuum correctly applied.

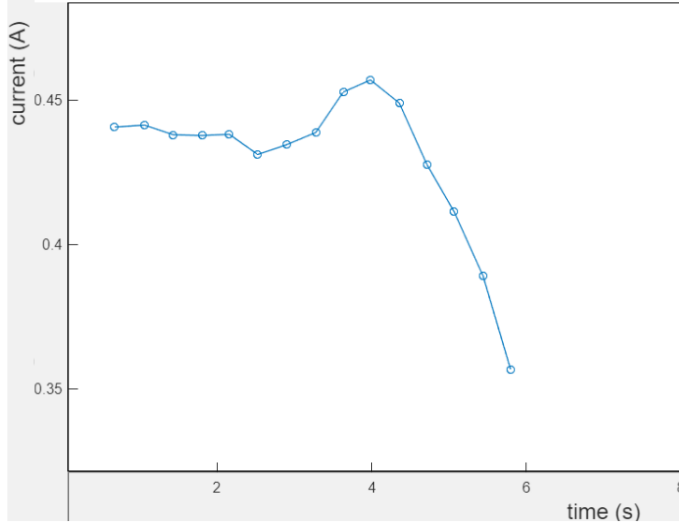


Figure 5.17: Current trend as function of time during the touch-down function used to find the point of contact between the pickup tool and the sensor and between the sensor and the core.

The plot in figure 5.17 represents the current behavior as function of time during the touch-down function: the current is measured each 0.3s and the drop comparison starts after 5s to let the vertical acceleration to stabilize. The small peak before the current drop is due to the initial contact with the sensor in which an external resistance is felt by the gantry before pushing on it [92].

The touch-down function is called twice during the full loading process: when the pickup tool goes down on the module placed on the vacuum jig and when the module is placed on the petal core. After the contact point that satisfies the function is reached, the  $z$  value is stored and used for the following times that the height value is required.

Another option instead of using the O-rings was the suction cups. In that case the touch-down function showed that the contact between module and suction cups is very smooth and the feedback current does not provide a significant drop because they are too soft to trigger a clear trend.

### 5.2.7 Software for the loading

The software that controls the whole loading procedure is developed in MATLAB GUI and it was developed by TRIUMF [93]. The code controls the gantry motion, the dispenser and the vacuum/air lines and it was optimized in order to achieve the best loading performances. It includes all the module placement's steps and allows to choose between different options: gluing, placement, survey. It requires little human intervention during the whole procedure. Figure 5.18 shows the graphical user interface (GUI) of the software when the R1 module is chosen for the loading on the core, front side, and a  $K$  sensor fiducial is fitted by the camera automatically. The

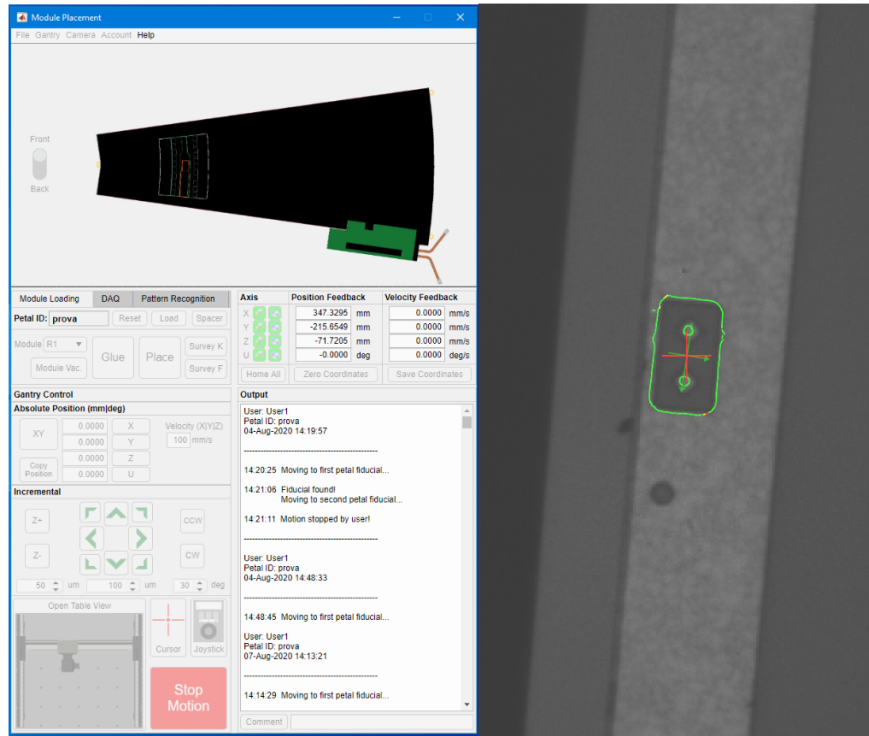


Figure 5.18: Matlab GUI interface of the module loading software and fit to a  $K$  sensor fiducial marker by the camera.

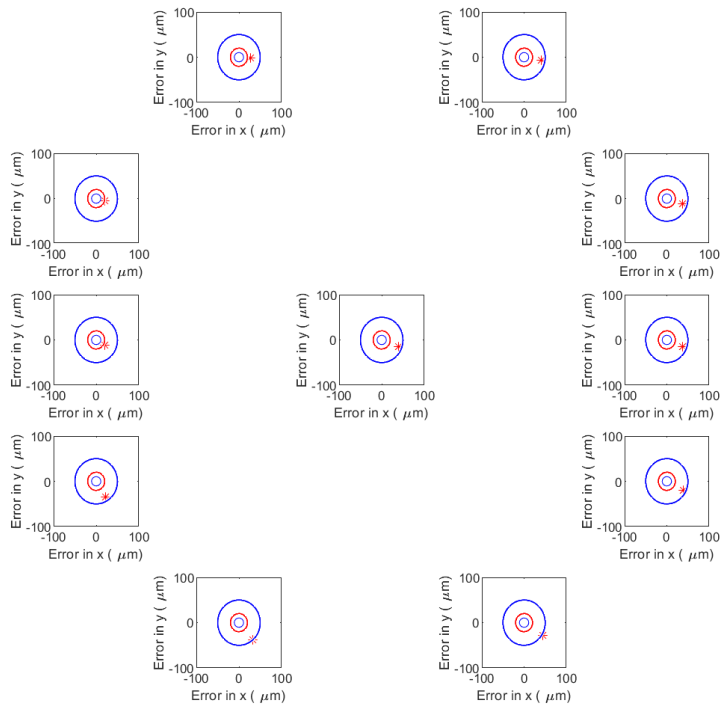


Figure 5.19: Result of a module placement after fitting 10x  $K$  fiducial marks.

red hair cross indicates the point used as reference to measure the fiducial position. The result of the survey of all 10  $K$  fiducials is shown in figure 5.19: the red circle indicates a 25  $\mu\text{m}$  discrepancy with the nominal position and the blue one 50  $\mu\text{m}$  discrepancy which is the maximum accepted. The plot in the middle corresponds to the sensor centre position calculated making use of the measured  $K$  markers, as explained in section 3.1.2.

The gluing and placement procedure, as explained in this chapter, were tested repetitively using mechanical components providing promising results. The conclusive check to confirm the readiness of the apparatus was performed with electrical components, as for the case of the semi-electrical petal, explained in the following section.

### 5.3 Semi-electrical petal

DESY is one of the four endcap module loading sites of the ITk strip collaboration. To test the assembly procedure, in January 2020, a petal was built with semi-electrical modules provided by different institutes. Those modules were assembled with the prototyping version components, *ABC130*. The silicon sensors were mechanical, while the read-out and the power electronics were fully functional. The only exception was for R0 module, which had an electrical sensor. The modules arrived at DESY fixed on their own test-frame and a reception test was required in order to confirm its status after shipment. A visual inspection was performed under the microscope, in particular to observe the wire-bonds status, the basic electrical tests were performed and results were compared with the ones obtained at the building institutes before shipping. In table 5.3 the origin of each module used for the loading is listed.

The loading of the back side of the petal core started with the manual placement of the passive board which mimics the EoS Slave card not available at that time, collecting the read-out data from each hybrid and streams the power and commands to the ASICs. The full assembly lasted roughly five hours. The biggest time-limiting

Module	Manufactured by
Fully-e R0	DESY-Zeuthen
Semi-e R1	Uni of Freiburg
Semi-e R2	Uni of Freiburg
Semi-e R3	Uni of Toronto
Semi-e R4	DESY-Zeuthen
Semi-e R5	Valencia (IFIC)

Table 5.3: Origin of each module that was loaded on the petal core.

factor was the glue curing time of each module (15 minutes), in which the gantry arm is kept in place. The glue was mixed five times in total, 10 g each, needed to dispense the pattern for two modules at the time (one in case of split modules). It started with R5 module, S0 portion first and then S1, as well as the placement. The only R0 module was glued alone. The glue dispensing order and curing timing is reflected into the out of plane measurements that is explained in the section 5.4.3. The loading order, from R5 to R0 module, was decided to keep the only electrical sensor, R0 one, in the nitrogen cabinet as long as possible. The loading order of a fully electrical petal has to be thought according to the disposition of the modules on the gantry table to avoid passing several times on top of them.

Roughly 5 g out of 10 g of the mixed glue amount was dispensed for two units. A part of it is lost into the mixing cup and filling the syringe with more glue than needed is important to avoid a sputter of glue over the petal core and next to modules when the syringe is getting empty.

In this petal the R0 module was the only one having the HV tab, as it was built with an electrical sensor. The HV tab is needed to provide the HV to the back plane of the sensor and it is connected to a specific pad on the bus tape. The official method to do it is bonding the tab to the pad. This technique was still under study at the time of the construction of the semi-electrical petal and the HV tab was connected using a conductive glue (Silver Epoxy) between the tab and the bus tape pad to

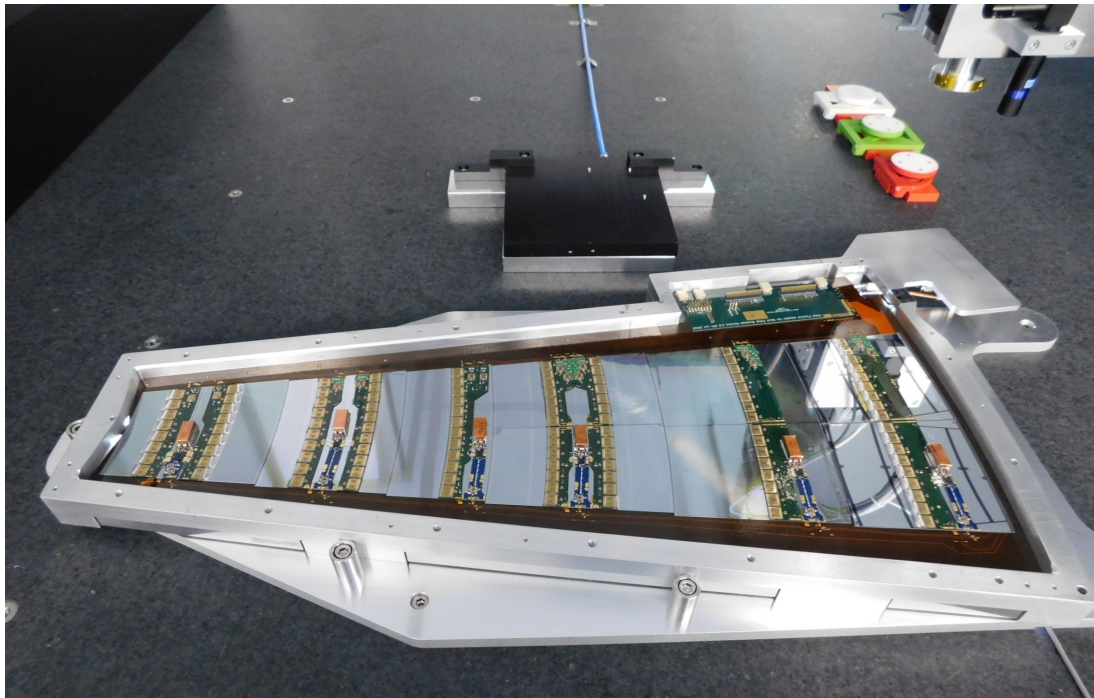


Figure 5.20: Semi-electrical petal built at DESY in January 2020.

provide the electrical connection.

The semi-electrical petal at the end of the loading is shown in figure 5.20.

## 5.4 Quality control on Petals

The QC check is the step required to define the final status and the performance of the assembled object. These tests determine the petals as ready for insertion in the endcap, or stored for reworking if needed and possible. A ranking scale is determined by the ITk collaboration depending on the quality of the petals [94]. A 10% more of the required components is produced to take into account possible irreversible failures during production. The QC tests on a loaded petal can be summarized as:

- glue amount check for material budget calculation;
- final sensor fiducial marks survey to define the precision of the module placement;
- out of plane measurement to measure the thickness of the glue layer;
- electrical test to confirm the correct functionality of all modules.

The following analysis is focused on tests performed on the semi-electrical petal built at DESY.

### 5.4.1 Glue amount

A rough estimation of the total amount of glue needed to load one core side with six modules can be obtained as follows. The density of the SE4445 glue is  $2.36 \text{ g/cm}^3$ , the nominal glue thickness is  $150 \mu\text{m}$  and the 80% of the sensor surface coverage is listed in table 5.4 for each module, therefore the total glue amount is estimated to be 22.3 g. This value matches with the amount used for the loading of all six modules, roughly 5 g used for each two units, plus 2.5 g used for the R0 module glued individually.

### 5.4.2 Final Survey on sensor fiducial marks

When the module is placed and glued on the core, the sensor fiducial survey is performed twice using the camera attached to the gantry:

- after the first minute from the placement: in case the error is found to be larger than  $20 \mu\text{m}$  fixed by the user ( $\sqrt{\Delta x^2 + \Delta y^2} > 20 \mu\text{m}$ ), there is the possibility to fine tune the module position. Once in contact with the glue after the

Module	80% Sensor area [cm <sup>2</sup> ]	glue [g]
R0	73.5	2.6
R1	72.8	2.6
R2	60.8	2.1
R3	65.6	4.6
R4	71.5	5.1
R5	74.4	5.3
		22.3

Table 5.4: Estimation of the total SE4445 glue amount needed for module on core to populate one side.

placement the module can be moved again in x and y, to get closer to the nominal position. This option also helps the glue to be more spread under the sensor;

- after 15 minutes from the first survey, when the glue is almost completely cured, this survey establishes the final precision of the loading.

The F fiducial markers are used for the loading of modules on the semi-electrical petal, as well as for the survey, due to the absence of the K markers on those mechanical sensors. Figure 5.21 shows examples of the F fiducials, they have different shapes and dimensions because the silicon wafers were produced by three companies using different fiducial mark versions: *Hamamatsu* (which produced R0 sensor), *CNM* in Barcelona (R5 sensor) and at *Simon Fraser University (SFU)* in Vancouver (from R1 to R4 sensors).

The green line around the marker indicates the successful pattern recognition performed by the camera and the cross hair identifies the position chosen as reference point for the survey. The result of the survey on all 4x F fiducials on the R0 module is shown in figure 5.22: here again the red circle sets the 25  $\mu\text{m}$  limit and the blue

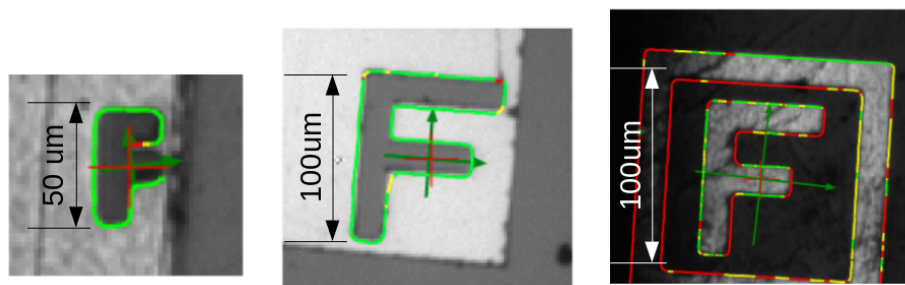


Figure 5.21: Examples of F sensor fiducials fitted by the camera.

one indicates the  $50\ \mu\text{m}$  accuracy.

The final accuracy of the placement achieved in the semi-electrical petal is  $(-8\pm 18)\ \mu\text{m}$ , as shown in the histogram in figure 5.23. The few entries on the left-hand side of the histogram at  $-80\ \mu\text{m}$  and  $-50\ \mu\text{m}$  are due to modules having broken corners already before the loading due to the particularly fragile nature of the silicon dummy sensors. Those corners were re-glued to the sensors that caused the fiducial positions to change. This is the case of R1, top left corner, R4S0, top right corner and R4S1, bottom left corner.

A second check needs to be performed using a different device to have a second survey performed with a different device allowing for a cross calibration. The Smartscope was used in this case, which also has a similar precision. The result of this survey is  $(-29\pm 33)\ \mu\text{m}$ . Both measurements can be considered as comparable within their

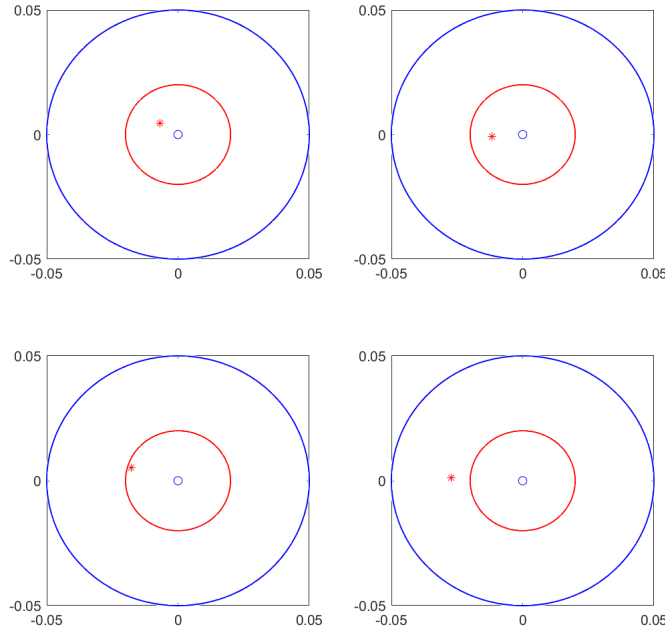


Figure 5.22: Survey result on the  $F$  fiducials after the placement of the R0 module on the core.

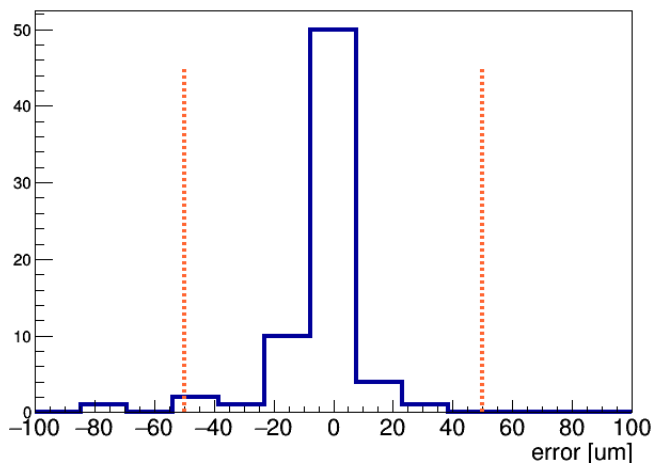


Figure 5.23: Module placement error of the semi-electrical modules, measured when the glue was fully cured. Red dashed lines indicate the required range of accuracy.

errors, but the main and substantial difference concerns the fiducial finding. While the camera is able to automatically find the position of the reference point by the pattern recognition implementation, the same point is measured manually with the Smartscope by moving the lens with the joystick. This means that the survey done with the camera is more reliable. The newer Smartscope's software allows for a pattern recognition too, but it was not implemented in the metrology routine at the time.

### 5.4.3 Metrology measurements

Once the loading is completed and the survey is done, a quick test concerning the module flatness can be performed using an additional laser device, also attached to the gantry arm, having a Z resolution of 13-27  $\mu\text{m}$  and a field of view of 69 mm. The SmartRay 3D sensor measures distances based on the laser triangulation principle. It measures the profile of the object, and scanning the object renders a 3D model of the object.

A scan on a R0 mechanical module is shown in figure 5.24 where hybrids, ASICs and wire-bonds are distinguishable. The software provides the 3D profile as well as the cloud of points to allow a deeper analysis. Those measurements include all module's components, but the laser shows an unreliable capability to measure reflective surfaces such as the sensor. Its resolution is not good enough to define the out of plane measurements for petals of few hundreds of microns, but it could be used for different purposes which do not require high resolution.

A more in-depth metrology on the fully loaded petal is performed using the Smartscope, which has a precision of  $\sim 1 \mu\text{m}$ . The grid projector function also helps to measure reflective surfaces, as described in section 4.3.1. Metrology measurements on modules are performed to establish the flatness, as defined in equation 4.3.1, the

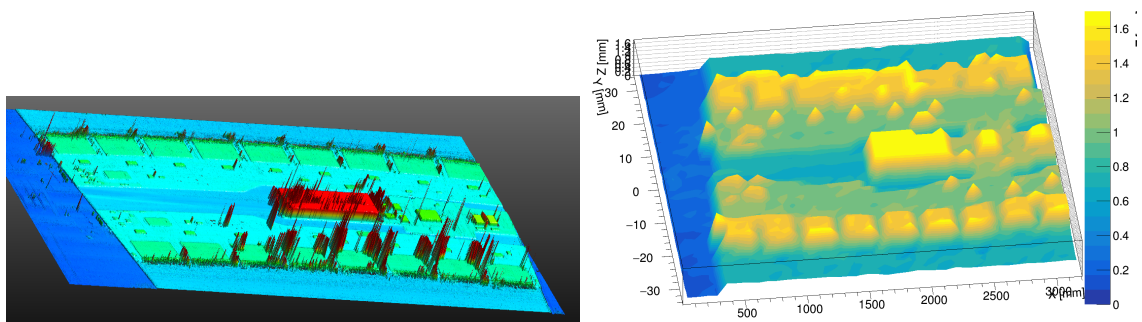


Figure 5.24: Laser measurements on a R0 module. Left side: profile provided by the software. Right side: 3D plot built using measured points.

out of plane and therefore the glue thickness considering a sensor  $320\ \mu\text{m}$  thick. Figure 5.25 shows the semi-electrical petal placed on the Smartscope glass and a grid of points is measured on all sensors excluding the hybrid and power-board areas and plotted in figure 5.26 in the xy plane. The same measurement is shown in the xz plane in figure 5.27 to observe the shape of the sensors after the placement.



Figure 5.25: Semi-electrical petal placed on the Smartscope glass for metrology measurements

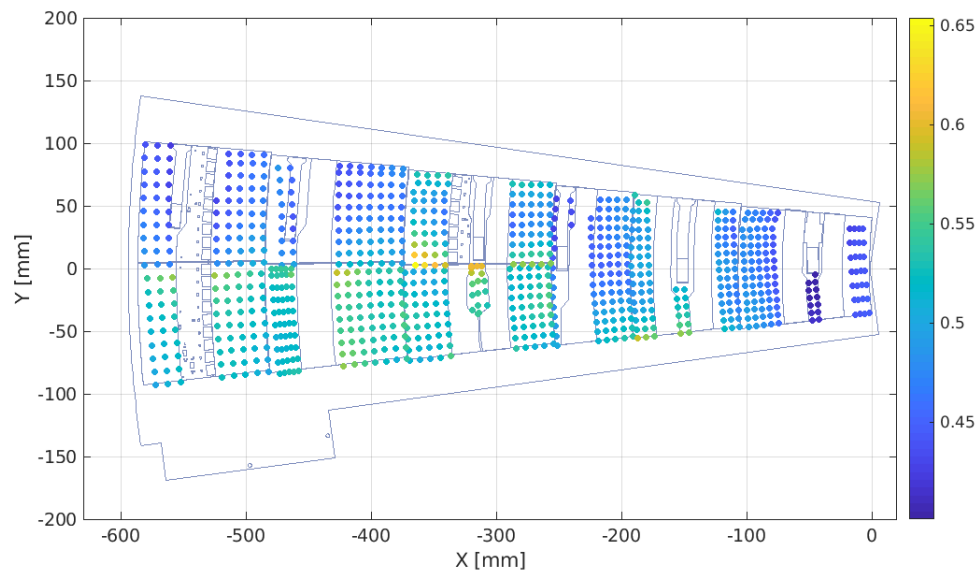


Figure 5.26: Metrology measurements performed on the semi-electrical petal. The z values include the sensor thickness ( $320\ \mu\text{m}$ ) and the core is used as reference plane.

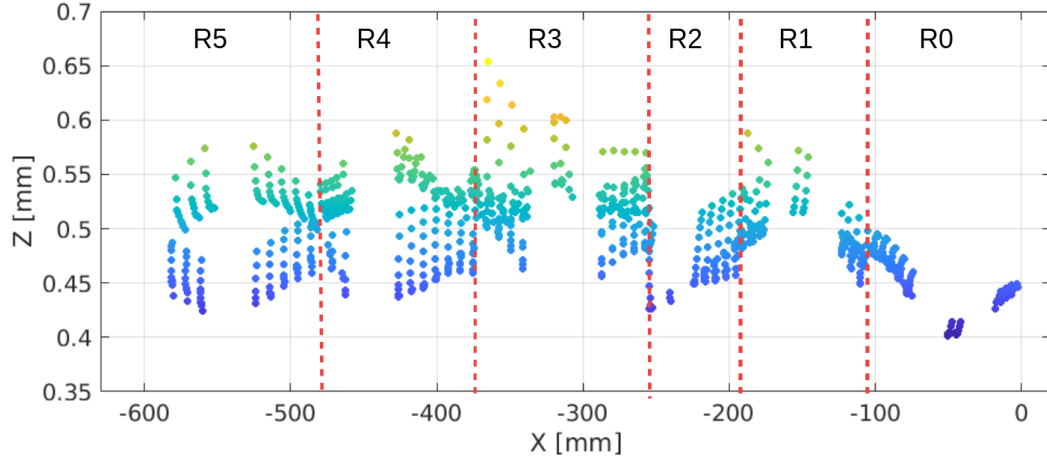


Figure 5.27: Metrology measurement on the semi-electrical petal shown in the  $xz$  plane.

Table 5.5 lists the number of points, the flatness value and the glue thickness obtained for each module, more than 800 points were measured on the sensors for which the core surface is used as reference plane. Looking at the glue height values the module loading order can be understood: the S0 part of the module are always lower than the S1 part because they were placed as first after dispensing the glue for both. The S1 part of the same module were placed after roughly 30 minutes during which the glue started already to cure and therefore it appeared to be less compressed. This observation is confirmed also by looking at the points distribution in the plot in figure 5.27. Therefore the out of plane measurements of the S1 split modules show that, considering their errors, they are close to the maximum accepted glue height of

Module	Points	Flatness [ $\mu\text{m}$ ]	Glue height [ $\mu\text{m}$ ]
R0	122	70	$133 \pm 24$
R1	106	95	$179 \pm 28$
R2	99	59	$154 \pm 26$
R3S0	100	193	$194 \pm 46$
R3S1	92	102	$204 \pm 21$
R4S0	114	77	$151 \pm 21$
R4S1	89	74	$215 \pm 16$
R5S0	65	45	$141 \pm 20$
R5S1	72	49	$206 \pm 18$
Global	859	239	$176 \pm 39$

Table 5.5: Values of flatness and glue thickness for each semi-electrical module loaded onto the petal.

200  $\mu\text{m}$ . R3 module (specially S0) was particularly bent already before loading and it is understandable observing its flatness value and again the plot in figure 5.27. It is important to mention that the semi-electrical modules were assembled with mechanical silicon sensors. The manufacturing process of a mechanical sensor is different compared to an electrical one, even though they have the same thickness. This affects the stiffness and rigidity of the module, as well as the fragility. A more realistic check has to be performed with electrical modules.

#### 5.4.4 Electrical test

The same sequence of electrical tests performed on the single module, previously described in section 4.3.2, were run on the petal. The petal was placed in a big ESD safe plastic enclosure flushed with dry air to keep the humidity as low as possible because of the R0 electrical sensor. A water chiller was used for cooling purpose and the tubes were attached to the petal pipes. The read out chain, as shown in figure 5.28, includes:

- two SLVSs: *Scalable Low-Voltage Signalling* used as signal converters. They collect data from R0 to R3 and from R4 to R5 modules;
- Digilent Nexys FPGA board;

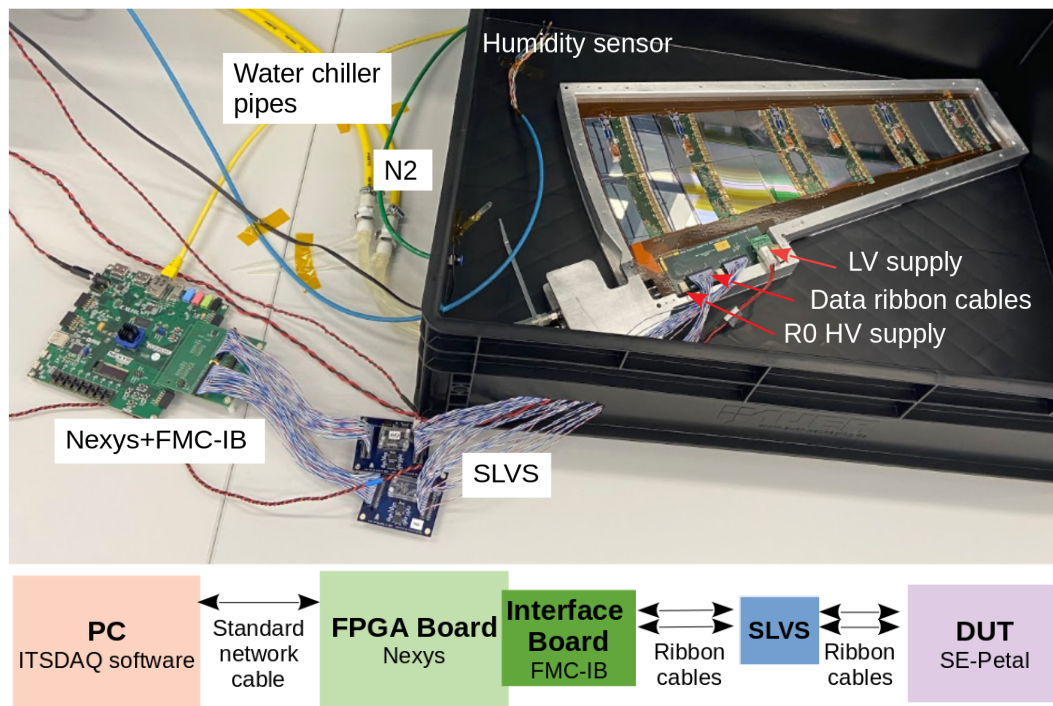


Figure 5.28: Testing setup and readout chain of the semi-electrical petal.

- one FMC-IB: *FPGA Mezzanine Card-Interface Board* to connect the ribbon cables to the FPGA;
- one HV cable to bias the electrical R0 sensor.

During the electrical test of the petal, the chiller was always operated at 8°C, the lowest temperature allowed by the chiller. The current of each module, read out by the power supply after they were individually configured is reported in table 5.6 and plotted in figure 5.29. Every module produced a current proportional to its number of ABC chips. R0 module produced a lower current compared to the general module behavior, the current discrepancy was not well understood. The HCCs in the R2 module read out the smallest number of front-end chips, six ABCs each. This could explain the slightly higher current measured on this module. The current value measured after the configuration of the full petal is in agreement with the previous linear trend of single module current.

Module	ABC chips	HCC chips	ABCs per HCC	Current [A]
R0	17	2	8/9	1.84
R1	21	2	10/11	1.90
R2	12	2	6	1.84
R3	28	4	7	1.95
R4	16	2	8	1.86
R5	18	2	9	1.87
TOT	112	14		2.40

Table 5.6: Summary of endcap module chips and current values measured by the power supply after the individual module configuration.

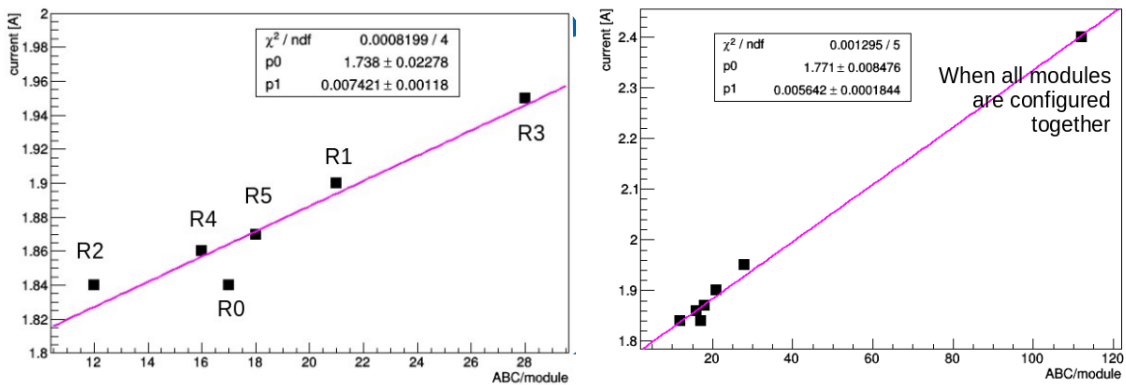


Figure 5.29: Low voltage current values as function of number of ABC 130 chips, after the individual configuration of the modules. A zoomed view is provided on the left side.

After some debugging and configuration settings needed to get the output from all the modules and to improve the results, the whole petal was responding correctly and functional. The comparison of the module's functionality before and after the loading is a valid investigation to prove that the core population was successfully done. The connections of the front-end chips to the sensor strips on the R0 module affects the input noise measurements, as explained in section 6.4.4. Therefore its noise is higher than the value measured on the other semi-electrical modules. In the following there is the report about the status of every module tested with the water chiller set to 8 °C:

- R0 was tested with high voltage ( $-400\text{ V}$ ) only after loading because the HV tab was not connected on the test-frame and therefore the comparison is not possible. The noise of both hybrids is within specifications [78], as shown in figure 5.30;
- R1 had a noise level identical to before for both hybrids, shown in figure 5.31;
- R2 showed issues while reading the module together with all the others and many channels were masked after the trim range test. The module was fully functional when it was tested before loading, but the read out was problematic when the whole petal was configured. Some channels were extremely noisy and others did not respond. This suggested that there are some configuration problems. Results are shown in figure 5.32;
- R3 module behaved as R2, only the single hybrid testing showed meaningful result. The communication got worse when all four hybrids were configured together and even worse configuring the full petal. A deeper investigation is provided in section 5.4.4. Before loading the input noise was already irregular, showing some noisy channels, as can be seen in figure 5.33. Here the noise behavior of R3H0 hybrid is shown as example when all modules are configured after loading;
- R4 module is reasonable, but few chips swapped their noise levels. This was not completely understood, but it is suspected that this is again related to communication issues. The noise level is still within specs and results are shown in figure 5.34;
- R5 also looked fine, even though in R5H0 the noise level is slightly higher after loading, as shown in figure 5.35.

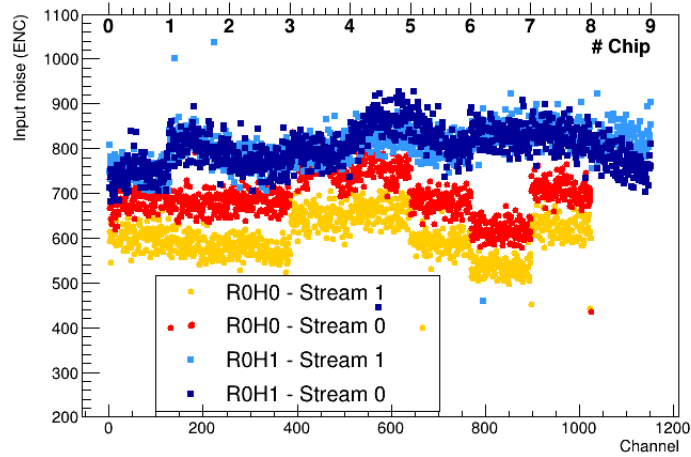


Figure 5.30: Noise results for R0 module after loading, sensor biased with  $-400$  V.

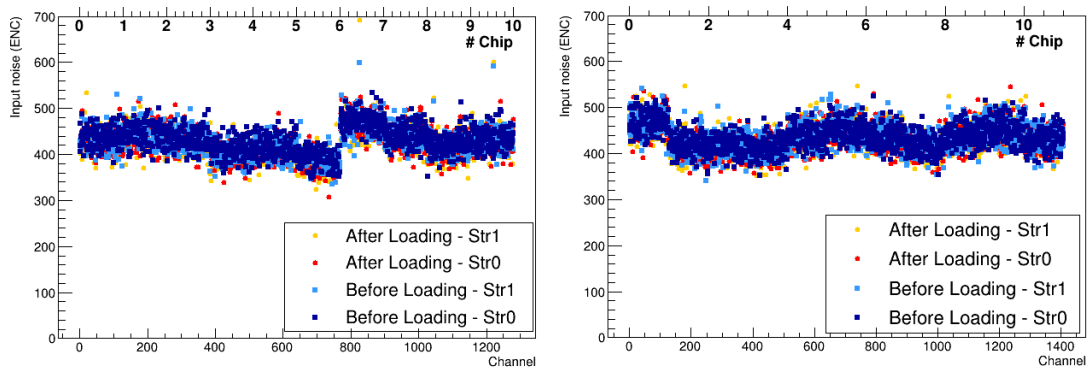


Figure 5.31: Before/after loading noise comparison for R1 module: H0 hybrid on the left-hand side and H1 on the right-hand side.

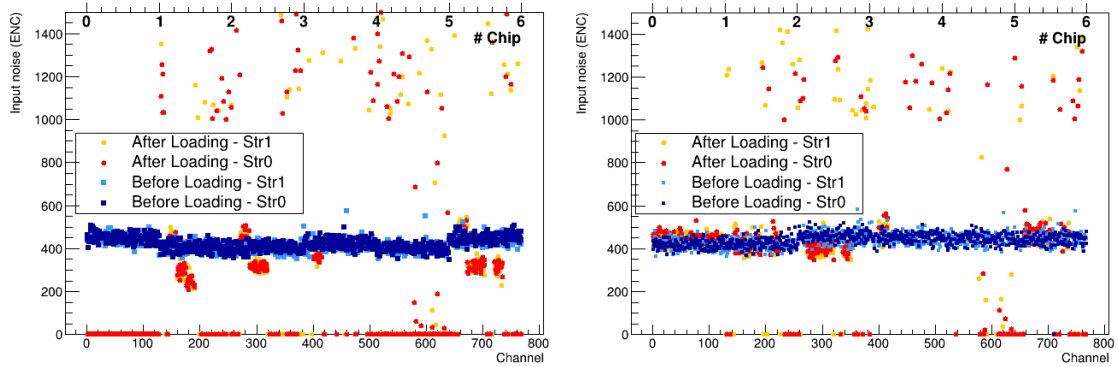


Figure 5.32: Before/after loading noise comparison for R2 module: H0 hybrid on the left-hand side and H1 on the right-hand side.

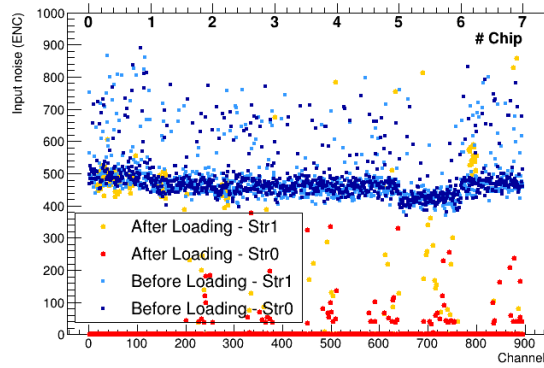


Figure 5.33: Before/after loading noise comparison for R3 module: H0 hybrid is shown as example.

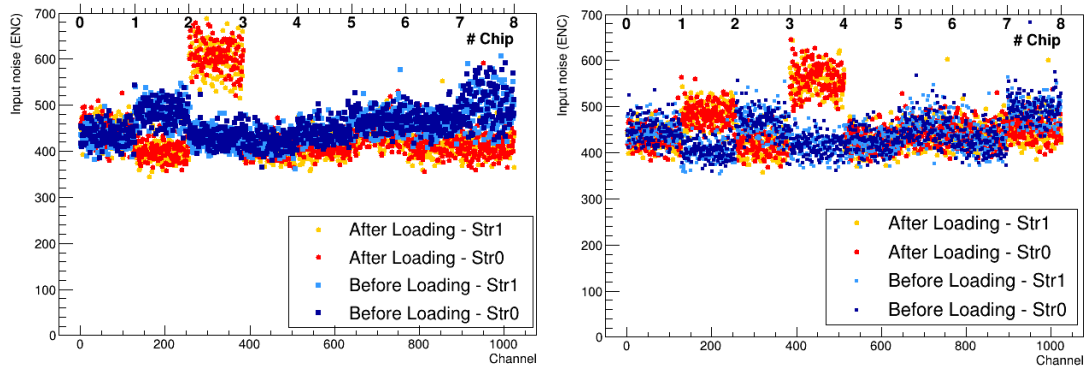


Figure 5.34: Before/after loading noise comparison for R4 module: H0 hybrid on the left-hand side and H1 on the right-hand side.

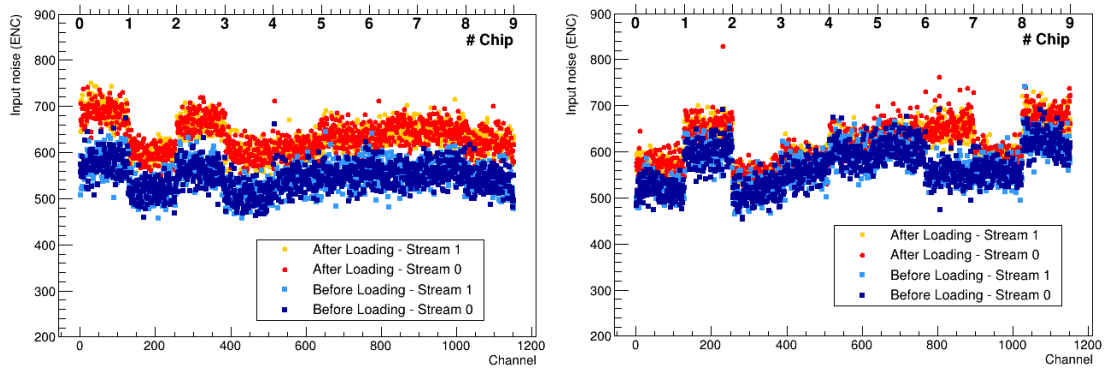


Figure 5.35: Before/after loading noise comparison for R5 module: H0 hybrid on the left-hand side and H1 on the right-hand side.

**Analysis on the electrical results of the R3 module** R2 and R3 modules were tested successfully before loading, but they showed some issues with the communication after loading especially when tested together with the other modules on the petal. A further investigation was carried out on all hybrids of the R3 module, stream 0, to understand the nature of the problem, the strobe delay was tested in different configurations:

- test on single hybrid, from R3H0 to R3H3, disabling the rest of modules. The result is shown in figure 5.36, most of the seven ABC chips respond and the communication is established correctly.
- all four R3 hybrids are configured together disabling the other modules, figure 5.37. Many channels showed a not clear strobe delay window and the communication with other channels is lost.
- R3 module is configured with the rest of the modules on petal, the portion of missing channels increased as shown in figure 5.38

The last chip in R3H2 never responds because it was disabled due to the wire-bonding connection to the sensor. As those mechanical sensors produced in Vancouver did not have the passive layer, all silicon strips were connected together causing a short circuit. The gap between chips in the strobe delay plot is due to the ordering of those in the configuration file.

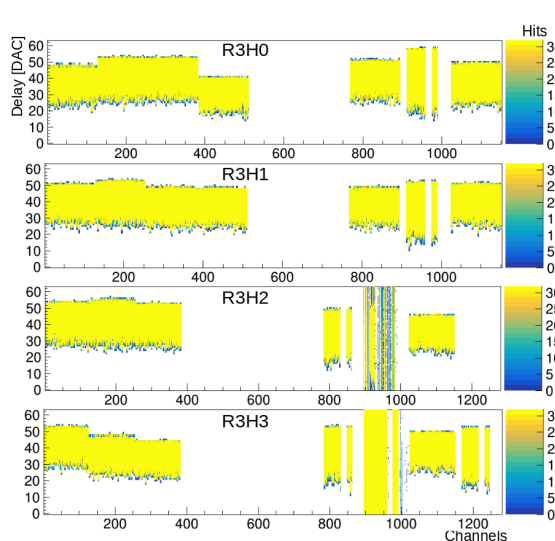


Figure 5.36: Strobe delay test on R3 hybrids on petal, configured individually. The other modules were disabled.

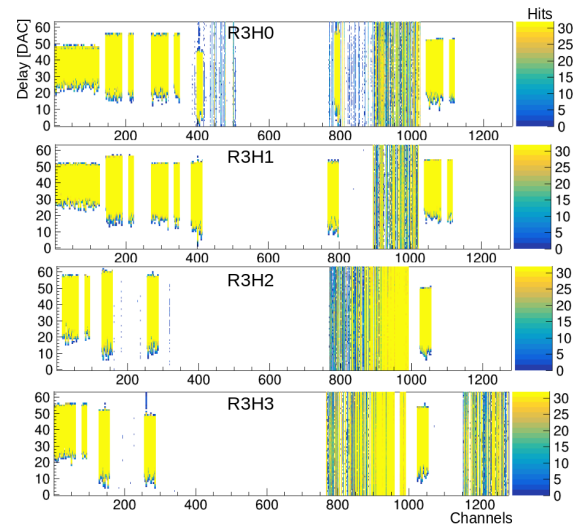


Figure 5.37: Strobe delay test on R3 module on petal with all hybrids configured. The other modules were disabled.

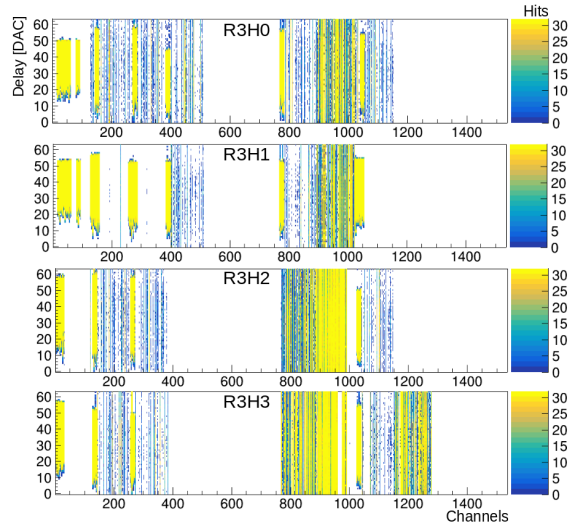


Figure 5.38: Strobe delay test on R3 module when all 4 hybrids are configured together with the other modules on petal.

Looking at the results from this test one can think that the nature of the issue is related to configuration parameters since the results get worse when the number of testing components increases. The water chiller was kept at  $8^{\circ}\text{C}$  during each test; the temperature plays a role in the electrical test as there is an increment of the heat produced when all modules are configured at the same time. The temperature variation could affect somehow the functionality of the modules.

**Conclusions** The core QC investigation included the analysis on the thermo-mechanical property of a prototyping petal core, which showed successful results. The thermal analysis on the core prototype using the dual-phase  $\text{CO}_2$  cooling showed that the infrared technique is a valid tool to qualify the thermal performances of a local support structure. The IR imaging technique needs an optimization to correct the variation of the emissivity coefficient due to different materials and the effect on the ambient condition.

The QC tests performed on the semi-electrical petal built at DESY showed that the module loading procedure, as explained in this chapter, fulfils the requirements:

- the survey on sensor fiducial marks defined a placement precision of  $(-8 \pm 18)\mu\text{m}$  which is well within the  $\pm 50\mu\text{m}$  tolerance, as shown in figure 5.23;
- the glue layer thickness between the core and modules is within the specification, as reported in table 5.5;
- the simultaneous electrical communication with all modules was mostly suc-

cessful, with the exception of R2 and R3 module. The input noise level is into the expected range for all working modules.

As already mentioned these modules were assembled using prototyping components, *ABC 130*, and the debugging becomes more difficult as they are obsolete due to the transition to the *ABC Star* architecture.

# Chapter 6

## Petal testing at low temperature

The building procedures and the quality control tests of modules, cores and petals have been explained in the previous chapters to describe the activity flow during the production. Most of them were performed on mechanical components due to a lack of real material as for the module building training or with modules populated with the previous prototype of readout chipset (*ABC 130* ASICs) as for the loading of the semi-electrical petal.

The first batch of electrical components of the endcap Star modules appeared in the collaboration in late 2020 and they were used to populate the front side of a petal core. The endcap modules were assembled and tested by the ATLAS ITk group at the University of Freiburg, as well as the loading on the core.

This chapter shows the test results for the quality control (QC) that were obtained on this populated petal under CO<sub>2</sub> cooling at DESY. The motivation and the importance of the investigation is provided in section 6.1. After a detailed description of the experimental setup, in section 6.2, the tests are explained. The study starts with a study on the power consumption of the Star chipset, described in section 6.3 and the estimation of the cooling power required for the endcap detector. Section 6.4 explains the electrical tests performed on the petal as function of CO<sub>2</sub> temperature in order to understand the electrical noise trend of each module. A comparison with nominal input noise values, and how they have been estimated, is also provided in this section. The analysis continues studying the thermal performances of the petal when all modules are powered on, described in section 6.5. A FEA simulation was developed in order to compare the estimates with the temperature of the electronics measured on the petal.

### 6.1 Motivation

The semi-electrical petal, described in section 5.3, was the only object produced so far by each endcap module loading site, the following step consists of the assembly

of a fully electrical petal. Due to the limited availability of endcap Star modules the loading was possible only on the front side of a petal core.

This petal was required to qualify and approve the design of most of the components, such as the bus tape and the EoS card, after being tested in a cold environment in the final stage of the petal assembly.

The local support was assembled at DESY and, after the thermal analysis as described in section 5.1.3, it was shipped to Freiburg for the loading of the modules. The R2 Star module built at DESY and described in chapter 4, was assembled to be placed on this core. The rest of endcap modules were mounted and tested in Freiburg, but no tools were used for gluing the electronics (except for the R0 and R2 module) due to their unavailability. Chip on hybrid and hybrid/power-board on sensor were glued manually and a significant glue seepage was observed due to the manual handling. The first version of the Star hybrids came from the first Star prototype production and they had design mistakes which were fixed adding bodge wires, additional capacitors and extra wire-bonds.

The loading, the wire-bonding and a first electrical test at room temperature were performed by Freiburg colleagues and afterwards the petal was shipped to Hamburg to perform the remaining QC tests.

Figure 6.1 shows the electrical petal loaded with the first batch of Star modules and a master EoS card. The petal was assembled and shipped in its assembly frame.

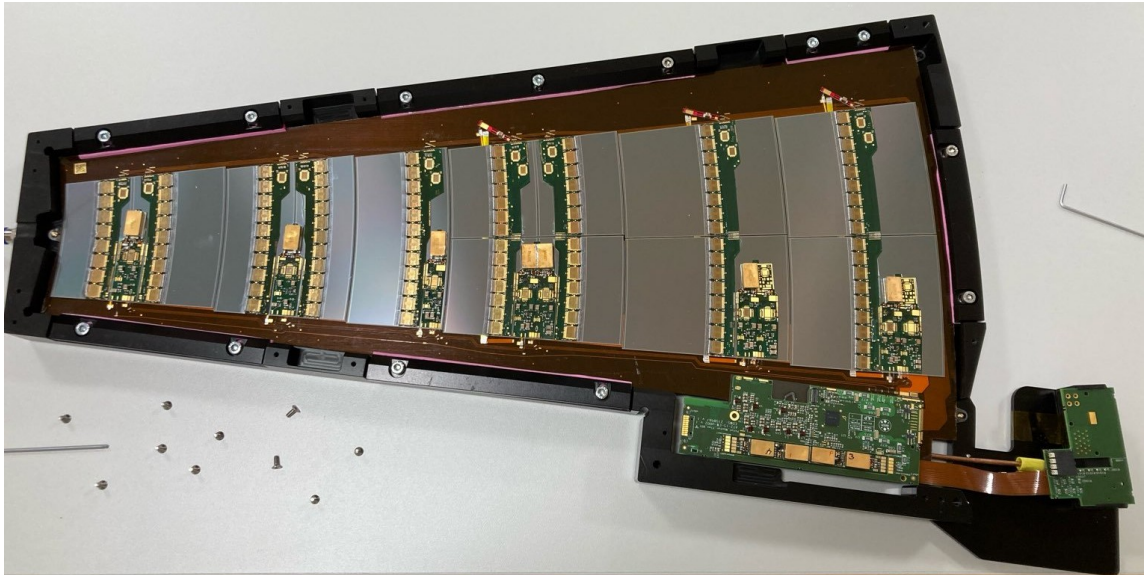


Figure 6.1: Electrical petal fully populated with Star modules and EoS master card on the front side.

## 6.2 Experimental setup

The testing setup used for the QC on the fully loaded petal is identical to the petal core QC, with the addition of the data readout chain. Tests were performed inside a custom-made box, called Petal Thermal Measurement chamber (PTM) with dimensions of  $(160 \times 140 \times 80)\text{cm}^3$ . Thanks to the attached thermal isolation layers, the PTM shields the thermal radiation from the laboratory to avoid influence on the sensitive infrared (IR) thermography. The IR camera used for the test is *VarioCAM® HD research 900* [95] that offers a picture of  $1024 \times 678$  pixels and a measurement accuracy of  $\pm 1$  °C. The IR camera is slightly rotated to avoid the reflection of the camera itself, known as Narcissus effect, when placed perpendicularly to the object. Internal reflections in the PTM are blocked by a high-absorbing fabric.

To avoid condensation when the petal is cooled down, regulated dry air flushing is used and the temperature and relative humidity are monitored by three sensors distributed in the chamber and read out by a Raspberry Pi. The temperature and pressure of  $\text{CO}_2$  at the inlet and outlet of the pipe are also recorded by thermocouples and a pressure transmitter which are read out by a *Keithley 2701* multimeter. The current value from the pressure transmitter and the voltage from the thermocouples are then converted into pressure and temperature using a calibration function implemented in a Python script.

The MARTA  $\text{CO}_2$  cooling system [84] is attached to the PTM to deliver cold  $\text{CO}_2$  to the cooling loop of the petal. The flow mass for thermal tests is set to its maximum 4 g/s in order to reach the required test temperature,  $-35$  °C is the  $\text{CO}_2$  temperature to be used for the ITk detector in the ATLAS experiment [37].

The electrical test on the petal requires a specific readout chain to send and receive commands and data by the optical fibers connected to the EoS via VL+ chip. A *Genesys2 Digilent* [96] board is used as FPGA to communicate with modules. The optical fiber is plugged to it through a *FMC-QSFP-ITk* board, designed in Freiburg to interface with the FPGA, as shown in figure 6.2. The ITSDAQ firmware is provided by a SD card to the Genesys. The entire readout chain is illustrated in figure 6.3. The petal is placed inside the PTM chamber together with the assembly frame and a custom-made holder is used to support the petal in a certain position in the field of view of the IR camera. The low and high voltages are supplied to the petal via a handmade connection due to the absence of the proper Gleinar connector on the pigtail of the master EoS. All the silicon sensors are biased through four HV channels and the bus tape lines group them as following: R0+R2, R4+R5, R1 and R3 individually.

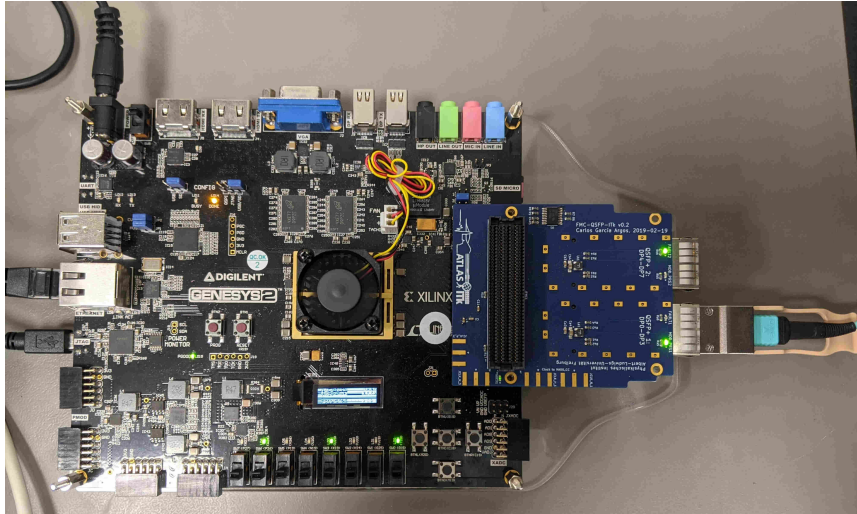


Figure 6.2: Digilent Genesys2 (black board) with FMC-QSFP-ITk (blue board) used to connect the optical fiber to the FPGA.

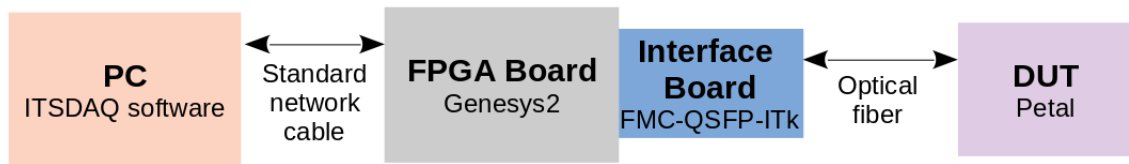


Figure 6.3: Readout chain for electrical petal testing.

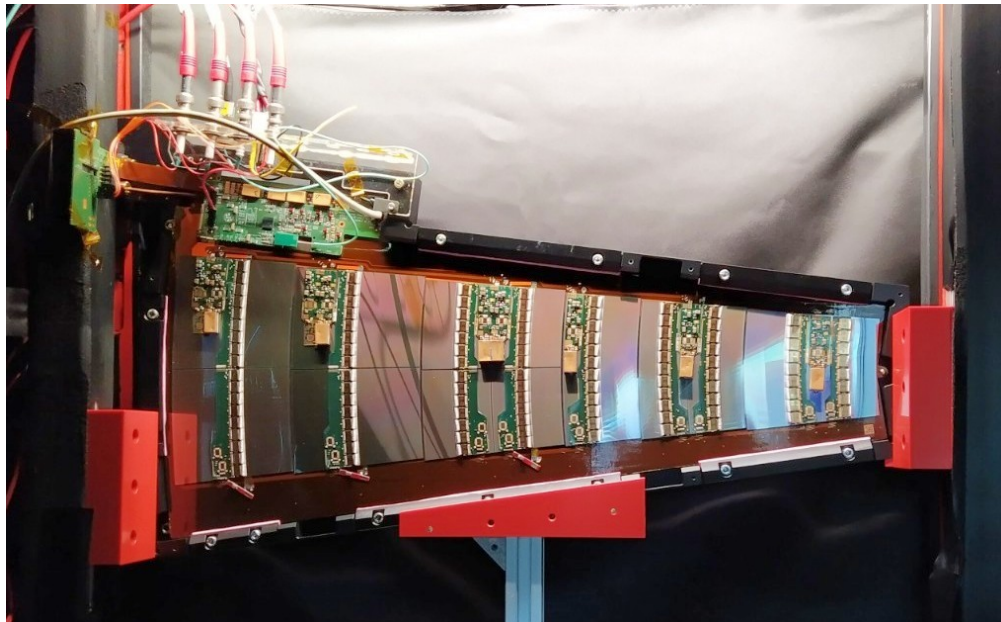


Figure 6.4: Placement of the petal inside the PTM with all cables plugged in the EoS region.

The petal and these power connections inside the PTM are shown in figure 6.4. A *CAEN DT1415ET* [97] is used as HV power supply. It can supply up to 8 channels in positive/negative polarity. A *TTi CPX400DP* [98] linear power supply is used to power the electronics.

### 6.2.1 Petal reception test

A petal reception test on the bench was needed before starting with the investigation in order to check the status of its components after the shipment. As for the modules, the reception test is focused on:

- visual inspection: all wire-bonds and HV tabs are checked visually under the microscope to ensure a working communication with the electronics. No damage was found caused by the shipment;
- electrical test on bench: low and high voltages are supplied to the petal to check if the communication line is established properly.

During the bench test the petal is placed inside a electrostatic discharge (ESD) safe box to ensure a dark and dry environment for the sensors, as showed in figure 6.5.

All tests showed reasonable results and comparable with the values measured by Freiburg colleagues before the shipment. Once the reception test was completed, the

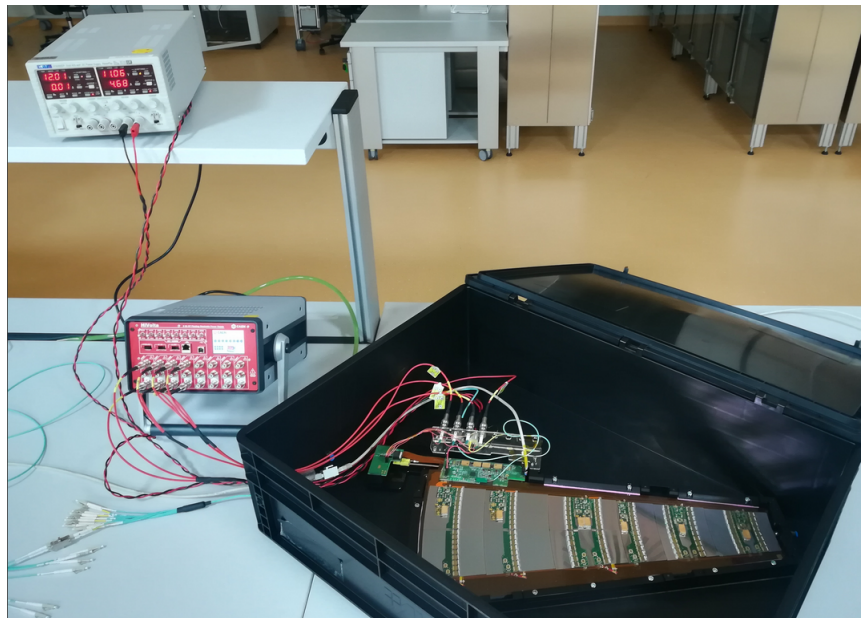


Figure 6.5: Equipment for electrical test on the bench during the petal reception test.

petal was moved into the PTM chamber to proceed with the investigation at cold temperature.

## 6.3 Power consumption of Star chipset

An accurate knowledge of the power consumption values for the petal electronics is needed to estimate the cooling requirements for the individual petal, which is then extended to the whole endcap. Understanding the thermal behaviour and the headroom to the thermal runaway is crucial for the design of a silicon detector system. Thus a thermo-electrical modelling of the ATLAS ITk Strip detector was developed in order to predict the behaviour of the silicon detector system. It provides estimates of the power that the detector generates over the lifetime of the experiment and is also used to optimize operational aspects like the temperature profile according to the radiation dose over time.

### 6.3.1 The thermo-electrical model

A thermo-electrical model for the ATLAS ITk Strip detector was created to predict the behaviour of the heat generation and dissipation from the electronics (ABCs and HCCs on hybrid, AMACs, linPOL12V and bPOL12V on power-board, lpGBT and VL+ on EoS, all described in section 3.1.2) and the silicon sensors [99]. The model takes also into account the radiation environment of the strip system, as several inputs depend on the radiation damage effects. Leakage currents in the sensor can become particularly significant after irradiation, and the heat generated by them, together with the heat from front-end electronic components, need to be removed by a cooling system. There are many reasons for the heat removal. The most important ones can be described as follows:

- to avoid the thermal runaway of silicon sensors: there is a critical temperature  $T_{crit}$  above which the heat cannot be removed quickly enough, and the detector becomes thermally unstable. Thermally generated charges within the sensor causes an avalanche effect that cause high currents damaging the silicon sensor. A FEA simulation of the petal heat behaviour as function of CO<sub>2</sub> temperature is developed to find  $T_{crit}$ , it is described in section 6.5.1;
- to decrease the noise measured during electrical tests. The electronics and the sensors generate extra noise when the temperature is high, especially with irradiated sensors in which the leakage current increases rapidly;

A consequence of the heat increment is the module power-off operated by the AMAC.

It disables the front-end chips and the sensor biasing due to the high leakage current when they reach the temperature limit (above 40 °C).

The capability of the cooling system to remove this heat is limited by the temperature of the coolant and the thermal impedance of the heat path between the source and the coolant. The thermo-electrical model emulates those impedances as simple electrical resistors. Figure 6.6 shows the thermal impedance of the system as resistors grouped in:

- $R_C$  is the core resistor which includes the thermal impedance of the bus tape, carbon fiber face sheet, carbon foam and the cooling loops;
- $R_M$  is the module impedance due to its electronics such as the bPOL12V, ABCs and HCCs, the sensor thermal impedance is considered negligible at beginning of life;
- $R_{EOS}$  includes the lpGBT, VL+, bPOL12V and bPOL2V5;
- $R_{MC} = R_C + R_M$  is the total resistor of core and modules.

The impedance values are obtained running a FEA simulation at fixed condition when a single heat source is powered on [99]. An example is provided in equation 6.1 to obtain the resistor given by the ABCs,  $R_{ABC}$ . In the simulation the ABC chips are the only ones powered on in all six modules by a know value.

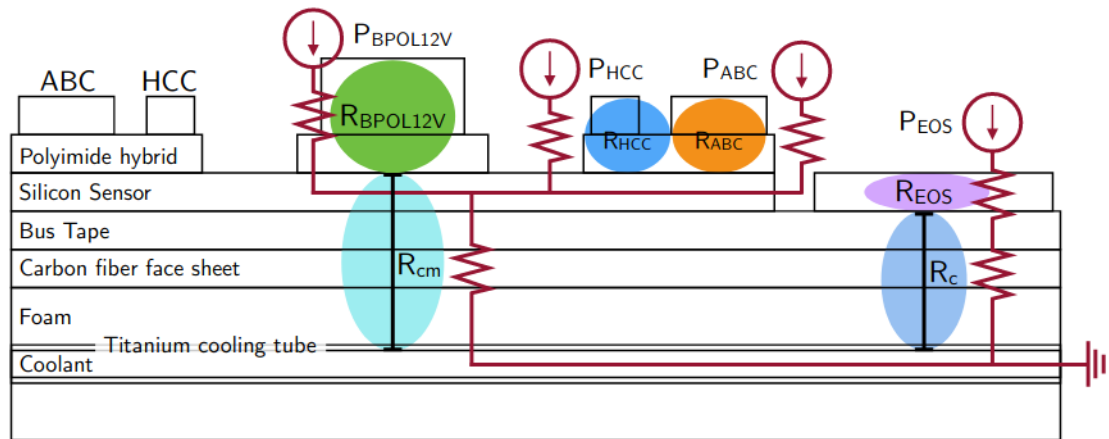


Figure 6.6: Thermo-electrical model for silicon modules loaded on a local support with thermal impedance represented as resistors [99].

Running the thermal FEA,  $\Delta T_{HCC}$  are measured on each module and its average is used to extract  $R_{MC}$  from the second equation in 6.1 and replaced in the first one.

$$\begin{cases} \Delta T_{ABC} = P_{ABC} \cdot (R_{ABC} + R_{MC}) \\ \Delta T_{HCC} = P_{ABC} \cdot R_{CM} \end{cases} \quad (6.1)$$

This procedure is repeated for each electrical component, one by one, to get their impedance.

The leakage current is another factor that needs to be considered in the thermo-electrical model. It increases with the temperature following the equation 6.2 [100]:

$$I(T) \propto T^2 \exp\left(\frac{-E_{eff}}{2kT}\right) \quad (6.2)$$

where  $E_{eff} = E_g + 2\Delta T = 1.21$  eV is called the effective energy in the temperature range (-30, -10)°C,  $E_g = 1.12$  eV the silicon band gap at 300 K and  $k$  the Boltzmann's constant. The radiation-induced sensor leakage current can be linearly parametrized as a function of the hadron fluence expressed in 1 MeV equivalent neutrons [101]. Experimental data are fitted and scaled with equation 6.2.

The power estimation of each of the heat sources are therefore obtained from the thermo-electrical model and compared with the nominal specifications. They are listed in figure 6.7 for each active Star component on the petal.

The total power produced by one petal, estimated by the thermo-electrical model is 61.1 W at beginning of life (not irradiated components), it is obtained by the sum of:

- 29.2 W generated by the modules on each side;
- 2.1 W is the power produced by the EoS master card;
- 0.7 W produced by the EoS slave card.

The power due to the cables is not taken into account in this calculation. Considering the total number of petals for both endcaps, 32 petals on each disk and six disks each endcap, the global power generated by the whole strip endcap detector is 23.5 kW. The same calculation can be done for the strip barrel, which is made of four layers [103]:

- two inner layers populated with *Short Strip modules* (SS), 56 and 80 staves each layer, producing 162 W each stave (22 kW in total)
- two outer layers populated with *Long Strip modules* (LS), 112 and 144 staves respectively, producing 90 W each stave (23 kW in total)

Therefore the whole Endcap strip barrel produces 45 kW at beginning of life and,

Description	input voltage	Specifications for 1 component			eff	<i>n</i> components per module (1 side)	Total power (1 side) [W]
	[V]	current [A]	% bumped	power [W]			
AMAC 1.5V	1.5	0.042		0.063		–	
AMAC 2.5V	2.5	0.002		0.005		–	
Total AMAC	–	–		0.068		R3: 2 All others: 1	0.136 0.068
ABC (digital)	1.5	0.027	110%	0.0405		–	
ABC (analog)	1.5	0.068		0.102		–	
Total ABC	–	0.095		0.1425*		R0: 17 R1: 21 R2: 12 R3: 28 R4: 16 R5: 18	2.423 2.993 1.710 3.990 2.280 2.565
HCC (digital)	1.5	0.210	25.5%	0.315		–	
HCC (analog)	1.5	0.0		0.0		–	
Total HCC	–	0.210		0.315*		R3: 4 All others: 2	1.260 0.630
bPOL12V (ABC,HCC,AMAC1.5)	–			$\frac{(1-\epsilon)}{\epsilon}(P_{ABC} + P_{HCC})^*$	72%	–	R0: 1.212 R1: 1.433 R2: 0.935 R3: 1.045+1.045 R4: 1.156 R5: 1.267
linPOL12V (for AMAC2.5)	–			see text		–	R3: 0.033 + 0.033 All others: 0.033
Total Module	–			*			R0: 4.365 R1: 5.157 R2: 3.376 R3: 7.543 R4: 4.167 R5: 4.563
EOS							
lpGBT	1.2	0.317		0.380		–	0.380
VTRx (VL+) GBLD 1.2V	1.2	0.025		0.030		–	
VTRx (VL+) GBLD 2.5V	2.5	0.07		0.175		–	
VTRx (VL+) GBTIA (legacy)	2.5	0.053		0.133		1	
Total VTRx (VL+)				0.338		1	0.338
bPOL2V5 (old DCDC2)					88%	2×, master only	0.056+0.056
bPOL12V					55%	2×, master only	0.633+0.633
EOS Master							2.096
EOS Slave							0.718
EOS both sides							2.814

Figure 6.7: Updated power values from the components specification and the estimation obtained using the thermo-electrical model [99][102].

adding the endcaps, the entire ITk Strip detector is thus producing 68.5 kW, calculated at beginning of life, without the power due to cables and the safety factor. Table 6.1 contains a summary of the power consumption for the strip barrel and endcaps. The pixel detector power has to be added to this value in order to understand the cooling system needed for the whole ATLAS ITk detector.

### 6.3.2 Experimental power calculation

Testing the electrical petal provided the possibility to check if the power estimation of the electronics that is powered on the petal is correct. The petal power chain can be configured to power up the modules individually. This allows to get the power (mul-

ITk Strip	number of Staves/Petals	Power [W]
Barrel SS	136	162
Barrel LS	256	90
Endcap	384	61.1
		68500

Table 6.1: Summary of the power consumption estimation of the ITk Strip detector: the total number of staves and petals is specified as well as the power required by each of them.

tipling the current from the LV supply by 11 V) produced by the module electronics independently. In order to communicate with the petal a few steps are needed to configure properly the electronics: switching on the LV supply providing 11 V, configuring the lpGBT and the AMACs (which require 0.46 A), enabling the module DCDC converters and afterwards running the ITSDAQ software. In table 6.2 the reading values are listed for each configured module and at different CO<sub>2</sub> temperature. They include the current produced by the single module electronics (ABC and HCC on hybrid, AMAC, linPOL12V, bPOL12V on power-board) and by the EoS (lpGBT, VL+ and bPOL12V). The error on those readings is  $\pm 0.3\% \cdot I_{meas} \pm 0.02$  A given by the current accuracy of the power supply [98]. There were two ABC chips that did not work in R0H1 hybrid and one chip in R3H3.

Figure 6.8 shows the behaviour of the current values listed in table 6.2 as function of number of ABC Star chips on each module at three different CO<sub>2</sub> temperatures. On the right-hand side a zoomed view on the single module is provided. The linear fits on the three set of points show a proportional increment of the current with the number of ABC Star chips, agreeing with the current measured with the full petal powered on. As expected, the power increases with the temperature of the CO<sub>2</sub> set

Module	ABC chips	Current [A]		
		-20 °C	-10 °C	0 °C
R0	15	0.85	0.87	0.88
R1	21	0.97	0.98	0.99
R2	12	0.79	0.79	0.80
R3	27	1.16	1.17	1.18
R4	16	0.86	0.87	0.88
R5	18	0.91	0.92	0.93
All	109	3.30	3.34	3.41

Table 6.2: Current values measured on the LV power supply for each module at each CO<sub>2</sub> set-points.

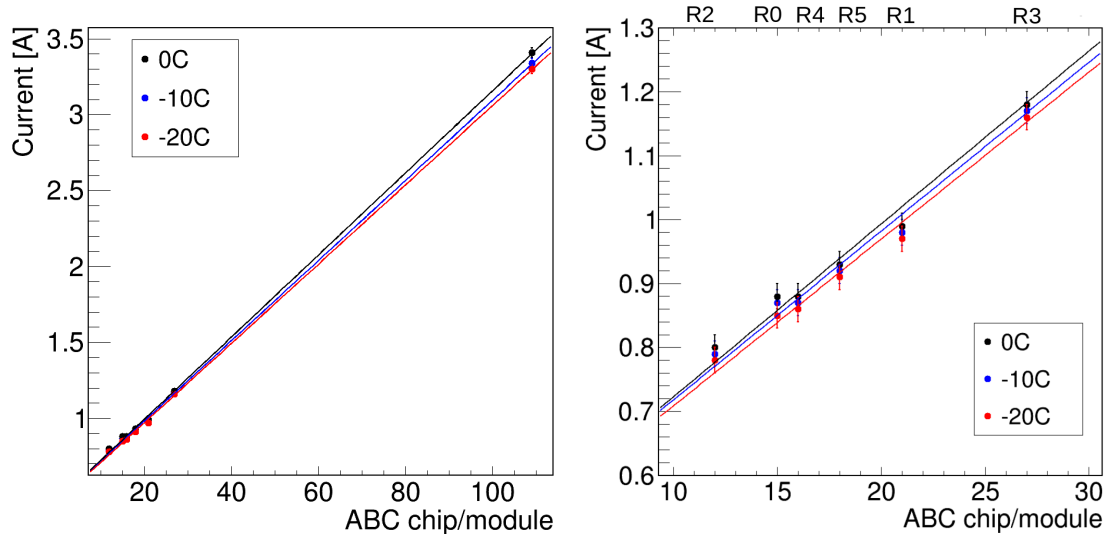


Figure 6.8: Current values, read out from the LV power supply, as function of number of ABC chip on each module. A zoomed view is provided on the right-hand side.

on the MARTA cooling machine.

The power consumed by the electrical petal, loaded on one side only and with a master EoS card when all the modules are powered on and configured at  $-20^{\circ}\text{C}$ , is:

$$P_{\text{petal}} = (3.30 \pm 0.03)\text{A} \cdot 11\text{V} = (36.3 \pm 0.3)\text{W}$$

which can be compared with  $29.1\text{W} + 2.1\text{W} = 31.2\text{W}$  obtained from the thermo-electrical model. Thus the power measured on the electrical petal is  $5\text{W}$  greater than the estimated value, meaning an increment of 15%.

The complexity of the petal electronics and the diversity of each module made difficult the calculation of the power for the single component. A better understanding on the configuration process is needed in order to obtain the power consumption of each electrical component.

## 6.4 Electrical at low $\text{CO}_2$ temperature

The main reason for the cold test is to check the level of electrical noise of each module comparing it with the estimated value. The study was performed at different  $\text{CO}_2$  temperature within the range allowed by the MARTA cooling machine, ranging from  $-35^{\circ}\text{C}$  to  $20^{\circ}\text{C}$ . The  $\text{CO}_2$  set-points used for this analysis are reported in table 6.3, which correspond to the pressures listed in the second column. An unstable behaviour was observed at the limits of the range and for this reason the tests are

Temperature [°C]	Pressure [bar]
+18	56
+10	45
0	35
-10	26
-20	20
-30	14
-34	10

Table 6.3: CO<sub>2</sub> set points during petal testing and conversion to pressure values.

performed at 18 °C and −34 °C, i.e. at the highest and lowest ends of the temperature range.

### 6.4.1 Module noise analysis

At each temperature set-point the strobe delay, noise occupancy and three point gain are performed supplying −350 V to the sensors and 11 V to the electronics, setting a voltage compliance of 4 A and 120 μA on the LV and HV supplies respectively. From the three point gain data the input noise value, defined in equation 4.7, can be extracted for each stream of all modules when 1 fC is injected. An example is provided for the R4 module in figure 6.9. Here the R4H0S0 stream (red points) shows a high peak measured in chip 6: this ABC chip reads out the strips that run under the DCDC converter of the power-board. The 400 ENC peak is caused by a deficient shielding of the coil which increases the noise via electromagnetic interactions. It is due to the prototyping stage of the existing power-boards at the

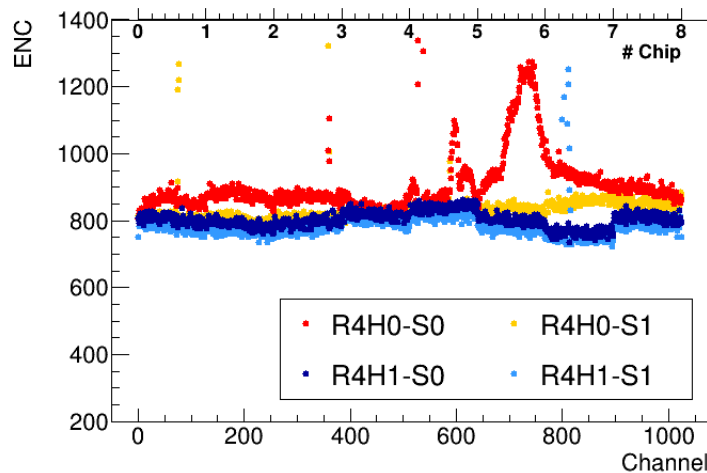


Figure 6.9: Input noise measured in R4 module when the CO<sub>2</sub> cooling is set to −20 °C. The result from four sensor streams are shown.

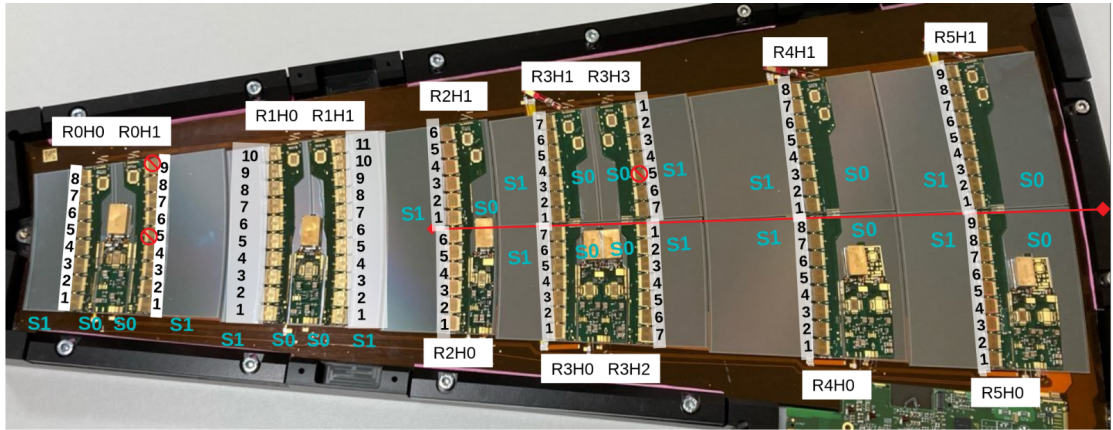


Figure 6.10: Closer look at the petal electronics with a focus on the hybrids, ABC chips and sensor streams nomenclature.

time of the module assembly.

To better understand the output that the ITSDAQ software produces, figure 6.10 is provided to clarify the front-end chip order, the stream and hybrid identification for every endcap module. Analysing the data measured from all modules at different  $\text{CO}_2$  set-points, the noise average per stream is calculated and plotted in figure 6.11 when the sensors are biased at  $-350$  V. The cyan points represent the expected values for module stream, an in-depth explanation on how they were estimated is provided in section 6.4.4. A worse agreement between the nominal and the measured noise value is found in the S0 sensor stream where the electronics is glued: the hybrid/power-board glue thickness is not under control due to manual module building without the proper set of tooling.

A few comments regarding the loaded modules that can help to understand the noise behaviour in comparison to the nominal values are reported in the following:

- *R0 module* was biased only up to  $-200$  V because of a chipped sensor corner (top right side), damaged before the loading, and the significant leakage current made impossible to supply higher voltages to this sensor (the others are biased with  $-350$  V). Measurements at  $-30^\circ\text{C}$  and  $-34^\circ\text{C}$   $\text{CO}_2$  temperature were not taken because the HV wire-bonds were removed in order to avoid the excessive build up of leakage current in the R0+R2 power line.
- *R1 module*, H0S0 is higher of about 100 ENC, most likely due to the hybrid gluing without the proper tool.
- *R2 module*: all measured points are shifted up; a possible reason for it can be found looking at the position of the power-board, this is the only module

having the board very close to the sensor guard ring and it can disturb the strip signal. An opposite trend is also observed in this module as function of  $\text{CO}_2$  temperature, in which the noise increases with the low temperature. A further explanation is given in the following section 6.4.2.

- *R3 module*: the noise is very close to the expected value;
- *R4 and R5 module*, in H0S0: those are populated with the same power-board designed for R3 because of the unavailability of the proper board. They were adapted for R4 and R5 module (e.g. one AMAC and one DCDC converter). They showed a particular high noise peak in the chip that collects the signal from strips running under the DCDC converter (as shown in figure 6.9 for the R4 module) due to a not complete shielding of the coil;

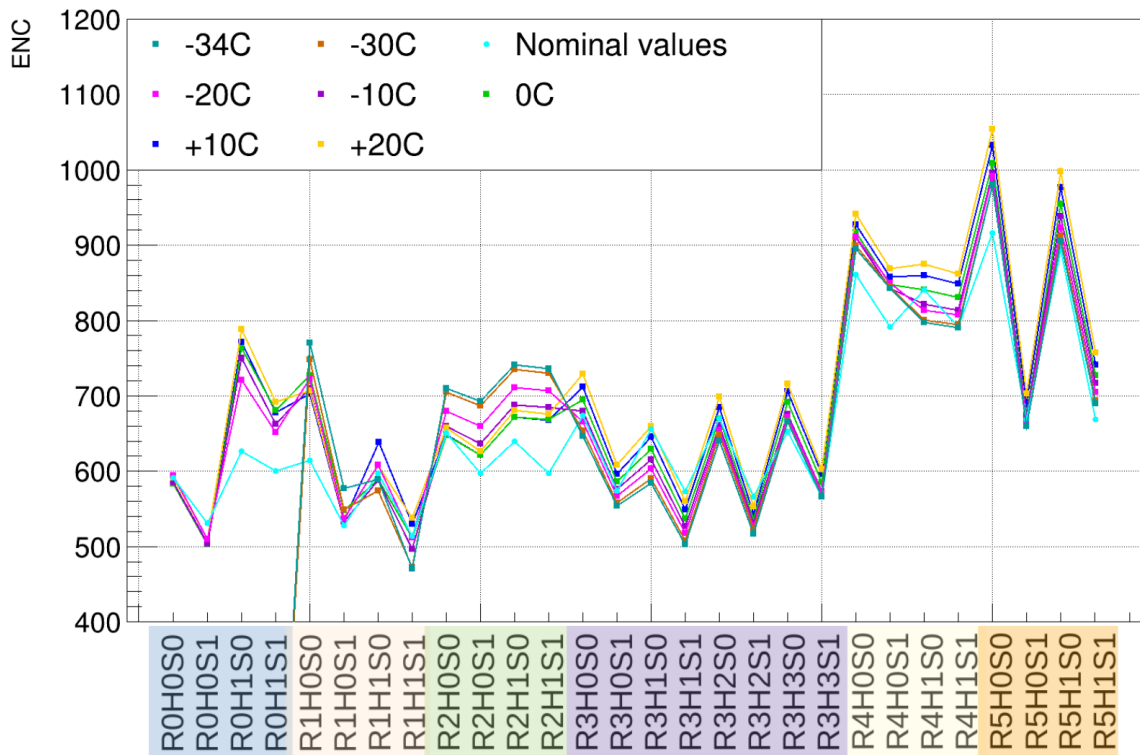


Figure 6.11: Input noise measured for all module streams at different  $\text{CO}_2$  temperature, when 1 fC is injected during the three point gain test. Sensors are biased with  $-350$  V (R0 sensor at  $-200$  V).

Values of noise were measured on those modules also on test frame at room temperature before the loading [104]. The comparison is shown in figures 6.12 and 6.13 where the input noise values, measured on modules before and after the loading respectively, are plotted as function of input capacitance  $C_{tot}$ , estimated in section 6.4.4. The black line is the same curve in both plots obtained from the equation 6.4 in section 6.4.4 and indicates the nominal noise values at a given capacitance. A better noise agreement is measured on the modules after the loading and a reasonable explanation for before-after loading noise discrepancy is provided by the cooling performances: the petal core is able to cool down the modules better than bench cooling setups. The test-frames, where the single module were tested before the loading, were not in their final design and the modules were arranged on only few test-frames due to a lack of all flavours. The best noise improvement is observed in module R3S1 (orange square) and R4S1 (blue square) in which the noise decreases by 25%.

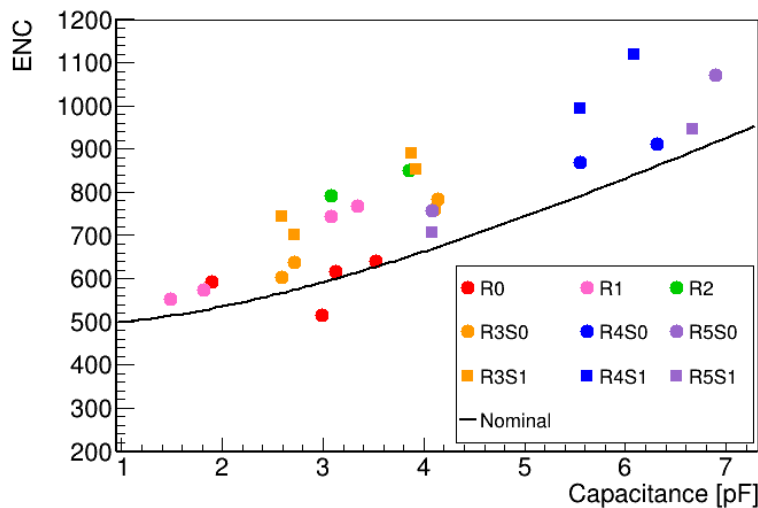


Figure 6.12: Input noise measured before the loading for all modules at  $-350$  V sensor bias (R0 at  $-100$  V) at room temperature, as function of input capacitance.

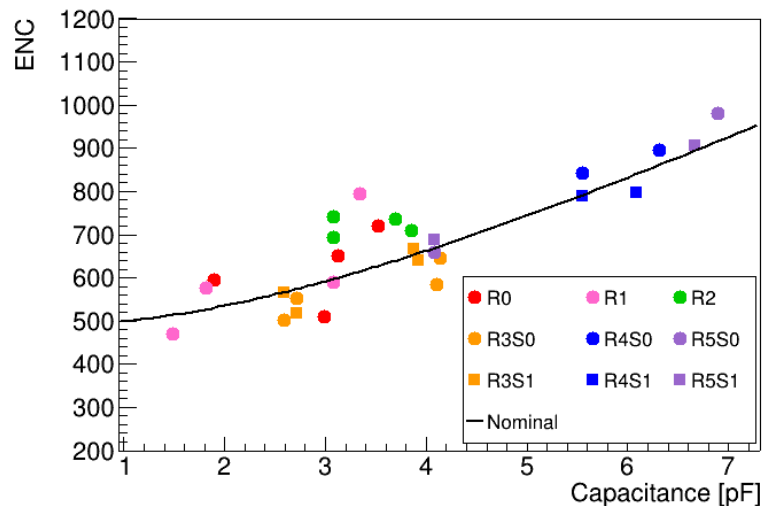


Figure 6.13: Input noise measured after the loading for all modules at  $-34^{\circ}\text{C}$   $\text{CO}_2$  temperature, at  $-350$  V sensor bias (R0 at  $-200$  V and at  $-20^{\circ}\text{C}$   $\text{CO}_2$  temperature) as function of input capacitance.

### 6.4.2 Noise investigation on the R2 module

A unique noise behaviour was observed on R2 module, opposite compared to the others: the values increased going down with the CO<sub>2</sub> temperature, as it can be observed in figure 6.14 for R2H1S0 hybrid. The lowest temperature reached in this case is  $-22^{\circ}\text{C}$  because TRACI (another CO<sub>2</sub> cooling machine used in replacement of MARTA at the time of these tests) did not allow to go lower in temperature. The small peak in the first channels of ABC 1 represents the tail of the noise increment due to the DCDC influence. The nominal noise value for this hybrid and stream is supposed to be around 640 ENC and a higher value is measured which keeps increasing going down in temperature.

The gain plot for each readout chip and output noise calculated as in equation 4.7, section 4.3.2 is shown in figure 6.15 and 6.16 respectively. It suggested that the issue did not concern the electronics because the front-end chips responded in the same way at each set-point.

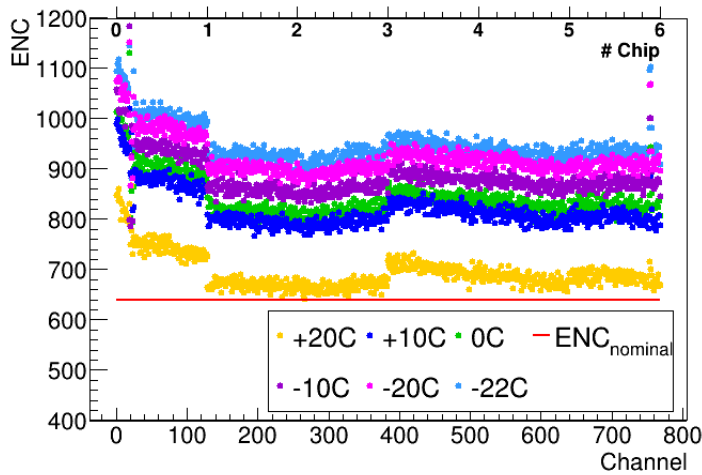


Figure 6.14: Input noise levels on R2 module (H1 hybrid, S0 stream) tested at  $-350\text{V}$  and at different CO<sub>2</sub> set-points.

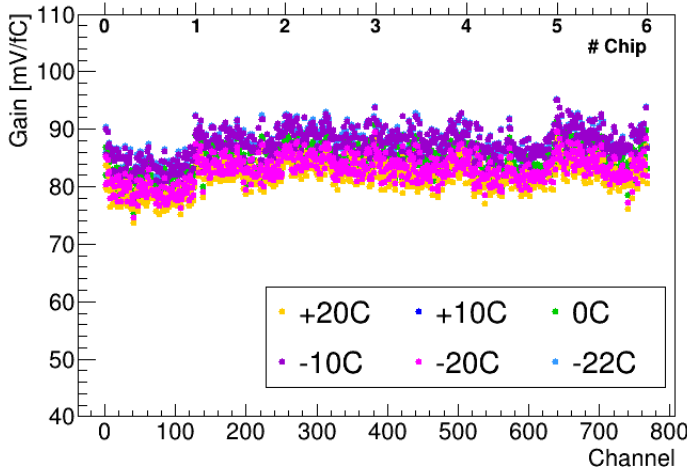


Figure 6.15: Gain values measured on the R2H1 hybrid at different CO<sub>2</sub> set-points, at  $-350\text{V}$  sensor biasing.

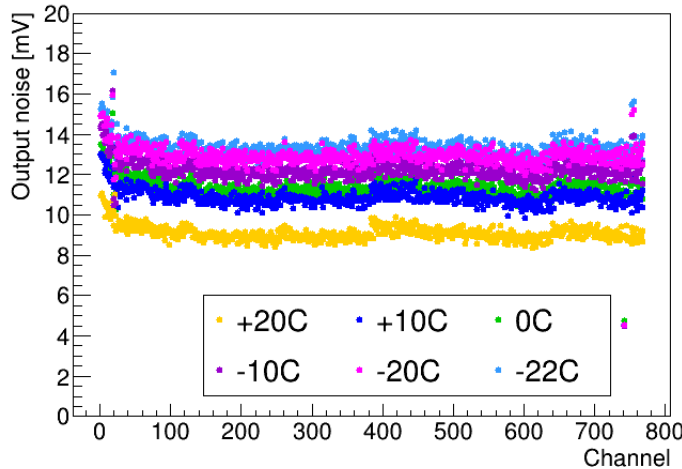


Figure 6.16: Output noise calculated in R2H1 hybrid at different CO<sub>2</sub> set-points, at  $-350$  V sensor biasing.

This consideration pointed to a HV biasing issue of the R2 sensor. The R0 HV wire-bonds were also removed to avoid disturbances of the R2 biasing due to the presence of R0 on the same HV line. The HV was provided to the sensor by an aluminum tab that was attached to the back side of the sensor and tab-bonded to the HV pad on the bus tape. For this particular module the HV tab was not attached properly to the sensor back-plane before the assembly, but only taped down with polyimide tape. The hypothesis for the strange noise trend was that the cold environment compressed the aluminum material and the contact between the tab and the sensor was gradually lost, reducing the applied HV to the sensor. This translates into an under-depleted sensor and a higher noise. The adopted solution was adding a secondary connection in order to bias the sensor from a sensor back-plane connection present on the front side of the sensor, as illustrated in figure 6.17. The HV was provided directly from the bus tape pad, where the HV tab was bonded (right-hand side of the figure), to the sensor opening (left-hand side) making use of a PCB glued on the bus tape. The white/transparent tape placed on top of it was used to regulate the emissivity of the golden pads. This method to bias the sensor is not used as primary HV application because it becomes unreliable when the sensors are irradiated due to the resistive nature of the sensor connection.

This solution partially addressed the noise issue of the R2 module: it allowed to get significant lower noise values, but did not invert the trend with the CO<sub>2</sub> temperature, as can be observed in figure 6.18. The noise trend is still not fully understood and there are different hypothesis to be tested in order to fully address it. A reasonable one could be related to the position of the DCDC on the power-board almost on top of the sensor guard ring: the magnetic field could affect the sensor performances, which may be temperature dependent. The R2 is the only endcap module where the power-board is placed nearby the sensor edge and this noise behaviour is observed.

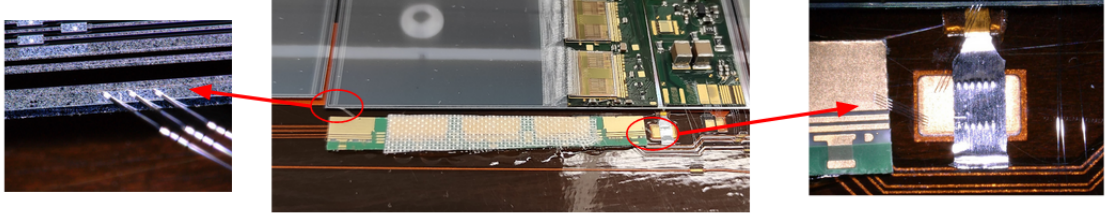


Figure 6.17: Additional HV biasing of the R2 sensor. On the right the HV is taken from the bonding pad and transferred through the PCB, glued on the bus tape, to the bottom right corner of the sensor where the opening of the sensor backplane is.

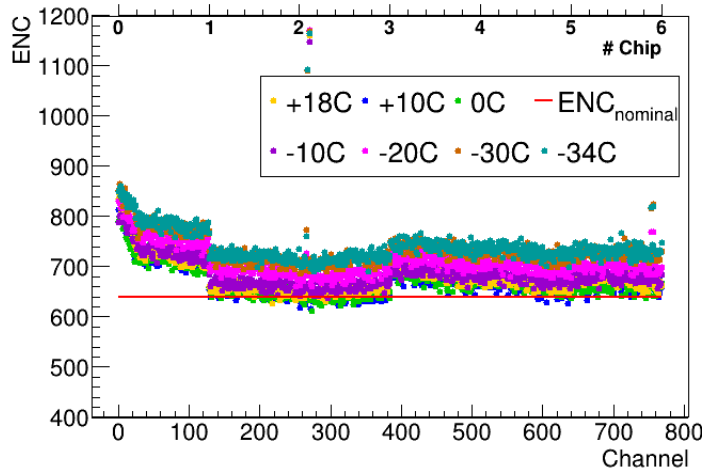


Figure 6.18: Noise levels on R2 module (H1S0) after the HV fix, tested at  $-350$  V and at different  $\text{CO}_2$  set-points.

Building another R2 module could provide answers and dedicated electrical test can help to clarify the source of the problem.

### 6.4.3 IV curves on sensors

The leakage current of the sensors is an important value to monitor, especially when the sensor are irradiated, as it directly affects the noise behaviour. Humidity plays a big role here and thus dry air flowed constantly inside the PTM to avoid condensation due to the low  $\text{CO}_2$  temperature. If the humidity is high, the dew point is reached and water droplets appear on the sensor surface that can freeze it.

Even though some modules shared the same HV channel on the bus tape, the AMAC allowed to enable/disable the bias of the sensor that hosts it, via the HVmux switcher circuitry, including the single sensor of split modules. To get the IV curve the current of single sensor was measured during the ramp up to  $-500$  V, performed in step of  $10$  V at  $1$  V/s and a waiting time of  $10$  s was included before moving to the next step. This ramp up reduced the risk of transients due to surface charge build-up. The measurements can be done in two different ways:

- via AMAC: this chip is able to read the sensor current by itself after a calibration is executed. The precision of the reading increases with high current values (i.e. for irradiated sensors).
- via HV power supply (CAEN): the values that the device reads are stored using a python script.

The value measured by the power supply includes a portion of current that is dissipated in a  $10\text{ M}\Omega$  filtering resistor present in the HVmux before being supplied to the sensor. The corrected values of current  $I_{corr\_supply} = I_{supply} - V/10\text{ M}\Omega$  are plotted in figure 6.19 when the  $\text{CO}_2$  was set to  $0^\circ\text{C}$ . The IV curves follow roughly the same trend for all sensors with the exception of the R0 sensor (yellow dots): the current compliance is reached at  $-200\text{ V}$  due to the chipped corner. R1 sensor (purple dots) also changes its trend at roughly  $-350\text{ V}$ .

A better agreement between the two reading methods is expected for high current values, as in case of irradiated sensors for example. On this petal the R0 module is the one having the highest leakage current and therefore the comparison is reasonable, as shown in figure 6.20 comparing the green curve (AMAC reading) with the cyan one (corrected supply reading).

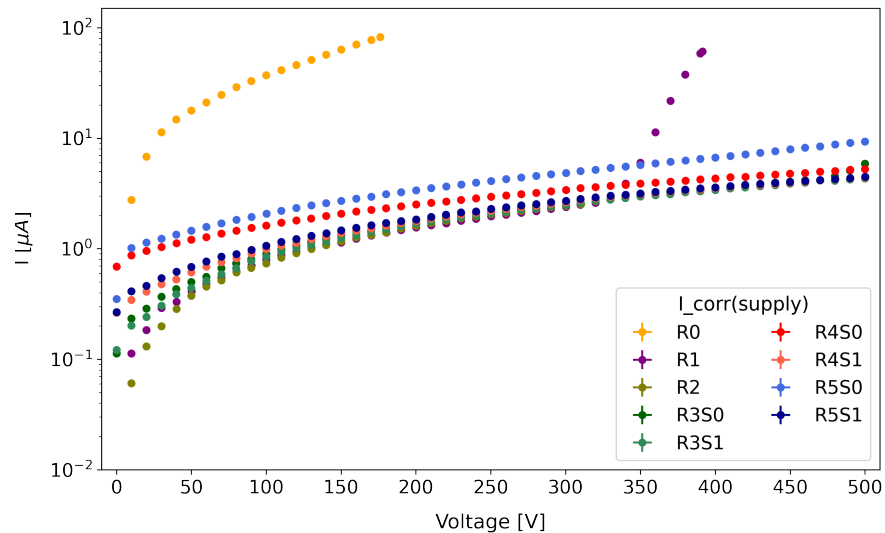


Figure 6.19: IV curves on single sensor at  $0^\circ\text{C}$   $\text{CO}_2$  temperature measured by the CAEN power supply.

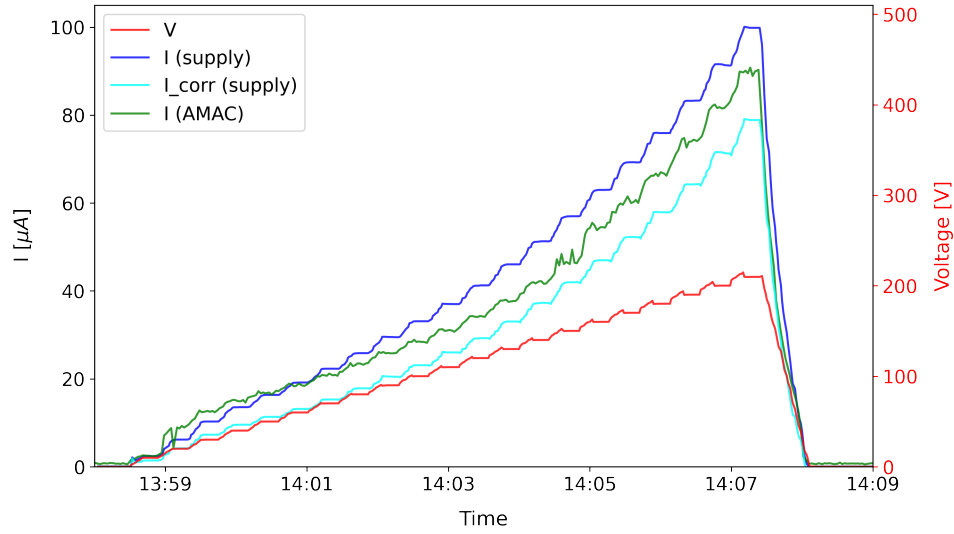


Figure 6.20: HV ramp up of the R0 module at  $-10^{\circ}\text{C}$   $\text{CO}_2$  temperature. Voltage and current values are logged as function of time.

#### 6.4.4 Input noise estimation on Star modules

The capacitance due to the silicon sensor is the leading cause for an increased module noise (before irradiation) compared to the hybrid noise value. The sensor load capacitance  $C_{tot}$  is mostly comprised of the inter-strip  $C_{int}$  and strip to back-plane  $C_{back}$  capacitance ( $C_{tot} = C_{int} + C_{back}$ ) [17]. There are other minor factors which contribute to the noise, like the parallel  $R_P$  and series  $R_S$  resistances and the leakage current  $I_L$ . The different contributions sum up quadratically as described in equation 6.3:

$$ENC = \sqrt{ENC_{C_{tot}}^2 + ENC_{I_L}^2 + ENC_{R_P}^2 + ENC_{R_S}^2} \quad (6.3)$$

The glue underneath the PCB where the electronics is placed, behaves also like a capacitor and therefore plays a role (of a few %) in the noise measurement of the sensor stream covered by the hybrid/power-board. This additional capacitance affects the sensor inter-strip capacitance due to the glue and the back-plane capacitance due to the hybrid ground. Those quantities are mainly proportional to the glue thickness (120  $\mu\text{m}$ ) and the portion of strip covered by glue, listed in table 6.4. The noise values for Star silicon modules were estimated using equation 6.4 as function of input capacitance  $C_{tot} = C_{sensor} + C_{int} + C_{bp}$ , where:

- $C_{sensor}$  is the value measured on real sensors by colleagues in Carleton [104];
- $C_{int}$  is the additional inter-strip capacitance due to the hybrid gluing;

- $C_{bp}$  is the back-plane capacitance due to the hybrid grounding.

$$ENC = \sqrt{12689.4 \cdot C_{tot}^2 + 236199} \quad (6.4)$$

The parameters in equation 6.4 are obtained from the fit to known noise values measured on barrel modules with *ATLAS12* sensors for which the noise trend is well understood [104], as the black curve in figure 6.12.

Comparing the nominal noise values in table 6.4, the noise in stream S0 is always greater than the one in stream S1 because this is where the electronics is glued on,

Module Stream	strip length [cm]	covered strip portion [cm]	$C_{sensor}$ [pF]	$C_{int}$ [pF]	$C_{bp}$ [pF]	Input noise ENC
R0H0S0	2.4	2	2.34	0.38	0.27	591.99
R0H0S1	1.9	0	1.89	0	0	530.59
R0H1S0	2.9	2	2.87	0.38	0.27	626.88
R0H1S1	3.2	0	3.13	0	0	600.43
R1H0S0	2.7	2	2.69	0.38	0.27	614.28
R1H0S1	1.8	0	1.82	0	0	527.48
R1H1S0	2.4	2	2.43	0.38	0.27	596.81
R1H1S1	1.5	0	1.49	0	0	514.17
R2H0S0	3.1	2.5	3.04	0.47	0.34	651.10
R2H0S1	3.1	0	3.08	0	0	597.14
R2H1S0	3.1	2	3.04	0.38	0.27	639.15
R2H1S1	3.1	0	3.08	0	0	597.14
R3H0S0	3.2	2.7	3.27	0.51	0.36	673.63
R3H0S1	2.6	0	2.71	0	0	573.92
R3H1S0	3.2	2	3.27	0.38	0.27	656.27
R3H1S1	2.6	0	2.71	0	0	573.92
R3H2S0	3.2	2.7	3.23	0.51	0.36	670.52
R3H2S1	2.6	0	2.59	0	0	566.85
R3H3S0	3.2	2	3.23	0.38	0.27	653.25
R3H3S1	2.6	0	2.59	0	0	566.85
R4H0S0	5.4	2.7	5.44	0.51	0.36	861.14
R4H0S1	5.4	0	5.55	0	0	791.87
R4H1S0	5.4	2	5.44	0.38	0.27	840.27
R4H1S1	5.4	0	5.55	0	0	791.86
R5H0S0	6.0	2.7	6.02	0.51	0.36	915.82
R5H0S1	4.0	0	4.08	0	0	668.90
R5H1S0	6.0	2	6.02	0.38	0.27	894.36
R5H1S1	4.0	0	4.08	0	0	668.90

Table 6.4: Nominal values of input noise calculated for each module stream according with their input capacitance.

as shown in figure 6.10. For split modules there is also a small difference between stream S0 left and S0 right side due to the power-board glued on the right side only.

## 6.5 Thermal analysis and comparison with FEA simulation

The setup used for the electrical measurements on the petal allowed a thermal study on it too. The IR camera was used first as debugging tool to ensure that the electronics was powered and configured correctly. Thermograms on the petal at different CO<sub>2</sub> temperature were recorded, as shown in figure 6.21, to perform an offline analysis and check the general behavior of the petal over a CO<sub>2</sub> cycle, from  $-34^{\circ}\text{C}$  to  $18^{\circ}\text{C}$ . In order to know the temperature on single module of the thermogram, a selection of pixels was made and their temperature average provided the module temperature.

An example is given in figure 6.22 which shows the IR picture taken on the petal at  $-34^{\circ}\text{C}$  and the pixel selection is highlighted in figure 6.23. The temperature average of each module at different CO<sub>2</sub> set-point is plotted in figure 6.24. The thin bar indicates the span (max and min values) over the pixels and the thick one is the standard deviation. The mean values follow the same behaviour for all the modules, as can be seen in figure 6.25 where they are plotted in function of CO<sub>2</sub> temperature. On the EoS region the coldest temperature is measured, it can be explained looking at the EoS area which is smaller compared with the modules, it has only few elec-

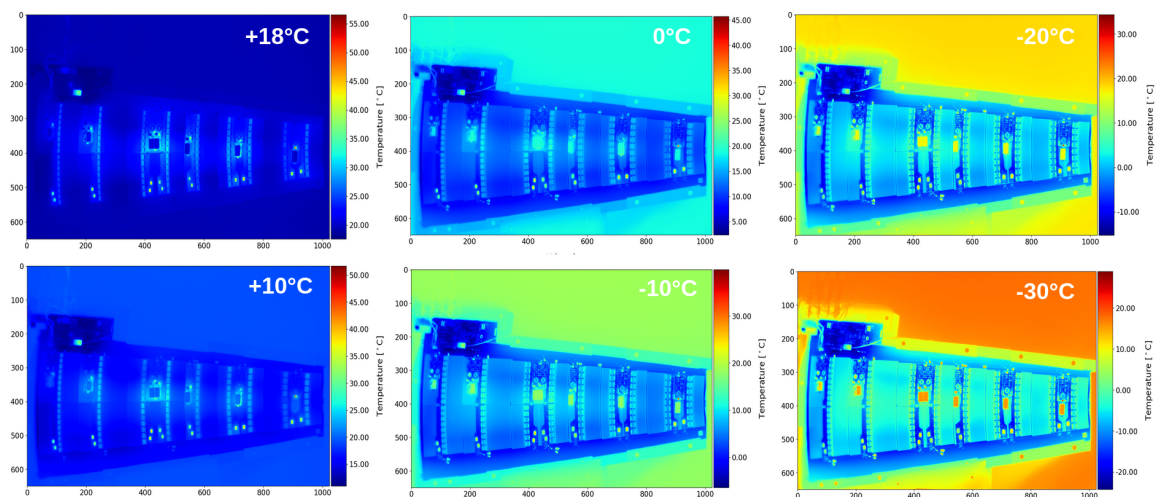


Figure 6.21: Petal thermograms (1024 x 678 pixels) for different CO<sub>2</sub> temperature, from  $18^{\circ}\text{C}$  to  $-30^{\circ}\text{C}$ .

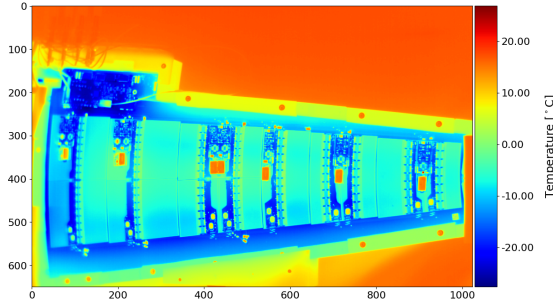


Figure 6.22: Petal thermogram at  $-34^{\circ}\text{C}$ .

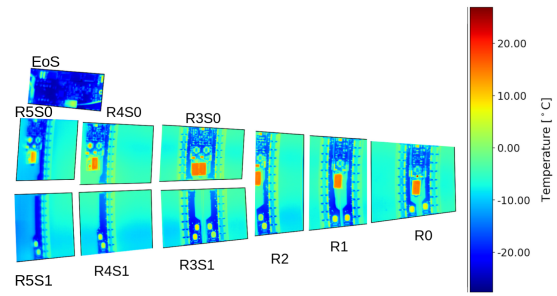


Figure 6.23: Selection to group the pixels in ten areas, including the EoS.

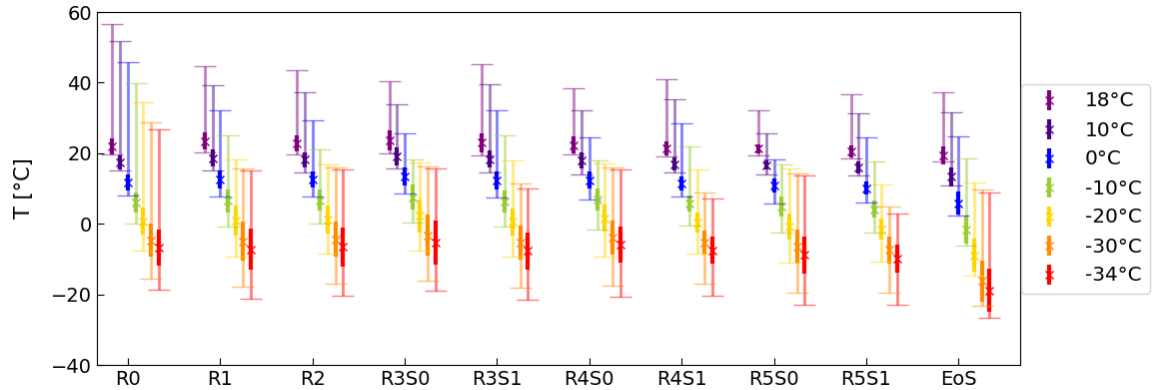


Figure 6.24: Temperature average (cross), standard deviation (thick line) and span (thin line) calculated for each module area and EoS card.

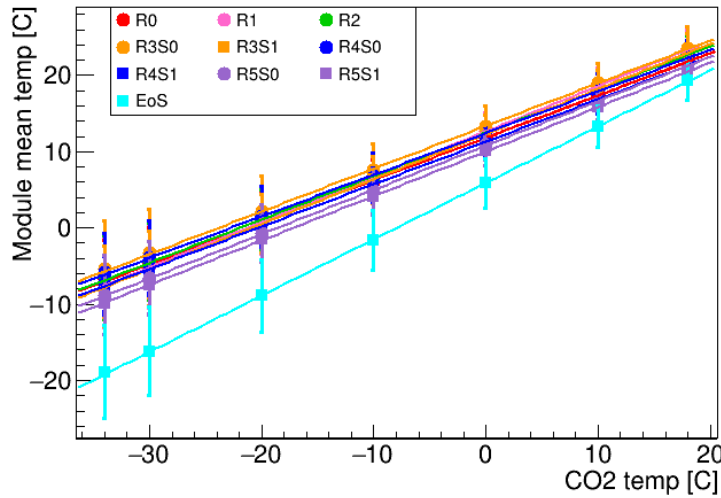


Figure 6.25: Mean temperature of each module as function of  $\text{CO}_2$  set-point on MARTA cooling machine.

trical components and it is covered by the cooling pipe all along its length. The highest temperature point on each module is measured on the shielding box as it is metallic, therefore its emissivity is very low and the ambient condition prevails on it, as already explained in section 5.1.3. This effect can be seen on the split modules:

the span is larger on the S0 portion, the one that hosts the power-board. Due to the presence of several materials with different emissivity, the measured values on the IR picture are not indicative of the real temperature, but they give an idea on the temperature behaviour.

A better comparison can be performed looking at the same module at different temperature, in this way the differences in emissivity due to the material can be ignored. The plot in figure 6.26 shows the result of this comparison: in each module the discrepancy is very consistent in most of the points, those are the values for which the CO<sub>2</sub> cycle moved in step of 10 °C. The purple point, as well as the red one, deviates from the trend because has 8 °C and 6 °C step difference, instead of 10. Figure 6.27 shows the same comparison with a zoomed view on the y axis to highlight the small temperature discrepancy between the measurements. This analysis confirmed that the module are cooled down in the same way, regardless of their position on the petal.

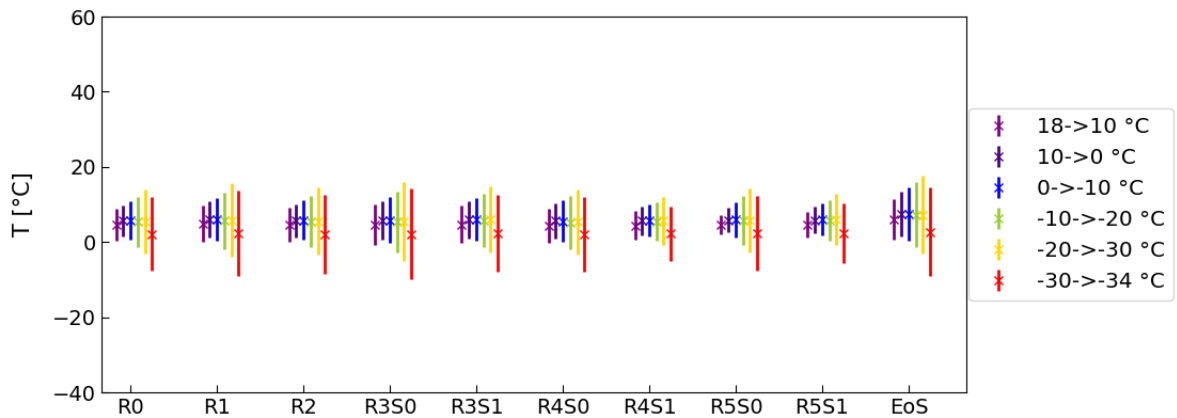


Figure 6.26: Temperature discrepancy (cross) between two following CO<sub>2</sub> set-points and standard deviation (error bar) on the same module area.

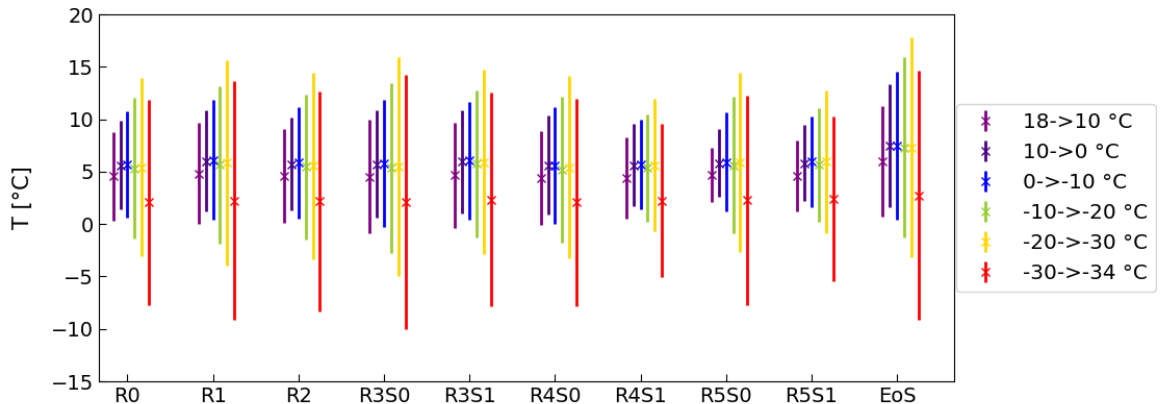


Figure 6.27: Zoomed view of the plot in figure 6.26.

### 6.5.1 FEA simulation

Many physical phenomena, such as structural or fluid behavior, thermal transport, wave propagation etc are described using partial differential equations. Numerical techniques, based on Finite Element Method (FEM), are developed to solve them, so called *Finite Element Analysis* (FEA). The FEA simulates any given physical phenomenon to estimate the structural behavior under a given load. To find a solution, the large system of the problem is divided into smaller and simpler parts, called finite elements. Solutions of the partial differential equations are found on each intersection point of a mesh applied to the complex object under study to discretize it.

The thermo-electrical FEA simulation of the electrical petal is performed importing the CAD file to visualize all the components. Several steps are needed to get started with the simulation, such as:

- definition of the mesh of points and its density, as shown in figure 6.28;
- definition of all materials involved in the petal design, specifying the contact surfaces and their *Heat Transfer Coefficient* (HTC), shown in the table in figure 6.29. It is obtained as  $K/thickness$ , with K being the thermal conductivity of the material;
- setting the power consumption values of the petal electronics, discussed in section 6.3.1 and listed in the table in figure 6.7;
- using the *CO<sub>2</sub> Branch Calculator* (CoBrA) [105] simulation to find the HTC value between the evaporative CO<sub>2</sub> and the titanium along the cooling pipe (the HTC value increases from 5000 W/m<sup>2</sup>K at the inlet to 9000 W/m<sup>2</sup>K at the outlet and an average of 7000 W/m<sup>2</sup>K is chosen for the FEA simulation);
- resistivity of silicon sensors: it is included in the simulation only when the sensors are irradiated. In this scenario the leakage current, that is correlated to the resistivity as  $I \propto 1/R$ , becomes important and generates significant heat at high currents. The trend is shown in figure 6.30 as function of CO<sub>2</sub> temperature. The values of resistivity are obtained on a sensor irradiated with  $\phi = 6.34 \cdot 10^{14} n_{eq}/cm^2$ , estimated as radiation fluence at the end of life of the detector;
- different sensor bias voltages are used to consider the different radiation doses of sensors due to their distance from the beam since the resistivity is kept

constant:  $-632\text{ V}$ ,  $-572\text{ V}$ ,  $-536\text{ V}$ ,  $-500\text{ V}$ ,  $-463\text{ V}$  and  $-436\text{ V}$  from R0 to R5 module.

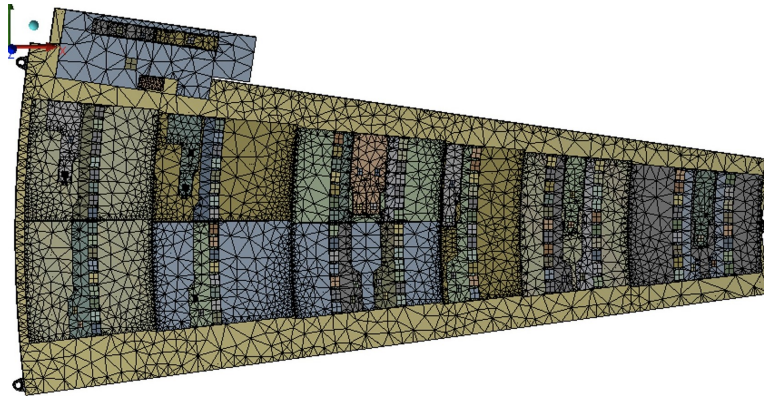


Figure 6.28: CAD file of fully populated petal and application of the mesh.

Part or contact	Material	$K_x/K_y/K_z$ [ $\text{W m}^{-1} \text{K}^{-1}$ ]	Thickness [mm]
ASIC	Silicon	191 (250 K)-148 (300 K)	0.30
ABC to hybrid	UV cure glue	0.5	0.08
HCC to hybrid	UV cure glue	0.5	0.08
Hybrid PCB	Cu/polymide	72/72/0.36	0.2
Power PCB	Cu/polymide	120/120/3	0.3
PBC to sensor	FH5313 Epolite	0.23	0.12
Sensor	Silicon	191 (250 K)-148 (300 K)	0.30
Sensor to bus	DC SE4445	2.	0.1-0.2
Bus tape	Polymide/Cu/Al	0.17/0.17/0.17	0.24
Bus to CF	ideal		
CF	0-90-0 CFRP	180/90/1	0.15
CF to allcomp	Hysol 9396 + graphyte	1	0.1
Allcomp	Allcomp 2 g/cm3	17	5
Allcomp to pipe	Hysol 9396 + graphyte	1	0.1
Pipe	Titanium	16.4	0.14-0.15

Figure 6.29: Petal components and materials with HTC specifications [103].

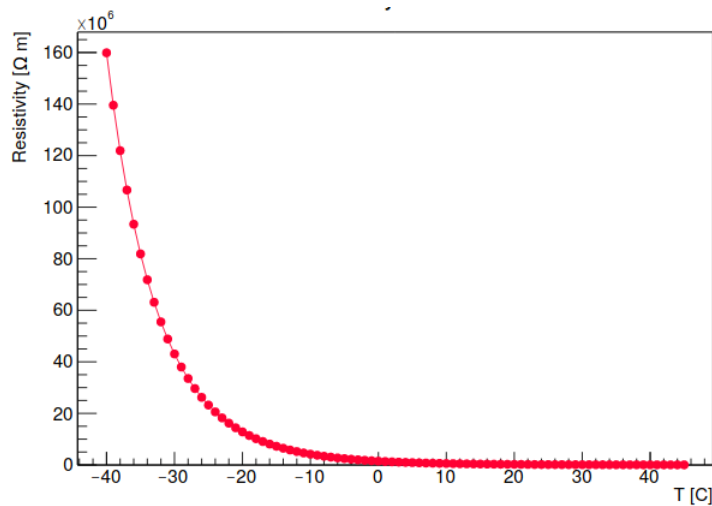


Figure 6.30: Silicon sensor resistivity versus  $\text{CO}_2$  temperature, used for FEA simulation with irradiated sensors [103]. The leakage current is correlated to the resistivity with inverse proportionality.

The FEA simulation gives an estimation of the critical temperature of the sensor runaway, which appears at  $-11\text{ }^{\circ}\text{C}$  of  $\text{CO}_2$  cooling. Figure 6.31 shows the temperature distribution on the petal when the  $\text{CO}_2$  is set to  $-10\text{ }^{\circ}\text{C}$  at the end of life. Here a massive amount of heat ( $500\text{ }^{\circ}\text{C}$ ) is generated by the split modules and not dissipated, in particular on the R4 module due to its position relative to the cooling loop shape. The plot in figure 6.32 shows the maximum temperature measured on the petal as function of  $\text{CO}_2$  temperature: for  $\text{CO}_2$  temperature higher than  $-10\text{ }^{\circ}\text{C}$  the petal can not be cooled down further because the sensors reached their critical temperature and the runaway status.

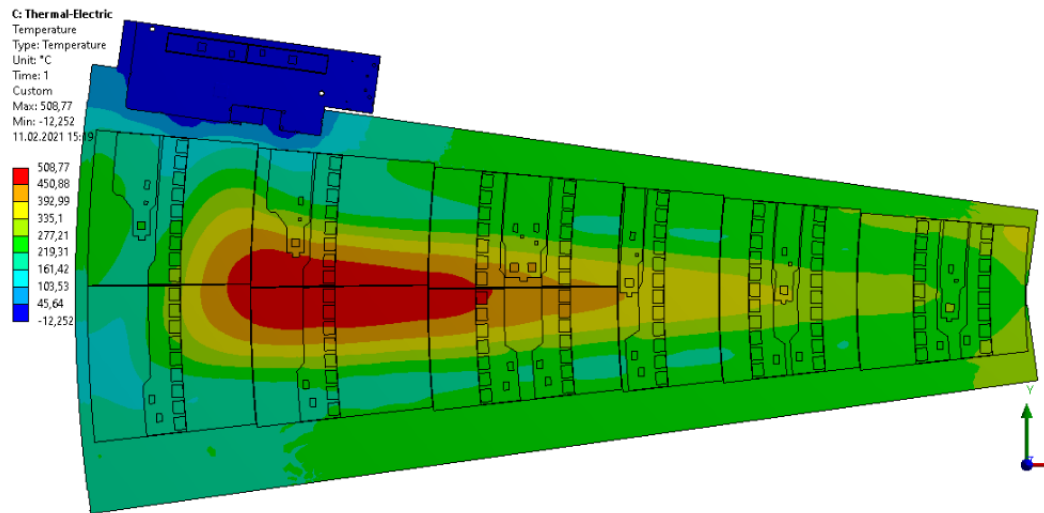


Figure 6.31: Thermo-electrical petal simulation at  $-10\text{ }^{\circ}\text{C}$   $\text{CO}_2$  temperature at end of life, the critical temperature of the sensor runaway is already reached [106]. The temperature range goes from  $-12\text{ }^{\circ}\text{C}$  in blue to  $500\text{ }^{\circ}\text{C}$  in red.

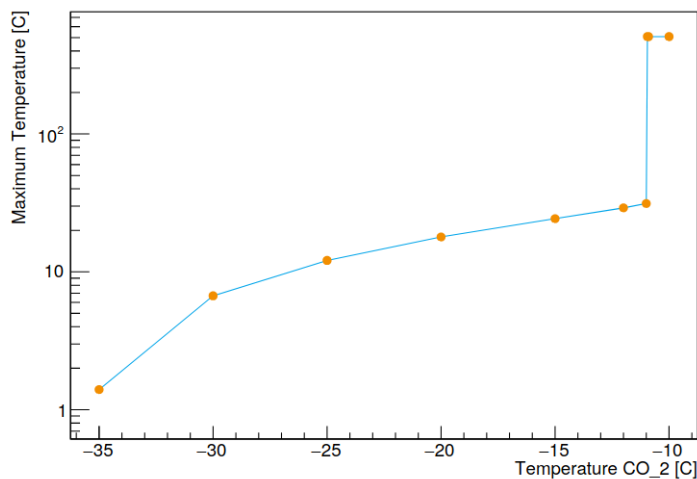


Figure 6.32: Maximum temperature simulated on petal plotted as function of  $\text{CO}_2$  cooling temperature at end of life [106].

## 6.5.2 Temperature comparison of the petal electronics

In order to get an estimation of the temperature on the petal, the FEA simulation was adapted to be as close as possible to the real petal under test [107]:

- petal powered only on the front side;
- HTC value for the air contact set to  $10 \text{ W/m}^2\text{K}$  (corresponding to air at  $20^\circ\text{C}$  inside the PTM);
- the sensor's resistivity is negligible due to the usage of non irradiated sensors;
- $\text{CO}_2$  temperature set to  $18^\circ\text{C}$ , as working set-point;

The temperature values provided by the simulation can be compared with measurements recorded by NTCs (Negative Temperature Coefficient) thermistors present on the modules. Each module has three NTCs: one placed on the power-board inside the shield-box, close to the DCDC, and one on each module hybrid. The NTCs are controlled via the AMAC and they need to be calibrated first. Figure 6.33 shows the FEA simulation of the petal with temperature probes placed where physically the NTCs are located. The values of temperature in table 6.5, obtained from the simulation and measured by the NTCs, are compared. R2 and R5 modules have listed only the simulated values because the NTCs were not functional on those modules. R3 module is divided in low and up because its power-board hosts 2 AMACs, one

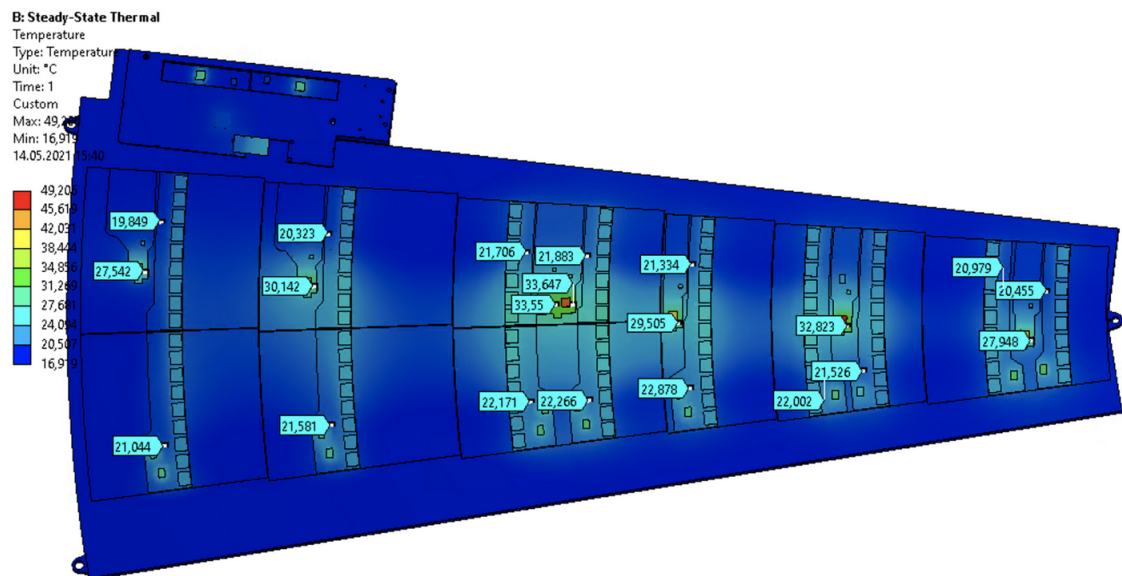


Figure 6.33: FEA thermal simulation with probes on the NTC positions to read the temperature.

	R0		R1		R2	R3 low		R3 up		R4		R5
	ntc	fea	ntc	fea	fea	ntc	fea	ntc	fea	ntc	fea	fea
H0	20.0	20.4	22.8	21.5	21.3	X	21.8	X	21.7	19.3	20.3	19.8
H1	19.4	21.0	22.9	22.0	22.8	21.9	22.2	21.1	22	21.5	21.6	30.1
PB	31.3	28.0	46.1	32.8	29.5	37.9	33.6	39.1	33.5	42.6	30.1	27.5

Table 6.5: Comparison of NTC readings and temperature results from the FEA simulation with CO<sub>2</sub> set to 18°C. All values are in °C. H0 and H1 indicate the value on hybrid 0 and 1 and PB the value on power-board.

controls R3H0 and R3H1 hybrids (*R3 low*) and the second one controls R3H2 and R3H3 (*R3 up*). The NTCs on R3H0 and on R3H2 were not functional either. The temperature on the power-board is known to be higher than the temperature on the hybrid because of the DCDC converter which is considered as the hottest component of the module. This is confirmed by the values in the table from both FEA and NTCs.

Comparing the simulated value with the NTC measurements, the best agreement is found on hybrids: in all modules the difference is about 1°C. A much larger difference is obtained on the power-board due to the non-simulated effect of the shield-box in the FEA. The NTC measures a higher temperature probably because the metallic box does not allow the heat dissipation by the air ventilation. The FEA simulation needs few improvements that concern the inclusion of the shield-box on the power-board and the correct glue pattern between modules and the petal core.

NTC measurement allowed the monitoring of the petal temperature also during a CO<sub>2</sub> cooling cycle if the AMACs are constantly powered on. The temperature trend measured by all NTCs is plotted in figure 6.34 during a CO<sub>2</sub> ramp down from 18°C to -34°C. The NTCs placed on power-board are showed with the pink palette, the ones on hybrid 0 (H0) in green palette and hybrid 1 (H1) in blue palette. The black curve represents the CO<sub>2</sub> temperature measured at the inlet. At each plateau with constant temperature, electrical tests were performed on the petal: the spikes on the AMACs' curves are due to the communication with the chips and the ones on the hybrid' curves are due to the testing. When all the electrical tests were completed, MARTA was switched off and the CO<sub>2</sub> temperature started to increase as well as the temperature of the electronics.

**Conclusions** All QC tests on a fully electrical petal were successfully performed for the first time with the support of the whole ITk strip collaboration. The power consumption investigation provided results in first approximation close enough to the estimated power generated on petal and simulated with a thermo-electrical model.

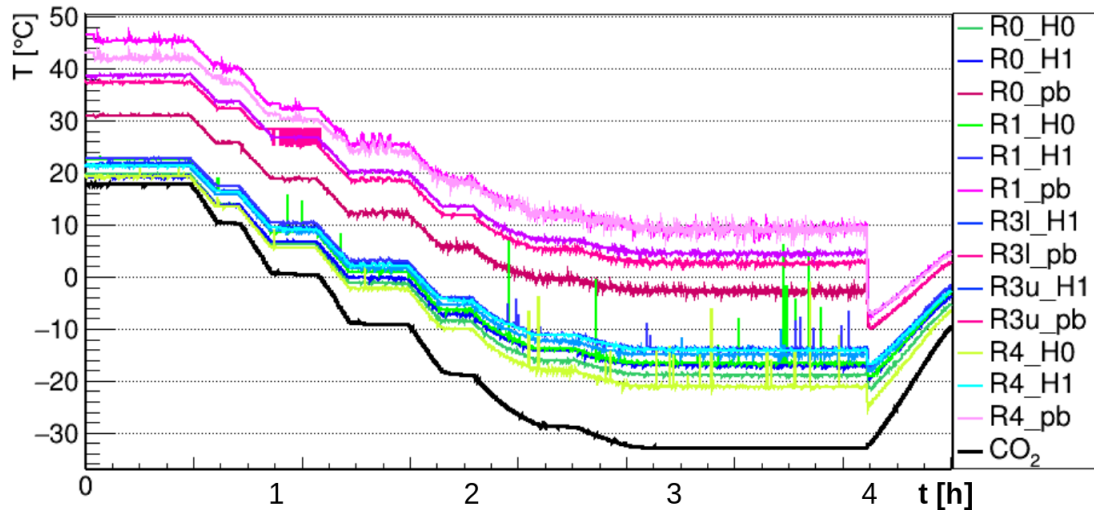


Figure 6.34: Temperature behaviour measured on hybrids and power-board for each module and CO<sub>2</sub> reading at the inlet as function of time during a full cycle. NTCs on R2 and R5 module were not functional.

The electrical results are very promising, the communication with EoS and modules via optical fiber worked and the input noise behaved as expected, except for the R2 module, for which more studies are needed to understand the inverse noise trend. Further electrical tests on modules assembled with building tools to have the glue thickness under control, can clarify the excess of noise in the S0 module stream.

The thermal analysis on loaded petals is not required by the designed QC routine, but it was a good practice to better understand the functionality of the petal at cold temperature and the heat dissipation. It was demonstrated that the FEA simulation is an excellent tool to foresee the petal behaviour in different conditions, such as CO<sub>2</sub> temperatures, irradiated/non-irradiated modules and to determine the critical temperature for the sensor runaway.

Results presented here proved that some improvements are required for the next generation of prototypes: modules built with proper tooling, updated hybrid design and power-boards for all modules with an improved coil shielding.

# Conclusions

This PhD project is focused on the upgraded design of the ATLAS tracker, the Inner Tracker (ITk) and in particular on the main component of the strip endcap, so-called petal. The assembly of silicon modules as well as the required quality control (QC) tests on a prototyping module were presented. The qualified modules are loaded on a local support structure following a routine which guarantees a very precise placement. The investigation aimed for the demonstration of the optimized building method of silicon modules and their mounting on the local support structure. The results of the QC tests performed on the petal at the final assembling stage provide the validation of the procedure thanks to the fulfillment of the specifications agreed by the ITk collaboration.

The most important results shown in this thesis are summarized in three big milestones: module building, module loading and electrical petal testing.

**Module Building** One copy of the R2 Star module of the strip endcap was successfully built at DESY using a dedicated set of tooling to glue the front-end chips on the hybrid and the hybrid on the sensor. A glue dispensing robot was used to dispense the glue in order to mount ABC and HCC Star chips on hybrid and hybrid on sensor. The metrology results showed that the glue layers heights are within the specification of  $(120 \pm 40) \mu\text{m}$  as well as the final module bowing. The electrical QC tests performed on the module demonstrated the success of the assembly procedure. The communication with the electronics was achieved, although two front-end chips were not read out correctly due to an improper setting in the configuration file. The glue pattern design for the power-boards stencils was also investigated, as an alternative to the glue dispensing robot. It was developed for all four flavours of board required for the endcap Star modules. Only the R0-R1 pattern was successfully tested with dummy parts due to a lack of mechanical components and tools, and the results of these tests were presented.

**QC on local support structure and Module Loading** The local support structure is subjected to QC tests after the assembly to be qualified as suitable for the loading of modules. A set of tests was presented in this project: mechanical, electrical and thermal analysis. Results on a petal core under thermal tests using evaporating CO<sub>2</sub> as coolant showed that the heat dissipation is uniform along the full length of the cooling pipe and the module areas are cooled down in the same way. The infrared imaging technique allows also to highlight possible defects during the core assembling that cause an interruption on the thermal path, thus the rejection of the core.

The performance and the precision of the module loading procedure was proved by the assembly of a semi-electrical petal. A petal core structure was populated with ABC 130 prototyping modules having mechanical silicon sensor and fully functional electronics. The assembly of the semi-electrical petal was shown together with the QC tests performed on it. The placement of six endcap modules was done successfully. The final survey of all the sensor fiducial marks established the accuracy of the placement: the global deviation in X and Y from the nominal position is  $(-8 \pm 18) \mu\text{m}$ , well within the required accuracy of  $\pm 50 \mu\text{m}$ .

The glue pattern developed for the mechanical stability of modules and for the heat dissipation is demonstrated to be adequate during the electrical test. The electrical tests performed simultaneously on all modules of the semi-electrical petal showed a proper communication with them and a level of input noise within the expectations. The noise measured on each module on test-frame before the loading and on petal after the loading is comparable, which means that the placement procedure did not affect the functionality of the modules.

**Electrical Petal Testing** The first petal loaded with electrical Star modules on the front side arrived at DESY to perform electrical tests at cold temperature. The main goal of this investigation was the confirmation that each petal component works as expected at the nominal cold temperature. The dual-phase CO<sub>2</sub> was supplied by the MARTA cooling machine at  $-35^\circ\text{C}$ , temperature at which the whole ITk detector is cooled down in the ATLAS experiment.

The input noise of each module was measured at different CO<sub>2</sub> temperatures in the range  $[-34, 18]^\circ\text{C}$  and compared with the estimated values. Some of those were higher than the estimation due to the manual gluing of the electronics on the sensor, which affects the glue layer thickness and thus the noise. The noise trend as function of CO<sub>2</sub> temperature followed the expectation for most of the modules, except for the R2 one which behaved differently, for reasons still to be clarified. The sensor current

of each module on the petal was also monitored during the sensor ramp up. The setup used for this study allowed a thermal analysis on the populated core. The infrared images on the petal as function of CO<sub>2</sub> temperature were analysed in order to investigate the dissipation of the modules heat. The cooling performance appeared to be uniform for all modules and the coldest temperature on the petal was measured on the EoS. The thermistors (NTCs) on hybrids and power-boards allowed the temperature monitoring of the electronics and they were compared with the values provided by a FEA simulation. A comparison at 18°C CO<sub>2</sub> temperature set on the cooling machine was investigated, demonstrating very consistent values on hybrids, rather than on the power-board.

This PhD project presented the building steps of the silicon strip modules for the ITk endcap detector. Starting from the performance studies on its most elementary unit, the silicon sensor, the investigation advanced towards the achievement of a fully loaded petal. The validation of the assembling methods is confirmed by the results of quality control tests performed at each building stage. Petals that satisfy all the mechanical, thermal and electrical requirements are allowed to be inserted into the global structure of the endcap being part of the ATLAS experiment during HL-LHC.

# Bibliography

- [1] L. Evans and P. Bryant. ‘LHC Machine’. In: *JINST* 3.08 (2008). DOI: 10.1088/1748-0221/3/08/s08001.
- [2] W. Herr and B. Muratori. ‘Concept of luminosity’. In: (2006). DOI: 10.5170/CERN-2006-002.361.
- [3] *The CERN accelerator complex*.
- [4] *LHC the guide faq*.
- [5] M. Thomson. *Modern Particle Physics*. Cambridge University Press, 2013. DOI: 10.1017/CB09781139525367.
- [6] ATLAS Collaboration. ‘The ATLAS Experiment at the CERN Large Hadron Collider’. In: *JINST* 3.08 (2008). DOI: 10.1088/1748-0221/3/08/s08003.
- [7] CMS Collaboration. ‘The CMS experiment at the CERN LHC’. In: *JINST* 3.08 (2008). DOI: 10.1088/1748-0221/3/08/s08004.
- [8] ALICE Collaboration. ‘The ALICE experiment at the CERN LHC’. In: *JINST* 3.08 (2008). DOI: 10.1088/1748-0221/3/08/s08002.
- [9] LHCb Collaboration. ‘The LHCb Detector at the LHC’. In: *JINST* 3.08 (2008). DOI: 10.1088/1748-0221/3/08/s08005.
- [10] *High-Luminosity LHC, project schedule, as in December 2021*.
- [11] B. Schmidt. ‘The High-Luminosity upgrade of the LHC: Physics and Technology Challenges for the Accelerator and the Experiments’. In: *Journal of Physics: Conference Series* 706 (2016). DOI: 10.1088/1742-6596/706/2/022002.
- [12] *Crab cavities at CERN*.
- [13] J. Pequeno and P. Schaffner. ‘How ATLAS detects particles: diagram of particle paths in the detector’. Jan. 2013.
- [14] H.H.J. Kate. ‘ATLAS superconducting toroids and solenoid’. In: *IEEE Transactions on Applied Superconductivity* 15.2 (2005). DOI: 10.1109/TASC.2005.849560.
- [15] ATLAS Collaboration. *ATLAS inner detector: Technical Design Report, 1*. Tech. rep. CERN-LHCC-97-016. Geneva, 1997.
- [16] H. Spieler. *Semiconductor detector systems*. Semiconductor Science and Technology. Oxford, 2005. DOI: 10.1093/acprof:oso/9780198527848.001.0001.

- [17] F. Hartmann. *Evolution of Silicon Sensor Technology in Particle Physics*. Vol. 275. Springer Tracts in Modern Physics. Springer, 2017. DOI: 10.1007/978-3-319-64436-3.
- [18] CW. Fabjan and F Gianotti. ‘Calorimetry for Particle Physics’. In: *Rev. Mod. Phys.* 75.CERN-EP-2003-075 (2003). DOI: 10.1103/RevModPhys.75.1243.
- [19] ATLAS Collaboration. *ATLAS liquid-argon calorimeter: Technical Design Report*. Tech. rep. Geneva, 1996.
- [20] ATLAS Collaboration. *ATLAS tile calorimeter: Technical Design Report*. Tech. rep. CERN-LHCC-96-042. Geneva, 1996.
- [21] ATLAS Collaboration. *ATLAS muon spectrometer: Technical Design Report*. Tech. rep. CERN-LHCC-97-022. Geneva, 1997.
- [22] William R Leo. *Techniques for nuclear and particle physics experiments: a how-to approach; 2nd ed.* Berlin: Springer, 1994. DOI: 10.1007/978-3-642-57920-2.
- [23] T. Kawamoto et al. *New Small Wheel Technical Design Report*. Tech. rep. CERN-LHCC-2013-006, ATLAS-TDR-020. 2013.
- [24] M Aleksa et al. *ATLAS Liquid Argon Calorimeter Phase-I Upgrade: Technical Design Report*. Tech. rep. CERN-LHCC-2013-017, ATLAS-TDR-022. 2013.
- [25] G. Aad et al. ‘Technical Design Report for the Phase-I Upgrade of the ATLAS TDAQ System’. In: CERN-LHCC-2013-018, ATLAS-TDR-023 (2013).
- [26] A. Farzinnia, Hong-Jian He and Jing Ren. ‘Natural electroweak symmetry breaking from scale invariant Higgs mechanism’. In: *Physics Letters B* 727.1 (2013). ISSN: 0370-2693. DOI: <https://doi.org/10.1016/j.physletb.2013.09.060>.
- [27] ATLAS Collaboration. ‘Observation of a new particle in the search for the Standard Model Higgs boson with the ATLAS detector at the LHC’. In: *Physics Letters B* 716.1 (2012).
- [28] CMS Collaboration. ‘Observation of a new boson at a mass of 125 GeV with the CMS experiment at the LHC’. In: *Physics Letters B* 716.1 (2012). DOI: <https://doi.org/10.1016/j.physletb.2012.08.021>.
- [29] *The Nobel Prize in Physics*. 2013.
- [30] G. Aad et al. ‘Combined Measurement of the Higgs Boson Mass in pp Collisions at  $\sqrt{s}=7$  and 8 TeV with the ATLAS and CMS Experiments’. In: *Physical review letters* 114.19 (2015).
- [31] A. Hebecker. ‘The Standard Model and Its Hierarchy Problem (s)’. In: *Naturalness, String Landscape and Multiverse*. Springer, 2021.
- [32] *The theory of Supersymmetry*.

- [33] *Dark Matter*.
- [34] L. Roszkowski, E. Sessolo and S. Trojanowski. ‘WIMP dark matter candidates and searches—current status and future prospects’. In: *Reports on Progress in Physics* 81.6 (2018). DOI: 10.1088/1361-6633/aab913.
- [35] A. Dainese et al. *Report on the Physics at the HL-LHC, and Perspectives for the HE-LHC*. Tech. rep. CERN-2019-007. Geneva, Switzerland, 2019. DOI: 10.23731/CYRM-2019-007.
- [36] A. Buras, F. Parodi and A. Stocchi. ‘The CKM Matrix and The Unitarity Triangle: Another Look’. In: 2003.01 (2003). DOI: 10.1088/1126-6708/2003/01/029.
- [37] ATLAS Collaboration. *Technical Design Report for the ATLAS Inner Tracker Strip Detector*. Tech. rep. CERN-LHCC-2017-005. Geneva: CERN, 2017.
- [38] R. Placakyte. ‘Parton Distribution Functions’. In: *arXiv preprint arXiv: 1111.5452* (2011).
- [39] ATLAS Collaboration. *Prospects for benchmark Supersymmetry searches at the high luminosity LHC with the ATLAS Detector*. Tech. rep. ATL-PHYS-PUB-2013-011. Geneva: CERN, 2013.
- [40] ATLAS Collaboration. *ATLAS Liquid Argon Calorimeter Phase-II Upgrade: Technical Design Report*. Tech. rep. CERN-LHCC-2017-018, ATLAS-TDR-027. Geneva: CERN, 2017.
- [41] ATLAS Collaboration. *Technical Design Report for the Phase-II Upgrade of the ATLAS Tile Calorimeter*. Tech. rep. CERN-LHCC-2017-019, ATLAS-TDR-028. Geneva: CERN, 2017.
- [42] ATLAS Collaboration. *Technical Design Report for the Phase-II Upgrade of the ATLAS Muon Spectrometer*. Tech. rep. CERN-LHCC-2017-017, ATLAS-TDR-026. Geneva: CERN, 2017.
- [43] ATLAS Collaboration. *Technical Design Report for the Phase-II Upgrade of the ATLAS TDAQ System*. Tech. rep. CERN-LHCC-2017-020, ATLAS-TDR-029. Geneva: CERN, 2017.
- [44] ATLAS Collaboration. *Technical Design Report for the ATLAS Inner Tracker Pixel Detector*. Tech. rep. CERN-LHCC-2017-021, ATLAS-TDR-030. Geneva: CERN, 2017.
- [45] ATLAS Collaboration. *Expected tracking and related performance with the updated ATLAS Inner Tracker layout at the High-Luminosity LHC*. Tech. rep. ATL-PHYS-PUB-2021-024. Geneva: CERN, 2021.

- [46] ATLAS Collaboration. *Expected Tracking Performance of the ATLAS Inner Tracker at the HL-LHC*. Tech. rep. ATL-PHYS-PUB-2019-014. Geneva: CERN, 2019.
- [47] ATLAS Collaboration. *Technical Proposal: A High-Granularity Timing Detector for the ATLAS Phase-II Upgrade*. Tech. rep. CERN-LHCC-2018-023, LHCC-P-012. Geneva: CERN, 2018.
- [48] H. Kolanoski and N. Wermes. *Particle Detectors: Fundamentals and Applications*. Oxford University Press, USA, 2020.
- [49] Gianluigi Casse. ‘Radiation hardness of p-type silicon detectors’. In: *Nuclear Instruments and Methods in Physics Research Section A: Accelerators, Spectrometers, Detectors and Associated Equipment* 612.3 (2010).
- [50] *Radiation Simulation Public Results* .
- [51] P.A. Zyla et al. ‘Review of Particle Physics’. In: *PTEP* 2020.8 (2020). DOI: 10.1093/ptep/ptaa104.
- [52] JH. Arling. ‘Detection and Identification of Electrons and Photons: Applications in the ATLAS Experiment, for the ATLAS ITk Detector and at the DESY II Test Beam’. PhD thesis. Dortmund U., 2020. DOI: 10.17877/DE290R-21676.
- [53] ATLAS Collaboration. *Letter of Intent for the Phase-II Upgrade of the ATLAS Experiment*. Tech. rep. CERN-LHCC-2012-022. Geneva: CERN, 2012.
- [54] F. Carrio Argos et al. *Design of Bus Tapes for the ATLAS Strip End-Cap at the HL-LHC*. Tech. rep. ATL-ITK-PROC-2020-009. Geneva: CERN, 2020.
- [55] *LOCTITE EA 9396*. URL: [https://tdsna.henkel.com/americas/na/adhesives/hnauttds.nsf/web/6E3301E8A06A082E85257BC60067B2D8/\\$File/LOCTITE%20EA%209396%20AERO-EN.pdf](https://tdsna.henkel.com/americas/na/adhesives/hnauttds.nsf/web/6E3301E8A06A082E85257BC60067B2D8/$File/LOCTITE%20EA%209396%20AERO-EN.pdf).
- [56] *Solvay Torlon 4301*.
- [57] *Petal core Technical Drawing, EDMS*.
- [58] C. Lacasta et al. *Design of the first full size ATLAS ITk Strip sensor for the endcap region*. Tech. rep. ATL-ITK-PROC-2018-010. Geneva: CERN, 2018.
- [59] W. Lu et al. ‘Development of the ABCStar front-end chip for the ATLAS silicon strip upgrade’. In: *JINST* 12.04 (2017). DOI: 10.1088/1748-0221/12/04/C04017.
- [60] A. Affolder et al. ‘DC-DC converters with reduced mass for trackers at the HL-LHC’. In: *JINST* 6 (2011). DOI: 10.1088/1748-0221/6/11/C11035.
- [61] C. Wanotayaroj et al. ‘The End-of-Substructure (EoS) card for the Strip Tracker Upgrade of the ATLAS experiment’. In: *PoS TWEPP2018* (2019). DOI: 10.22323/1.343.0130.

- [62] *ELGOline company*.
- [63] *AVS company*.
- [64] J. Neundorf. *Testing the Prototype of the Endcap Coldbox*. Tech. rep. ATL-COM-ITK-2021-003. Geneva: CERN, 2021.
- [65] A. Wongel. *ATLAS ITK Endcap service trays, qualification task report*. 2020.
- [66] *LUCASZ CO<sub>2</sub> cooling machine*.
- [67] W. Wu. ‘FELIX: the New Detector Interface for the ATLAS Experiment’. In: *IEEE Transactions on Nuclear Science* 66.7 (2019).
- [68] *Hamamatsu company*.
- [69] J. Fernández-Tejero et al. ‘Humidity sensitivity of large area silicon sensors: Study and implications’. In: *Nuclear Instruments and Methods in Physics Research Section A: Accelerators, Spectrometers, Detectors and Associated Equipment* 978 (2020).
- [70] *Henkel Loctite AA 3525 technical data sheet*.
- [71] *Nordson EFD PROPlus, Automated dispensing system*.
- [72] *Ultimus V Nordson EFD glue dispenser*.
- [73] *SmartScope OGP CNC 670*.
- [74] *ISO Standard 12781 for flatness definition*.
- [75] M. Warren et al. *Strips Upgrade DAQ*. 2020.
- [76] B.J. Gallop et al. *ITSDAQ software for module testing, Gitlab*.
- [77] *Digilent Inc., Nexys Video FPGA development board documentation*.
- [78] L. Poley et al. ‘The ABC130 barrel module prototyping programme for the ATLAS strip tracker’. In: *JINST* 15.09 (2020). DOI: 10.1088/1748-0221/15/09/p09004.
- [79] A. Rodriguez Rodriguez et al. *Test beam performance of ITk-Strip ABCStar Module*. Dec. 2021.
- [80] *Petal core specifications, EDMS*.
- [81] *ITk grounding and shielding requirements, EDMS*.
- [82] M. Vollmer and KP. Möllmann. *Infrared thermal imaging: fundamentals, research and applications*. John Wiley & Sons, 2017.
- [83] *ATLAS ITk detector specification for cooling system design, EDMS*.
- [84] P. Petagna et al. *MARTA Monoblock Approach for a Refrigeration Technical Application*. 2017.
- [85] *Ansys Mechanical Finite Element Analysis (FEA) Software for Structural Engineering*.
- [86] *Module loading specifications, EDMS*.
- [87] *Aerotech AGS10000 Gantry System specifications*.

- [88] *COGNEX in-sight 8000 camera.*
- [89] *SmartRay 3D sensors.*
- [90] *National Instrument NI 9476 switch.*
- [91] *Dow Corning SE4445 Datasheet.*
- [92] *Scott Beaupre. Private communication in March 2021.*
- [93] *Assembly procedure of petals, EDMS.*
- [94] *Rework policy for Loaded Local Supports of the ATLAS ITk Strip Tracker, EDMS.*
- [95] *InfraTec GmbH, "VarioCAM HD research 900".*
- [96] *Digilent, Genesys2 board.*
- [97] *CAEN HiVolta (DT1415ET) power supply.*
- [98] *TTi CPX400DP power supply.*
- [99] K. Brendlinger et al. *The Endcap Thermal Model, EDMS.* 2018.
- [100] A Chilingarov. 'Temperature dependence of the current generated in Si bulk'. In: *JINST* 8.10 (2013).
- [101] G. Beck et al. 'Thermo-electrical modelling of the ATLAS ITk Strip Detector'. In: *Nuclear Instruments and Methods in Physics Research Section A: Accelerators, Spectrometers, Detectors and Associated Equipment* 969 (2020). DOI: <https://doi.org/10.1016/j.nima.2020.164023>.
- [102] *Kurt Brendlinger. Private communication in September 2021.*
- [103] *Graham Beck. Private communication in September 2021.*
- [104] *First Endcap Star module test.*
- [105] B. Verlaat. *Evaporative CO<sub>2</sub> cooling for thermal control of scientific equipments.*
- [106] M. Baselga. *Thermoelectrical FEA simulations for the petal end of life.* 2021.
- [107] *Marta Baselga. Private communication in August 2021.*

# Acknowledgements

The development of this PhD project was achievable thanks to Ingrid that gave me the opportunity to join the DESY ATLAS upgrade team and to Kevin for accepting my supervision at University of Dortmund. I am glad to have been part of this amazing group and to have contributed to the ITk strip endcap detector construction. The biggest acknowledgement is for Sergio who guided me along the whole project, thanks to be always by my side during the good and also bad moments in which we went through.

The work presented here is the result achieved together with many other people that I met during the time I spent at DESY. Thanks to Marta, Ruchi, Sarah, Sonia, Othmane, Jan-Hendrik and Will for joining me during the daily adventures of the cleanroom. Thank you all for your collaboration, I think we did an excellent job! Thanks to Frauke for sharing with me her knowledge on the evaporative CO<sub>2</sub> cooling and allowed me to meet her best friends TRACI, MARTA and LUCASZ. I would like to thank Marta again for being available for any kind of clarification about silicon sensor technologies and for her help in providing the FEA simulation. Thanks to be such a good friend also outside the work and for sweetening the lockdown in the dark time of the Covid pandemic. I don't forget the huge help received by the DESY engineers and technicians, Anna-Lena, Lisa, Sören, Dario and Christian. Thank you for your support and the tons of good advises that you provided me on the mechanical aspect of things. Thanks to the world-wide ITk collaboration members, in primis Scott, Ingo and Jens, that have been always ready to answer my questions and providing very good suggestions to advance with my work. I learnt a lot from all of you and I will treasure this experience.

Now is the moment to thank all the other DESY students with which I enjoyed my free time in Hamburg, playing volleyball, experimenting new restaurants and traveling around Europe. A special thank is direct to Claire, the person who was close to me since my first day at DESY and helped me to get a smoother approach to a new city and in a new work environment.

Finally I have to thank my family, they have supported me in all my decisions since

my choice of the University, believing in my capability even without understanding the meaning of my work. Vi voglio bene!